TECHNISCHE UNIVERSITÄT DRESDEN

Fakultät für Physik
Institut für Festkörper- und Materialphysik

Topological Transport Effects and Pure Spin Currents in Nanostructures

Dissertation

zur Erlangung des akademischen Grades
Doctor rerum naturalium
(Dr. rer. nat.)

vorgelegt von

Richard Schlitz

geboren am 22.07.1990 in Meckenheim

Erstgutachter (Betreuer)	Prof. Dr. Sebastian T. B. Goennenwein
Zweitgutachter	Prof. Dr. Felix Casanova

TECHNISCHE UNIVERSITÄT DRESDEN

ct.qmat
Complexity and Topology
in Quantum Matter

SFB 1143

Just for the fun of it :)

Abstract

Magnetoresistive effects are powerful tools for studying the intricate structure of solid state electronic systems, and have many applications in our current information technology. In particular, the electronic system reflects the crystal symmetry and the orbital structure of the atoms of a given solid, and thus is crucial to understanding magnetism, superconductivity and many other effects which are of key interest to current solid state research. Consequently, studies of the electrical transport properties of solid state matter allow to evaluate this imprint and in turn draw conclusions about the interactions within a material. In this thesis, we will exploit the capabilities of magnetotransport measurements to infer the properties of a multitude of magnetic systems. In turn, this allows us to push the understanding of transport phenomena in magnetic materials.

The first part of this work is focused on the magnetoresistance observed in spin Hall active metals in contact with a magnetic insulator. In such bilayers, the interfacial spin accumulation caused by the spin Hall effect in the metal can interact with the magnetic insulator, giving rise to interesting magnetoresistive effects. In the framework of this thesis, bilayers with several magnetic insulators are studied, including antiferomagnets, ferrimagnets and paramagnets (disordered magnets). For the disordered magnetic insulators, we find that the established spin Hall magnetoresistance framework does not allow to consistently describe the observed transport response. Consequently, we propose an alternative explanation of the magnetoresistance in such heterostructures, using the Hanle magnetoresistance and assuming an interface which has a finite electrical conductivity. This alternative model can serve to generalize the theory of the spin Hall magnetoresistance, providing addition information on the microscopic picture for the loss of the transverse spin component. Additionally, by partly removing the magnetic insulator and studying the ensuing changes, we verify that magnons are crucial for the observation of a non-local magnetoresistance in bilayers of a magnetic insulator and a metal. Finally, the local and non-local spin Seebeck effect (i.e. the electric field generated by a thermally driven pure spin current) is investigated in bilayers of Cr_2O_3 and Pt where the occurrence

of a spin superfluid ground state was reported. In our sample, however, the transport response is consistent with the antiferromagnetic spin Seebeck effect mediated by the small magnetic field induced magnetization also reported for other antiferromagnet/metal heterostructures. As such, we cannot verify the presence of a spin superfluid ground state in the system.

In the second part of this thesis, the topological properties of the electronic system and the related changes of the magnetoelectric and magnetothermal transport response are investigated. To that end, we first demonstrate a novel measurement technique, the alternating thermal gradient technique, allowing to separate the relevant thermovoltages from spurious other voltages generated within the measurement setup. We employ this novel technique for measuring the topological Nernst effect in $Mn_{1.8}PtSn$ and show the possibility to combine the magnetoelectric and magnetothermal transport response to evaluate the presence of topological transport signatures without requiring magnetization measurements. Additionally, we show that the anomalous Nernst effect in the non-collinear antiferromagnet Mn_3Sn is connected to the antiferromagnetic domain structure: Using spatially resolved measurements of the anomalous Nernst effect, direct access to the antiferromagnetic domain structure is demonstrated. Additionally, a thermally assisted domain writing scheme is implemented, allowing the preparation of Mn_3Sn into a defined antiferromagnetic domain state.

Contents

Chapter 1

INTRODUCTION

1.1 Motivation

Magnetoresistive effects have permeated the history of fundamental solid state research, where new magnetoresistive effects often led to new discoveries and sometimes even applications. Thus, this thesis will begin with a short history of magnetoresistive effects to establish their significance in the context of fundamental research as well as to demonstrate some of their applications in modern technology. The first observation of a magnetoresistance (MR), i.e. a change of resistance upon application of a magnetic field, was reported by Lord Kelvin in 1856 in Ni and Fe.[18] Lord Kelvin recognized that the resistance of these (ferromagnetic) metals depends on the relative orientation of the electric current and the magnetic field. Thus, the magnetoresistance was named anisotropic magnetoresistance (AMR). The understanding that the (magnetic) properties and the external magnetic and electric fields around a material reflect in the electrical resistance is one fundamental observation upon which all further studies of magnetotransport are based. Another magnetoresistive effect is the Hall effect, uncovered by Edwin Hall some thirty years after the discovery of the AMR.[19,20] The Hall effect arises when a magnetic field is applied perpendicular to an electric current, generating an electric field in the third orthogonal direction. In a free electron gas (or in materials with only one parabolic conduction band) the Hall effect allows to determine the carrier concentration as well as the carrier type. The AMR and the Hall effect have found many applications in sensors of magnetic field orientation and strength. Today's smartphones are one prominent example where both types of effects are used: They feature a proximity sensor based on the Hall effect to detect whether the screen needs to be turned on or off and an AMR sensor used as a compass[21–23].

In addition, the ability to use magnetoresistive elements as electric sensors for mag-

1

netic fields opened the door to efficient high density magnetic data storage. One of the most prominent examples where this direct conversion from magnetic fields to electric voltages is used are hard drives: The first available devices used induction voltages generated by the moving magnetic bits for readout, such that the storage density and scalability of the drives was limited.[24] Only due to the larger sensitivity to magnetic fields of AMR elements it became possible to further increase the storage density in hard drives. Further improvements were achieved by using the giant magnetoresistance (GMR)[25,26] superseded more recently by the tunneling magnetoresistance (TMR).[27–29] Both effects show a larger magnetoresistance compared to the AMR, i.e. an even greater sensitivity to magnetic fields.[24,30]

Recently, there have been efforts to utilize not only the charge of electrons for computing but additionally their spin. In this field, tools to electrically detect spin currents have been discovered. Most notably, the spin Hall effect[31–34] allows to electrically generate and detect spin currents in non-magnetic metals (NM) with finite spin orbit coupling. In these NMs, where Pt is the prime representative, applying a charge current leads to the generation of a transverse spin current due to spin-dependent electron scattering or band structure effects.[35] However, in these NMs, the spin current is still carried by electrons and thus inherits all the associated downsides (e.g. ohmic losses and low diffusion distance).[36]

Therefore, in an effort to decouple the spin and charge degree of freedom, ferromagnetic insulator (FMI)/NM heterostructures have been intensively studied in different ways.[16,37–45] In such bilayers, similar magnetoresistive effects as in ferromagnetic metals can be found: The spin Hall magnetoresistance (SMR), caused by the interplay of the spin Hall effect and its inverse, becomes evident as a dependence of the NM resistance on the magnetization orientation of the FMI. In the SMR, a finite (pure) spin current can enter into the FMI through the FMI/NM interface more or less efficiently depending on the orientation of the magnetization. Thus, an additional channel for energy dissipation, depending on the magnetization direction, is present, which consequently changes the metal resistance.[42–44]

While the SMR is only a local probe, measuring the spin current and thus the dissipation flowing into the FMI, a second "non-local" detector, (electrically) insulated from the first one, can be placed in close vicinity to a local injector in more complex FMI/NM heterostructures. If, in such a configuration, a spin current is generated below the injector (i.e. by converting an electric current via the spin Hall effect), it can diffuse through the FMI and, given a small enough separation, reach the detector. There, the spin current can be electrically measured using the inverse spin Hall effect. This non-local effect is often called the magnon-mediated magnetoresistance (MMR) and allows to study the propagation of pure spin (magnon) currents.[16,40,41,45]

First experiments using such pure spin currents generated by the spin Hall effect for direct electrical writing of magnetic storage media have been presented.[46–48] There, a spin Hall active metal is used to inject a sufficiently large spin current into an adjacent (thin) ferromagnetic layer, inverting its magnetization via the spin orbit torque. A potential application has already been put forward: The spin orbit torque magnetic random access

memory (SOT–MRAM) in which the mechanism mentioned above is used for writing the magnetic state. The readout in these SOT–MRAMs is implemented using the TMR due to its large sensitivity. It was recently shown that such SOT–MRAMs can be integrated with the current CMOS technology, allowing the utilization as non-volatile integrated memory.[49]

Apart from these obvious applications in our current technology, magnetoresistive effects allow to study a zoo of interesting fundamental effects present in magnetic media. For example, non-collinear phases in ferrimagnetic insulators can be detected using the spin Hall magnetoresistance.[15,50,51] Additionally, the topology of the band structure can give rise to further interesting phenomena like the quantum Hall effect or the topological Hall effect.[52–54] The prior is present if a large magnetic field is applied to a 2D electron gas making the interior of the material insulating and allowing only the edges to be conductive in a quantized fashion (i.e. mimicking a topological insulator).[52,55–57] The latter can be caused either by topological defects of the spin texture (e.g. Skyrmions) or a non-coplanar alignment of multiple magnetic sublattices in ferrimagnetic materials.[53,58,59] These "topological" transport effects, in turn, can be used to probe the phase boundaries of topological phases, e.g. the Skyrmion phase.[58]

As such, magnetoresistive effects, yielding crucial insights into the inner structure of solid state matter, are highly relevant for fundamental research.

1.2 Outline

Before a more detailed description of some of the above-introduced effects will be given in Sec. 1.3, a brief overview of the thesis is outlined below to establish the relevance of the effects in the context of this work. In this thesis three main topics are addressed, where the first topic covers the experimental requirements and the design of the setups used for the state-of-the-art magnetotransport experiments covered in the other two topics. The second topic deals with the investigation of pure spin current phenomena in bilayers of a magnetic insulator and a spin Hall active metal. Finally, the impact of topology and non-trivial magnetization textures/states on the transverse magnetotransport response is the subject of the third topic. These three topics are distributed over eight chapters as described in the following:

Magnetotransport measurements require the integration of sample mounting, temperature control, magnetic field and readout electronics into one measurement setup. The design of the setups used during this thesis and how the integration is accomplished in detail is discussed in Ch. 2. Additionally, relevant information on how the magnetotransport measurements are carried out and what measurement concepts are utilized are presented there.

As part of the second topic, studies of the spin Hall magnetoresistance in non-crystalline $Y_3Fe_5O_{12}$/Pt bilayers and heterostructures of Cr_2O_3 and Pt or Ta are discussed in Ch. 3. This chapter mainly deals with the nature of the microscopic mechanisms of the SMR and the interactions at the interface between the magnetic insulator and the metal. Chapter 4 is dedicated to the magnon-mediated magnetoresistance in $Y_3Fe_5O_{12}$/Pt het-

erostructures: The possible contribution of phonon currents to the non-local magneto-transport is elucidated and excluded by using a focused ion beam to remove the magnetic material in between the injector and detector. Additionally, the evolution of the MMR (and the SMR) towards the Curie temperature of $Y_3Fe_5O_{12}$ is studied. Finally, a non-local second harmonic magnetoresistance was reported as evidence for spin superfluidity in bilayers of Cr_2O_3 and Pt in Ref. [60]. In Ch. 5 similar experiments are carried out in Cr_2O_3/Pt heterostructures to validate this finding.

The third topic covers the transverse magnetoresistance and the transverse magnetothermopower measured in $Mn_{1.8}PtSn$, where a large topological Hall effect and topological Nernst effect are observed (c.f. Ch. 6). Furthermore, spatially resolved measurements of the anomalous Nernst effect allow to infer the antiferromagnetic domain structure of Mn_3Sn thin films (c.f. Ch. 7). Both $Mn_{1.8}PtSn$ and Mn_3Sn are reported to have non-trivial magnetic topology, crucially impacting the transport response.

Finally, in the last Ch. 8 a summary of all experiments presented in this thesis is given.

1.3 Background

In this section, a more detailed description of the effects introduced in Sec. 1.1, which are relevant in the context of this thesis, will be given. Additionally, the current theoretical picture of the mentioned effects and the novel questions recently addressed in literature will be summarized.

1.3.1 Spin Hall Magnetoresistance

The spin Hall magnetoresistance (SMR) arises due to the simultaneous action of the spin Hall effect and its inverse in normal (i.e. non-magnetic)[1] metals (NM) with large spin orbit interaction interfaced with a ferromagnetic insulator.[42–44] If a charge current[2] J_c is driven in such a normal metal, band structure effects or spin-dependent scattering can give rise to a disparate transverse deflection of spin up and down electrons.[31,32,35,61]

Consequently, a transverse spin current J_s with polarization along s arises:[44,62]

$$\mathbf{J}_s = \theta_{SH}\mathbf{s} \times \mathbf{J}_c. \tag{1.1}$$

Here, the charge current and spin current are particle flows and θ_{SH} is the spin Hall angle, a measure for the efficiency of the charge to spin conversion. This effect, named spin Hall effect (SHE)[31] is sketched for a spin polarization $\mathbf{s} = \mp\mathbf{y}$ in Fig. 1.1a.

Analogously, for the inverse spin Hall effect (ISHE) the same scattering converts a spin current to a charge current (c.f. Fig. 1.1b).[35,62]

$$\mathbf{J}_c = \theta_{SH}\mathbf{s} \times \mathbf{J}_s \tag{1.2}$$

---

[1]Non-magnetic in this thesis refers to metals which do not have a long-range magnetic order, i.e. are neither ferro-, ferri- or antiferromagnetic.

[2]In this chapter, charge and spin "currents" refer to the respective particle current densities.
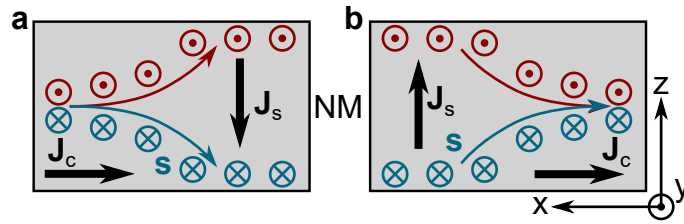
Figure 1.1: **a** A schematic of the spin Hall effect is shown. If a charge current $\mathbf{J}_c$ is applied in normal metal with finite spin orbit coupling, electrons with spin up (circles with point) and spin down (circles with cross) are scattered differently. This spin dependent scattering gives rise to a spin current perpendicular to the spin accumulation and the charge current. **b** The inverse spin Hall effect generates a charge current from a spin current. Please note, that the spin current as drawn here is associated with spin down spins (i.e. $\mathbf{s} = -\mathbf{y}$)

With a charge current flowing, spins will accumulate at the interfaces of the NM. In steady state, this spin imbalance in turn generates a spin current canceling the original spin current, leading to zero net spin current flow. Thus, the incoming and outgoing charge currents in such a device would be equal. In this case, the incoming and outgoing charge currents refer to the current flowing in the device with a constant applied electric field in the absence or presence of the spin Hall effect, respectively.[3] If a ferromagnetic insulator (FMI) with magnetization $\mathbf{M}$ is now attached to one interface of the NM two cases can be considered: First, the magnetization is aligned parallel to the spin polarization $\mathbf{s}$ of the spin accumulation (c.f. Fig. 1.2a).[42–44] In this case, the magnetization cannot interact with the spin accumulation at least in a first order approximation. Thus, this case, depicted in Fig. 1.2a, resembles the vacuum case, where no FMI is present (c.f. Fig. 1.1a).
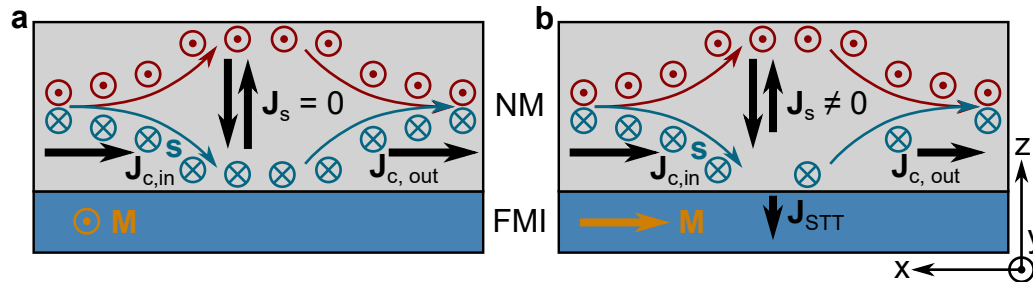
Figure 1.2: **a** In a FMI/NM heterostructure with the magnetization $\mathbf{M}$ aligned along the direction of the interface spin accumulation $\mathbf{s}$, the steady state spin current is zero. Thus, the incoming and outgoing charge currents are equal. **b** If $\mathbf{M}$ and $\mathbf{s}$ enclose a finite angle, the spin accumulation can enact a torque on the magnetization. In this case, angular momentum is transferred to the FMI and the steady state spin current is non-zero. Consequently, also the incoming and outgoing charge currents are unequal: The resistance of the normal metal is higher if a spin current is flowing into the FMI due to the angular momentum loss.

---

[3]We also assume that the spin is conserved.

On the other hand, if the magnetization encloses a finite angle with **s**, the spin accumulation enacts a torque on the magnetization, viz. the spin transfer torque[44]

$$\tau_{\mathrm{STT}} \propto \mathbf{m} \times (\mathbf{m} \times \mathbf{s}). \tag{1.3}$$

Thus, angular momentum is absorbed by the FMI resulting in a steady state spin current flowing in the NM. Consequently, the incoming and outgoing charge currents are unequal, which can be interpreted as a resistance increase in the NM due to the angular momentum loss over the interface to the FMI (c.f. Fig. 1.2b). In summary, the resistance of the normal metal changes depending on the relative alignment of the ferromagnetic insulator magnetization and the spin accumulation in the normal metal.
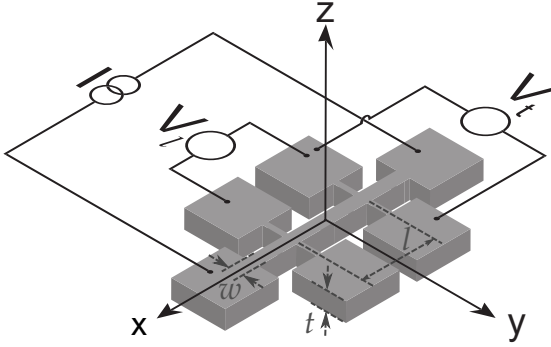

Figure 1.3: Resistivity measurements are typically carried out in a Hall bar geometry, where the geometry given by the thickness t and the width w of the conduction channel as well as the length l between the longitudinal contacts is well defined. In such a Hall bar, the longitudinal and transverse resistivities can be inferred from the respective voltages V_ℓ and V_t and the applied electric current I as shown in Eq. (1.4) and Eq. (1.5).

The modulation dependence of the longitudinal (ρ_ℓ) and transverse (ρ_t) resistivities for $\mathbf{J_c} \parallel -\mathbf{x}$ and spin accumulation $\mathbf{s} \parallel -\mathbf{y}$ (c.f. Fig. 1.2) can be described by Eq. (1.4) and Eq. (1.5), respectively.[44]

$$\rho_\ell = \frac{V_\ell}{I}\frac{wt}{l} = \rho_0 + \Delta\rho(1 - m_y^2) \tag{1.4}$$

$$\rho_t = \frac{V_t}{I}t = \Delta\rho\, m_x m_y + \Delta\rho_{\mathrm{H}} m_z, \tag{1.5}$$

where, V_ℓ and V_t are the longitudinal and transverse voltages measured on a normal metal Hall bar and I is the electrical current used to drive the system (c.f. Fig. 1.3).[4] To infer the resistivity, the geometry of the Hall bar needs to be included, where w, l and t are the width, length and thickness of the NM, as shown in Fig. 1.3.

Furthermore, $m_i = \frac{M_i}{|M|}$ are the normalized magnetization components along the Cartesian axes, ρ_0 is the resistivity of the normal metal without the FMI attached[5] and $\Delta\rho > 0$ is the resistivity change due to the SMR. Consequently, the SMR amplitude is given by $\frac{\Delta\rho}{\rho_0}$. $\Delta\rho_{\mathrm{H}}$ is the amplitude of the spin Hall anomalous Hall effect arising through the exchange

---

[4]For electrons, the electrical current is related to the charge current by $I = -|e|J_c A$, with the conductor cross section $A = w \cdot t$ and the electron charge e

[5]Please note, that ρ_0 in the original work refers to the Drude resistivity, whereas here, ρ_0 includes all contributions to the resistivity which are independent of the magnetization

field at the FMI/NM interface.[44,63] To provide a visual perception of the signature characteristic to the SMR, the longitudinal and transverse resistivities are shown for rotations of the magnetization within the three planes spanned by the Cartesian axes $\mathbf{x}$, $\mathbf{y}$ and $\mathbf{z}$ in Fig. 1.4.
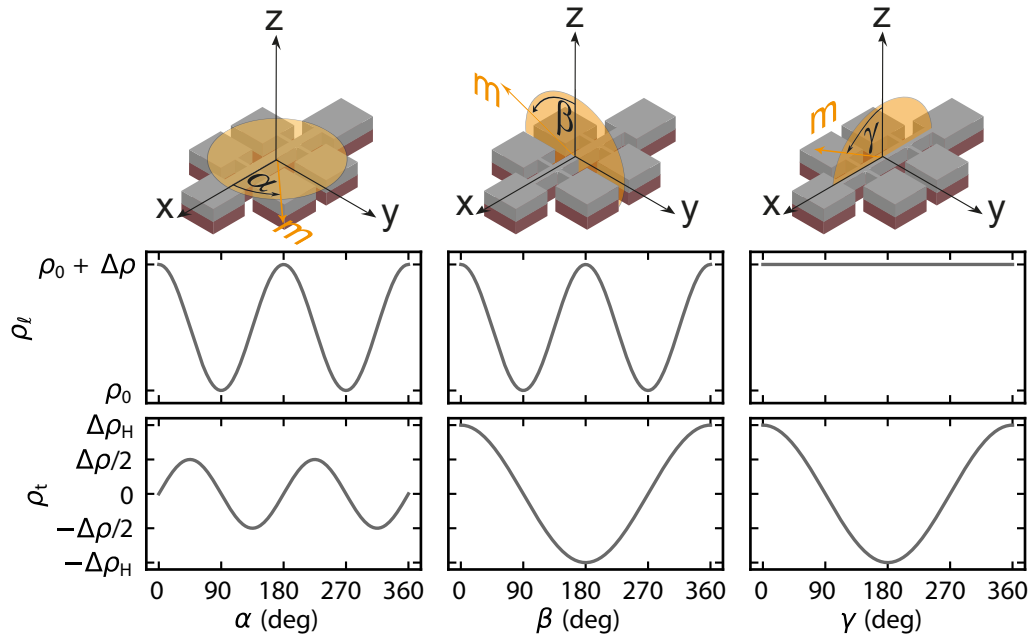

Figure 1.4: The modulation of the longitudinal (**a-c**) and transverse (**d-f**) resistivity given by Eq. (1.4) and Eq. (1.5), respectively, is sketched here. The three columns correspond to rotations of the normalized magnetization $\mathbf{m} = \mathbf{M}/|\mathbf{M}|$ in the three planes spanned by the Cartesian axes (i.e. **xy**, **zy** and **zx**). Only if the $\mathbf{y}$ component of the magnetization m_y changes a modulation of ρ_ℓ is evident (**a,b**). Insets adapted from Ref. [10].

Several studies of the SMR in systems with more than one magnetic sublattice, i.e. ferrimagnets, antiferromagnets and chiral magnets, were carried out to date. In such systems, it was theoretically shown that the spin transfer torque does not necessarily couple (only) to the net magnetization of the material but to the individual sublattices.[64] This theoretical picture was corroborated by experimental data taken in the non-collinear phase of helimagnets and ferrimagnets with a magnetic compensation temperature, where the spin accumulation was shown to couple to the individual magnetic sublattices.[15,50,51] Consequently, the SMR can even be observed in antiferromagnets, since it is symmetric upon magnetization reversal (c.f. Eq. (1.4)).[11,65,66]

Finally, some additional effects with an angular dependence similar to the SMR are summarized in the following, as they are currently vividly discussed in literature: In addition to the magnetization in the FMI absorbing angular momentum from the NM via the spin transfer torque, magnons can be generated in the FMI by the spin accumulation in the NM.[16,40,41,45] This mechanism, present if the magnetization is aligned parallel to

the spin polarization, will be discussed in the context of the non-local magnon-mediated magnetoresistance (MMR, c.f. Sec. 1.3.2). Here, the additional spin current entering the FMI for $\mathbf{M} \parallel \mathbf{s}$ effectively reduces the SMR amplitude as there is always finite dissipation. Since this direct exchange of spins parallel to the magnetization (i.e. spin flip scattering of an electron at the interface generating or destroying an incoherent magnon in the FMI) is considered to be small in ordered magnetic insulators, these contributions have only been included in very recent theories.[63]

Last but not least, the magnetic field can also directly interact with the spins at the interface. This is not considered in the original SMR theory, where only the effects due to the magnetization of the FMI are taken into account.[44] In experiment, the magnetization orientation can only be controlled indirectly by applying an external magnetic field. Consequently, the SMR symmetry in experiment usually refers to the direction of the magnetic field as the extrinsic (experimentally controllable) parameter.[43] However, even in the absence of a FMI, a magnetoresistance with the same symmetry as the SMR with respect to the direction of the magnetic field can be observed.[67,68] This magnetoresistance, called the Hanle magnetoresistance (HMR) arises due to the interaction of the magnetic field with the interfacial spin accumulation, lowering the spin lifetime and thus again reducing the spin accumulation (i.e. providing a dissipative channel).

There have been recent efforts to generalize the SMR and HMR theory into one microscopic theory by Zhang et al. and Velez et al. in Refs. [63] and [69], respectively. Their theory already provides a general explanation for the SMR and HMR for heterostructures of long-range ordered and paramagnetic insulators and a spin Hall active metals from a microscopic perspective: By including an interfacial layer of magnetic impurities, they model the exchange field at the interface allowing to describe the loss of spin information from the normal metal in terms of relaxation times. However, although taking into account most of the additional effects, diffusive processes and direct electronic exchange of spin has so far not been included in this theory.

Since all of the effects mentioned above show the same symmetry as the SMR and might depend on the magnetic field (a field dependence is known for the HMR and the non-local magnetoresistance), disentangling SMR, HMR and locally observed MMR is particularly tedious. To do so, the experimental approach would be a systematic study of the magnetic field dependence of the resistivity in the three high symmetry directions up to high magnetic fields. Since the effect sizes (depending on the materials) differ by orders of magnitude, extreme care has to be taken with the alignment of the sample to mitigate intermixing of the signals.

1.3.2 Non-Local Magnon-Mediated Magnetoresistance

By spatially separating the spin injection via the SHE and the spin detection via the ISHE (which takes place in simultaneously for the SMR, c.f. Fig. 1.2), it should be possible to study the spin transport through a magnetic insulator by simple electrical measurements. Such a structure can for example be made laterally using lithography on a FMI/NM heterostructure: Two electrically insulated NM wires are placed in close vicin-

ity of each other on top of a FMI (c.f. Fig. 1.5). If a current is driven in one of the NM wires (the injector), a spin current will flow into the FMI which can be detected in a small enough distance by the inverse spin Hall effect in the other wire (the detector) as a "non-local" current $\mathbf{J}_{c,nl}$.
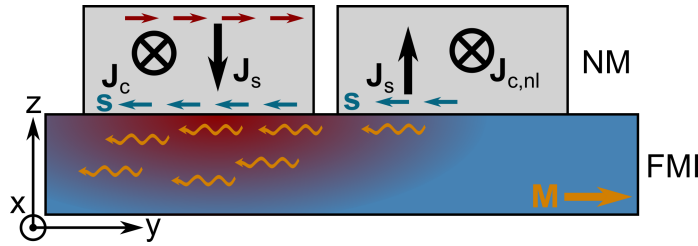

Figure 1.5: A charge current in a NM wire (injector) generates a spin accumulation at an FMI/NM interface via the spin Hall effect. If this spin accumulation **s** is parallel to the magnetization **M** of the FMI, magnons are injected at the interface. By diffusion, these magnons can reach a second NM wire (detector), which is electrically insulated from the injector. There, the magnons can again generate a spin accumulation (and thus a spin current) which is converted to a charge current via the inverse spin Hall effect. Using this non-local magnon-mediated magnetoresistance the magnon transport in the FMI can be investigated.

This simple thought experiment led to the discovery of the non-local magnon-mediated magnetoresistance.[16,40,41,45] It turns out, however, that the mechanism for the spin current generation is not the spin transfer torque - as one would naively expect from the SMR - but spin flip scattering at the interface. The spin flip scattering due to the exchange coupling of the NM's conduction electrons and the magnetic ions in the adjacent FMI leads to the generation or annihilation of magnons in the FMI.[41] Thus, the magnetization component parallel to the spin accumulation is relevant. Please note, that the direction component has to be squared because both, the injection and detection, impose a projection of the magnetization due to the geometry of the experiment (c.f. Eq. (1.1) and Eq. (1.2)). For the geometry depicted in Fig. 1.5, the spin Hall effect and inverse spin Hall effect can be generated/detected for the magnetization component along **y**.

$$\mathbf{J}_{c,nl} \propto (\mathbf{m} \cdot \mathbf{s})^2 = m_y^2 \qquad (1.6)$$

Consequently, the effect can be understood in a magnon diffusion picture: The spin accumulation at the FMI/NM interface of the injector generates a non-equilibrium magnon accumulation. These magnons, in turn, diffuse through the FMI and are detected via the ISHE in the second NM wire. Please note, that for this lateral structure, the direction of the two charge currents is parallel (and the two spin currents are antiparallel). Consequently, with open boundary conditions, the sign of the non-local voltage will be opposite to the voltage on the local contacts.[16,45] For a vertical NM/FMI/NM stack this will be exactly opposite (both spin currents are parallel), so that here the same voltage polarity is observed.[70]

Thus, the MMR allows to study the transport of incoherent magnons in a FMI using

purely DC currents.[16] Typical magnon diffusion lengths λ_m in magnetic insulators (e.g. $Y_3Fe_5O_{12}$ or $NiFe_2O_4$) are in the range of a few $100\,nm$ to $10\,\mu m$.[16,45,71–73]

   More recently non-local magnetotransport experiments in lateral heterostructures consisting of a magnetic insulator with a more complicated magnetic structure and Pt were carried out. In particular, it was shown that in bilayers of Pt and the ferrimagnetic insulators $Gd_3Fe_5O_{12}$, having a compensation temperature T_{comp} close to room temperature, the non-local magnetotransport vanishes at T_{comp}.[74] This is speculated to be a result of inefficient magnon generation or magnetic domain formation.[75] Additionally, results on antiferromagnetic insulators were presented by Lebrun et al. in Ref. [76]. In their γ–Fe_2O_3/Pt heterostructures, they observe an electrically driven non-local magnetotransport over large distances of up to $10\,\mu m$.

   Finally, the possibility to modify the magnon transport by using an additional gate in between the injector and detector was reported.[15] Using this gate, the magnon current from the injector to the detector can be turned on or off. In this geometry additional non-linear processes can be observed: If the magnon population below the gate is excited by magnon injection (i.e. driving a large current through the gate) the diffusion length and transport efficiency can be altered.[77] For very thin FMI films, the system can even be driven into damping compensation by the spin orbit (antidamping) torque below the gate.[78] Thus, very efficient long-distance transport might be possible in such structures.
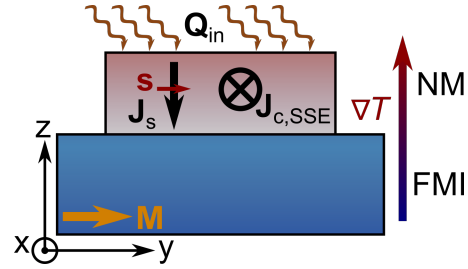
1.3.3 Spin Seebeck Effect

   We now turn to the spin Seebeck effect (SSE) typically observed in FMI/NM heterostructure. For the observation of the SSE a thermal gradient instead of a current is applied to the heterostructure, with the heat flowing from the NM (hot) to the FMI (cold). Consequently, a spin current will arise, flowing along to the heat gradient.[79,80] This spin current can then be electrically detected in the adjacent NM layer via the inverse spin Hall effect.[81] It was shown that the resulting charge current in the NM depends crucially on the difference between the electronic temperature of the NM and temperature of the magnonic system of the FMI.[79,82] Since the spin current generated by the thermal gradient is polarized along the magnetization direction $\mathbf{s} \parallel \mathbf{m}$, the symmetry is given by

$$\mathbf{J}_{c,SSE} \propto \mathbf{m} \times \mathbf{z}, \tag{1.7}$$

where $\mathbf{z}$ is the direction perpendicular to the plane (i.e. the direction of the spin current/heat flow, c.f. Fig. 1.6). The cross product stems from the symmetry of the inverse spin Hall effect in the normal metal (c.f. Eq. (1.2)). Consequently, $\mathbf{J}_{c,SSE}$ will only be detectable, if the magnetization is in the plane perpendicular to the heat flow and encloses a finite angle with the direction along which the current is measured. The effect is sketched in Fig. 1.6 for $\mathbf{m} \parallel \mathbf{y}$, where the resulting charge current $J_{c,SSE} \propto m_y$ will flow along $\mathbf{x}$.

   Again, systems beyond simple ferromagnets have been studied, where it was found that the spin Seebeck effect crucially depends on the magnon spectrum of the insulator.[83,84] Additionally, the spin Seebeck effect was found to be present also in antiferromagnetic[85–89] and even paramagnetic insulators.[90] In these systems, the magnitude of the

Figure 1.6: A thermal gradient is applied perpendicular to the stacking order in a FMI/NM heterostructure. If this gradient drives a spin current from the normal metal into the FMI, a perpendicular charge current will arise due to the inverse spin Hall effect.

spin Seebeck effect follows the spin susceptibility of the system and the external magnetic field, or more specifically the induced magnetization.[91]

Finally, the spin Seebeck effect can be used for spatial imaging if a localized gradient is used for driving the system.[39] Recently, it was shown that this even works for AFMI/NM structures, where the spin Seebeck effect is claimed to be sensitive to the Néel vector orientation.[85,92]

1.3.4   Hall Effect and Nernst Effect

Consider a current $\mathbf{J}_c$ of particles with charge q (e.g. electrons) flowing in a normal metal. If a magnetic field $\mathbf{H}$ is applied perpendicular to this current, the particles will get deflected by the Lorentz force. Thus, the particles acquire a finite momentum into the direction perpendicular to both, the initial charge current and magnetic field. This additional transverse momentum can be understood as charge current. In steady state and with open transverse boundaries,[6] this transverse charge current has to vanish, leading to an additional electric field

$$\mathbf{E}_{\text{Hall}} \propto q\mathbf{J}_c \times \mathbf{H}, \tag{1.8}$$

which can be measured by attaching contacts to the sides of the normal metal.[19]

An equivalent discussion can be made for the Nernst effect, where the charged particles are moved by the application of a thermal gradient instead of an external electric field: When heating a normal metal on one side, free particles will diffuse towards the cold side.[93] Consequently, a charge current as described for the Hall effect will flow, get deflected by the magnetic field and give rise to a transverse electric field[94]

$$\mathbf{E}_{\text{Nernst}} \propto q\mathbf{J}_c \times \mathbf{H}. \tag{1.9}$$

The Hall and Nernst effect are sketched in Fig. 1.7a and b, respectively.

Both, the Hall effect and Nernst effect are linearly increasing with magnetic field strength and change their sign upon magnetic field reversal. This behavior is usually referred to as "ordinary", justifying the name ordinary Hall and Nernst effect to distinguish them from the effects introduced in the following. We thus can describe the ordinary Hall effect terms of the transverse electrical resistivity

$$\rho_t = \rho_{xy} = R_0 H_z, \tag{1.10}$$

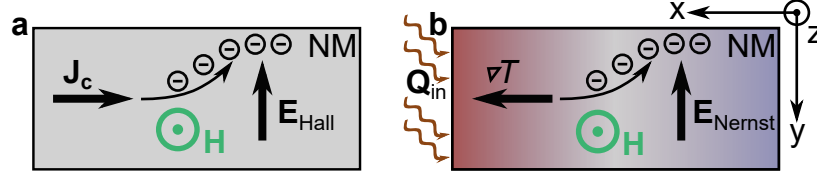[6]For open transverse boundaries no current can flow through the transverse metal boundaries.

Figure 1.7: **a** A charge current in a normal metal is carried by charged particles (e.g. electrons). If a magnetic field **H** is applied perpendicular to the charge current $\mathbf{J}_c$, the charged particles will be deflected by the Lorentz force into the third orthogonal direction, giving rise to a charge accumulation at the interfaces. Thus, an electric field $\mathbf{E}_{\text{Hall}}$ will arise in this direction. This phenomenon is called the Hall effect. **b** Similarly, charged particles can be moved by a thermal gradient: Here, one side of the normal metal is heated, giving rise to thermal diffusion of the charge carriers from the hot side to the cold side. In analogy to the Hall effect, the moving particles get deflected, giving rise to an electric field $\mathbf{E}_{\text{Nernst}}$ in the direction perpendicular to the thermal gradient and the magnetic field. This is the Nernst effect.

with the ordinary Hall coefficient R_0.

If the normal metal is replaced by a magnetic one (e.g. iron), an additional transverse electric field will be visible, which is not directly proportional to the magnetic field.[20] This anomalous Hall effect does not stem from the additional stray field from the magnetization (i.e. $H \rightarrow H + M$) but from spin dependent scattering and/or intrinsic contributions.[95–99] These intrinsic contributions originate from the band structure and are usually treated using the Berry formalism.[53,100,101] In this formalism, the anomalous Hall effect is a consequence of the Berry curvature of the band structure.

In most magnetic metals, the magnitude of the anomalous Hall (and Nernst) effect are proportional to the magnitude of the magnetization.[95,102,103] Thus, the transverse electric resistivity of the normal metal (c.f. Eq. (1.10)) is modified by including another term[95]

$$\rho_t = \rho_{xy} = R_0 H_z + R_s M_z, \tag{1.11}$$

where R_s is the coefficient of the anomalous Hall effect.[7] Please note, that through R_s, which can scale with the resistivity ρ_{xx}, also the anomalous Hall effect can depend on the magnetic field.[95]

Recently, reports accumulated where this scaling seems to be violated.[58,103–108] Although the physical origin, i.e. a finite Berry curvature, is similar, two types of system are usually distinguished due to their different dependence on the magnetization:

First, there are systems with non-coplanar spin textures, where the spin chirality gives rise to an additional Hall effect, often referred to as the topological Hall effect.[54,95,109] Such non-coplanar spin textures include Skyrmions[110,111] and conical phases.[59,112] As the presence of such non-coplanar spin textures can depend on the phase diagram, no general

---

[7]There will also be an ordinary Hall effect due to the magnetic stray field (i.e. $H \rightarrow H + M$). This contribution, however, is typically absorbed into the anomalous Hall coefficient due to the difficulty in separating the two effects.

scaling with the magnetic field or magnetization has been found yet.

The second kind of systems are non-collinear antiferromagnets, where a large anomalous Hall and Nernst effect is observed.[103,107] In these system, the anomalous Hall effect follows the magnetization loop as a function of the magnetic field, but the negligible magnetization is significantly too small to explain the large effect sizes. This finding is associated with the non-collinear spin structure breaking the time reversal and spatial inversion symmetry. Such a spontaneously broken symmetry is required for observing an anomalous Hall effect as otherwise the Berry curvature, and consequently the anomalous Hall effect, have to vanish.[113]

Finally, it was also proposed recently that even in collinear antiferromagnets, a finite anomalous Hall effect can be observed.[114] In this case, the symmetry is broken by the non-magnetic atoms in the crystal structure.

Please note, that the discussion in this section focused mostly on the Hall effect, which, as already discussed above, is closely related to the Nernst effect.[115,116] As such, most of the findings discussed above in context of the Hall effect, also apply to the Nernst effect.

Chapter 2

Experimental Setups and Details

In this chapter, the experimental facilities which were designed and used in the course of this thesis will be introduced. This chapter will begin with a short introduction to the requirements of (magneto-)transport measurements and a short summary of the basic concepts underlying the measurement setups (c.f. Sec. 2.1). This introduction will be followed by the description of the design of the different measuring inserts assembled as part of this thesis, and the measurement geometry in the different magnet setups. Additionally, a scanning laser setup used for spatially resolved measurements of thermally generated voltages will be specified in Sec. 2.5. The chapter will conclude by an explanation of the used measurement schemes and devices as well as a discussion of the typical measurement noise and resolution (c.f. Sec. 2.6).

Before going into details, and to provide some orientation for the reader, the different magnet systems will be listed here shortly. First of all, there are three magnet cryostats, one with a 3D vector magnet named "Chaos", another with a split coil magnet called "Oscar" and finally, one with a solenoid magnet referred to as the "VSM cryostat". To enable transport experiments in these magnets, two measuring inserts were assembled in the course of this thesis, where the first one fits only the Chaos and the VSM cryostat. The second, improved measuring insert has a smaller outer diameter and thus fits all three magnet systems. It also features an interchangable "puck" system, allowing to mount the sample in three orthogonal orientations.

On the other hand, several room temperature magnets are described in this thesis. These include three similar Halbach magnet setups with different fixed magnetic fields and a 2D vector electromagnet. The corresponding measuring inserts can fit into either of these magnets, where versions with Peltier control or resistive heaters are available to control the temperature in a window around room temperature. Furthermore, a high temperature measuring insert is available, which additionally fits into a 3D printed smaller

Halbach array. Finally, although not further discussed in this chapter, all measurements are automated using a custom Python measurement program which has been written in the course of this thesis (c.f. App. C).

2.1 Experimental Requirements and Design Ideas

In order to measure the resistance of a given material, viz. the sample, it must be electrically contacted to the measurement electronics (c.f. Fig. 2.1). Additionally, since the goal is the study of the magnetotransport response, the sample additionally needs to be subjected to a magnetic field and possibly low (or high) temperatures. Since the sensitive measurement electronics should not be exposed to such harsh conditions, a spatial separation between the sample and the electronics is required. To that end, the sample needs to be attached to a measuring insert, extending the electrical contacts, which in turn is inserted to the magnet (cryostat). Since such a design would require the measuring insert to be modified for each individual sample, a slightly more complex approach was chosen here: To allow flexible use of a sample in the various setups, the sample is mounted on a chip carrier and contacted by wedge bonding with Al wire. This chip carrier can then be attached to a socket on the measuring insert. To be compatible with industry standards and allow more sophisticated measurement schemes requiring a large number of contacts, we decided to use commercially available 32pin ceramic leadless chip carrier (CLCC). Additionally, to further increase the usability and the flexibility of our measurement setup, the measuring insert is connected to a breakout box (c.f. Sec. 2.6) to allow flexible connection to the measurement electronics. A contacted sample on such a chip carrier can be seen in Fig. 2.2a.
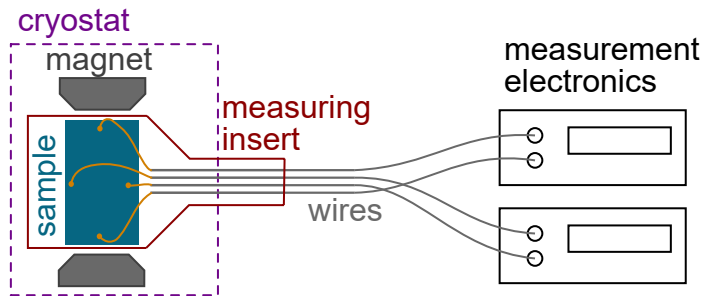

Figure 2.1: A sketch of a very basic measurement setup to determine the magnetotransport response is shown here to demonstrate the minimal requirements. The sample has to be inserted into a magnet (cryostat), which is accomplished by using a measuring insert. Additionally, electrical contact from the measurement electronics to the sample is required.

In the following, the two typical magnetotransport measurement schemes will be described: First, there are field dependent magnetoresistance (FDMR) measurements, where the resistance is measured as a function of the magnetic field strength. These

FDMR measurements (often also called field sweeps) can be carried out with the magnetic field applied along different directions with respect to the sample. Secondly, instead of varying the magnetic field strength, it can be helpful to keep the magnetic field constant and vary the angle under which it is applied. These angle resolved magnetoresistance (ARMR) measurements are typically carried out for the three mutually orthogonal rotation planes spanned by the Cartesian coordinate system. Collecting a full set of ARMR data (i.e. for all three rotation planes) can be very helpful for distinguishing between different magnetoresistive effects (e.g. to identify the spin Hall magnetoresistance, c.f. Sec. 1.3.1 and Fig. 1.4). To allow consistent and easy comparison between different samples, measurements and measurement setups, a standard coordinate system with respect to the Hall bar is defined and used during this thesis, unless specifically denoted otherwise. This coordinate system is defined by the current direction $\mathbf{x} = \mathbf{j}$, the transverse direction $\mathbf{y} = \mathbf{t}$ and the surface normal $\mathbf{z} = \mathbf{n}$ of the thin film sample. The polarity of the
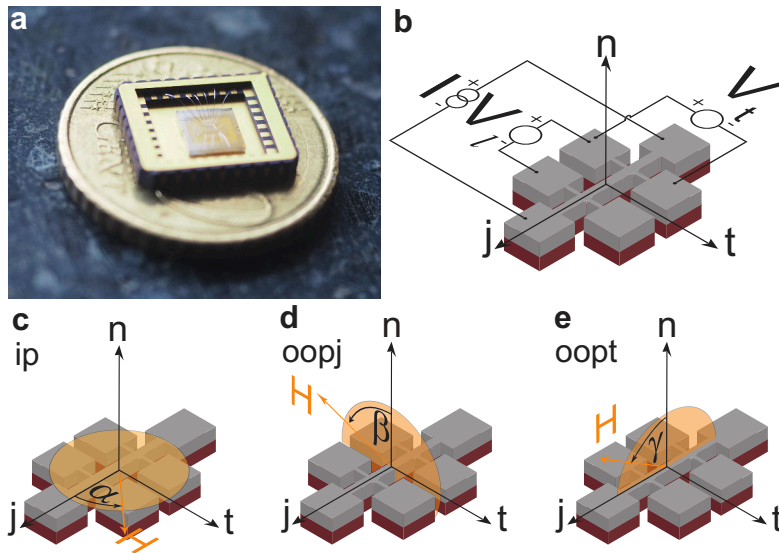

Figure 2.2: **a** The 32 pin ceramic leadless chip carrier (CLCC) used in the setups assembled during this thesis has lateral dimensions of 14 mm × 11.5 mm and can fit samples of up to 8.8 mm × 7.5 mm. Including a custom made socket, it can fit into a cylinder with ⌀22 mm. A Hall bar sample is mounted and wirebonded onto it. **b** Sketch of a Hall bar with the coordinate system used throughout this thesis. The polarity of the current is chosen, so that a positive electric current (i.e. from + to −) is flowing along **j**. The longitudinal voltage V_ℓ is measured along the current direction **j**, while the transverse voltage V_t is measured along the transverse direction **t**.
c-e Angle resolved magnetoresistance measurements performed during this thesis are typically carried out within the three planes spanned by the coordinate system shown in panel **b**. Thus, the magnetic field is either rotated around the surface normal of the thin film sample (**c**, in-plane, ip), around the current direction (**d**, out-of-plane around **j**, oopj) or around the transverse direction (**e**, out-of-plane around **t**, oopt). Adapted from Ref. [10]

contacts is chosen so that a positive current (technical current direction, from + to −) is flowing in the positive **j** direction, as depicted in Fig. 2.2b. The rotation angles α, β and γ of the magnetic fields in the three orthogonal rotation planes are depicted in Fig. 2.2c-e, respectively. For an in-plane rotation (ip, Fig. 2.2c), the magnetic field is rotated from the current direction **j** towards the transverse direction **t** in the film plane. For the two out-of-plane rotations, the magnetic field is rotated from the surface normal **n** either around the current direction **j** (oopj, d) or around the transverse direction **t** (oopt, e). The sense of rotation is always counter-clockwise when looking onto the rotation plane into the negative third direction (i.e. looking onto the tip of the vector).

2.2 Measuring Insert for Halbach Setup

Originally built by a PhD student in Munich,[117] the first setup available in Dresden was a hollow cylindrical Halbach array,[118] with a diametrically oriented magnetic field of $\mu_0 H_{ext} \approx 1.1\,\mathrm{T}$ and a clear bore of 40 mm.[1] By rotating the array, the magnetic field is rotated around the cylindrical axis of the system. To define the three rotation planes discussed above, three sample holders were constructed and wired. The sample holders and the respective coordinate axes are shown in Fig. 2.3(a-c). Additionally, the setup was
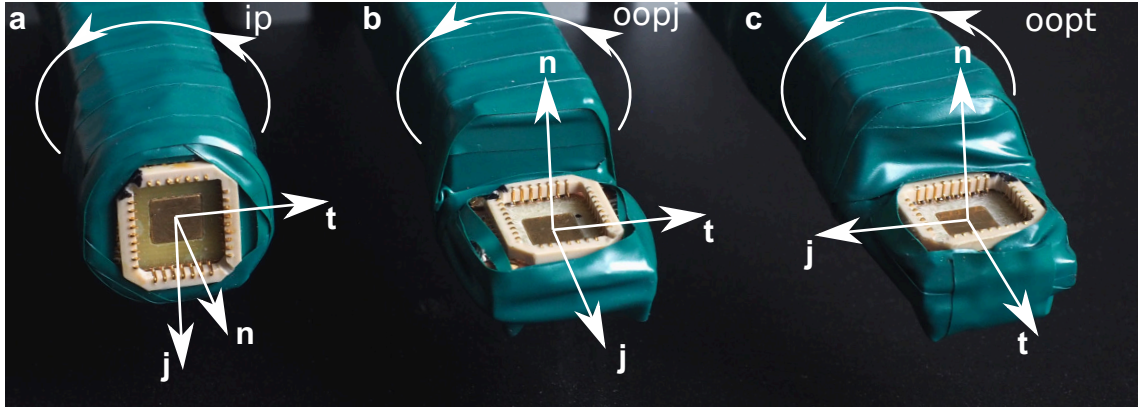

Figure 2.3: **a-c** The three rotation planes and the coordinate system defined by the mounted chip carrier. Please note, that in this case positive voltage/current is applied on top of the chip carrier (dark corner).

outfitted with a 2D Hall probe for measuring the magnetic field, which is read out by a custom made Raspberry Pi based measurement device. The two readings for the vertical (H_x) and horizontal (H_y) magnetic fields can then be combined to yield the magnetic field angle for a given rotation plane. The Python function as well as a description of the Hall probe measurement electronics can be found in the appendix (c.f. Sec. A.1).

Finally, means to change and measure the sample temperature have been added to the

---

[1]The setup was build another two times, where Halbach arrays with a magnetic field of $\mu_0 H_{ext} \approx 400\,\mathrm{mT}$ and 800 mT are used to allow access to different magnetic fields.

setup. The sample temperature can be determined using a Pt100 resistance thermometer attached close to the sample position. The readout is done by a Keithley 2000 multimeter in a four point measurement scheme. Additionally, the sample temperature can be varied using a water cooled Peltier element clamped onto the neck of the insets, giving access to temperatures from $285\,\mathrm{K} \lesssim T \lesssim 340\,\mathrm{K}$. The individual components of the insert are labeled in Fig. 2.4. To insert the sample into the magnet array, the measuring insert is slid onto an Item profile and fixed with the handle shown on the left in Fig. 2.4.
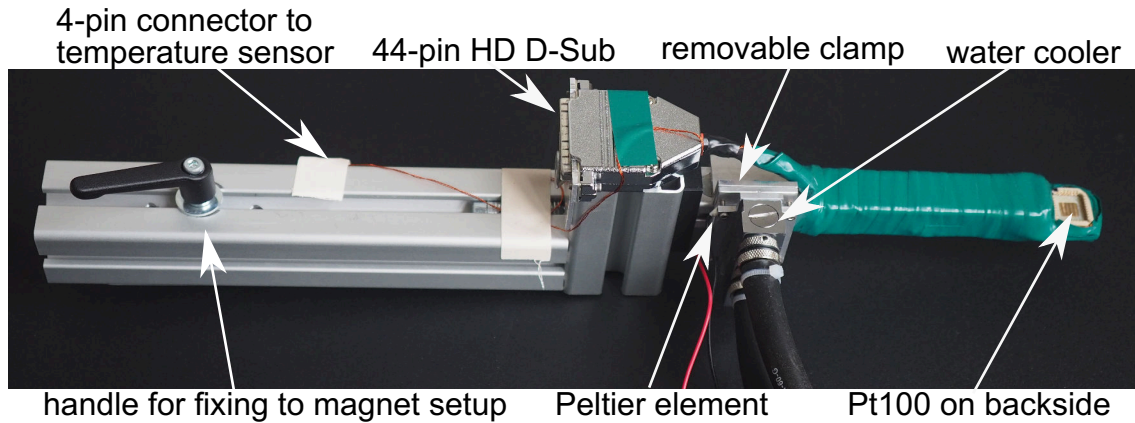

Figure 2.4: Insert for the Halbach measurement setup. The individual component locations are marked by the arrows.

The temperature in this setup cannot be regulated (i.e. stabilized) due to the large spatial separation of the heat source and the measurement resistor. However, in principle, it should be possible to stabilize the temperature using a well-tuned PID loop. Since this was not done yet, a sufficiently long waiting time ($\sim 30\,\mathrm{min}$) has to be implemented after changing the voltage applied to the Peltier element. Using this Peltier element for temperature control, the low and high temperature limit are given by the dew point (condensation on the sample) and the demagnetization temperature of the NdFeB magnets in the Halbach array ($T_C \sim 350\,\mathrm{K}$), respectively.

2.3 High Temperature Measuring Insert

In order to perform transport experiments at even higher temperatures, well above room temperature, another more insulated measuring insert is required due to the limits discussed above. This measuring insert should, for example, allow to perform measurements in the paramagnetic phase of yttrium iron garnet ($\mathrm{Y_3Fe_5O_{12}}$), having a Curie temperature $T_C = 560\,\mathrm{K}$.[119] To enable such experiments, a high temperature measuring insert was designed and assembled by Martin Belger in the course of his master thesis work.[120] This sample insert allows to perform in-plane rotations of the magnetic field in the Halbach setup (outer diameter 38 mm). The experimentally accessible temperature range is $\approx 300\,\mathrm{K} \leq T \leq 650\,\mathrm{K}$, with the sample being enclosed in a vacuum shroud to reduce con-

vective heat losses. Again, the setup should allow the use of the standard 32pin CLCC. While the CLCC can withstand such temperatures without any problems, it is necessary to use silver paint for attaching the sample to the chip carrier instead of the typically used GE varnish (GE 7031). The latter varnish is only specified to withstand temperatures of up to 423 K. A detailed description of the design can be found in Martin Belger's thesis (c.f. Ref. [120]).

However, in the course of testing the insert it became clear that the radiation losses are high enough for the outside of the vacuum shroud to reach temperatures above 340 K (i.e. close to T_C of the NdFeB permanent magnets) with the sample at $T \approx 600$ K. In order to avoid demagnetization of the large field Halbach array, an additional small Halbach array was designed and 3D printed. To reduce heat accumulation it has a wider central bore of 44 mm. The magnetic field $\mu_0 H_\mathrm{ext} = 70$ mT in this array is generated by 12 cubic ($10 \times 10 \times 10$ mm^3) NdFeB magnets. As the length of the array is only 10 mm, the field homogeneity is expected to be rather poor. This issue could be alleviated by stacking several of the NdFeB magnets to increase the array length. However, since the magnet was designed specifically for experiments with yttrium iron garnet, the magnetic field required to align the magnetization in the sample plane is very small,[42] so that the exact magnitude of the magnetic field is not crucial. To allow rotations, the Halbach array is attached to a geared rotation stage driven by a stepper motor. A photograph of the array including the rotation stage and the high temperature measuring insert is shown in Fig. 2.5.
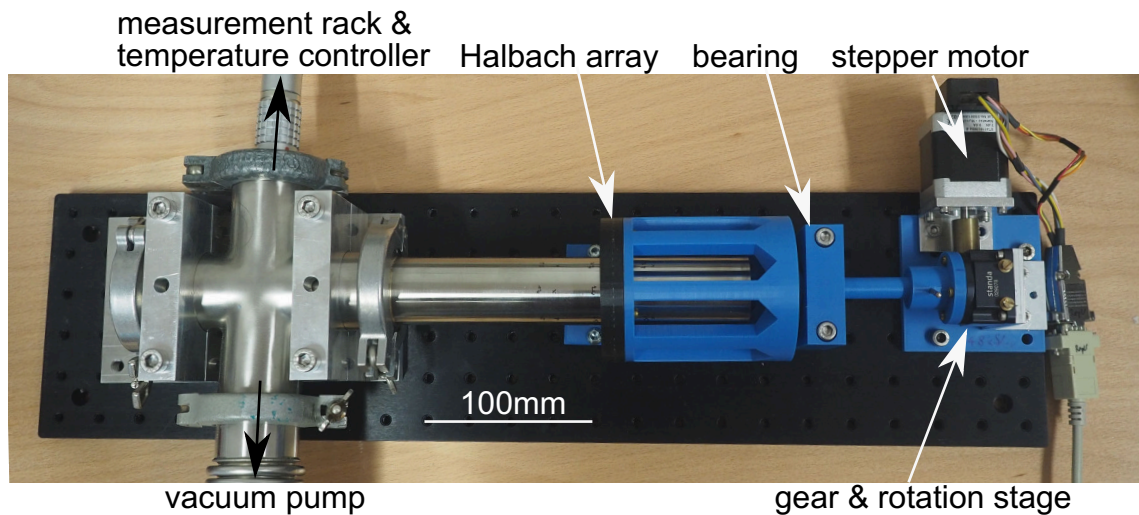

Figure 2.5: The high temperature insert on the left is inserted into the Halbach array (black part). The Halbach array can be rotated using the stepper motor attached to a geared rotation stage.
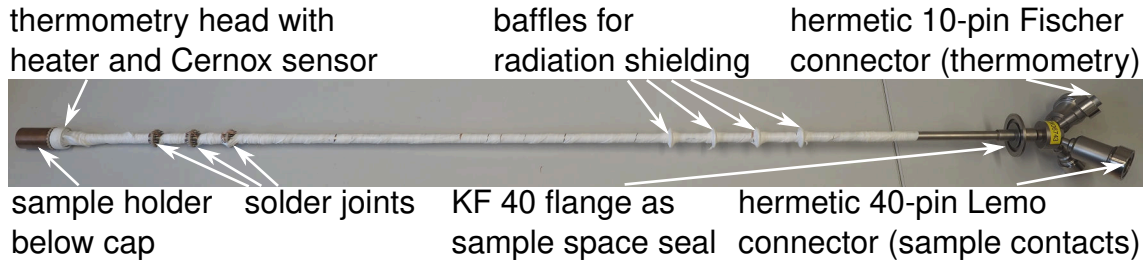
thermometry head with heater and Cernox sensor — baffles for radiation shielding — hermetic 10-pin Fischer connector (thermometry)

sample holder below cap — solder joints — KF 40 flange as sample space seal — hermetic 40-pin Lemo connector (sample contacts)

Figure 2.6: Measuring insert for the vector cryostat.

2.4 Measuring Inserts for Magnet Cryostats

To enable magnetotransport measurements also at low temperatures, an Oxford Instruments magnet cryostat (the "Chaos") with a variable temperature insert (VTI) was outfitted with a new measuring insert. The magnet inside this cryostat allows to generate magnetic fields along an arbitrary direction within a sphere with radius $\mu_0|\mathbf{H}| \leq 2\,\text{T}$. Alternatively, if only the individual axes are used magnetic fields of $\mu_0|H_x| \leq 2\,\text{T}$, $\mu_0|H_y| \leq 2\,\text{T}$ and $\mu_0|H_z| \leq 6\,\text{T}$ can be applied. The VTI is specified for temperatures in the range of 3 K to 300 K and has an inner diameter of $\sim 30\,\text{mm}$.

The (first) new measuring insert (c.f. Fig. 2.6) was designed with an outer diameter of $d_{\text{MI}} = 28\,\text{mm}$ and a length of $l_{\text{MI}} = 1267\,\text{mm}$ from the sample center to the KF40 flange terminating the insert. The sample is placed in such a way, that the out-of-plane direction corresponds to the H_z magnetic field orientation to allow magnetotransport with out-of-plane fields of up to 6 T (c.f. Fig. 2.7a). The sample holder and the thermometry head were designed from scratch, while the rest of the insert was adapted from drawings made by Thomas Brenninger at the Walther-Meißner-Institute (WMI) in Munich.
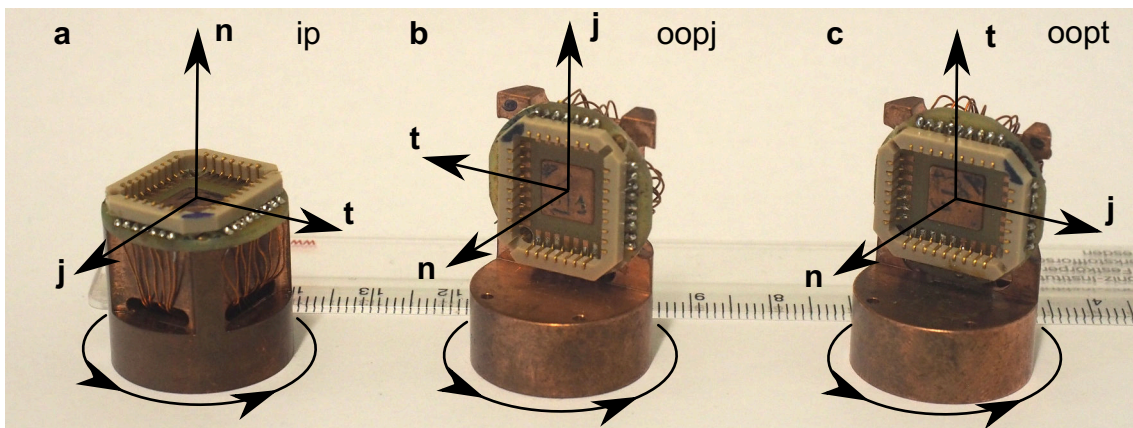

Figure 2.7: Panels **a**, **b** and **c** show the three pucks that can be attached to the measuring insert with a 40 pin Samtec connector and allow for rotations in the three mutually orthogonal rotation planes ip, oopj and oopt, respectively.

The sample temperature can be determined by measuring the resistance of a Cernox CX1030 temperature sensor which is glued into a copper cartridge with Stycast 2850 and screwed into the thermometry head. The temperature sensor was calibrated against a factory-calibrated Cernox sensor mounted on a CLCC on the sample position. Additionally, a heater cartridge (Watlow Firerod, $50\,\Omega$, $50\,W$) is inserted into the thermometry head. The readout and PID control of the sample temperature is done with either a Lakeshore 340 or 335 temperature controller. Temperatures from $4\,K \leq T \leq 320\,K$ can be stabilized usually to within $|\Delta T| \leq 20\,mK$.

To allow ARMR and FDMR measurements to even higher magnetic fields, we used a second magnet magnet cryostat. This cryostat (the "Oscar") has a split coil magnet which can generate horizontal magnetic fields of $\mu_0 H_{ext} = 7\,T$ while its VTI has an inner diameter of only $d_{SC} \sim 24.5\,mm$. To account for this, a second improved version of the low temperature measuring insert, with an exchangeable "puck" and an outer diameter of $24\,mm$ was designed and assembled. By using three different pucks, the three rotation planes can be defined (c.f. Fig. 2.7)
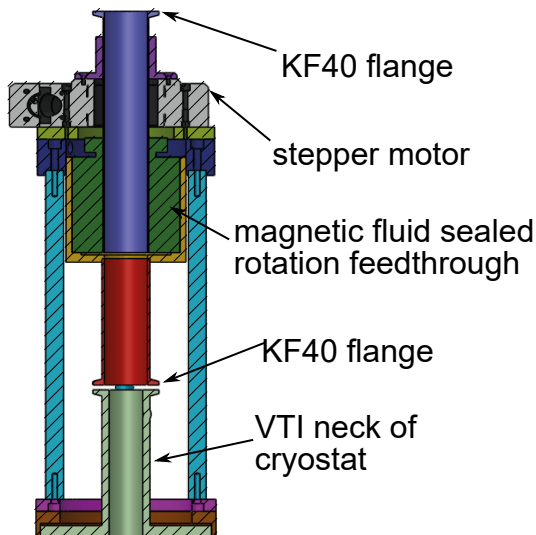

Figure 2.8: Cross section of the extension designed for the split coil cryostat. The magnetic-fluid-sealed rotational feedthrough (green) separates the VTI from the atmosphere. A stepper motor (gray) is used to rotate the upper (purple) part of the extension, to which the measuring insert is attached (KF40 flange on top) with respect to the part of the extension (yellow, blue, turquoise, brown) fixed to the cryostat. The extension is attached to the VTI neck using the available KF40 flange.

Labels in figure: KF40 flange; stepper motor; magnetic fluid sealed rotation feedthrough; KF40 flange; VTI neck of cryostat

To enable rotations of the sample in the horizontal magnetic field, the cryostat was furthermore equipped with a rotation mechanism: The idea is to rotate the entire measuring insert with respect to the magnet cryostat. The design was again adapted from drawings made by Thomas Brenninger at the Walther-Meißner-Institute in Munich and a cross section is shown in Fig. 2.8. The measuring insert is attached to the upper part of the extension via the KF40 flange on top. By rotating this part with respect to the rest of the extension and the cryostat, we can rotate the sample in the horizontal field. The rotation is automated with an Owis stepper motor connected to the rotatble upper part and the fixed part of the attachment (and thus the cryostat). To ensure that the VTI of the cryostat is sealed from the atmosphere, a rotational vacuum feedthrough with a magnetic fluid seal is used. In addition to allowing rotations, the attachment serves as an extension to the magnet cryostat: It increases the distance from the top flange to the center of the

magnetic field to be the same as for the Chaos cryostat. As such, the puck dipstick can be universally used in all cryostats.

Finally, a solenoid magnet (the "VSM cryostat") with a magnetic field $\mu_0 H_{ext} \leq 13.5\,\mathrm{T}$ is available for magnetotransport, where a simple tube terminated by two KF40 flanges was machined to match the length of the VTI of this cryostat to the standard length of the measuring inserts. In conjunction with the three different pucks, the magnetic field can be applied along the three high symmetry directions to study the high field evolution of the magnetoresistance.

A detailed list of the parts used in manufacturing the measuring inserts including the serial numbers of the installed temperature sensors can be found in the appendix (c.f. Sec. A.2)

2.5 Scanning Laser Microscope

In this section, the construction of a setup for measurements of spatially resolved thermally generated voltages as presented in Ch. 7 is discussed. The setup design was inspired by reports in Ref. [39], extending the capabilities of the setup presented there. Spatially resolved measurements of (magneto-)thermal voltages require mainly three things: First, a local thermal gradient needs to be applied to the sample, generated e.g. by a focused laser beam or a heated tip. Additionally, the thermal gradient has be scanned over the sample to measure the spatial evolution of the ensuing thermal voltage by correlating the observed voltage with the position of the heat source. Secondly, the sample has to be electrically contacted to measure the thermal voltages arising due to the applied thermal gradient. Finally, the sample needs to be brought into a magnetic field, to align the magnetization.

Before introducing the individual components of the setup in detail, a short overview will be presented. To that end, a picture of the central part of the setup with the laser focused onto a sample in the insert is shown in Fig. 2.9a. The sample is mounted on a measuring insert very similar to the inserts of the Halbach magnets (c.f. Sec. 2.2). The thermal gradient is induced by a laser focused onto the sample, which can be positioned using a moving x-y-z-stage. Additionally, the measuring insert is centrally placed in a 2D vector electromagnet used for generating the magnetic field.

First, a detailed description of the laser setup and the scanning stage will be provided in the following. A standard $\emptyset 5.6\,\mathrm{mm}$ TO-packaged laser diode with an output power of $P_{max} = 100\,\mathrm{mW}$ and a wavelength $\lambda = 637\,\mathrm{nm}$ is used as laser source. The diode is mounted on a thermoelectric cooler (TEC), to stabilize its temperature and reduced drifts of the laser power. Both, the temperature of the TEC as well as the laser power are controlled by a Thorlabs ITC 4001 controller. The laser beam is then collimated and passes through an optical chopper to allow a lock-in detection of the electrical signal. It is then, brought onto one optical axis with a single mode (SM) fiber using steering mirrors. Subsequently, the beam is coupled into the fiber by focusing it onto the polished end of the fiber with a commercially available fiber launch system (Thorlabs KT110). Finally, after exiting the fiber, the beam is collimated and shaped to have a Gaussian profile in a
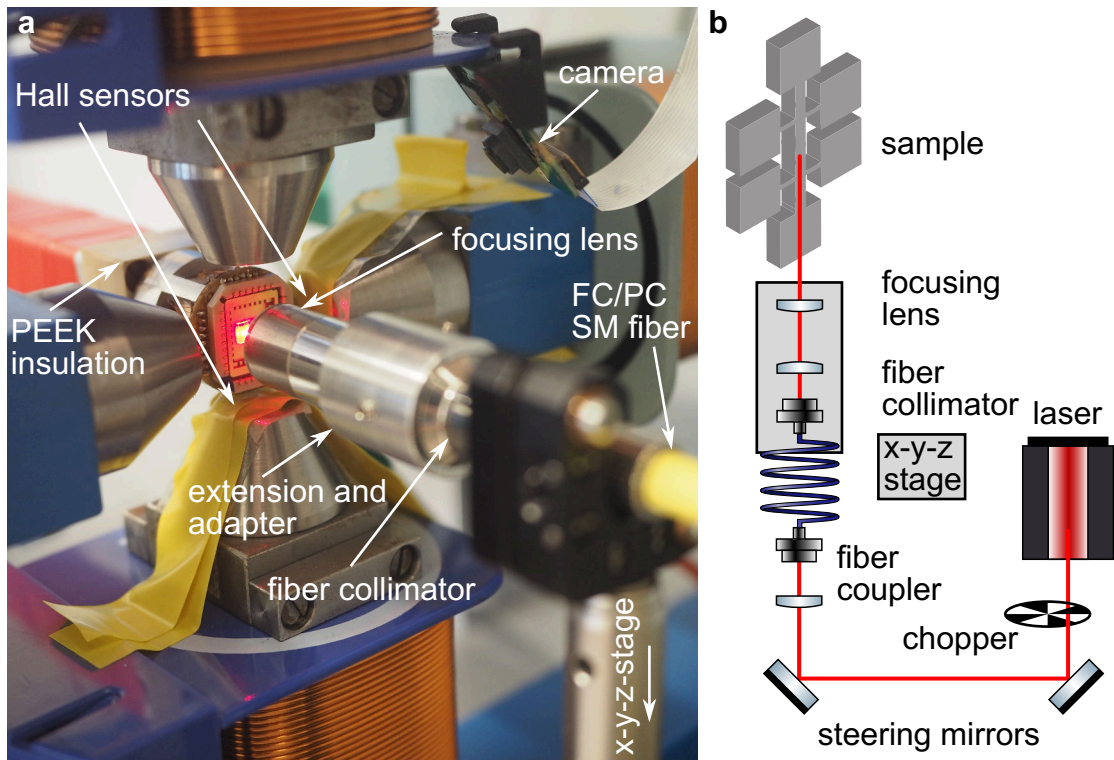
Figure 2.9: **a** A picture of the sample holder in the magnet with the laser focused on the sample is shown. The complete right hand part including the fiber is mounted on and moved by an x-y-z-stage to be able to position and focus the laser spot. **b** The beam path of the setup.

triplet fiber collimator. Afterwards, it is focused onto the sample with an aspheric lens. The working distance of the lens with focal length $f = 11\,\text{mm}$ is roughly $7\,\text{mm}$, giving enough free space to allow observing the sample with the camera. The full width at half maximum (FWHM) of the beam was estimated to be between $1.5\,\mu\text{m}$ and $3\,\mu\text{m}$ using a line scan over the edge of a Hall bar: By comparing the resulting line shape of the signal to a convolution of a Gaussian with a rectangle, the FWHM can be determined.[121]

Both, the fiber collimator and the focusing lens are mounted on a motorized x-y-z-stage to control the spot position with respect to the sample. This is in particular important to refocus the beam onto the sample plane when the focal plane changes due to thermal expansion of the sample holder at elevated temperatures. The full beam path is sketched in Fig. 2.9b.[2]

The measuring insert and the magnet are presented next. To bring the sample into the magnetic field, an insert very similar to the one described in Sec. 2.2 is used. As the setup was designed to perform the measurements presented in Ch. 7, where the non-collinear

---

[2]I would like to acknowledge Alexander Franzen for providing the optical symbols in his "ComponentLibrary"

antiferromagnet Mn_3Sn was investigated, one requirement was to be able to perform experiments above its Néel temperature. To that end, a high temperature modification was added to the insert, allowing to heat the sample to at least $450\,K > T_N \approx 420\,K$. An aluminum version of the in-plane puck (c.f. Fig. 2.7a) used for the low temperature insert was modified to that end: Two slots were milled into the puck, to accommodate a $50\,\Omega$ TO-220 resistor for heating and a Pt100 resistance thermometer. The slot for the heating resistor has a very small tolerance, such that the resistor is held in place by the tight fit. On the other hand, the Pt resistance thermometer has an uneven shape and is thus pressed against the insert by an additional brass screw to ensure proper thermal contact. The heater and the resistance thermometer are placed roughly 1 cm from the sample position. Consequently, the temperature of the puck (and thus the sample) can be increased up to $450\,K$ using a Lakeshore 335 temperature controller.[3]

To avoid the heat from flowing from the puck into aluminum profile holding it and extending the sample holder, a PEEK spacer was included in the design as insulation (c.f. Fig. 2.9a and Fig. 2.10). The thickness of this spacer t_{PEEK} was determined by a finite element simulation carried out in Solidworks. For the simulation the insert is surrounded by air with an ambient temperature of 300 K. Furthermore, a thermal heat transfer coefficient of $10\,W\,m^{-2}\,K^{-1}$ from the insert to the surrounding air was estimated. The temperature profile obtained from the simulation can be seen in Fig. 2.10 and confirms that an insulation thickness $t_{PEEK} = 15\,mm$ is sufficient: Even with the sample holder tip (CLCC contact point) at $450\,K$, the Item profile only heats up barely ($T_{Item} \approx 305\,K$).

Figure 2.10: The temperature profile inside the measuring insert determined by a finite elements simulation carried out in Solidworks. The temperature on the CLCC contact point (far left) was fixed to 450 K. Apart from this, convective air cooling was taken into account. The simulation verifies that a PEEK insulation thickness of 15 mm is appropriate to insulate the tip of the measuring insert and the Aluminum fixture.
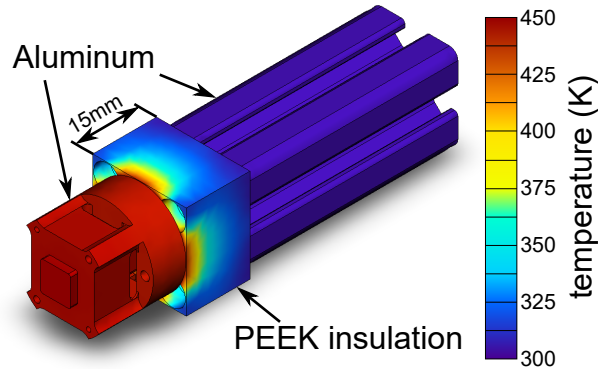
The 2D vector electromagnet is able to generate magnetic vector fields in the sample plane of $\mu_0|\mathbf{H}| \lesssim 140\,mT$ for a pole shoe separation of $\approx 30\,mm$. In order to measure the magnetic field, two Hall probes were glued to the pole shoe centers, one for each axis. The readout is again performed by the custom Raspberry Pi based measurement device (c.f. Sec. A.1). Additionally, this device generates two analog voltages for controlling the magnet current sourced by two Kepco BOP 20-20D.[4]

---

[3]Please note, that the rate of change for the temperature when heating must not be larger than $10\,K\,min^{-1}$ to avoid an overshoot of the heater temperature. In this case, the solder on the resistor contact melts and the wires have to be reattached.

[4]Please note that the voltage control of the Kepco BOP has to be used for low noise measurements. Sig-

2.6 Electrical Measurements

After the chip carrier with the sample has been mounted into one of the measuring in-
serts, the CLCC contacts can be accessed via a BNC breakout box (c.f. Fig. 2.11). The box
allows individually grounding all contacts for electrostatic discharge (ESD) protection. A
part list and the schematic can be found in the appendix (c.f. Sec. A.3). To avoid ground
loops, giving rise to spurious voltages, the only grounding connection to the measure-
ment setup and insert is via this breakout box. All other connections to the earth ground
(i.e. the individual device grounds, the connection to the cryostat etc.) have been severed
in the respective device breakout boxes (e.g. in the breakout box for the Keithley 2182
nanovoltmeter) where possible.

Figure 2.11: The 32pin BNC breakout box
used to connect the measuring inserts
(via a 44 pin High Density D-Sub connec-
tor, see top of figure) with the devices.
The grounding wire can be seen on the
left side.

Most measurements presented in this thesis were carried out using a DC measurement
setup consisting of one or more Keithley 2450 source measure units used for sourcing the
currents. The voltages are detected using two or more Keithley 2182 nanovoltmeters. All
devices are interfaced using Ethernet, installing serial-to-Ethernet converters where no
internal Ethernet interface is present. The control and measurements of the devices is
performed using a custom Python measurement program written during this thesis (c.f.
App. C). A picture of a typical setup can be seen in Fig. 2.12.

---

nificant voltage pickups are present on the measured signal if current control is used, which are most likely
caused by oscillations in the current regulation circuit.

Figure 2.12: Typical configuration of a measurement setup used for the transport experiments.
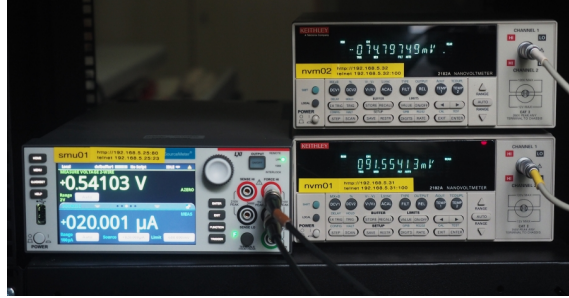
To further enhance the sensitivity and to remove thermoelectric offset voltages, a current reversal technique (also called delta method)[122] can be implemented using our custom measurement software. Here, two measurements with opposite current polarity $V(+I)$ and $V(-I)$ are taken and joined into one reading as shown in Eq. (2.1) and Eq. (2.2).

$$V^{\mathrm{a}} = \frac{V(+I) - V(-I)}{2} \tag{2.1}$$

$$V^{\mathrm{s}} = \frac{V(+I) + V(-I)}{2} \tag{2.2}$$

The current reversal technique, in addition to removing noise and spurious offsets, can be used in a stable environment (i.e. where the offset drifts are small) also to separate different contributions to the measurement signal. In particular, the contributions scaling antisymmetric ($V^{\mathrm{a}} \propto I^{2n-1}$, $n \in \mathbb{N}_+$) and symmetric in current ($V^{\mathrm{s}} \propto I^{2n}$, $n \in \mathbb{N}_+$) can be distinguished. This separation is essential e.g. for separating the spin Seebeck effect ($\propto I^2$) from the spin Hall magnetoresistance response ($\propto I$) as performed in Ch. 3 and Ch. 5.

There is another implementation, where three instead of two measurement values are combined. This method is implemented in way, that the first (V_1) and last (V_3) measurement are taken for a positive current, while the second (V_2) reading is taken for a negative current. The three measurements are then combined as follows:

$$V^{\mathrm{a}} = \frac{V_1(+I) - 2V_2(-I) + V_3(+I)}{4} \tag{2.3}$$

$$V^{\mathrm{s}} = \frac{V_1(+I) + 2V_2(-I) + V_3(+I)}{4} \tag{2.4}$$

Using three measurement values has the advantage of also removing linear drifts of the offset, changing the voltage between the individual readings, from the signal typically of interest in transport (V^{a}).[122,123] Please note, that considered from a higher level of abstraction, the delta method can be understood as a low frequency, square modulated lock-in measurement, shifting the measurement frequency towards or above the 1/f corner of the measurement devices.[5][123]

---

[5]The measurement frequency e.g. of the two point current reversal corresponds to the inverse of the time between two current reversal readings.
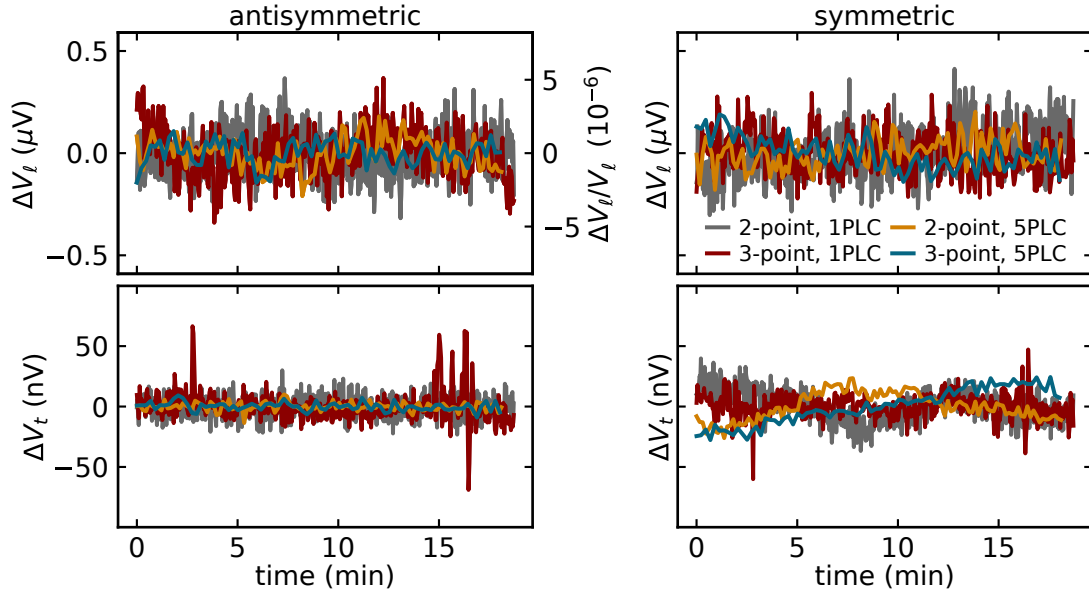
Figure 2.13: Noise measurements on a typical Hall bar with a longitudinal resistance (4-point) of $R_{\mathrm{sample}} = V_\ell/I = 720\,\Omega$ (c.f. Fig. 2.2b). The rms values of the noise are summarized in Tab. 2.1. A second order polynomial was subtracted from the data to remove drifts (caused by changes of the room temperature) from the antisymmetric longitudinal voltage to allow estimating the noise of the signal. For all other signals, the mean of the voltage in the time window was subtracted.

In the following, the noise response of the two different approaches (i.e. two point and three point) implemented in the custom measurement software is compared for some of the typical settings of the measurement setup. To this end a Pt Hall bar ($t_{\mathrm{Pt}} = 5\,\mathrm{nm}$) was inserted into the Halbach setup (c.f. Sec. 2.2) and a constant current $I = 100\,\mu\mathrm{A}$ was sourced along the Hall bar. The longitudinal V_ℓ and transverse V_t voltages were then detected as shown in Fig. 2.2 for roughly 18 min. The nanovoltmeters were set to the 10 mV (100 mV) range for V_t (V_ℓ) and configured to use a 10 point repeating filter and an integration time given by the denoted number of power line cycles (PLC). The resulting curves are shown in Fig. 2.13 for the antisymmetric and symmetric part of V_ℓ and V_t. Please note, that for the longitudinal antisymmetric voltage a polynomial was subtracted from the data, to remove drifts (rooted in changes of the environmental temperature) and that the total integration time for all the different measurements is not the same. It is clear already from the raw data that, as expected, the noise is decreased if the number of power line cycles and thus the integration time is increased. To allow a straightforward comparison, the standard deviation of the curves is summarized in Tab. 2.1.

First, no significant difference between the three point and two point method (i.e. between the first and second or third and fourth row) is evident. This is not the expected behavior, as one would expect a noise reduction at least by a factor of $\sqrt{3/2} = 1.2$ due to the higher integration time. Only guesses can be made as to the cause: It might be rooted

NPLC (T_{int})	$\left(\frac{\Delta V_\ell^a}{V_\ell^a}\right)_{rms}$ in 1×10^{-6}	$(\Delta V_\ell^a)_{rms}$ in nV	$(\Delta V_t^a)_{rms}$ in nV	$(\Delta V_\ell^s)_{rms}$ in nV	$(\Delta V_t^s)_{rms}$ in nV
2p, 1 PLC (400 ms)	1.6	111.8	8.6	124.4	12.7
3p, 1 PLC (600 ms)	1.7	120.8	13.0	101.7	10.0
2p, 5 PLC (4 s)	1.1	76.5	3.4	71.2	11.3
3p, 5 PLC (6 s)	0.8	59.7	3.4	77.2	14.5

Table 2.1: Collected rms values for the measurement shown in Fig. 2.13. Both nanovolt-meters were configured to take 10 averages, each having an integration time given by the number of power line cycles (PLC, 1PLC(50 Hz) = 20 ms). Additionally, the averaging filter was set to always record a completely new set of data after the measurement was read from the device (repeating filter). The ranges of the nanovoltmeters were 100 mV and 10 mV for the voltages detected along (longitudinal, V_ℓ) and transverse (V_t) to the direction of current flow, respectively.

in the small time window not accurately representing the actual noise level. Another explanation might be that there are additional drifts impacting the third reading (the total time for finishing one three point reading is 15 s compared to 10 s for the two point reading) or that there are simply no linear drifts on this timescale.[6] Secondly, although one would expect the noise to be actually lower for the measurement with 1 PLC due to a modulation frequency (1 Hz) closer to the $1/f$ noise corner of the setup (≈ 10 Hz)[123] while with 5 PLC one has a modulation frequency of only 100 mHz. This, however, cannot be verified by the present data as the noise in the 5 PLC measurement is lower by roughly a factor of 2 ($\sqrt{5} = 2.2$) as expected for the higher integration time with constant noise power. One possible reason for this is the implementation of the three point and two point method on the software level: As the devices are triggered by the measurement software, which also handles all other device communications, there will be significant jitter in the timing of the measurements. Thus, even if there are linear drifts, they do not properly cancel with the three point method as it is performed here, due to the unequal time between the different readings. This could be alleviated by using proper (hardware) triggering and buffered readings. In this case, no device communications and related lags would delay the measurement sequence. Consequently, the time for performing the full measurement and as such the impact of drifts would be reduced (as well as constant). In summary, no significant performance difference between the two and three point current reversal method can be seen, so that during this thesis only the two point method is used due to the reduced measurement time required.

The generally increased noise observed in the longitudinal signal is most likely caused by two things: Firstly, the amplifier of the nanovoltmeter has a limited dynamic range defined by the (constant and amplification independent) noise of the digitization stage. Therefore, if the input amplification is reduced (i.e. a larger range is selected), the absolute value of the digitization noise will be higher. Secondly, there will be additional noise

---

[6]The acquisition of one voltage reading takes $\sim$ 5 s in total. This includes the time for triggering, the settling time, the measurement itself and the readout of the result.

introduced by the source meter used to drive the current due to the noise of the digital to analog conversion.[7]

In the following, the typical performance is summarized once more. A typical noise of $\Delta V^{\text{a}}_{\text{rms}} \sim 5\,\text{nV}$ and $\Delta V^{\text{s}}_{\text{rms}} \sim 20\,\text{nV}$ can be achieved in the lowest range of the Keithley 2182 nanovoltmeter (10 mV range, integration time per point $T_{\text{int}} = 2\,\text{s}$, $f_{\text{mod}} \sim 0.1\,\text{Hz}$, $R_{\text{sample}} \sim 1\,\text{k}\Omega$). This is the configuration typically used for measurements of the transverse (or non-local) voltage. The (rms) thermal voltage noise density of the $1\,\text{k}\Omega$ resistor at $T = 300\,\text{K}$ is $\sqrt{v^2_{\text{JN}}} = \sqrt{4k_{\text{B}}TR} \approx 4\,\text{nV}/\sqrt{\text{Hz}}$.[124,125] To estimate the rms noise voltage stemming from this noise density, the measurement bandwidth of $\frac{1}{2T_{\text{int}}} = 0.25\,\text{Hz}$ needs to be accounted for. Consequently, one can expect a noise of the resistor of $\Delta V_{\text{JN}} = 2\,\text{nV}$. As such, the noise performance of our measurement setup is already close to the limit given by the thermal fluctuations of the resistor. For the longitudinal contacts, typically a (relative) noise of $\left(\frac{\Delta V^{\text{a}}}{V^{\text{a}}}\right)_{\text{rms}} \sim 1.5 \times 10^{-6}$ is observed in the 100 mV range of the nanovoltmeter with otherwise unchanged settings.

Finally, another extension to the current reversal technique shall be briefly discussed. By taking not only alternating readings but additionally changing the current amplitude, the symmetric and antisymmetric parts can be further separated into individual orders in the current I. The limiting case of this approach would be to measure an I-V curve at every point to get the full information about all present orders of the current from a polynomial fit to the data. However, since the contributions to the voltage $\propto I^n$ with $n > 3$ are expected to be small, four current values (e.g. $\pm I$ and $\pm 2I$) are sufficient to receive reasonable results. Roughly the same information can be obtained using a lock-in amplifier detecting the first three harmonics of the signal.[8] The four voltages (scaled for current I) can then be extracted using Eqs. (2.5) to (2.8)

$$V_0 = \frac{1}{3}(4V^{\text{s}}(I) - V^{\text{s}}(2I)) \propto I^0 \tag{2.5}$$

$$V_1 = \frac{1}{6}(8V^{\text{a}}(I) - V^{\text{a}}(2I)) \propto I^1 \tag{2.6}$$

$$V_2 = \frac{1}{3}(V^{\text{s}}(2I) - V^{\text{s}}(I)) \propto I^2 \tag{2.7}$$

$$V_3 = \frac{1}{6}(V^{\text{s}}(2I) - 2V^{\text{s}}(I)) \propto I^3 \tag{2.8}$$

---

[7]For the transverse voltage this noise is not observed, as the transverse resistance is typically close to 0, so that a 1×10^{-6} noise in the current does not impact the voltage reading. Thus, the noise of the source meter is not as relevant for the transverse voltage, which is typically limited by the input noise of the nanovoltmeter.

[8]Please note, that the higher harmonics of the lock-in amplifier do not directly compare to the orders in current: e.g. $\sin^3(\omega t) = \frac{1}{4}(3\sin(\omega t) - \sin(3\omega t))$ giving rise to an intermixing of the I^3 signal into the first and third harmonic.

Chapter 3

SPIN HALL MAGNETORESISTANCE

The spin Hall magnetoresistance (SMR) so far has been mostly studied in heterostructures consisting of a magnetically ordered insulator (MI)[1] and a spin Hall active metal (NM).[42–44] One prototypical example for such a MI/NM heterostructure used for SMR experiments is $Y_3Fe_5O_{12}$/Pt.[42,43,126] Initially, it was assumed that the SMR is mediated by a coupling between the spin Hall spin accumulation (generated at the MI/NM interface via the spin Hall effect in the NM) and the net magnetization of the magnetic insulator.[44] However, further experiments in magnetic insulators with more than one magnetic sublattice (e.g. ferrimagnets and antiferromagnets) revealed that the spin Hall spin accumulation at the MI/NM interface actually couples to the individual magnetic sublattices of the MI.[11,15,50,64–66,127–129] Until now, the SMR response of materials without long range magnetic order (i.e. paramagnets) has not been studied rigorously. Consequently, no detailed microscopic understanding of the coupling mechanisms of the paramagnetic moments to the interfacial spin accumulation have been established so far. In particular, the description of the coupling mechanism (i.e. the transverse spin transfer accross the MI/NM interface)[44,63,126] in terms of magnetic sublattices should reach its limiting case for paramagnetic systems. In a paramagnet the individual spins can be understood as an "infinite" amount of magnetic sublattices which are not coupled over long length scales but randomly oriented (when no magnetic field is applied). Thus, the study of the SMR in disordered MI/NM heterostructures is particularly interesting, as the interaction would have to be mediated by the individual paramagnetic spins within the magnetic insulator.

This chapter is dedicated to the study of the SMR effect in heterostructures consisting of a disordered (para-)magnetic insulator and a spin Hall active metal. In these heterostructures, we aim to elucidate the mechanisms by which the spin Hall spin accumu-

---

[1]By magnetically ordered insulator we refer to ferro-, ferri- or antiferromagnetic insulators in their ordered phase, i.e. magnetic insulators with a long range magnetic order.

lation couples to the paramagnetic (i.e. disordered) spin system. Three different material systems have been studied in this regard in the course of this thesis. Two of them are addressed in this chapter, while the third will be discussed in the context of the magnon mediated magnetoresistance in Ch. 4 (c.f. Sec. 4.2). In the first section of this chapter (Sec. 3.1) the SMR in heterostructures made from a paramagnetic oxide and Pt – that do not show spontaneous magnetic ordering in the temperature range investigated – is presented. In contrast, in Sec. 3.2 the SMR in bilayers of the antiferromagnetic insulator Cr_2O_3 and Pt or Ta will be studied above the Néel temperature of the antiferromagnet, i.e. in the paramagnetic phase.

3.1 Non-Crystalline $Y_3Fe_5O_{12}$/Pt Heterostructures

The use of heterostructures of yttrium iron garnet ($Y_3Fe_5O_{12}$, YIG) and Pt would be highly desirable for studies of the SMR in the disordered phase, since the spin Hall magnetoresistance is very well characterized in this system.[42,43,126] However, YIG on the first glance is a poor choice from an experimental perspective, as crystalline $Y_3Fe_5O_{12}$ has an ordering temperature $T_C = 560\,K$, well above room temperature.[119] To overcome the issue of the high ordering temperature of crystalline YIG, amorphous (i.e. non-crystalline) YIG can be used: Non-crystalline YIG (nc-YIG) is an insulator with antiferromagnetic interactions between the individual Fe spins and an ordering temperature of only $T_N \sim 50\,K$.[130–133] Additionally, even below its ordering temperature no long-range magnetic order, but a speromagnetic state is realized.[131] In this state, the Fe spins are locally ordered but no long-range magnetic order is realized, since no preferential direction is given due to the lack of a crystal lattice.[119] Consequently, a speromagnet can show a similar response to external magnetic fields as a paramagnet even in its ordered phase.[119]

Consequently, nc-YIG seems like a perfect candidate for studies of the SMR in disordered systems. Additionally, the growth of non-crystalline layers of YIG using sputtering and pulsed laser deposition was already demonstrated in literature.[132,134–136] Thus, this section will focus on the magnetoresistance in heterostructures of the disordered magnetic insulator nc-YIG and Pt.

The contents of this section are reproduced in part from M. Lammel et al., Applied Physics Letters **114**, 252402 (2019) (Ref. [5]) with permission from AIP Publishing. For this publication, I performed the transport measurements and participated actively in the evaluation and discussion of the data as well as the preparation of the manuscript.

3.1.1 Sample Preparation

The non-crystalline yttrium iron garnet/Pt bilayers were prepared by radio frequency sputtering at room temperature by from a stoichiometric $Y_3Fe_5O_{12}$ (YIG) target, while the Pt was deposited using DC magnetron sputtering. Please note, that the sputtering is performed at room temperature without subsequent annealing results to obtain yttrium iron garnet films without crystalline order.[132,134,136] Two sets of samples were prepared, where the first one was deposited on (111)-oriented $Y_3Al_5O_{12}$ (YAG) substrates by Savio Fabretti

(Technische Universität Dresden). To exclude influences of the close lattice matching of YIG and YAG, the second series was deposited on (100)-oriented Si substrates terminated with a 1 μm thick thermal oxide layer by Kevin Geishendorf (Leibniz Institute for Solid State and Materials Research Dresden, IFW Dresden). Both depositions (i.e. YIG and Pt) were performed in sequence, without breaking the vacuum. By sputtering for 6000 s at 80 W a YIG layer thickness of 30 nm was achieved, while the 2.5 nm thick Pt layer was deposited in 73 s using a power of 30 W.
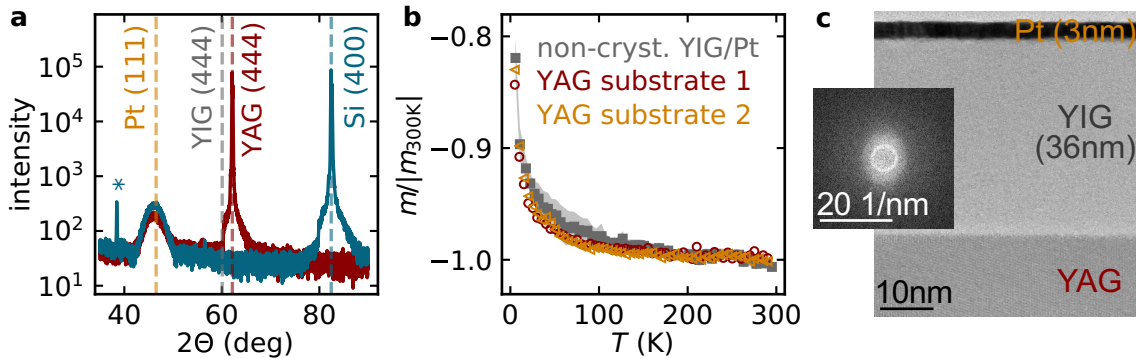

Figure 3.1: **a** An X-ray diffraction measurements on nc-YIG/Pt heterostructures deposited on YAG (red) and Si/SiOx (teal) is shown. No diffraction peak associated with YIG can be resolved, while the Pt film exhibits a (111) texture. **b** Temperature dependent magnetic moment measurements on the nc-YIG sample grown on YAG and two bare YAG substrates without a (nc-)YIG film are plotted. Since the samples had different lateral dimensions, the data has been normalized to the respective magnetic moment at 300 K for straightforward comparison. A paramagnetic background is evident in all samples towards low temperatures likely stemming from paramagnetic impurities in the substrates. **c** A transmission electron image of a cut of a nc-YIG/Pt deposited on YAG is shown including the Fourier transformation (inset) is shown. The Fourier image verifies the absence of any preferential directions or lattice ordering in the nc-YIG films. Adapted from Ref. [5].

To further verify the absence of crystalline order in the as-sputtered YIG layer, X-ray diffraction measurements using $\text{Co}_{\text{K}_\alpha}$ radiation were performed by Michaela Lammel (IFW Dresden) in a Bruker D8 Advanced diffractometer (c.f. Fig. 3.1a). We do not observe any diffraction peaks associated with YIG, while the Pt exhibits a (111) texture, which is the preferred growth orientation for Pt deposited at room temperature.[137] Please note, that the sharp step at $2\Theta = 60°$ is caused by the iron filter necessary for the suppression the $\text{Co}_{\text{K}_\beta}$ radiation. Additionally, transmission electron microscopy images were taken by Rene Huebner (Helmholtz-Zentrum Dresden Rossendorf), which further confirm the absence of any crystalline order in the YIG layer (c.f. Fig. 3.1b). The magnetic characterization was performed by Helena Reichlova (Technische Universität Dresden) and Michaela Lammel, using a Quantum Design MPMS-XL7 SQUID magnetometer. The magnetic moment observed as a function of temperature at an applied magnetic field of $\mu_0 H = 500\,\text{mT}$ is shown in Fig. 3.1c. To separate the contributions stemming from the substrate and the film, two bare substrates, onto which no YIG film was deposited, were

additionally measured. Please note, that the magnetic moments have been normalized to
the respective value at 300 K due to the different lateral size of the samples. By comparison
of the substrates and the heterostructure, we conclude that no spontaneous magnetization
is present in our nc-YIG/Pt bilayer. For high temperatures, only the moment of the dia-
magnetic substrate is visible, while an additional paramagnetic (i.e. $\propto T^{-1}$) contribution
to the magnetic moment is observed towards low temperatures. This paramagnetic back-
ground, however, is also observed in the bare YAG substrates, such that paramagnetic
impurities in the substrates likely are main origin of this signal. Thus, even at low tem-
perature no additional magnetic moment due to the nc-YIG film is evident, as expected
if it orders into a speromagnetic phase around 50 K.[130–133]

    After the magnetic characterization, the samples were patterned into Hall bars using
optical lithography and Ar ion milling. The measurements were performed as described
in Sec. 2.6 using a current of $I_\mathrm{s} = 90\,\mu$A.

3.1.2   Results and Discussion

    The angle resolved magnetoresistance (ARMR) measured at 200 K for the three mutu-
ally orthogonal rotation planes described in Ch. 2 is shown in Fig. 3.2. Here, a modulation
of the resistivity is evident for the in-plane (ip) and out-of-plane rotation around the cur-
rent direction (oopj), while no modulation is observed for the third rotation plane (oopt).
This is the symmetry expected for the spin Hall magnetoresistance (SMR), i.e. the resis-
tivity depends on the projection of the magnetization onto the **t** direction (or the spin
direction, c.f. Sec. 1.3.1):[42–44] Consequently, in our coordinate system, the dependence of
the resistivity can be described by

$$\rho_\ell = \rho_0 + \Delta\rho\left(1 - \sin^2(\alpha,\beta)\right) \text{ or} \tag{3.1}$$

$$\frac{\delta\rho_\ell}{\rho_0} = \frac{\rho_\ell - \rho_0}{\rho_0} = \frac{\Delta\rho}{\rho_0}\left(1 - \sin^2(\alpha,\beta)\right). \tag{3.2}$$

We thus find a minimum resistivity for **m** ∥ **t** and a maximum resistivity for **m** ⊥ **t**, where
the magnetoresistance ratio is $\Delta\rho/\rho_0 = 3 \times 10^{-5}$ at $\mu_0 H = 2\,$T.[2] Please note, that as also
described in Sec. 1.3.1, the Hanle magnetoresistance (HMR) has the same symmetry as
the SMR as it stems from a similar mechanism: For the HMR, the spin accumulation at
the Pt interfaces is dephased (lost) due to spin precession in a perpendicular magnetic
field, consequently leading to additional loss of spin information and thus a higher re-
sistivity.[67,68] However, the magnitude of the HMR effect expected in Pt at the maximum
magnetic field $\mu_0 H = 2\,$T used in this study, is $\Delta\rho_\mathrm{HMR} \sim 2.5 \times 10^{-6}$,[5,68] which is much
smaller than the magnetoresistance observed here ($\Delta\rho/\rho_0 = 3 \times 10^{-5}$).

    Although $\Delta\rho/\rho_0 \sim 3 \times 10^{-5}$ is still roughly one order of magnitude smaller than the
value observed for heterostructures of crystalline YIG and Pt, the magnitude is still sur-

---

[2]Although using the notation shown in Eq. (3.2) temperature drifts can make the extraction of $\rho_0 = \rho_\ell(\alpha = 90°, \beta = 270°)$ difficult. Thus, the data was shifted to ensure that the normalized resistivity $\delta\rho/\rho_0$ for a given orientation of the magnetic field is in agreement for the different rotation planes, i.e. for **m** ∥ **n** ($\beta, \gamma = 0°$) and for **m** ∥ **t** ($\alpha = 90°, \beta = 270°$)
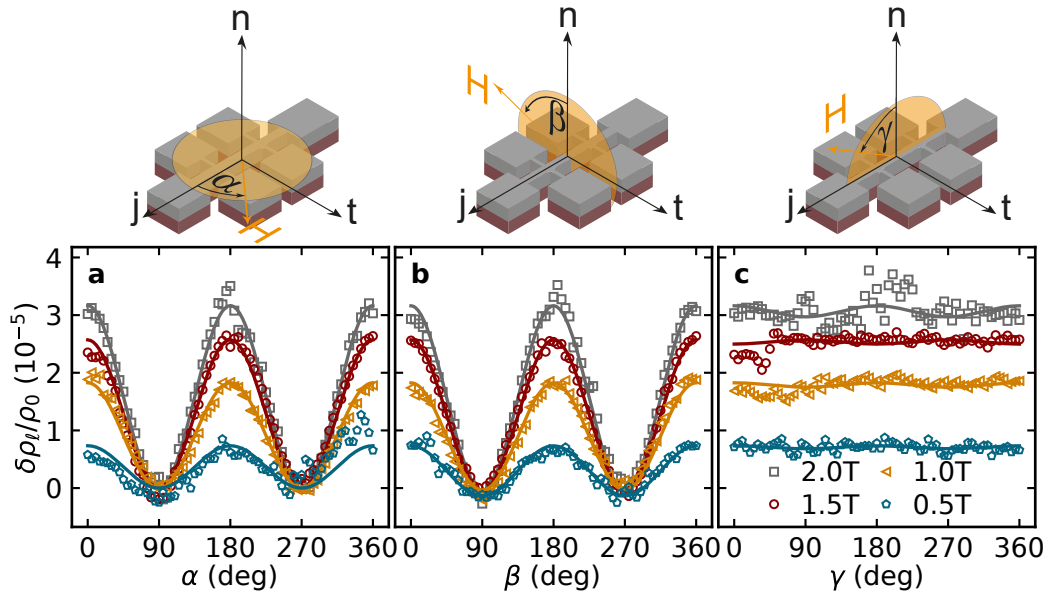
Figure 3.2: **a-c** Angle resolved magnetoresistance measurements on a nc-YIG/Pt heterostructure at $T = 200\,\text{K}$. A clear $\sin^2(\alpha, \beta)$ modulation of the resistivity with a strongly field dependent amplitude can be seen in ip (panel **a**) and oopj rotations (panel **b**). As expected for the SMR, no modulation can be seen for the oopt rotation (panel **c**). A linear drift in time (presumably stemming from a drift of the temperature of the variable temperature insert of the cryostat) has been subtracted from the raw data. Adapted from Ref. [5].

prising for a paramagnetic material: For heterostructure of crystalline YIG and Pt with a Pt thickness of $d_{\text{Pt}} \sim 3\,\text{nm}$ a SMR amplitude in the range of 1×10^{-4} to 1×10^{-3} is expected.[43] Consequently, assuming otherwise similar properties and that the full alignment of the moments in the amorphous film would give rise to the same SMR amplitude as a crystalline heterostructure (i.e. $\Delta\rho/\rho_0 \sim 6 \times 10^{-4}$),[3] $\Delta\rho/\rho_0 \sim 3 \times 10^{-5}$ would suggest a magnetic polarization of around 5 %. As the Zeeman energy ($E_{\text{Z}}/e = g\mu_{\text{B}}\mu_0 HS/e \approx 0.6\,\text{meV}$, assuming $g = 2$, $S = 5/2$ and $\mu_0 H = 2\,\text{T}$) is small compared to the thermal energy ($E_{\text{T}}/e = k_{\text{B}}T/e \approx 18\,\text{meV}$ at $T = 200\,\text{K}$), a maximum polarization of

$$\frac{M}{M_{\text{s}}} = \frac{2S+1}{2S}\coth\left(\frac{2S+1}{2J}\frac{E_{\text{Z}}}{E_{\text{T}}}\right) - \frac{1}{2S}\coth\left(\frac{1}{2J}\frac{E_{\text{Z}}}{E_{\text{T}}}\right) \approx 1.6\,\% \tag{3.3}$$

is expected from the Brillouin function.[138] Additionally, the signal should drastically increase towards lower temperatures, since the thermal energy decreases and thus the polarization would increase (c.f. Eq. (3.3)).

To evaluate the evolution with temperature, we performed additional field dependent

---

[3]The value 6×10^{-4} was chosen from the range of amplitudes reported for the SMR, as a similar sample where the YIG layer was annealed in vacuum prior to the deposition of the 3 nm Pt layer deposition showed an SMR of $\Delta\rho/\rho_0 \sim 6 \times 10^{-4}$

measurements of the magnetoresistance for several different temperatures with the magnetic field applied along the three high symmetry directions ($H \parallel j, t, n$). The respective resulting data are summarized in Fig. 3.3a-c. At temperatures above 100 K a magnetoresistance with a changing slope is observed for $H \parallel j$ and n, whereas no change of resistivity is evident for $H \parallel t$. If the temperature is lowered to 10 K, an additional contribution is evident for $H \parallel t$ and the magnetoresistance for $H \parallel j$ and n are not in agreement anymore. This additional contribution is always present for $H \perp j$ and is likely caused either by the ordinary magnetoresistance or weak anti-localization of the electrons in Pt, giving rise to an additional magnetoresistance.[68,139] Interestingly, except for this additional contribution from Pt no significant difference between the magnetoresistance at 10 K and 100 K is observed. This suggests that there is no difference between the magnetotransport of the nc-YIG/Pt heterostructure for the speromagnetic and paramagnetic phase. Due to the absence of long-range magnetic order in either phase, this is the anticipated behavior.[119,131,133] Most importantly, however, we find that the naive expectation of an increased magnetoresistance for lower temperatures is not corroborated by the data (the amplitude in panels a and c directly correspond to $\Delta\rho/\rho_0$). Surprisingly, the exact opposite behavior is observed, i.e. an increase of the magnetoresistance with increasing temperature. Thus, the magnetoresistance can not simply stem from the field induced magnetization in the nc-YIG/Pt heterostructure, which should increase towards lower temperatures and increasing magnetic fields.[130] One might still argue, that the spin Hall effect in Pt and the spin mixing conductance might give rise to an additional temperature dependence, reducing the SMR towards lower temperatures.[140] However, while at high temperatures an onset of saturation seems to be present, at low temperatures this is not observed, contrary to the expectation for a paramagnet: The magnetic saturation of a paramagnet should be evident for lower magnetic fields if the temperature is reduced.
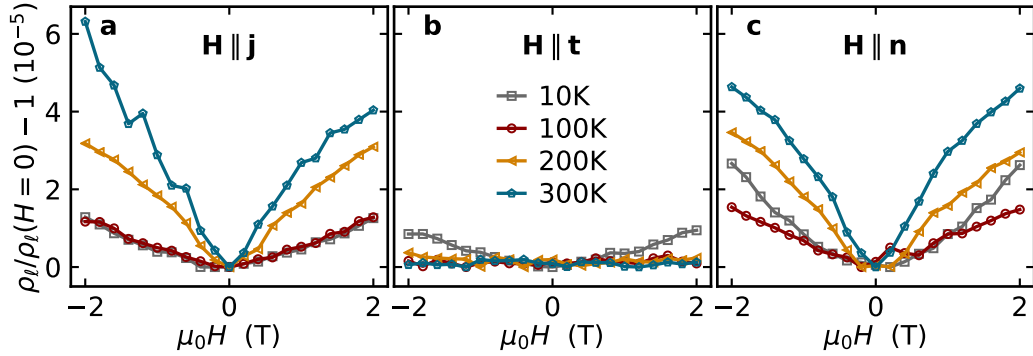

Figure 3.3: **a-c** Field dependent magnetoresistance measurements on a nc-YIG/Pt heterostructure for several different temperatures. The field was applied either along the current direction **j** (panel **a**), the transverse direction **t** (panel **b**) or the surface normal **n** (panel **c**). Adapted from Ref. [5].

In the following, we will take a step back and motivate what the expected response of the SMR in a paramagnet is and compare that to the magnetoresistance observed in

Fig. 3.3. To this end, two limiting cases will be considered: For the first case (model A), the spin current over the interface is governed by individually interacting moments, i.e. the individual magnetic ions interact with the spin Hall spin accumulation.[4] For the second case (model B), the spin Hall spin accumulation couples to the net moment in the paramagnet. In a paramagnet without applied magnetic field, all moments are randomly distributed, as sketched in Fig. 3.4. For a high magnetic field $H \rightarrow \pm H_{\text{sat}}$, all moments will align with the external magnetic field. As the SMR is sensitive to the projection m_t^2 of the magnetization onto the $\mathbf{t}$ direction (c.f. Sec. 1.3.1), one would expect the low resistance state ρ_0, if all moments are aligned along $\mathbf{t}$. The high resistance state $\rho_0 + \Delta\rho$, would then be observed when all moments are either parallel to $\mathbf{j}$ or $\mathbf{n}$.[42–44]

For the case of the individually interacting moments (model A), each magnetic ion contributes individually. Consequently, m_t^2 has to be averaged for all individual moments, i.e. $\langle m_t^2 \rangle$. As required, the high magnetic field values $H \rightarrow \pm H_{\text{sat}}$ are in agreement with the above discussion (c.f. Fig. 3.4a-c). Without magnetic field, however, an intermediate resistance state should be realized: As the moments are randomly distributed, there is a finite amount of moments oriented along the $\mathbf{t}$ direction at any given time. Thus, $\langle m_t^2 \rangle$ will be non-zero, leading to an intermediate resistance state (c.f. Fig. 3.4b).
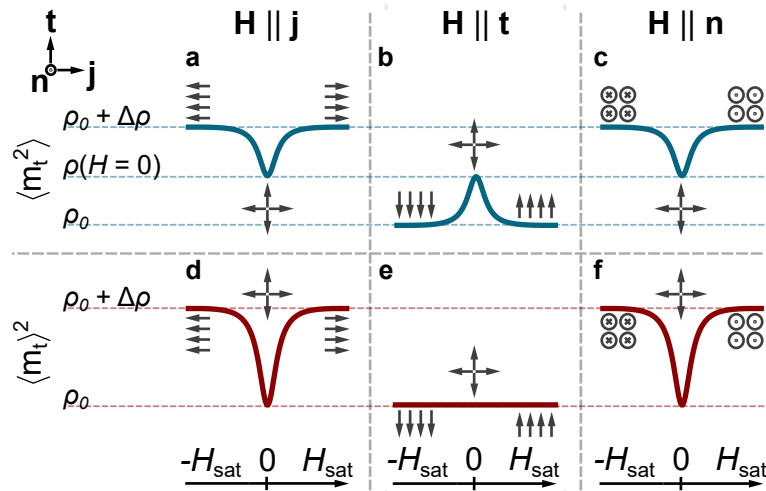

Figure 3.4: Modeling of the SMR response for individually interacting spins (panels **a-c**) and jointly interacting spins (panels **d-f**). **a-c** For model A, the spin transfer torque acts on the individual moments, such that the averaging over the full ensemble is performed as the final step. Here, a finite spin current will flow even with no external magnetic field applied, as the moments are completely random. Consequently, a finite portion of the moments is aligned perpendicular to the transverse direction, and can absorb spin angular momentum. **d-f** In contrast, model B assumes that only the ensemble average spin (i.e. the net magnetization) interacts with the Pt spin accumulation. For this case, no spin current will flow over the interface at zero applied magnetic field, as the ensemble average vanishes. Adapted from Ref. [5].

---

[4]The spin Hall spin accumulation refers to the spin accumulation generated via the spin Hall effect in Pt.

If the net moment interacts with the spin accumulation (model B), m_t^2 has to be considered as $\langle m_t \rangle^2$, i.e. the moment is averaged and only then projected onto the **t** direction. Again, the high magnetic field $H \rightarrow \pm H_{sat}$ case will result in the high or low resistance state for **H** $\perp$ **t** and **H** $\parallel$ **t**, respectively (c.f. Fig. 3.4d-f). However, without applied magnetic field, the magnetization vanishes, so that also $\langle m_t \rangle^2 = 0$. Consequently, in the case of zero applied magnetic field we find the low resistance value ρ_0 (c.f. Fig. 3.4e).

If the expected behavior is compared to the observed magnetoresistance (c.f. Fig. 3.3), we find a good agreement with the SMR generated by the net moment interacting with the spin accumulation. This can be seen in the absence of a decrease of the resistance for **H** $\parallel$ **t** (c.f. Fig. 3.3b), expected in the case of the individually interacting moments. Please note, that this is also the behavior expected for the HMR, which will be discussed in more detail in the next section.

We thus conclude, that in bilayers of a paramagnetic insulator and Pt the spin accumulation seems to be sensitive to the net magnetization in the paramagnet, and not to individual moment orientations. This in particular is in contradiction with previous reports in compensated garnets and antiferromagnets, where the SMR results can be consistently described by the individual interaction of the different magnetic sublattices.[11,15,51,65]

Absence of the Spin Seebeck Effect

Finally, in order to verify the absence of exchange coupling between the moments (or spontaneous magnetic order) in our samples, we measured the current induced spin Seebeck effect in the nc-YIG/Pt heterostructures.[82] In this approach, a large charge current is driven through the Pt layer, resulting in Joule heating and thus an out-of-plane thermal gradient. As the spin Seebeck effect depends on magnons, it requires the presence of some exchange interaction, coupling the individual moments to each other.[141] Please note, that at least in a simple picture, applying a magnetic field is not sufficient to allow magnon transfer: Even though all moments align with the magnetic field, a spin flip on one lattice site cannot be transferred to the next lattice site, as the two spins will not be coupled. Although this is obviously simplified as there will be at least dipolar coupling between the spins in any system, it allows to motivate why in a fully disordered system, one would not expect any spin Seebeck effect. In contrast, for ordered systems, there can be short lived (local) correlations viz. paramagnons even above the Curie/Néel temperature of the system.[142–144]

To allow comparing the Seebeck effect of a nc-YIG sample to a similarly grown but crystalline sample, we deposited a YIG/Pt heterostructure, where the nc-YIG was annealed at 900 °C for 4 h in the deposition chamber, before the room temperature deposition of the Pt. In these samples, the annealing leads to a (partial) crystallization of the YIG, so that a static magnetization is present.[135] The measurement of the induced spin Seebeck voltage during an in-plane rotation of the magnetic field is shown in Fig. 3.5. No modulation to within our experimental resolution ($\sim 5\,\text{nV}$) is observed in the as-deposited nc-YIG sample, while a clear $\cos(\alpha)$ modulation with an amplitude $\Delta V_t^{SSE} \sim 150\,\text{nV}$ is evident for the annealed heterostructure. Thus, the spin Seebeck effect is lower by at least
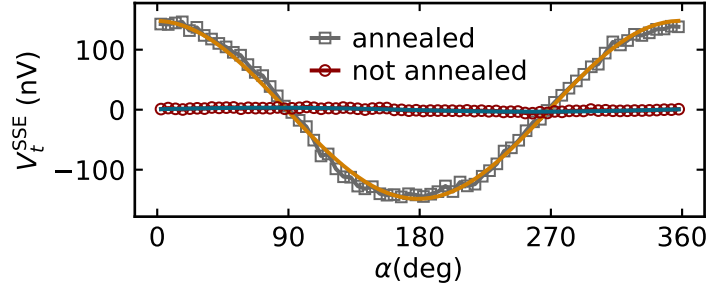
Figure 3.5: Measurement of the spin Seebeck effect of a nc-YIG/Pt heterostructure and an in-situ annealed sputtered YIG/Pt sample. While the latter exhibits a spin Seebeck voltage with an amplitude of $\Delta V_{\mathrm{SSE}} \sim 150\,\mathrm{nV}$, no signal to within our experimental resolution ($\Delta V_{\mathrm{SSE}} \sim 5\,\mathrm{nV}$) is observed in the nc-YIG, verifying the absence of spontaneous magnetic order. The measurement was performed at room temperature with an applied magnetic field $\mu_0 H = 1.1\,\mathrm{T}$.

a factor of 30 in the nc-YIG. For comparison, the SMR in the nc-YIG/Pt heterostructures has a magnitude of $\Delta\rho/\rho_0 \sim 3 \times 10^{-5}$ at 300 K and $\mu_0 H = 2\,\mathrm{T}$, which is only a factor ~ 20 smaller then the SMR magnitude $\Delta\rho/\rho_0 \sim 6 \times 10^{-4}$ observed for the crystalline sample. Consequently, it is reasonable to assume that no magnetic ordering or correlation is present in our nc-YIG/Pt heterostructures. Please note, that also the spin Seebeck effect has not been studied in detail for paramagnetic systems, which is something that remains interesting, in particular in the light of long distance spin transport reported in paramagnetic insulator/Pt bilayers.[145] However, such a study is beyond the scope of this thesis work.

3.1.3 Summary

In this section, the magnetoresistive response of bilayers of non-crystalline YIG and Pt was investigated. To that end, we recorded the magnetoresistance during rotations of several constant magnetic fields in three mutually orthogonal rotation planes at $T = 200\,\mathrm{K}$. Our data revealed the symmetry expected for the spin Hall magnetoresistance or the Hanle magnetoresistance. A magnitude of the magnetoresistance $\Delta\rho/\rho_0 = 3 \times 10^{-5}$ was found at $\mu_0 H = 2\,\mathrm{T}$, decreasing for lower applied magnetic fields. In a next step, the dependence of the resistivity on the magnetic field was studied along the three high symmetry directions (i.e. for $\mathbf{H} \parallel \mathbf{j}$, $\mathbf{n}$ and $\mathbf{t}$). Interestingly, no change of the resistivity with the magnetic field $\mathbf{H} \parallel \mathbf{t}$ was observed, while a strongly field dependent resistivity was evident for $\mathbf{H} \parallel \mathbf{j}, \mathbf{n}$. To establish what signal would be expected for the spin Hall magnetoresistance in a paramagnetic insulator/Pt heterostructure, we put forward two different models: Model A described the SMR due to the interaction of the spin Hall spin accumulation in Pt with individual paramagnetic spins in the magnetic insulator (i.e. $\langle m_{\mathrm{t}}^2 \rangle$). This model described the behavior of the SMR anticipated from experiments in ordered magnetic insulators with multiple magnetic sublattices. In contrast, model B described the

SMR that would arise if only the (magnetic field induced) net magnetic moment would couple to the spin Hall spin accumulation in Pt (i.e. $\langle m_t \rangle^2$). The two models could be distinguished by their different magnetoresistive response if the magnetic field is applied along the **t** direction (i.e. the polarization axis of the spin Hall spin accumulation): While model A suggested that a decrease of the resistivity for increasing magnetic fields should be observed, for model B a constant resistivity is anticipated. Thus, by comparison with the experimental findings we concluded that contrary to the expectation the net magnetic moment model (B) reflects the salient features of the experiment. We would like to point out, that the observed signature can also be explained by the Hanle magnetoresistance. However, the magnitude of the HMR reported so far is much smaller than the magnetoresistance observed here. Finally, we investigated the spin Seebeck effect in the nc-YIG/Pt bilayers, where no signal can be observed to within our experimental resolution. We thus concluded that the SMR response suggests that the moments in the paramagnetic insulator interact in a collective (i.e. net moment) way with the spin accumulation in the Pt. However, the temperature and magnetic field dependence of the magnetoresistance hints at a more complex scaling with the net magnetic moment: A simple linear dependence on the induced net magnetic moment does not conclusively fit to our data.

3.2   Antiferromagnetic Insulator Cr$_2$O$_3$/Pt and Cr$_2$O$_3$/Ta Heterostructures

This section will focus on the magnetoresistance in bilayers of an antiferromagnetic insulator and a normal metal in the vicinity of the ordering (Néel) temperature T_N: Below T_N the system is antiferromagnetic, and the spin Hall magnetoresistance should depend on the individual magnetic sublattices, as shown for many other magnetic insulators.[11,15,50,64,65,127,128] Above T_N, the magnetic state in an antiferromagnet should resemble a paramagnet (with an ordering temperature $T_O = -T_N$ instead of $T_O = 0$ for a "perfect" paramagnet), i.e. should be comparable to the results in the previous Sec. 3.1 taken at room temperature.[146] For investigating possible differences between the magnetoresistive response of a perfect paramagnet (i.e. a material which has no internal correlations) and a system with an ordered magnetic phase (i.e. a material where the internal correlations are suppressed by thermal fluctuations), the behavior of the magnetoresistance in the transition region will be elucidated. To that end, we use bilayers of the antiferromagnetic insulator Cr$_2$O$_3$ and Pt or Ta. Please note, that although it is not addressed in this chapter, a bilayer of the ferrimagnetic insulator YIG and Pt was also investigated close to its ordering temperature (c.f. Sec. 4.2).

The contents of this section have been partly reproduced from R. Schlitz et al., Applied Physics Letters **112**, 132401 (2018) (Ref. [10]) with permission from AIP Publishing.

3.2.1 Sample Preparation

Two sets of samples were studied, both grown on c-cut Al_2O_3 substrates by Tobias Kosub (Helmholtz-Zentrum Dresden Rossendorf). The 250 nm thick Cr_2O_3 layer of the first set (**S1**) was deposited in an oxygen atmosphere ($p_{Ox} = 1 \times 10^{-5}$ mbar) using reactive evaporation of Cr from a Knudsen cell. The initial substrate temperature of 700 °C was reduced to 500 °C after the deposition of the first few monolayers. After the growth of the Cr_2O_3 layer, the samples were post-annealed in vacuum at 750 °C, giving rise to an easy axis anisotropy of the Néel vector along the surface normal.[147,148] Finally, after annealing the Cr_2O_3 layer, a 3 nm Pt layer was sputter-deposited in-situ with a substrate temperature of 100 °C. Alternatively, the samples were covered with a 5 nm thick Ta layer which was then capped with a 0.5 nm thick Pt layer to slow down oxidation.

In the second set of samples (**S2**), 200 nm Cr_2O_3 were deposited using radio frequency magnetron sputtering from a stoichiometric target. A substrate temperature of 700 °C and a rate of 2 nm min^{-1} were used. An Ar atmosphere was used during deposition. After cooling down to below 100 °C a 3 nm thick Pt layer was deposited directly, without breaking the vacuum. The same magnetic structure (i.e. easy axis along the surface normal) is realized here. Samples from the second set were mostly used for the transport experiments shown in Ch. 5.

After the growth, the samples were patterned into Hall bars using optical lithography and Ar ion milling. The electrical measurements were performed as described in Sec. 2.6. While for the Pt capped sample, a current of 180 µA was used, the measurements on the Cr_2O_3/Ta device were performed with a current of 20 µA. A lower current was chosen for the Cr_2O_3/Ta device, due to the higher resistivity of Ta compared to Pt. Thus, to maintain low Joule heating by the electrical current, it was reduced accordingly in Ta.

3.2.2 Results and Discussion

Angle resolved magnetoresistance (ARMR) measurements for the three mutually orthogonal magnetic field rotation planes described in Ch. 2 were performed in the Halbach setup (c.f. Sec. 2.2, $\mu_0 H = 1.1$ T) at different sample temperatures in the vicinity of the Néel temperature $T_N \sim 310$ K ~ 37 °C.[119,149] Three sets of ARMR data are shown in Fig. 3.6 measured at a temperature below T_N (turmeric symbols), close to T_N (red symbols) and above T_N (gray symbols). As introduced in the previous section (c.f. Eq. (3.2)) for the spin Hall magnetoresistance (SMR), and also the Hanle magnetoresistance (HMR), a minimum of the resistance for **H** ∥ **t** is expected, while it is increasing for all other directions. Consequently, a modulation should only be present in the in-plane (ip) and out-of-plane around **j** (oopj) rotation. We start the discussion with the data obtained during the ip and oopj rotation of the magnetic field (c.f. Fig. 3.6a,b). For both rotation planes a $\sin^2(\alpha, \beta)$ modulation is observed at $T \sim 47$ °C and 37 °C $\gtrsim T_N$, with an amplitude that is decreasing for lower temperatures. At the lowest temperature $T \sim 21$ °C almost no modulation is evident, as one naively would expect considering that at 21 °C the system is in the antiferromagnetic state and that the antiferromagnetic spin structure is not affected by our moderate magnetic field.

In addition to the resistance modulation observed for the ip and oopj rotation, a $\sin^2(\gamma)$-like modulation is evident also for the oopt rotation plane contrary to the expectation for SMR. This might be attributed to a thin interface layer, where the Cr_2O_3 layer induces a small proximity magnetization in the Pt layer. Such a magnetization would also match to the field invariant anomalous Hall contribution evident in our samples below the ordering temperature (see also Refs. [147] and [150]). However, it might also be rooted in the finite crystallinity of the Pt layer giving rise to a more complex resistivity tensor due to symmetry, which has already been observed for the anisotropic magnetoresistance.[151]

The amplitude of the modulation of $\delta\rho_\ell/\rho_0$ (i.e. the MR magnitude $\Delta\rho_\ell/\rho_0$) is extracted using $\sin^2(\alpha, \beta, \gamma)$-fits to obtain $\Delta\rho_\ell/\rho_0$ for all temperatures and the three rotation planes. All resulting amplitudes are summarized in Fig. 3.7. Additionally, measurements of the field invariant anomalous Hall effect were performed together with Tobias Kosub
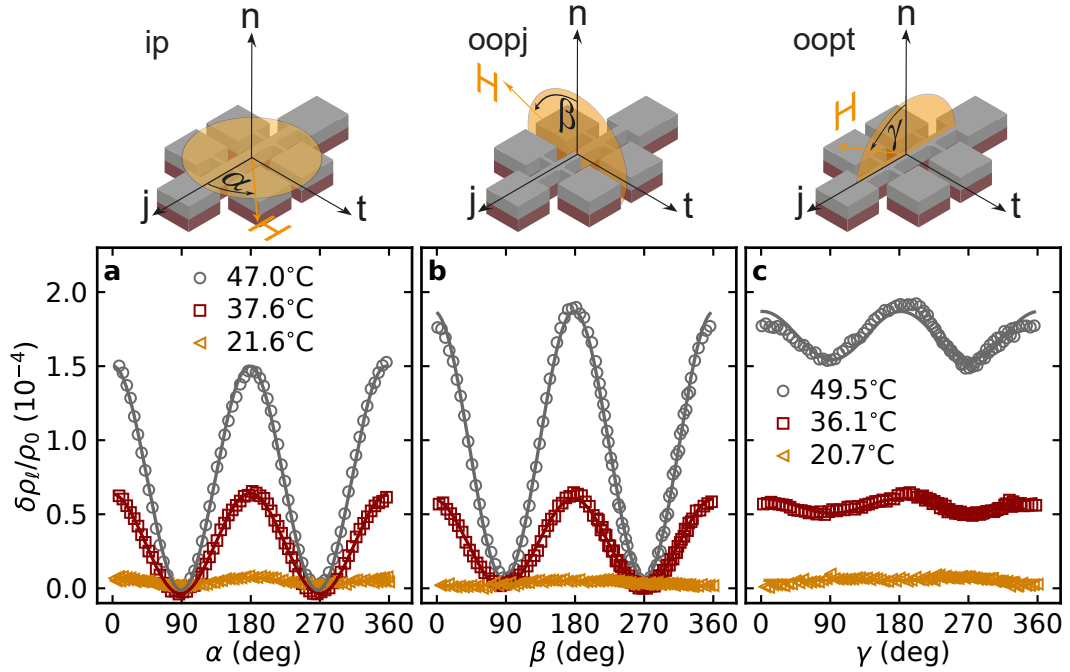

Figure 3.6: Panels **a**, **b** and **c** show the magnetoresistance of a Cr_2O_3/Pt heterostructure (**S1**) obtained during rotations of the magnetic flux density $\mu_0 H = 1.1\,T$ for three temperatures in ip, oopj and oopt configuration, respectively. The gray circles correspond to measurements above the Néel temperature. The data represented by the red squares were measured in the vicinity of the Néel temperature, while the data shown as turmeric triangles were recorded just below. $\sin^2(\alpha, \beta, \gamma)$ fits, shown as lines, were performed to extract the modulation amplitude of $\delta\rho_\ell/\rho_0$. As in the previous Sec. 3.1 (c.f. Fig. 3.1) a linear slope was subtracted from the data to remove drifts, and the data have been shifted (not scaled) such that the high symmetry points agree between the rotation planes, i.e. **H ∥ t** (**H ∥ n**) for ip and oopj (oopj and oopt). Please note that the temperatures for panels b and c are the same as they were measured simultaneously on two orthogonal Hall bars. Adapted from Ref. [10].

(Helmholtz-Zentrum Dresden Rossendorf) to determine the exact Néel temperature of our Cr_2O_3 layer.[147] For these measurements, the sample is field cooled in a magnetic field $\mu_0 \mathbf{H} = 1.1\,T \parallel \pm \mathbf{n}$ from above T_N. Then, the magnetic field is removed and the transverse resistance is measured using a spinning Hall approach (c.f. App. B and Ref. [147]) while the temperature is increased to above T_N. In this measurement, the uncompensated surface of the Cr_2O_3 leads to a finite (spin Hall) anomalous Hall signal R_H in the transverse resistance of the Pt layer even in the absence of magnetic field. This anomalous Hall signal vanishes when Cr_2O_3 is heated to above T_N due to the rapid decay of the magnetic order parameter when Cr_2O_3 enters the paramagnetic phase. The resulting Hall signal R_H is shown in Fig. 3.7 for positive (gray line) and negative (red line) cooling fields. A dashed brown line marks the point were these two lines intersect, which agrees nicely with the expected Néel temperature of bulk Cr_2O_3.[119,149] Interestingly, while the magnetoresistance changes around the same temperature, the transition is distributed over a much broader temperature range as compared to the Hall measurement.

Figure 3.7: **a** The magnetic field invariant contribution R_H to the transverse resistance acquired together with Tobias Kosub (Helmholtz-Zentrum Dresden Rossendorf) by spinning anomalous Hall magnetometry on the Cr_2O_3/Pt sample (**S1**) is shown for positive (gray line) and negative cooling field (red line) (c.f. Ref. [147] and App. B), vanishing at T_N. **b** The magnetoresistance $\Delta\rho_\ell/\rho_0$ of the sample obtained from $\sin^2(\alpha, \beta, \gamma)$ fits to the angle resolved data (c.f. Fig. 3.6) for all three rotation planes and temperatures are summarized. The Néel temperature is indicated by the brown dashed line. A vanishing MR is observed for all three rotation planes below T_N. When increasing the temperature, the MR increases until $T \sim 45\,°C$ where it seems to saturate. Adapted from Ref. [10].
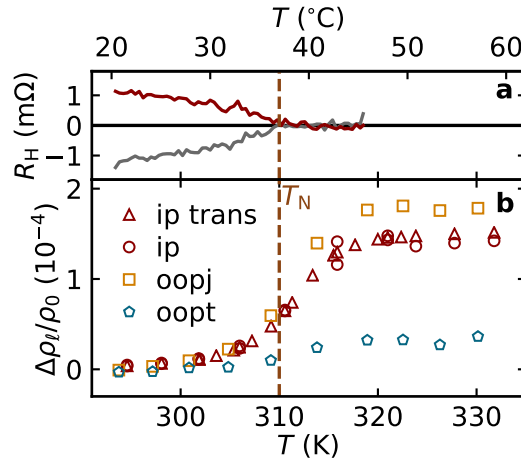
The different width of the transitions might hint at a discrepancy between the moments probed by the anomalous Hall effect and the SMR. An alternative explanation is that the application of magnetic field (the Hall data is measured without magnetic field) alters the transition region, an issue to which we will come back later. Another interesting fact is that contrary to what is expected from the net magnetization in the paramagnetic state, the SMR increases with temperature even in the paramagnetic phase and saturates at a level of $\Delta\rho_\ell/\rho_0 > 1 \times 10^{-4}$ around $T \sim 45\,°C$. This clearly disagrees with the expected behavior of the induced magnetization, which decays as $M \propto \frac{1}{T+T_N}$.[119] While a non-vanishing magnetoresistance above the ordering temperature was observed already in bilayers of the ferrimagnetic insulator Cu_2OSeO_3 and Pt by Aqeel et al. in Ref. [50],

they associate the signal with the induced paramagnetic magnetization in the samples. However, their magnetoresistance is at least two orders of magnitude smaller than what we observe here and their measurements are limited in several ways: To begin with, only in-plane rotations are performed, which do not allow to disentangle a proximity induced effect (i.e. anisotropic magnetoresistance) and the spin Hall magnetoresistance. In contrast, in our measurements we can separate the contributions which have the symmetry of the spin Hall magnetoresistance (i.e. giving rise to resistance modulation in oopj rotations) and other spurious effects (visible in oopt rotations). Additionally, they observe a transverse magnetoresistance of $R_{trans} = 0.07\,m\Omega$ in their Pt films, which together with a Pt layer thickness 5 nm yields a magnitude of $\Delta\rho/\rho_0 \sim 2 \times 10^{-6}$. This is the order of magnitude which is expected also in bare Pt layers due to the Hanle magnetoresistance.[68] Finally, although the magnetoresistance observed in Ref. [50] increases with temperature (which is unexpected for the induced magnetization), no saturation of the magnetoresistance was reported by these authors even at 200 K above the ordering temperature, in contrast to our observations. We thus conclude that the mechanism giving rise to the magnetoresistance in our case must be of a different origin than what is reported by Aqeel et al. in Ref. [50]. In particular, their explanation of the spin Hall magnetoresistance in terms of the saturation magnetization seems to be in contradiction to the observed signatures in our measurements.

To further elucidate whether a field induced paramagnetic magnetization is sufficient to observe large a large SMR-like magnetoresistance, we deposited a 3 nm thick Pt layer on a $Gd_3Ga_5O_{12}$ (GGG) substrate. In particular, GGG has a susceptibility of $\chi_{GGG} \sim 6.8 \times 10^{-3}$ according to both, a Curie-Weiss susceptibility calculation and experiments.[152] For comparison, the susceptibility of Cr_2O_3 was reported to be $\chi_{Cr_2O_3} \sim 1.6 \times 10^{-3}$ at room temperature.[153] Consequently, with the same magnetic field applied, the induced magnetization of GGG should be larger by a factor 4 compared to Cr_2O_3. In spite of this fact, our control experiments on GGG/Pt revealed only a very small magnetoresistance $\Delta\rho_\ell/\rho_0 \leq 1 \times 10^{-6}$ at room temperature with the same applied magnetic field. This is smaller by more than two orders of magnitude compared to the magnetoresistance observed in Cr_2O_3/Pt bilayers. One possible explanation for the discrepancy might be rooted in the different spin mixing conductance of the GGG/Pt and Cr_2O_3/Pt interface: While for the prior, the coupling is mediated by strongly localized $4f$ moments, the latter interacts via its $3d$ moments. Consequently, a much higher orbital overlap at the interface might be found for Cr_2O_3/Pt. This is consistent with the observation by Aqeel et al. for Cu_2OSeO_3/Pt, where $3d$ moments are responsible for the magnetism. Additionally, more recent results revealed a very similar behavior also in thin layers of $MnTiO_3$ covered with Pt[154] and experiments in CoO/Pt bilayers which have been carried out in Ref. [155] up to high magnetic fields of 24 T. In the latter system, a finite magnetoresistance is only observed for very large magnetic fields above $\sim 15\,T$. A connection to these experiments and a possible alternative explanation for the large MR in the paramagnetic phase will be presented later in this section in conjunction with investigation the high field magnetoresistance in the paramagnetic phase (c.f. Fig. 3.11).

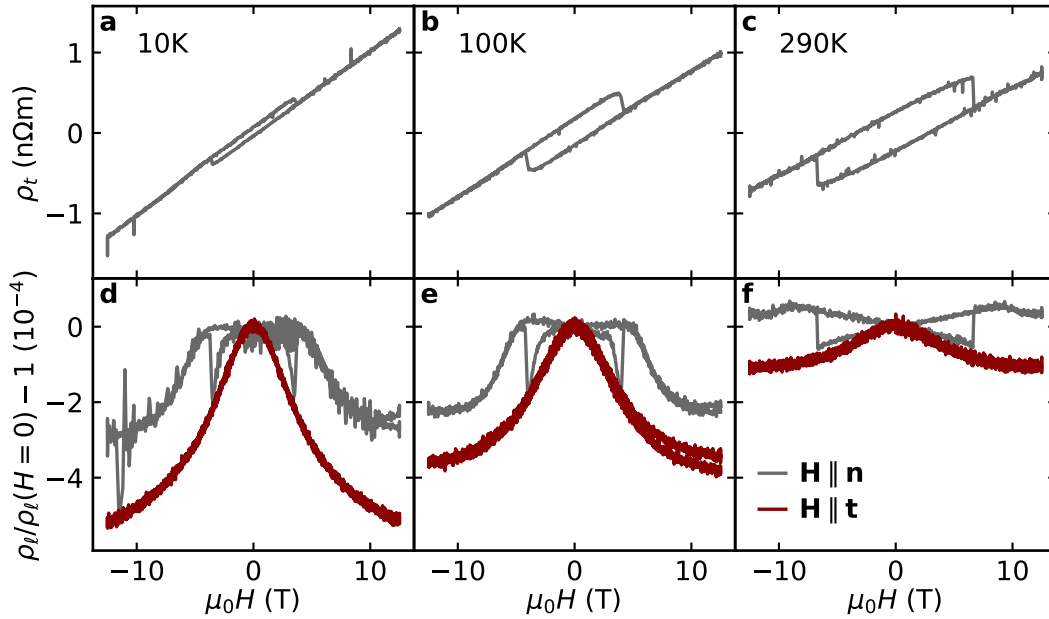Having found a significant deviation from the anticipated behavior of the SMR above

Figure 3.8: **a-c** The transverse (Hall) resistivity for the Cr_2O_3/Ta sample (**S1**) is plotted for several temperatures below T_N measured with the magnetic field applied along the surface normal (**H** ∥ **n**). In addition to the ordinary Hall effect (i.e. a linear slope) an anomalous Hall-like behavior is observed: a clear hysteretic jump between two constant resistivity levels. Interestingly, the hysteresis closure field in the transverse resistivity below T_N matches the sharp hysteretic feature between 3 T and 7 T observed in the magnetoresistance. Panels **d-f** show the magnetoresistance $\rho_\ell/\rho_\ell(H = 0) - 1$. The magnetoresistance is measured with the magnetic field applied either along the surface normal (**H** ∥ **n**, gray lines) or the transverse direction (**H** ∥ **t**, red lines). Except for $T = 290$ K, the resistivity decreases when the magnetic field is increased along either direction.

T_N, the question arose whether the SMR in the ordered phase shows the salient features reported in other systems, i.e. depends on the sublattice magnetizations. To that end, we study the magnetoresistance in the ordered phase at high field magnetic fields up to 12.5 T in the samples covered with Ta (series **S1**) at low temperatures.[5] First, the transverse resistivity measured with the magnetic field applied along the surface normal **H** ∥ **n** (i.e. the Hall effect) will be discussed: Interestingly, for all temperatures below T_N the transverse resistivity resembles the anomalous Hall effect of an easy axis ferromagnet, i.e. a hysteretic jump between two stable levels is observed (c.f. Fig. 3.8a-c). The coercive (or switching) field increases from 3.5 T at 10 K to 6.8 T at 290 K. In addition, a temperature dependent change of the ordinary Hall effect (slope in the saturated regime) is evident in the measurements.

Similarly, the magnetoresistance $\rho_\ell/\rho_\ell(H = 0) - 1$ shown in Fig. 3.8(d-f) has an hys-

---

[5]The samples covered with Ta are used for this investigation, as they do not show a modulation of the magnetoresistance for oopt rotations above T_N. Consequently, the observed magnetoresistance can be directly connected to to the spin Hall magnetoresistance in these samples.

teretic feature at the same magnetic fields at which the jump in the transverse resistivity is evident for **H** ∥ **n**. However, after the jump, the resistivity returns to the original value as it is quadratic with respect to the magnetization ($\propto m^2$), in contrast to the anomalous Hall effect ($\propto m$).[44] With magnetic fields larger than the switching field, a decrease of the resistivity is present except for 290 K, where the magnetization still increases slightly before decreasing again. The increase of the resistance at 290 K might be understood with the magnetic field stabilizing the ordered magnetic state in some grains of the thin film which have a lower ordering temperature.[156] Finally, if the magnetic field is applied along the transverse direction **H** ∥ **t**, a decrease of the resistivity is observed for all temperatures, where the slope is reduced towards high magnetic fields. For both directions of the applied magnetic field, an increase of the magnitude of the magnetoresistance is found towards low temperatures, with a maximum of $\sim 5 \times 10^{-4}$ at 10 K. Please note, that the data has been normalized to the value at zero magnetic field, which likely corresponds to the high resistance state, since the easy axis is parallel to the surface normal, viz. perpendicular to the spin polarization at the interface.
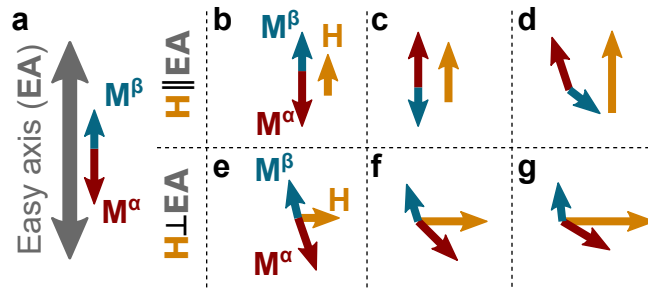

Figure 3.9: **a** For a nearly compensated antiferromagnet without applied magnetic field, both magnetic sublattices align parallel to the easy axis. **b-d** If an increasing magnetic field is applied along the easy axis, the larger moment "jumps" to align parallel to the field. For even larger magnetic fields, i.e. when the Zeeman energy becomes comparable to the exchange enhanced anisotropy, the second sublattice also rotates towards the magnetic field, giving rise to a canted state. **e-g** If an increasing magnetic field is applied perpendicular to the easy axis, both sublattices cant towards the magnetic field, with the canting of the larger sublattice being larger. These two cases explain all salient features of the low temperature magnetoresistance shown in Fig. 3.8.

In the following, a model to explain the salient features of the magnetotransport in the ordered phase will be presented. To this end, we will assume in the following, that one of the two magnetic sublattices of Cr_2O_3 has a slightly larger magnetization ($|\mathbf{M}^\alpha| > |\mathbf{M}^\beta|$). While this might seem odd for an antiferromagnet, step dislocations or other defects in Cr_2O_3 have been shown to give rise to a small magnetization.[150,156] With these assumptions, a ground state as shown in Fig. 3.9a is realized: Without applied magnetic field, the moments in both magnetic sublattices are aligned antiparallel with respect to each other and oriented along the easy axis. Since the easy axis is perpendicular to the spin accumulation direction, we thus find a high resistivity for the SMR for the ground state. If a small magnetic field is applied along the easy axis and along the smaller magnetiza-

tion ($\mathbf{H} \parallel \mathbf{M}^\beta \parallel \mathbf{EA}$) the configuration does not change, since the Zeeman energy is too small to overcome the uniaxial anisotropy (c.f. Fig. 3.9b). Upon increasing the magnetic field in this configuration, the Zeeman energy at some point will be sufficient to flip both sublattices, so that the sublattices invert as depicted in panel c. The resistivity is equal for the two configurations shown in Fig. 3.9b and c, as it is expected to be proportional to $\left(\mathbf{M}^{\alpha,\beta}\right)^2$.[44] However, in the process of switching, the sublattices have to cant away from the easy axis (i.e. towards the $\mathbf{t}$ direction), giving rise to the sharp hysteretic features observed in Fig. 3.8d-f, having a lower resistivity. Please note, that the anomalous Hall effect will change its sign between the configurations depicted in Fig. 3.9b and c, as it depends linearly on the magnetization $\rho_t \propto M_n^{\alpha,\beta}$, where $M_n^{\alpha,\beta}$ is the projection of $\mathbf{M}^{\alpha,\beta}$ onto the $\mathbf{n}$ direction. This corresponds to the jump observed in the transverse resistivity in Fig. 3.8a-c. If the magnetic field is increased even further (i.e. so that the Zeeman energy is on the order of the exchange energy), the system will enter a canted state (panel d).[15] Consequently, a finite projection of the two magnetizations onto the $\mathbf{t}$ direction is realized, leading to a lower resistivity. In summary, for $\mathbf{H} \parallel \mathbf{n}$, we find a constant longitudinal resistivity ρ_ℓ for moderate magnetic field followed by a hysteretic feature in ρ_ℓ and a change of in ρ_t. For even higher magnetic fields a decrease of ρ_ℓ is observed, as the two sublattices cant with respect to each other and towards the plane of the film (i.e. when the Zeeman energy approaches the scale of the exchange energy). This describes the salient features observed in the experiment (c.f. Fig. 3.8, gray lines)

We will now turn to the case, where the magnetic field is applied along the transverse or spin accumulation direction, i.e. $\mathbf{H} \parallel \mathbf{t}$. In this case, even a small magnetic field will lead to a finite canting of the two sublattice magnetizations away from the easy axis. This can be motivated as with the magnetic field acting perpendicular to the anisotropy, a vectorial addition always leads to a finite effective field component along the external magnetic field (c.f. Fig. 3.9e). If the magnetic field is increased, the two magnetic sublattices will start canting with respect to each other (panels f and g), very similar to the case depicted in panel d. Consequently, the resistivity will monotonously decrease beginning at very small magnetic fields for $\mathbf{H} \parallel \mathbf{t}$, as we observe it in the experiment. However, it might be possible that there is a plateau or even an increase of the magnetization for very large fields, viz. large canting angles, as the one possible configuration is similar to a canted spin flop phase,[119] where the sublattices align perpendicular to the magnetic field. To extract the exact angles of the two sublattice magnetizations as well as the small uncompensated moment, a thorough simulation of the two sublattice system including the anisotropy and the temperature dependence of the two sublattice magnetizations would be required. While it might be very rewarding, this is a very challenging problem which has not been solved so far. Thus, while attempts have been made, no successful solution to the problem could be found.[6]

---

[6]One possible way to tackle the problem which was not attempted so far is as follows: First, the magnitude of the two sublattices is calculated as a function of temperature for a given set of directions of the internal and external fields (including the anisotropy parametrized as magnetic field). Then, using a Stoner-Wohlfahrt approach, the new equilibrium position of the sublattices is evaluated and fed back into the calculation of the temperature dependence. These steps have to be repeated until the system converges to a definite solution.

We conclude, that the low temperature model presented above explains all salient features and seems to be a reasonable approximation to the system. In particular, also the temperature dependence expected from our model matches the trend described by the magnetoresistance: If there is an uncompensated net moment, its magnitude will increase towards lower temperature due to the lower thermal excitation of the system, while the anisotropy will remain roughly constant until close to T_N.[153] Thus, the larger uncompensated net moment will increase the Zeeman energy compared to the anisotropy energy and thus decrease the coercive field, as it is observed in the experiment (c.f. Fig. 3.8). Additionally, it might explain why the magnetoresistance is much larger at 10 K than at 290 K as also the canting angles will be increased if the Zeeman energy is higher.
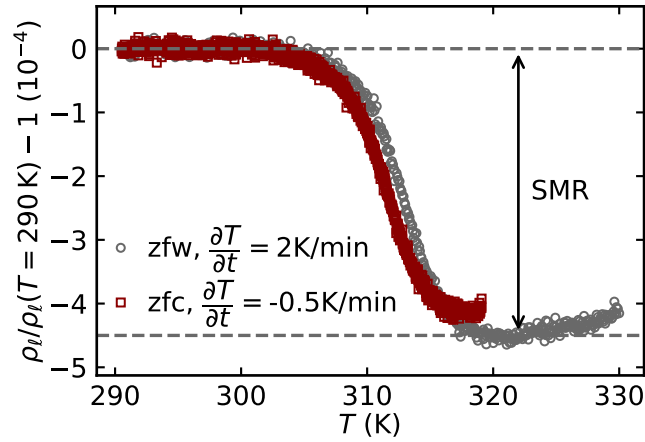

Figure 3.10: The normalized resistivity measured in a Cr_2O_3/Ta sample (**S1**) during a zero-field warming and cooling is shown by the gray and red symbols respectively. Both curves were normalized to their respective value at 290 K and the linear slope of the resistance change with temperature has been subtracted. As the sublattices are aligned with the easy axis (i.e. the surface normal) below T_N, a maximum absorption of spin is realized here, giving rise to an increased resistance there. Above T_N the sublattice magnetizations vanish, leading to a decrease of the resistivity due to the removal of the additional dissipation channel.

Finally, before returning to discuss the paramagnetic state, we will try to evaluate whether the configuration without magnetic field actually corresponds to the high resistance state as one would naively expect from the low temperature model presented here. To that end, we performed a zero-field warming and cooling, i.e. measured the temperature dependent resistivity $\rho_\ell(T)$ when warming (cooling) from below (above) T_N to above (below) T_N without applying a magnetic field. The resulting data are shown in Fig. 3.10 and have been normalized to the respective value at 290 K and a linear slope was removed from the data to remove the inherent temperature dependence of the resistivity. We find a clear decrease of the ρ_ℓ on the order of 4.5×10^{-4}, which nicely corresponds to the magnetoresistance observed at 10 K, and thus has the order of magnitude expected for SMR. Consequently, these experiments further corroborate the low temperature model put forward above, where without an applied magnetic field the spins align

along the surface normal, i.e. perpendicular to the **t** direction. Interestingly, the transition window is very similar to the measurements in the Cr_2O_3/Pt heterostructure, suggesting that even without applied magnetic field, the anomalous Hall effect and the magnetoresistance are slightly different. In summary, the magnetoresistance measurements in the ordered phase below T_N suggest that the observed behavior is consistent with SMR being mediated by the individual magnetic sublattices.[15,50,65] Thus, at least in the ordered phase a good agreement with the current SMR picture is found, which makes the deviation in the paramagnetic phase even more surprising.

We will now return to the discussion of the magnetoresistance in the paramagnetic phase. As the experiments on the Cr_2O_3/Pt bilayers (**S1**) were carried out with a fixed magnetic field (c.f. Fig. 3.6 and Fig. 3.7), no statements about the evolution with the magnetic field could be made. This will be addressed in the following via an additional set of experiments in the Cr_2O_3/Ta bilayers (**S1**). The normalized longitudinal resistivity measured at $T = 320\,K > T_N$ as a function of the applied magnetic field is shown in Fig. 3.11a for the two high symmetry directions (i.e. **H** ∥ **n** and **H** ∥ **t**). For **H** ∥ **n** a steep increase of the magnetoresistance is found for $\mu_0 H \lesssim 3\,T$ with the slope decreasing for higher magnetic fields. If the magnetic field is applied along the **t** direction, no significant change of the resistivity is observed. Consequently, we find the same phenomenology as for the non-crystalline $Y_3Fe_5O_{12}$/Pt bilayers discussed in the previous Sec. 3.1.[7] In addition to the large magnetoresistance, a sharp step around $H = 0$ is found in the transverse resistivity (Fig. 3.11b), showing no hysteresis but otherwise resembling the fingerprint of a ferromagnetic anomalous Hall effect (or spin Hall anomalous Hall effect).[43,44]

Thus, the magnetoresistance above T_N is neither consistent with an SMR due to the induced net magnetization, which should show no saturation. Nor can we explain our findings with an SMR mediated by the individual spins, where the magnetoresistance should decrease with the magnetic field applied parallel to the **t** direction (c.f. Fig. 3.4). Thus, an explanation of the observed magnetoresistance in terms of the spin Hall magnetoresistance seems to be impossible. Consequently, we now apply a different approach to model our data in order to explain the large signals and the magnetic field dependence observed above the Néel temperature and will motivate this approach. The spin Hall magnetoresistance and the Hanle magnetoresistance stem from the same physical origin: While the prior addresses the interaction of the normal metal spin accumulation with an adjacent magnetic insulator,[44] the latter formalizes the same interaction but with an external magnetic field.[67,68] The fundamental mechanism giving rise to the modulation of the normal metal resistivity, however, is the same in both cases, viz. an additional dissipation channel reducing the interfacial spin accumulation in the normal metal. Until now, all experiments suggested, that the HMR is much smaller than the SMR in all typical material systems.[5,68,87,157] However, since the physical origin is the same, the maximum SMR and HMR is identical (i.e. when all spin accumulation is lost). This can be directly

---

[7]Please note, that we have repeated the rotations also on the samples with Cr_2O_3/Ta. Almost the same angular dependence as for the Cr_2O_3/Pt samples is found, with the exception that the resistance modulation in the oopt rotation plane is vanishing completely. Thus, no proximity magnetized layer or other spurious contributions to the signal should be present in this sample.
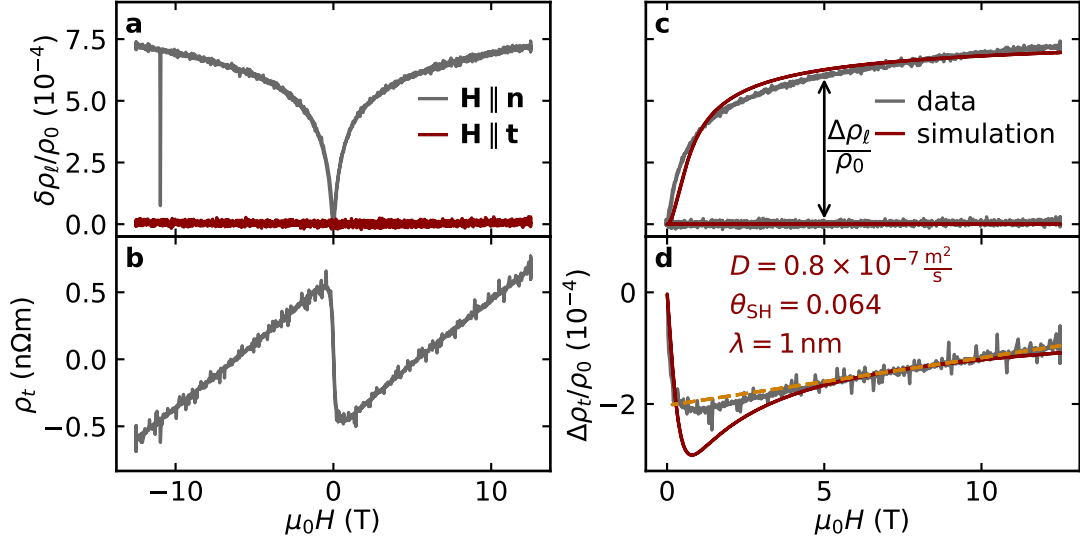
Figure 3.11: Panels **a** and **b** show the normalized longitudinal and transverse resistivities of a Cr_2O_3/Ta sample (**S1**) measured at 320 K, respectively. **c, d** A simultaneous simulation of the magnetoresistance using Eq. (3.4) and Eq. (3.5) (solid lines) shows good agreement with the general trends observed in the data. Please note, that to remove the ordinary Hall effect from the transverse data, the slope in the saturated regime measured at 290 K (c.f. Fig. 3.8h) has been subtracted from the data. Apart from the diffusion constant D, the other parameters are in the range of reported values for Ta films.[68]

seen from the SMR or HMR theories,[8] when an infinite spin mixing conductance or an infinitely large field is assumed, respectively. The resulting maximum magnetoresistance of a single interface[9] is $\sim 3 \times 10^{-3}$ for a 3 nm thick Pt layer[10] or $\sim 8 \times 10^{-4}$ for a 5 nm thick layer of Ta.[11][44]

Consequently, under special circumstances, the HMR might actually be of similar magnitude or larger than the SMR. To elucidate, whether the salient features observed in the experiment, summarized in Fig. 3.6, Fig. 3.7 and Fig. 3.11, can be explained by HMR, we will apply the HMR theory given by Eq. (3.4) and Eq. (3.5) to our system.[68]

$$\frac{\Delta \rho_\ell}{\rho_0} = \frac{2\theta_{SH}^2}{d_N} \left(\lambda \tanh \left(\frac{d_N}{2\lambda} \right) - \mathfrak{Re} \left[\Lambda \tanh \left(\frac{d_N}{2\Lambda} \right) \right] \right) \tag{3.4}$$

$$\frac{\Delta \rho_t}{\rho_0} = \frac{2\theta_{SH}^2}{d_N} \mathfrak{Im} \left[\Lambda \tanh \left(\frac{d_N}{2\Lambda} \right) \right] \tag{3.5}$$

---

[8]For the SMR theory this is given by Eq. (47) from Ref. [44] with $G_r \to \infty$, i.e. $\frac{2\theta_{SH}^2 \lambda}{d_N} \tanh \left(\frac{d_N}{2\lambda} \right)$, which directly corresponds to Eq. (3) with $\Lambda \to 0$ (i.e. $B \to \infty$)). Please note, that as the HMR considers both interfaces equally, the MI/N/MI case from the SMR theory was used to allow for easy comparison.

[9]Calculated with including the spin backflow correction, i.e. using Eq. (29) from Ref. [44]

[10]Assuming a spin diffusion length $\lambda = 1.5$ nm and a spin Hall angle of $\theta_{SH} = 0.1$[43,158]

[11]Assuming $\lambda = 1$ nm and $\theta_{SH} = 0.064$[68,159]

where θ_{SH} is the spin Hall angle, λ the spin diffusion length and d_N the metal layer thickness. The additional parameters are the $(1/\Lambda) = \sqrt{1/\lambda^2 + i/\lambda_m^2}$ with the spin precession length $\lambda_m = \sqrt{D/\omega_L} = \sqrt{D\hbar/g\mu_B\mu_0 H}$ and the diffusion constant $D = \sigma_0/2\nu e^2$ with the Drude conductivity σ_0 and the density of states per spin species ν.[68] Please note, that for small magnetic fields the dominant field dependence is $\omega_L^2/D^2 \propto (H/D)^2$, which will become important later.

For comparing the HMR theory to our results, first the ordinary Hall effect has to be removed from the transverse resistivity: To this end, the contribution of the ordinary Hall effect is estimated by fitting the linear slope in the saturated regime at 290 K (c.f. Fig. 3.8c). This linear slope is then removed from the data at 320 K. While this is only an approximation, neglecting the temperature dependence of the ordinary Hall coefficient, it should be close to the correct slope, as the two temperatures are only apart by 30 K. Additionally, since the system is (mostly) in the ordered state at 290 K, no significant contributions are expected from the (spin Hall) anomalous Hall effect in the saturated regime (except from the small canting of the sublattices).

The magnetoresistance and the transverse resistivity corrected for the ordinary Hall effect as discussed above, both normalized to ρ_0 (i.e. the resistivity for **H** ∥ **t**) are shown in Fig. 3.11c and d, respectively. Please note, that for better visibility only positive magnetic fields are shown. The solid red lines correspond to the respective resistivities calculated using Eq. (3.4) and Eq. (3.5). We find a reasonable agreement between theory and experiment assuming $\lambda = 1$ nm, $\theta_{SH} = 0.046$ and $D = 0.8 \times 10^{-8}$ m^2/s. While θ_{SH} and λ are both in the range of reported parameters, D is much smaller than reported, where we will address possible reasons in the next paragraph.[68,159] As discussed above, the dominant low field dependence is given by $(H/D)^2$ for small magnetic fields, so that a small diffusion constant effectively increases the impact of the magnetic field. Thus, the HMR allows to reproduce the saturating behavior observed already for moderate magnetic fields in the transverse and longitudinal resistivity in addition to matching the effect magnitudes. Interestingly the magnitude of the magnetoresistance seems to be close to the maximum signal possible in Ta for the given spin transport parameters. Most notably, however, the overshoot observed in the transverse resistivity for intermediate magnetic fields is captured by the simulation (c.f. turmeric dashed line for the linear slope in the saturated regime extrapolated back to the low field regime). While a similar overshoot has been reported in other Cr_2O_3/Pt heterostructures in Ref. [160], the authors of this paper only find its presence for very thin Cr_2O_3 layers ($t_{Cr_2O_3} < 6$ nm) and in a more narrow window of magnetic fields. The overshoot is interpreted as evidence of a topological spin texture at the interface stabilized by the Dzyaloshinskii-Moriya interaction, which seems unlikely to be present in our thick Cr_2O_3 layers ($t_{Cr_2O_3} = 200$ nm). Please note, that the transverse resistivity as a function of magnetic field the authors of Ref. [160] find for their samples resembles the curve simulated here, so that the modeling in terms of the HMR put forward here might also be applicable to their samples.

In the following, we will try to motivate possible reasons for the large HMR, viz. the small diffusion constant required to explain our findings in the context of the HMR framework. To that end, we will take an excursion to electron spin resonance (ESR) to motivate

one of two possible concepts explaining the increased HMR in our system:[161] For ESR, an external magnetic field is used to partially align the electron spins in a material viz. imprint an additional (Zeeman) energy on the system. The electron spins are then driven into resonance by an external microwave magnetic field with the correct frequency (i.e. the Lamor frequency) applied perpendicular to the external magnetic field. For localized electron spins, i.e. in insulating materials, there are two spin relaxation channels, namely the spin-lattice decay and the spin-spin decay which are governed by the T_1 and T_2 time, respectively. In the case of a conducting system the situation is slightly different: First of all, since the electrons are mobile, the spin-spin and spin-lattice decays partake on the same timescale, i.e. $T_1 = T_2$.[161] Additionally, the impinging microwave used for driving the resonance is screened by the mobile charge carriers and thus only has a finite penetration depth (the skin depth). Consequently, only electron spins that are close to the surface (in a slice with thickness of the skin depth of the microwave) will be resonantly excited. Considering the loss of coherence in this configuration, it becomes obvious that there must be an additional loss channel: If an electron spin from the surface slice is diffusing into the bulk material and replaced by another electron from the bulk, the phase of the precession is lost. This is characterized by the diffusion time T_D, which is a measure of the time it takes for the electron to pass through the skin depth.[161] Consequently, if the material is a good conductor, i.e. has a small skin depth, then $T_D < T_2$ and the diffusive losses will dominate in the system. In ESR, this can be observed by a change of the line shape of the resonance.[161]

When we now try to apply this discussion to the HMR at the interface we can find the following for our system: In the case where the normal metal is in contact to a perfect insulator (or vacuum), the HMR diffusion constant is given by the intrinsic spin relaxation in the metal, which can include diffusive processes, and spin relaxation processes. If the insulator, however, is replaced by a poor conductor the spins at the interface can diffuse also into the adjacent material and dephase there. Consequently, there is now an additional diffusive loss channel which modifies the diffusion constant relevant for the HMR at the interface between the poor conductor and the normal metal. This is in analogy to the ESR picture, where a transition from localized electrons to a free electrons leads to additional diffusive losses. However, the surface slice given by the skin depth in the ESR is replaced by the spin Hall active surface slice (i.e. by the spin diffusion length in the normal metal). Thus, for an applied magnetic field perpendicular to the spin accumulation at the interface (i.e. when the HMR is turned on), the electron spins with a given precession phase at the interface can diffuse into the poor conductor. Since the net electronic current needs to vanish, the electron will be replaced by another electron with a different phase from the poor conductor. The spin coherence is therefore lost more efficiently compared to the case where the normal metal is interfaced with an insulator, effectively increasing the magnitude of the HMR at constant magnetic field. Please note, that although the spin decay in the poor conductor is not considered, it still has to be finite (or the poor conductor has to be infinitely thick). Otherwise, the electron spin will eventually return to the normal metal. Additionally, contrary to the approach in Ref. [68] the interface of the normal metal with vacuum and the poor conductor must be treated separately, as the diffusion

Figure 3.12: The resistance of Cr_2O_3 measured on a non-local device on a Cr_2O_3/Pt sample from series **S2** in the same way as shown in Sec. 4.2 (c.f. Fig. 4.8 and Fig. 4.9). An activation energy of $E_A \approx$ 300 meV is found, much lower than the expected band gap of 3.4 eV of Cr_2O_3.[162]
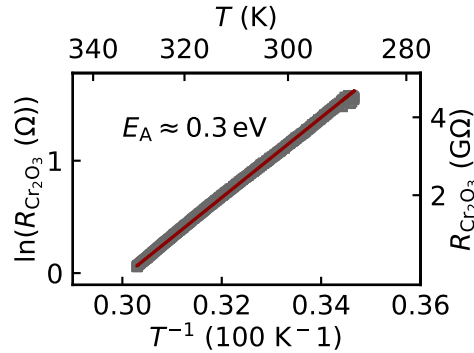
constant can differ significantly for these interfaces as long as they are well separated (i.e. the metal thickness is significantly larger than the spin diffusion length).

An alternative explanation for the low diffusion constant might be that due to the finite conductivity across the interface, the effective density of states is increased here. The impact would be particularly strong if there are d-orbitals present close to the Fermi surface, as these can have a very high density of states.[138] Whatever picture is applied, it requires a finite conductivity through the interface. To convince the reader, that this is not a wild speculation, the cross conductivity between two metal strips on Cr_2O_3 was measured.[12] The resulting resistance is shown as an Arrhenius graph in Fig. 3.12, where we find a slope (i.e. an activation energy) $E_A \approx 300$ meV $\ll E_G = 3.4$ eV much lower than the gap energy of Cr_2O_3.[162] This might hint at the presence of defects (e.g. oxygen deficiencies) in the crystal, giving rise to a defect band within the band gap of Cr_2O_3. Consequently, although not a direct proof of the modified diffusion constant, in conjunction with the large saturating MR in the paramagnetic phase, it is good evidence that this "diffusion-enhanced HMR"(deHMR) model is not completely off. Additionally, a finite cross conductivity can also be found for the nc-YIG/Pt samples investigated in the previous Sec. 3.1. This cross conductivity would also explain the temperature dependence of the observed magnetoresistance in these nc-YIG/Pt samples, increasing for higher temperatures like the conductivity of an insulator, contrary to the decreasing magnetic moment of a paramagnet. Furthermore, the experiments on $MnTiO_3$/Pt and CoO/Pt bilayers would also fit into the picture.[154,155] In these experiments the $MnTiO_3$ layers might have a finite conductivity giving rise to the observed magnetoresistance resembling our findings. In contrast the CoO layers could be well insulating, so that the magnetoresistance only becomes observable for very large magnetic fields. This would also explain the absence of a large magnetoresistance in the GGG/Pt bilayers, as a very well insulating GGG single crystal is used.

In summary, we find that the observed magnetoresistance above T_N can be consistently explained in terms of a diffusion-enhanced HMR model. This "deHMR" model

---

[12]Please note, that the device is from the second growth series (**S2**), while the other measurements discussed in this section are performed on samples from the first series (**S1**). While the magnitudes of the magnetoresistance are slightly different for the two series, the general behavior between the two series is very similar.

assumes that the diffusion constant governing the "loss" of the spin Hall spin accumulation is drastically reduced at the MI/NM interface, rooted in a finite conductivity of the MI. In particular, due to the finite conductivity, the electronic spins can diffuse out of the NM into the MI and lose their spin there, thus providing an additional loss channel for the spin accumulation. Additionally, we find that the model allows to explain many "surprising" findings of the SMR observed around the phase transitions also in other experiments.

While all these observations are circumstantial, a range of reference experiments which would more convincingly proof the "deHMR" model are possible: The prime experiment would be to use a NM/NM heterostructure (where one of the NM has a spin Hall effect and the other no SHE but still significant spin losses). If the model is correct, then a large HMR very similar to what we find here should be observable. Possible good candidates (i.e. paramagnets without long range order at room temperature but having both, d and f electron to increase the spin losses/density of states) might be Gd, Ce, Lu, La sandwiched with Pt. Please note, that e.g. Cu/Pt might be a poor choice, as the spin relaxation time in Cu is very long.[163] Thus, the electron spin can not dephase, returning to the normal metal as discussed above.

Another possibility to verify the "deHMR" model is to use a stack of two spin Hall active metals with opposite spin Hall angle which might be a good model system: In such a stack, a finite spin accumulation will be present at the interface between the two metals. However, here it is potentially more difficult to separate the contributions of the individual layers so that the experiment might be more involved. In particular, even the spins "lost" from the first to the second normal metal might still generate a signal in the second normal metal due to the spin Hall effect, rendering the separation impossible if the spin Hall effect in the two metals has the same magnitude. Anyway, as the experiment is very simple it should be tested.

Another possible indicator that the "deHMR" model outlined above might be correct, is the large SMR found in metallic bilayers like CoFeB/Pt. Here, the HMR picture could be modified in two ways: First of all, the magnetic metal can act as a sink for the spin current, changing the diffusion constant of the FM/NM interface. Additionally, the precession frequency (viz. Lamor frequency) of the spins at the interface might be modified by the presence of the exchange field in the ferromagnetic layer, i.e. $\omega_{\mathrm{L}} = \hbar/g\mu_{\mathrm{B}}\mu_0 H \rightarrow \hbar/g\mu_{\mathrm{B}}\mu_0(H + H_{\mathrm{ex}})$. Consequently, not only is the HMR increased drastically due to the lower diffusion constant, but there is also a finite magnetoresistance in the absence of externally applied magnetic field now, i.e. something which resembles the SMR. A study of the magnetoresistance to very high magnetic field in such a sample might allow to probe the diffusion constant. First steps for this inclusion of the SMR contribution in terms of the Lamor frequency have already been taken by Zhang et al. in Ref. [63].

This framework also allows to describe the case of insulating ferromagnets within the same framework: While the diffusion constant is not altered due to the presence of the insulator (except for a lower spin diffusion length in the NM),[163] the orbital overlap at the interface gives rise to a correction of the Lamor frequency as shown in the previous

paragraph. It would be important to try to estimate this exchange field at the interface in order to see the validity of the model in this case. This formalism might then be used to replace or extend the spin mixing interface conductance framework used so far.[44,126,164] Such an effort entails a lot of work, as the spin mixing interface conductance concept has been used to explain a wide variety of effects, so that a novel framework will need to straightforwardly describe also all of these effects. However, as mentioned above, first efforts to that end have already been undertaken by Zhang et al. in Ref. [63], so that a complete microscopic theory for magnetoresistive effects arising due to the spin Hall effect seems to be on the horizon.

3.2.3   Summary

In this section (Sec. 3.2), we reported the magnetoresistance in heterostructures of Cr_2O_3 and Pt or Ta. In the first part of this section the evolution of the magnetoresistance around the Néel temperature was studied for a fixed magnetic field. There, we found a magnetoresistance with the angular dependence inherent to the spin Hall magnetoresistance, only in the vicinity of T_N and saturating at a surprisingly large magnitude of 2×10^{-4} above T_N. Further studies up to high magnetic fields ($|\mu_0 H| \leq 12.5\,\mathrm{T}$) were carried out on samples capped with Ta revealing an even higher signal magnitude in the paramagnetic phase.

By studying the magnetoresistance in the ordered state (i.e. below T_N), we concluded that the Cr_2O_3 films used here are not a perfect antiferromagnet but likely are ferrimagnetic with a small uncompensated magnetic moment. This small moment acts as handle for aligning the individual sublattices with the external magnetic field and gives rise to additional phenomena like spin canting and a spin flip (i.e. an inversion of both magnetic sublattices) even for moderate magnetic fields.

Furthermore, we applied the framework of the Hanle magnetoresistance to explain the large signal magnitude in the paramagnetic phase. To that end, we assume that there is a small diffusion constant at play in our system caused by a finite conductivity of the magnetic insulator. Using this "diffusion-enhanced HMR" model, where the spin Hall spin accumulation is not lost by spin relaxation inside the NM but by "direct" diffusion into the adjacent magnetic insulator, we can reproduce the magnitude and shape of the magnetoresistance. In particular, the longitudinal and transverse magnetoresistance could both be modeled with this assumption, using otherwise realistic spin transport parameters. The above "deHMR" model could also provide a reasonable explanation for the findings presented in the previous Sec. 3.1.

Finally, a perspective to include the HMR and SMR into one theoretical framework was outlined in this section. To that end, we proposed to extend the theory reported by Zhang et al. in Ref. [63], where the SMR is parametrized by an exchange enhancement of the Lamor frequency at the interface (i.e. $H \rightarrow H + H_{ex}$ with the exchange field H_{ex}): Taking into account also diffusive spin loss of the spin Hall spin accumulation in this theory framework, the SMR in conductive FM/NM heterostructures as well as NM/NM heterostructures as well as insulating MI/NM heterostructures could be consistently ex-

plained in one framework. In particular, in conductive heterostructures the out-diffusion of the interfacial spin Hall spin accumulation might be the dominant loss mechanism. Thus, such a generalized microscopic theory might unify and conclude the efforts to establish a complete theory for the magnetoresistance mediated via the spin Hall effect for all material systems.[44,126,164]

Chapter 4

NON-LOCAL MAGNON-MEDIATED MAGNETORESISTANCE

4.1 Scratch Test for the Non-Local Transport in $Y_3Fe_5O_{12}$/Pt Heterostructures

One possibility to investigate the magnetic and magnonic properties of magnetic insulators is to bring a spin Hall active metal like platinum into contact with it. Studying the pure spin current flow through the interface between the two materials then allows to draw conclusions about the microscopic magnetic structure and the magnon transport properties. This is accomplished either by investigating the spin Hall magnetoresistance or the non-local magnon-mediated magnetoresistance.[11,13,16,40–45,50,65,66] While the non-local transport experiments reported in literature were so far discussed and modeled in a magnon diffusion picture, a conclusive proof that magnons are the transport quanta has not been put forward. Moreover, recently there have been studies suggesting a novel mechanism for angular momentum transport via phonons.[165,166] Furthermore, long distance angular momentum transport through a paramagnetic insulator was reported, suggesting that magnons might not be as important for the transport of angular momentum as previously thought.[145] Finally, higher order effects like magnon swasing have been proposed and reported.[77,78,167,168]

In this section, we present experiments which corroborate that magnons are the transport quanta relevant for the non-local magnon-mediated magnetoresistance observed in yttrium iron garnet/Pt heterostructures. The basic idea for these experiments is to remove the magnetic insulator in between the laterally separated Pt wires used for measuring non-local transport. Without the magnetic medium, magnon transport is suppressed, while phonons can still pass through the lattice matched gadolinium gallium garnet substrate

(c.f. Fig. 4.1a).

The contents of this section are reproduced in part from R. Schlitz et al., Applied Physics Letters **114**, 252401 (2019) (Ref. [6]) with permission from AIP Publishing.

4.1.1   Sample Preparation and Methods

3 nm thick Pt layers were sputter-deposited by Savio Fabretti (Technische Universität Dresden) onto commercially available 180 nm thick yttrium iron garnet (YIG, $Y_3Fe_5O_{12}$) thin films grown by liquid phase epitaxy. Before the Pt deposition, the YIG substrates were cleaned by etching in a Piranha solution[1] and annealed at 200 °C for 1 h in ultra high vacuum. The Piranha cleaning removes organic constituents while the annealing helps to desorb the residual water from the YIG surface.[12,169] After sputtering, the Pt on top of the YIG was patterned into long parallel wires via optical lithography and Ar ion milling,[2] to define the non-local devices (c.f. Fig. 4.1b). The length of the wires is $l \sim 100\,\mu m$ and their width is $w \sim 2\,\mu m$. A separation of $d_{NL} \approx 1\,\mu m$ can be achieved with this method. Please note, that due to the small size of our samples the thickness of the resist layer was spatially inhomogeneous (i.e. there was a large edge wall). Therefore, and due to the resolution limit of the optical lithography, the exact dimensions of the devices vary by up to $\lesssim 1\,\mu m$ and the yield of the lithography (i.e. the ratio of working devices compared to devices with a short) was only $\sim 50\,\%$. The electric response was measured with our standard setup using a current of $I = 200\,\mu A$ and the current reversal method as introduced in Sec. 2.6. All measurements were carried out on one of the samples described above in the Halbach setup ($\mu_0 H = 1.1\,T$, c.f. Sec. 2.2). The contacting scheme including the polarities can be seen in Fig. 4.1b.

The patterning with the focused ion beam (FIB) modification was performed together with Toni Helm (Helmholtz-Zentrum Dresden Rossendorf) on a FEI Helios NanoLab DualBeam system. We chose an aperture of 0.34 nA and an acceleration voltage of 30 kV for the focused Ga ion beam. A scanning ion image of the full device is displayed in Fig. 4.1c. One overview image of each structure was taken with the FIB to locate the region to be modified. Although possible, we did not use the electron beam image due to the finite mismatch between the electron and ion beam. Thus, all devices have been irradiated over the full area with a finite amount of Ga ions. Possible consequences of this irradiation will be addressed later in this section when the data is discussed. The structure after cutting imaged by the scanning electron beam under an angle of 52° is depicted in Fig. 4.1d. A depth of the cut of $\approx 400\,nm$ was determined from this image, well above the thickness of the YIG film. Thus, the YIG is completely removed in between the two Pt wires after the Ga ion treatment.

---

[1]The etching was performed by Michaela Lammel and Sabrina Piontek (Leibniz Institute for Solid State and Materials Research Dresden) using H_2SO_4:H_2O_2 in a 1:1 volumetric ratio.
[2]The Ar ion milling was performed together with Tommy Schönherr (Helmholtz-Zentrum Dresden Rossendorf).
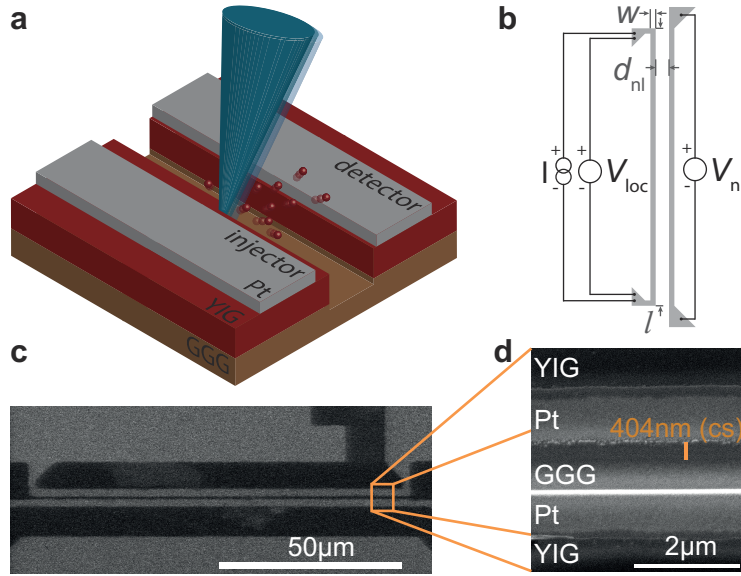
Figure 4.1: **a** The device geometry and a sketch of the FIB modification of the device are shown. The focused ion beam is used to remove the magnetic yttrium iron garnet film between the Pt detector and injector. Panel **b** depicts the contacting scheme of the structure. A current I is sourced through the injector (left strip) and the non-local voltage V_{nl} is measured on the detector (right strip). Additionally, the two-wire voltage V_{loc} is measured on the injector. Panel **c** shows an image of the device as seen by the Ga ion microscope used for locating the area to be cut. **d** A zoomed-in scanning electron image of the already cut device is depicted. To allow the determination of the depth of cut, the image was recorded under a viewing angle of 52° with respect to the surface normal. The bright white line above the lower Pt electrode is the lower edge of the trench, while the depth can be seen on the upper edge (below the upper Pt electrode). Adapted from Ref. [6].

4.1.2 Results and Discussion

In the following, we will verify that the magnetotransport response of the virgin (unmodified) device shows the anticipated transport signatures before addressing the FIB induced changes. In particular, in the local and non-local magnetotransport response, we should observe the spin Hall magnetoresistance (SMR, c.f. Sec. 1.3.1 and Fig. 1.4) and the non-local magnon-mediated magnetoresistance (MMR, c.f. Sec. 1.3.2), respectively. Thus, the local (upper row) and non-local (lower row) transport response of one device prior to the FIB treatment is summarized in Fig. 4.2 for the three rotation planes (c.f. Sec. 2.1 and Fig. 2.2). The local response (where $\delta\rho_{loc} = \rho_{loc} - \rho_0$) mostly matches the transport signature of the SMR, i.e. shows a similar $\sin^2(\alpha)$ and $\sin^2(\beta)$ modulation for the first two columns (ip and oopj rotation, c.f. Fig. 1.4). The magnitude of the SMR (i.e. the amplitude of the $\sin^2(\alpha)$ modulation) $\Delta\rho/\rho_0 \approx 4.5 \times 10^{-4}$ (c.f. Eq. (1.4)) is on-par with reports in literature for YIG/Pt heterostructures where the Pt is deposited ex-situ via sputtering.[9,12] However, a (smaller) $\sin^2(\gamma)$ modulation is also visible in the third column (oopt rota-
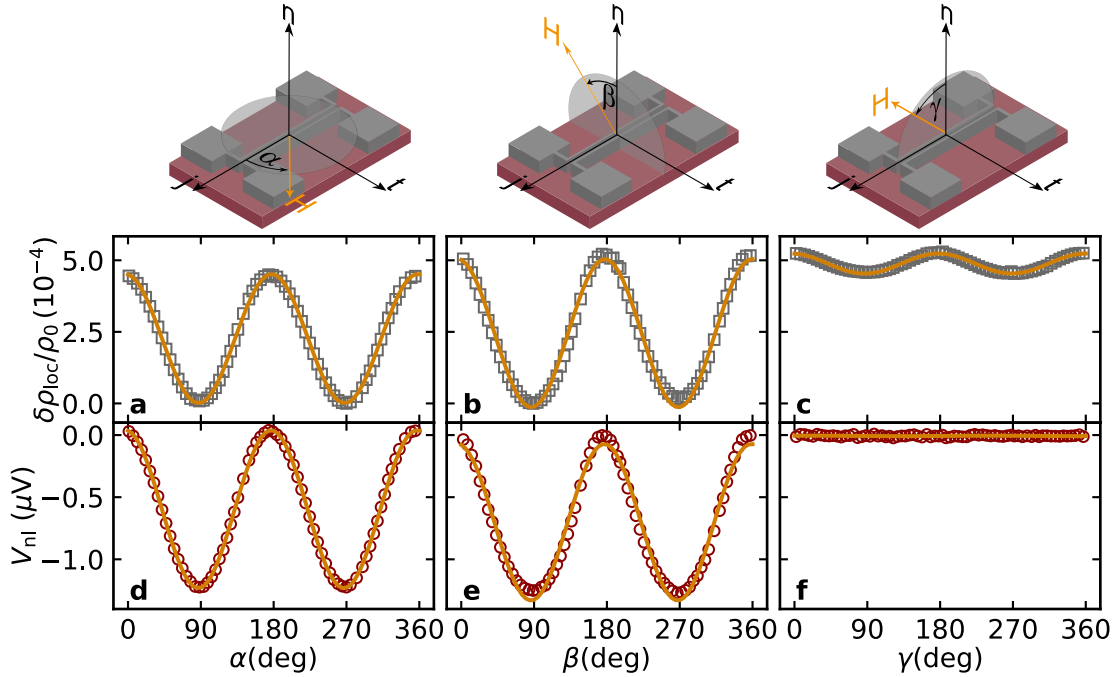
Figure 4.2: Local (panel **a-c**) and non-local (**d-f**) response of a typical device prior to FIB cutting for ip, oopj and oopt rotation, respectively (c.f. sketches above the panels and Ch. 2 for the nomenclature of the field rotations). The local transport response mostly exhibits the behavior expected for the spin Hall magnetoresistance, i.e. a large modulation for ip and oopj rotations and no modulation for the oopt rotation. The finite modulation observed in oopt is due to the imperfect contact geometry of the device, where the current flow is not always along one direction (c.f. Fig. 4.1). The non-local signal has the symmetry of the magnon-mediated magnetoresistance, namely a negative voltage for finite projection of the magnetic field (and thus the magnetization) onto the **t** direction and a vanishing voltage if the magnetization is perpendicular to the **t** direction.

tion), where a constant resistivity should be observed for SMR. This can be rationalized, however, by considering the geometry of the device (c.f. Fig. 4.1c), where the current in the parts of the device that are perpendicular to the long wire contributes a signal due to the different direction of current flow.[3] For these "side arms", the oopt rotation with respoect to the long wire is the oopj rotation as the current direction is rotated by 90° in the plane. Please note, that for the three rotations planes, the normalized signals were shifted so that the values at the high symmetry points (i.e. **H** ∥ **t** and **H** ∥ **n**) are equal for the different planes. This is necessary due to the different measuring inserts used for the three rotation planes, resulting in slightly different temperatures, and thus slightly different ρ_0 for each measurement.

---

[3]If the geometry of the device and the relative contribution of the "side arms" and the long wire to the total resistivity is estimated, a factor of 1/10 is found. This factor is in agreement with the difference in the SMR amplitude observed here.

In contrast, for the non-local signals we find perfect agreement with the expected MMR signature (c.f. Sec. 1.3.2 and Eq. (1.6)):[16,45] The voltage is negative when there is a finite projection of the magnetic field (and thus the magnetization) onto the **t** direction (c.f. Fig. 4.2d and e) and very close to zero otherwise (c.f. Fig. 4.2f). This then leads to the observed $\sin^2(\alpha)$ and $\sin^2(\beta)$ modulation with an equal magnitude of $|\Delta V_{nl}| \sim 1.2\,\mu V$ for the ip ond oopj rotations. Please note, that no offset has been subtracted from the non-local voltage. Additionally, for the non-local signal the side arms giving rise to an additional signal for the oopt rotation cannot contribute to the MMR, since the injector and detector, and thus the polarization of the injected and detected spins, are orthogonal there.

Having established, that the signal shows the anticipated transport response before being exposed to the focused ion beam, we will now turn to the impact of the FIB modification. In Fig. 4.3 we show the transport response of a device before (panels a and d) and after FIB cutting using the same contacts (b and e) and with inverted injector and detector (c and f). As discussed above, the $\sin^2(\alpha)$ modulation of the non-local voltage has a magnitude of $1.2\,\mu V$ before the FIB cut, while the (local) SMR has a magnitude of $\Delta\rho/\rho_0 \approx 4.5 \times 10^{-4}$.

After characterizing the transport of the initial device, we removed a portion of the YIG layer a width, length and depth of $500\,nm$, $120\,\mu m$ and $400\,nm$, respectively between the two Pt wires with the FIB. The ensuing changes of the transport are shown in Fig. 4.3b and e: The SMR decreases by roughly a factor of 5 to 1×10^{-4}. In contrast, the MMR (i.e. the non-local modulation) vanishes to within our experimental resolution ($\approx 5\,nV$, c.f. Sec. 2.6). This corresponds to a suppression of the MMR by at least a factor of 200. Additionally, a positive offset signal arises in the non-local data (best seen in the inset). This can be traced back to a finite cross conductivity between the two Pt wires, likely caused by Ga implantation.

One possible explanation for the absence of the MMR could be that the second wire is altered in a way that its spin Hall effect vanishes. To exclude such an effect, we repeated the magnetotransport experiments with inverted contacts, i.e. driving the current in the right wire and detecting the non-local voltage on the left wire (c.f. Fig. 4.3c, f). These measurements confirm that the second wire indeed shows SMR, indicating that a spin current can still be injected and/or detected by it. Please note, that the slightly larger SMR magnitude originates from the missing "side arms" in the second wire, such that all current flows from top to bottom. Consequently, we can conclude that the spin Hall effect in the Pt wires is reduced at most by a factor of $\sqrt{5}$, as the SMR depends on the square of the spin Hall angle θ_{SH} (i.e. the spin to charge conversion efficiency) and the SMR is reduced by a factor of 5. As such, if this would be the dominating effect, also the non-local signal should be reduced only by a factor of 5, since also the MMR scales with θ_{SH}^2.[40,41,43–45] Clearly, this is not sufficient to explain the measured reduction of the non-local signal by a factor $\gtrsim 200$. Thus, the data in Fig. 4.3 suggest that magnon transport is indeed the dominating transport mechanism mediating the non-local magnetoresistance in YIG/Pt: Since the FIB cut removes the magnon transport channel, no modulation of the non-local voltage, i.e. no MMR, can be seen after its removal.

Finally, we can use our findings to establish an upper boundary for the size of additional transport effects (e.g. by phonons): If there were such effects superimposed on the MMR, giving rise to an additional voltage modulation, they would still be present after the FIB modification. As we do not find such a modulation after FIB cutting, the maximum contribution of these effects are given by the signal to noise ratio of the measurements, which is on the order of 200 for the voltage modulation observed in this device. Thus, the maximum size of the additional transport effects is on the order of 0.5 % of the MMR.
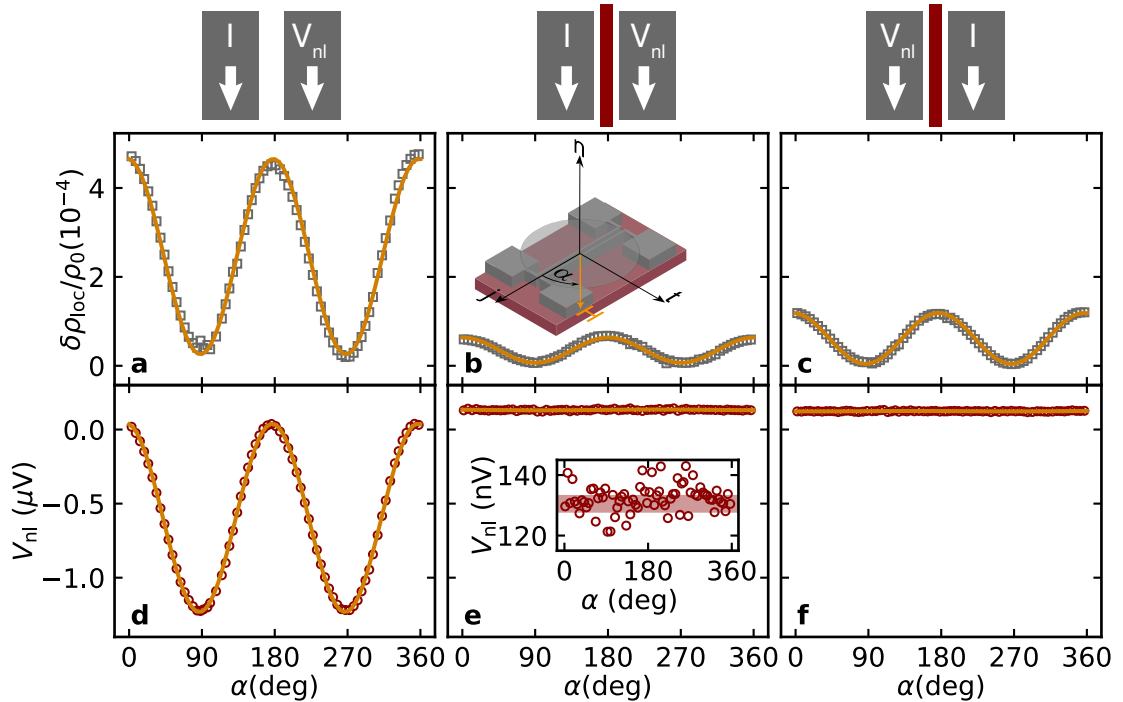

Figure 4.3: Comparison of the transport response measured before the FIB cut (panels **a** and **d**) to the transport response after removing the YIG layer with the FIB (panels **b** and **e**). After cutting, the SMR is decreased significantly and the modulation of the non-local voltage (i.e. the MMR) vanishes. **e** To improve the visibility, a zoomed in view of the data is shown as inset, verifying the absence of the MMR to a threshold of 5 nV. A small positive offset is visible in the non-local voltage after the FIB modification, hinting at a finite cross conductivity (substrate conductivity) due to Ga implantation. **c**, **f** To verify that both Pt strips are still spin Hall active, the injector and detector are exchanged. The corresponding data corroborate the findings of the original contact geometry, i.e. a reduced SMR and no modulation of the non-local signal. Adapted from Ref. [6].

In the following we will attempt to further elucidate the modifications the heterostructure experiences under Ga ion irradiation by considering incomplete cuts of the structure. To this end, two different cuts are discussed:

First, we removed only half of the length of the YIG channel, expecting a reduction of the MMR by a factor of 2. The corresponding data before and after the FIB cut are shown
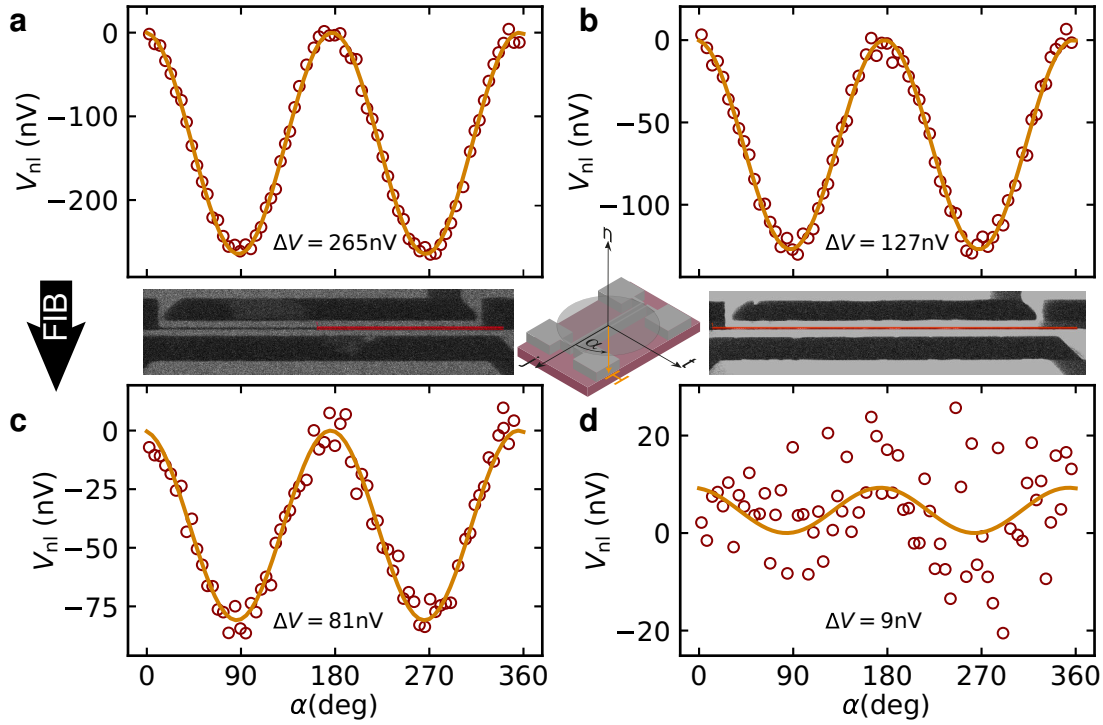
Figure 4.4: **a**, **b** Non-local transport response measured prior to FIB cutting and **c**, **d** after the removal of the yttrium iron garnet. For panel **c**, half of the length of the channel was removed, while for panel **d**, half of the YIG thickness has been removed over the full length (see insets). Even after cutting, a modulation of the non-local voltage (viz. MMR) is observed for both cuts. However, the MMR is lowered by more than the expected factor of two in both cases (for removing half of the YIG channel in width or thickness). Adapted from Ref. [6].

in Fig. 4.4a and c, respectively. Here, the amplitude of the MMR is reduced approximately by a factor of 3, significantly differing from the expected factor of 2. Interestingly, the SMR in this device is reduced to 60 % of its original value (in contrast to a reduction to 20 % for the full cut). From these two observations, we speculate that the reason for the reduction of SMR and MMR is a combination two effects. For one, the YIG/Pt interface or the spin Hall effect in Pt might be altered even by imaging the full structure with the Ga FIB. Secondly, the imperfect beam profile of the ion beam might lead to additional peripheral damage.[170] Thus, damage by the ion beam seems reasonably to assume when considering the approximate penetration depth $\approx 10\,\text{nm}$ of the Ga ions for the given acceleration voltage.[171] We will now try to extract this reduction x of the MMR due to the irradiation from imaging. Using our initial assumption, i.e. that the MMR is reduced to 50 % of its original value and the actual reduction to 33 %, we can solve

$$\Delta V_{\text{nl}} = 0.33 \cdot \Delta V_{\text{nl}}^0 \triangleq 0.5 \cdot x \cdot \Delta V_{\text{nl}}^0, \tag{4.1}$$

for x, where ΔV_{nl} and ΔV_{nl}^0 are the amplitudes of the MMR before and after the FIB cut, respectively. Thus, the additional reduction due to imaging can be determined as $x \approx 0.7$ (70 %). Interestingly, this reduction shows reasonable agreement with the reduction of the SMR in the device. This corroborates our interpretation, since the SMR and MMR depend in the same way on θ_{SH}. The reduction might, however, also be explained by a modified spin mixing interface conductance $G_{\uparrow\downarrow}$. Since the SMR and MMR are sensitive to different parts of $G_{\uparrow\downarrow}$[40,44,63] and no clear understanding of how these parts would be impacted by the Ga implantation is available, the exact origin of the reduction cannot be narrowed down further. Anyway, it is crucial to note that the absence of the modulation in the non-local transport response of the first device cannot be explained by this global irradiation effect (as $5/0.7 \ll 200$).

The third device we prepared was altered with a shallow cut over the full length, removing approximately half of the YIG thickness ($50 - 70$ nm). The corresponding data are shown in Fig. 4.4b and d. Please note, that also in this device the SMR is reduced to 60 % of its original value. Thus, we can extrapolate the expected size of the MMR by using the previously determined irradiation damage induced reduction x: The signal should be lowered due to the overall ion beam irradiation and the reduced channel width by roughly a factor of $0.7 \cdot 0.5 = 0.35$. In contrast, we find a reduction of the MMR by at least a factor of 10. From this we conclude that either the constriction of the YIG channel imposes additional boundary conditions[172] for the magnon transport or that the FIB is highly efficient in altering the transport properties of the YIG. There have been reports hinting to the second fact: A local change of the saturation magnetization upon ion irradiation can be found.[173] Either way, magnons clearly are of key importance of the MMR. Consequently, FIB irradiation might prove to be a valuable tool to prepare periodic modulations of the YIG properties necessary e.g. for magnonic crystals.[172] Clearly, it would be interesting in the future to study the MMR in such magnetically modulated samples.

4.1.3 Summary

All data presented above consistently showed that FIB irradiation significantly modifies the local and non-local magnetotransport response of YIG/Pt heterostructures. Our results demonstrated that magnons are of key importance for the MMR, supporting the magnon picture put forward to explain the non-local magnetoresistance in such structures. Additionally, our experiments put a firm boundary of 0.5 % of the MMR as maximum contribution of other transport effects (e.g. by phonons) to the non-local transport. Finally, we infer that FIB irradiation sensitively affects the YIG/Pt devices, which could be utilized for spatially tailoring the magnetic properties of the YIG and studying the corresponding modifications in the non-local transport response.

4.2 Evolution at Elevated Temperatures in $Y_3Fe_5O_{12}$/Pt Heterostructures

As already addressed in Ch. 3, it is interesting to study how the spin transport evolves across magnetic phase transitions in magnetic insulator/normal metal heterostructures. In such systems, the magnetic phase transition becomes evident in the transport response of the normal metal due to the magnetization dependence of the spin Hall magnetoresistance. The evolution of the non-local magnon-mediated magnetoresistance across such a magnetic phase transition is still uncharted.

Wesenberg et al. reported long distance spin transport in as-sputtered YIG/Pt bilayers (i.e. disordered YIG, c.f. Ref. [136] and Sec. 3.1). These results, however, are critically discussed in the meantime, as they might be an artifact of a finite electric conductivity of the YIG films upon thermal activation.[174,175] Additionally, only a small modulation of the non-local signal with the magnetic field has been reported in these experiments, attributed to the absence of an ordered magnetic state. Furthermore, strongly field dependent non-local transport on GGG/Pt heterostructures was reported at low temperatures ($T < 100\,\mathrm{K}$) by Oyanagi et al. in Ref. [145]. GGG ($Gd_3Ga_5O_{12}$) is a paramagnet, ordering only at very low temperatures $T \lesssim 1\,\mathrm{K}$.[176] Consequently, it is surprising to observe non-local transport so far above the ordering temperature. Since the exact magnetic configuration of the as-sputtered YIG remains elusive[5] and the non-local transport in the GGG depends sensitively on the exact magnetic configuration,[145] it appears attractive to use a well established magnetic insulator such as YIG. Using YIG, measurements of the MMR could be carried out as a function of increasing temperature, transitioning from the ordered into the disordered (paramagnetic) phase.

In contrast to the systems discussed above and in Ch. 3, this section thus will focus on the best studied material system for SMR and MMR experiments: crystalline YIG/Pt heterostructures. We will elucidate the local as well as the non-local transport response in such bilayers to evaluate how the MMR evolves when approaching the Curie temperature $T_C \approx 560\,\mathrm{K}$ of yttrium iron garnet.[119] To this end, we will use the high temperature setup described in Sec. 2.3. The sample investigated in this section was prepared together with the sample studied in Sec. 4.1 above. Thus, we will not repeat the sample preparation procedure here. However, please note, that the layout of the previous device was modified to include a Hall bar for well-defined measurements of the local response of the sample.

4.2.1 Results and Discussion

Before addressing the results, we first want to introduce an alternative way of extracting the SMR amplitude $\Delta\rho/\rho_0$. To that end Eq. (1.4) and Eq. (1.5) from Sec. 1.3.1 are summarized again below for convenience:

$$\rho_\ell = \rho_0 + \Delta\rho(1 - m_y^2) \tag{4.2}$$

$$\rho_t = \Delta\rho\, m_x m_y + \Delta\rho_H m_z \tag{4.3}$$

Instead of measuring the longitudinal voltage V_ℓ and the corresponding voltage modulation, one can also measure the transverse voltage V_t (c.f. Fig. 1.4). The main advantage of using V_t is the independence of the transverse voltage on temperature, which significantly reduces the impact of spurious thermal drifts. After determining the longitudinal and transverse resistivities from the voltages (c.f. Eq. (4.2) and Eq. (4.3)), the amplitude of the $m_x m_y$ modulation in the transverse signal, or $\cos(\alpha)\sin(\alpha)$ in our coordinate system, corresponds directly to $\Delta\rho$.[43,44] Thus, we can use the transverse voltage to extract $\Delta\rho$ and compare this to ρ_0 extracted from the longitudinal voltage to obtain the SMR amplitude $\Delta\rho/\rho_0$. Although $\Delta\rho/\rho_0$ extracted using the longitudinal and transverse resistivity should be equal, we find a $\approx 40\,\%$ larger $\Delta\rho/\rho_0$ when using the transverse resistivity. This is likely due to the fact, that our samples are not perfectly homogeneous: The longitduinal voltage averages the SMR over the full Hall bar, while the transverse voltage probes only the small portion of the Hall bar between the side contacts (c.f. Fig. 2.2). Thus, in the presence of spatial inhomogeneities, the SMR extracted using the longitudinal and transverse contacts can differ.[4] To allow for a straightforward evaluation of the amplitude, it is useful to show ρ_t/ρ_0, i.e. the (angular resolved) transverse resistivity normalized to ρ_0 extracted from the longitudinal resistivity. A similar approach was chosen in Ref. [50].

Using the transverse resistivity approach, we find a $\Delta\rho/\rho_0 \sim 5 \times 10^{-5}$ for our device at $T = 300\,\mathrm{K}$.[5] The normalized transverse resistivity ρ_t/ρ_0 is shown in Fig. 4.5a and b for a set of lower and higher temperatures, respectively. A monotonous decrease of the modulation amplitude Δ_ρ/ρ_0 can be observed for increasing temperature. The modulation of ρ_t/ρ_0 at the highest shown temperature $T = 540\,\mathrm{K}$ is only barely visible ($\Delta\rho/\rho_0 \lesssim 5 \times 10^{-6}$).

The non-local voltage V_{nl} plotted in Fig. 4.5c,d shows the clear $\sin^2(\alpha)$ modulation excepted for the MMR (see Sec. 4.1). Interestingly, here the modulation amplitude ΔV_{nl} first increases from room temperature towards higher temperatures. At very high temperatures, ΔV_{nl} then decreases and an additional positive offset voltage becomes visible (panel d). For the highest temperature $T = 540\,\mathrm{K}$, no clear modulation of the non-local voltage can be observed anymore ($\Delta V_{nl} \lesssim 10\,\mathrm{nV}$), suggesting, that the MMR vanishes upon approaching the Curie temperature. An increase of the MMR from $T \sim 300\,\mathrm{K}$ towards higher temperatures is expected: Ideally, the generation and detection mechanisms of magnons impose a power law dependence with temperature, such that the MMR is $\propto T^\alpha$ with $\alpha = 3/2$ or $5/2$.[40,41] However, previous studies already suggested that there is a crossover of the temperature dependence from $T^{5/2}$ below $100\,\mathrm{K}$ to $T^{3/2}$ above.[16] Additionally, the magnon diffusion can also impose a further temperature dependence.[73]

For a more quantitative discussion, we will now turn to the amplitudes of the SMR $\Delta\rho/\rho_0$ and MMR ΔV_{nl}. Both were determined by fitting the appropriate modulation func-

---

[4]This is further corroborated by the SMR amplitude of the non-local device, where a $\approx 160\,\%$ larger value than on the transverse contacts of the Hall bar is found. Please note that, at the temperatures where the SMR could be extracted from the longitudinal voltage, it shows the same trends as a function of temperature as the SMR extracted using the transverse voltage.

[5]Please note, that this value is observed during the final run, where the full temperature range was measured. The initial value was higher as can be seen also in Fig. 4.6a (run 1).
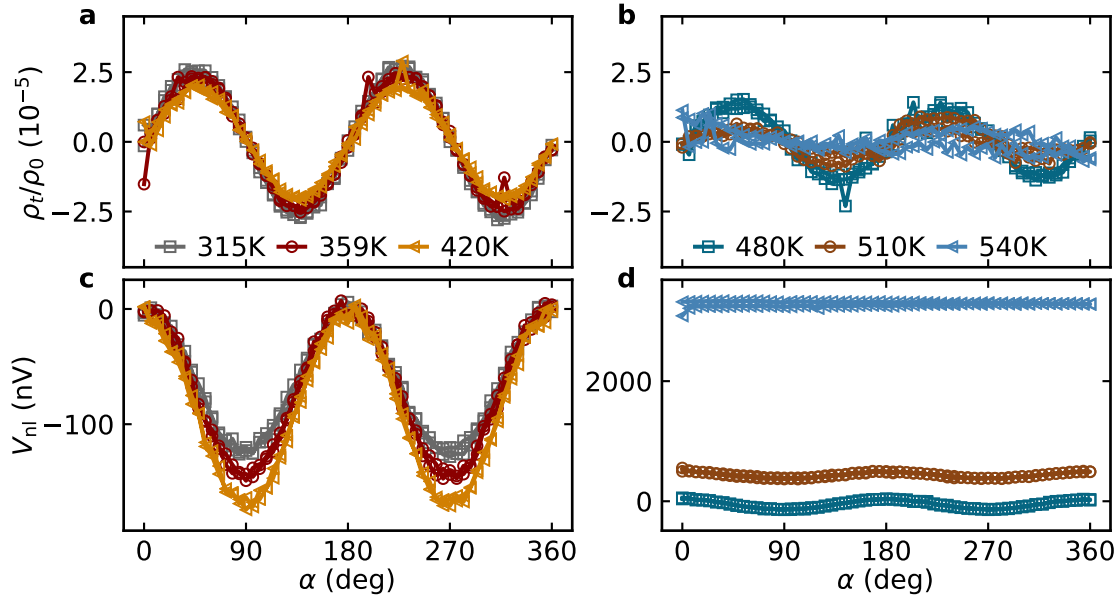
Figure 4.5: Angle resolved magnetoresistance measurements taken during in-plane rotations of the magnetic field $\mu_0 H \approx 70\,\mathrm{mT}$ on a YIG/Pt heterostructure at $T = 300\,\mathrm{K}$. **a** and **b** The transverse resistivity normalized to ρ_0 (corresponding to $\delta\rho_{loc}/\rho_0$ used in Sec. 4.1) is shown for lower and higher temperatures, respectively. Please note, that the mean value of the transverse resistivity has been subtracted. In this way, only the magnetic field (and thus magnetization) dependent modulation of the resistivity prevails, while the temperature dependent spurious offset present in the transverse resistivity is removed. The full amplitude of the $\sin(\alpha)\cos(\alpha)$ modulation corresponds to $\Delta\rho/\rho_0$ and thus is the SMR amplitude. A decrease of the modulation amplitude for increasing temperatures is evident from the measurements. **c** and **d** The non-local voltage is shown in for the same set of temperatures. In contrast to the local response, an increase of the $\sin^2(\alpha)$ modulation is observed at least until $420\,\mathrm{K}$. For even higher temperatures, the amplitude decreases and an additional positive (orientation-independent) offset is observed.

tion to the data (i.e. a $\cos(\alpha)\sin(\alpha)$ for the local and a $\sin^2(\alpha)$ for the non-local signals). The thus obtained amplitudes of the SMR and the MMR are summarized in Fig. 4.6a and b, respectively. Additionally, the non-local offset voltage is included in Fig. 4.6b. The SMR amplitude decreases monotonously and approaches 0 at around $510\,\mathrm{K}$. This decrease resembles the (sublattice) magnetization curve of a ferromagnet, being mostly constant well below the Curie temperature and then steeply decreasing towards the Curie temperature. To graphically show this, we calculated the saturation magnetization of YIG as a function of temperature using a mean field model with two antiferromagnetically coupled iron sublattices.[177,178] The two $M(T)$ curves shown in Fig. 4.6a were calculated to yield Curie temperatures of $T_C = 560\,\mathrm{K}$ and $T_C = 510\,\mathrm{K}$ using the parameters given by Anderson in Ref. [177] (yielding $T_C = 560\,\mathrm{K}$) and the same parameters divided by 1.1 (yielding $T_C = 510\,\mathrm{K}$), respectively. The code and a table with the parameters for the first calculation can be found in App. D. As one might expect, the original set of parameters

quoted by Anderson yields a Curie temperature closely matching the literature value of YIG ($T_C = 560$ K).[119] A good congruence of the net magnetization with the SMR data (gray points and turmeric line) can be found until ~ 450 K.[63] Above this temperature, a clear deviation is evident. To estimate whether a different Curie temperature might account for this difference, the second calculation with a lower T_C was performed. Here, although the vanishing point agrees, no good agreement between the data and the calculated $M(T)$ can be found.
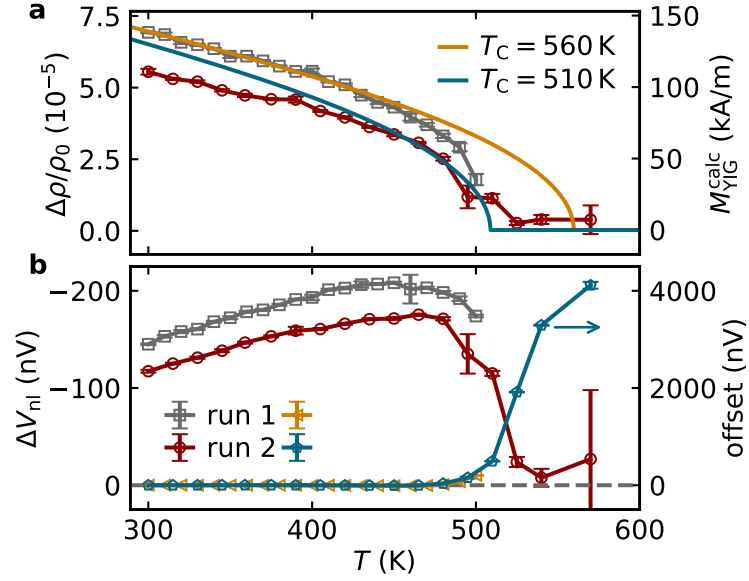
Figure 4.6: **a** The SMR amplitude $\Delta\rho/\rho_0$ determined by fitting a $\sin(\alpha)\cos(\alpha)$ to the local data is shown. The SMR amplitude obtained during the first the subsequent second measurement run (red and gray curves) decreases monotonously for increasing temperatures and approaches 0 at above $T = 510$ K. This temperature is well below $T_C = 560$ K. The decrease of the SMR follows the (calculated) net magnetization of the YIG films (turmeric and teal lines). Here, two different sets of parameters were used for calculating the $M(T)$, resulting in a Curie temperature of $T_C = 560$ K (turmeric) and $T_C = 510$ K (teal), where only the prior allows to fit $\Delta\rho/\rho_0$. **b** By fitting a $\sin^2(\alpha)$ to the non-local data shown in Fig. 4.5, the amplitude of the MMR ΔV_{nl} is determined. The MMR (red and gray curves) increases with increasing temperature, peaking around ~ 450 K. Similar to the SMR, the MMR is suppressed towards 510 K well below the Curie temperature. The offset signal of the non-local voltage (teal and turmeric curves), increasing steeply above 500 K.

We now turn to the temperature dependence of the MMR. Here, an increase of ΔV_{nl} is observed for increasing temperatures, leveling off around 450 K. As already discussed above, this agrees with the expectations for the MMR ($\propto T^{3/2}$ at 300 K)[16] and will be addressed in detail later in the context of Fig. 4.7b. Similarly to the SMR, the MMR then sharply decreases and vanishes above 510 K. Interestingly, in the high temperature regime ($T > 470$ K), the SMR and MMR seem to vanish congruently. Additionally, the positive offset voltage evident already in Fig. 4.5d can be seen to increase steeply above 470 K.

We attribute this to an onset of the conductivity of the YIG film. Please note, that the offset voltage $V_{\mathrm{nl,leak}} \sim 4\,\mu\mathrm{V}$ is still well below the voltage drop along the local wire $V_{\mathrm{loc}} \sim 0.35\,\mathrm{V}$.

Before further discussing the conductivity of the YIG film and its impact on the transport, we will first try to elucidate whether the sample ages during the measurements at high temperatures. To judge this, two measurement runs were performed up to 500 K (run 1) and 600 K (run 2). A clear change is evident in the amplitudes of the two measurements, remaining even at 300 K after the sample has cooled down following the first run. Both, the SMR and the MMR amplitude, are decreased by about $\sim 24\,\%$. This suggests, that either the spin Hall effect in the Pt or the interface transparency of the YIG/Pt interface changes by oxidation or interdiffusion (e.g. by formation of an interfacial FePt layer).[6] As discussed already in the context of the focused ion beam modification in Sec. 4.1, the SMR and MMR depend on different parts of the spin mixing interface conductance $G_{\uparrow\downarrow}$, where changes to the interface due to interdiffusion might still affect both parts of $G_{\uparrow\downarrow}$ in a similar way.[63] If an interfacial layer is present, it could also explain the decrease of the SMR and MMR already well below T_{C}: FePt has a similar Curie temperature compared to YIG, in the range of 570 K to 750 K, being very sensitive to the exact composition.[179] Thus, a sub-stoichiometric or similar compound (e.g. Pt-doped YIG) might give rise to a lower ordering temperature of the interfacial layer. As both, the SMR and MMR are very sensitive to the YIG/Pt interface, an alteration of the magnetic properties there will sensitively impact the transport response.[69] It is important to know, that the sample stays at each temperature for around 1.5 h, since it takes time to stabilize a given temperature and perform the ARMR measurement. In total, the sample was thus heated for about $\sim 32\,\mathrm{h}$ in the first measurement run. Consequently, it appears natural that some form of annealing could have taken place.

To further elucidate the mechanism of the sample aging, we plot the resistivity of the Pt layer in Fig. 4.7. Here, a linear trend is evident for the Pt resistivity until 460 K as expected for a metal. However, in the region shaded in teal ($T > 460\,\mathrm{K}$), a deviation from the linear trend is observed, where the slope of the temperature dependence of the Pt resistivity changes. Upon cooling down the sample and starting the next measurement run, a persistent reduction of the resistance is present at 300 K. This decrease of the resistivity is a further hint towards interdiffusion: We again speculate that an FePt layer might form at the interface, increasing the effective conductive cross section of the Pt layer. Additionally, this might explain the decrease of the SMR and MMR: As the FePt layer forms at the YIG/Pt interface, it can suppress the spin current flow. After the measurements to 600 K, no SMR can be seen at room temperature, and several of the sample contacts broke, suggesting that the sample is damaged irrevocably. This might be a consequence of island formation of the Pt layer or a similar effect. Interestingly, this diffusion has to be slow at least at 500 K, as no cross conductivity (i.e. finite non-local offset voltage) can be seen at 300 K also in the second run. Thus, the YIG layer in the region between the injector and

---

[6]Since only a membrane pump was used to generate the vacuum for the high temperature insert, a finite partial pressure of oxygen must have been present in the measuring insert (likely in the range of $p \sim 1 \times 10^{-1}\,\mathrm{mbar}$).
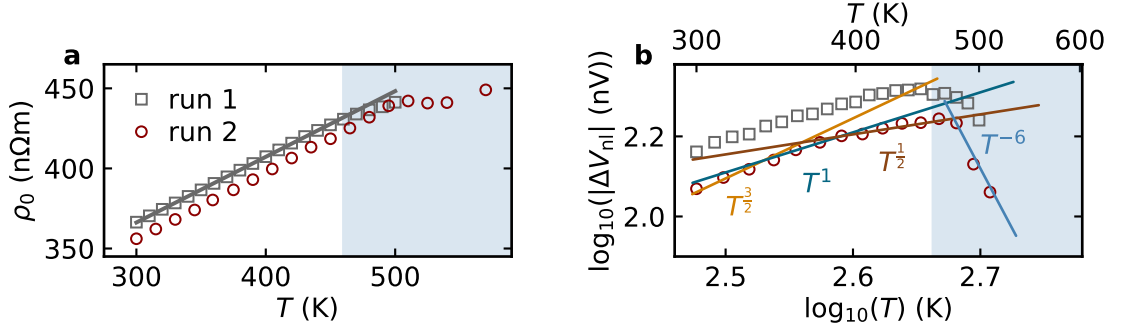
Figure 4.7: **a** The evolution of the Pt resistivity is shown. A linear trend is maintained until $\approx 460\,\mathrm{K}$ (gray fit). Above this temperature (shaded teal region) a deviation from the linear behavior is evident. Additionally, a persistent change of the resistivity from run 1 to run 2 is observed, suggesting that the sample is permanently altered at high temperatures. Panel **b** depicts the data already shown in Fig. 4.6b but now in a double logarithmic plot to allow determining the power law scaling of the non-local signal. For $T < 380\,\mathrm{K}$, a $T^{\frac{3}{2}}$ scaling is observed (turmeric line), while it decreases to a $T^{\frac{1}{2}}$ scaling (teal line) above that temperature. At very high temperatures ($T > 490\,\mathrm{K}$) the signal decreases rapidly.

detector has not been completely altered. While certainly interesting, a full study of the properties of the YIG/Pt layer upon annealing is beyond of the scope of this work.

Finally, we now address the scaling behavior (T^α power law) of the MMR with temperature. To this end, a double logarithmic plot of ΔV_{nl} against temperature is shown in Fig. 4.7b. Here, two regimes can be found: In the first regime, a positive power is found, where $\alpha \sim 1$ (teal line) roughly describes the data. However, from reports in Ref. [16] for similar YIG/Pt samples, we expect a power law with $\alpha \sim 3/2$ close to 300 K. Indeed, if $\alpha(300\,\mathrm{K}) \sim 3/2$ and an additional power $\alpha(450\,\mathrm{K}) \sim 1/2$ (turmeric and brown lines) is included, the temperature dependence of thr MMR in the regime until $T \sim 470\,\mathrm{K}$ can be reproduced. We speculate that in this regime, the temperature dependence is dominated by the decrease of the magnon diffusion length, reducing α for increasing temperatures: This can be motivated by considering that more and more thermally excited magnons scatter with the non-equilibrium magnon accumulation. Thus, the magnon diffusion length, on which the MMR depends exponentially, is effectively reduced, so that a changing power is observed.[45] In the high temperature region ($T \gtrsim 470\,\mathrm{K}$), the sharp decrease of the signal scales at least with T^{-6}. This decrease is either rooted in the rapidly decreasing (and ultimately vanishing) magnetic order of the YIG film or the interface layer (which would agree with the SMR also vanishing at the same temperature). An alternative explanation might be, that the YIG film acquires a finite electrical conductivity at high temperatures due to a finite mobility of the electrons in the YIG film, the magnons can relax via this additional electronic channel, thus drastically reducing the diffusion distance.

To evaluate, whether the conductivity of the YIG film is finite at the temperatures discussed above (i.e. between 450 K and 550 K), we now study the origin of the non-local offset voltage in more detail. This is particularly important in light of the magnetic field

independent non-local transport reported in Ref. [136]. In other words, we speculate that the offset voltage we observe in our samples is the "non-local transport" signature observed in Ref. [136]. To evaluate the resistance, we consider the simplified equivalent circuit diagram of the non-local device shown in Fig. 4.8. The two Pt strips have a resistance of $R_{Pt} \sim 3\,k\Omega$ (at 300 K), which are shorted on the top and bottom by the YIG layer resistance. This obviously is a strongly simplified picture, as the YIG channel is present over the full Pt strip length and not only at the two ends of the Pt strip. However, for a simple estimation this model should suffice.

Figure 4.8: Equivalent circuit diagram of the non-local device. The two Pt wires have a resistance of R_{Pt} and are connected by the resistance of the YIG layer R_{YIG} at the two endpoints. If a leakage current will flow through the YIG it gives rise to a finite offset voltage $V_{nl,leak}$.[7]
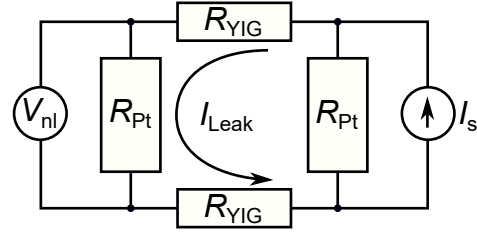
We will now solve for V_{nl} as a function of the YIG resistance. The solution is then used to calculate R_{YIG} from the positive offset voltage $V_{nl,leak}$ observed in the experiment. To begin, the non-local voltage is

$$V_{nl,leak} = R_{Pt}I_{leak} = \frac{V_{loc}R_{Pt}}{R_{Pt} + 2R_{YIG}}, \tag{4.4}$$

where V_{loc} is the voltage on the first Pt strip. V_{loc} in turn can be calculated from the constant source current I_s by

$$V_{loc} = I_s \frac{R_{Pt}^2 + 2R_{YIG}R_{Pt}}{2(R_{Pt} + R_{YIG})} \tag{4.5}$$

Combining Eq. (4.4) and Eq. (4.5) we obtain

$$V_{nl,leak} = \frac{I_s R_{Pt}^2}{2(R_{Pt} + R_{YIG})}. \tag{4.6}$$

Finally, we can reformulate Eq. (4.6) to yield R_{YIG} as a function of the non-local offset voltage:

$$R_{YIG} = \frac{I_s R_{Pt}^2}{2V_{nl,leak}} - R_{Pt} \approx \frac{I_s R_{Pt}^2}{2V_{nl,leak}} \tag{4.7}$$

As one would naively expect, the YIG resistance is inversely proportional to the non-local

---

[7]Adding another resistor with R_{YIG}^A in the center of the circuit (i.e. when splitting each Pt resistor into two resistors with $R_{Pt}/2$) will not change the equation system, as no current will flow through it. This can be motivated, as both branches of the circuit have an equivalent voltage drop of $V_{loc}/2$ at the point where R_{YIG}^A would be connected, such that the voltage drop across R_{YIG}^A in this case is 0. V_{loc} refers to the voltage drop along the right Pt resistor.

offset voltage as long as $R_{\text{Pt}} \ll R_{\text{YIG}}$. Thus, a finite resistance of the YIG results in a spurious signal measured on the second wire, which is not due to spin transport but due to electrical shorting of the two non-local wires. This also naturally explains why V_{nl} is not dependent on the magnetic field orientation - R_{YIG} is simply due to the semiconducting properties of the YIG, which do not show a (large) magnetoresistance.
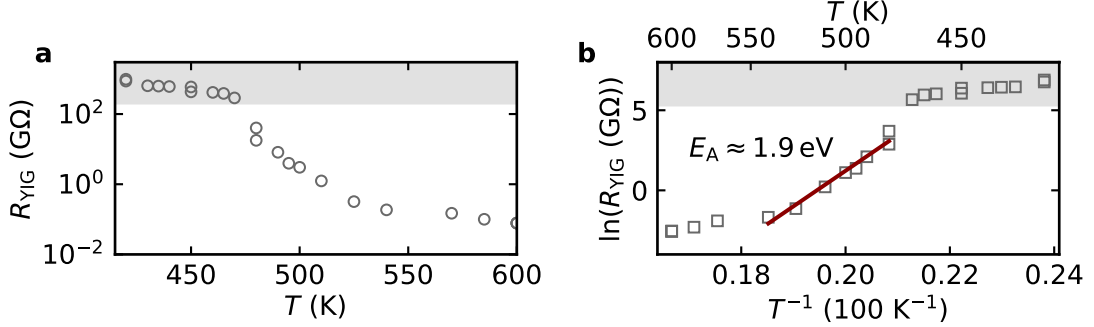

Figure 4.9: Panel **a** shows the YIG resistance R_{YIG} determined using Eq. (4.7). For $T < 470\,$K R_{YIG} is well above $100\,$GΩ, such that the YIG indeed can be considered as fully insulating. A decrease of R_{YIG} by at least three orders of magnitude is observed above $\sim 470\,$K. Panel **b** depicts the same data in an Arrhenius graph, i.e. the logarithm of R_{YIG} is plotted against the inverse temperature. This Arrhenius graph allows to determine the activation energy E_{A} of the physical quantity that is thermally activated according to $\exp(-\frac{E_{\text{A}}}{k_{\text{B}}T})$ by extracting the linear slope (red fit), where in the ideal case of an undoped semiconductor E_{A} would be the gap energy.[138] The region shaded in gray in both panels graphically shows the noise floor of our measurement setup $\sim 3\,$nV (c.f. Sec. 2.6).

The resistance R_{YIG} determined from our offset data and Eq. (4.7) is summarized in Fig. 4.9a and b. An "infinite" resistance can be observed below $T < 470\,$K – the value $R_{\text{YIG}} \sim 200\,G\Omega$ is given by our noise floor of $\sim 3\,$nV (graphically represented by the region shaded in gray). For higher temperatures, the resistance steeply drops and decreases down to $80\,$MΩ at $600\,$K. This is still large compared to $R_{\text{Pt}} \sim 3.5\,$kΩ at the same temperature, explaining the small magnitude of the offset voltage. However, this increase nicely explains the positive offset reported for large current densities in many works.[72,78,136,167,174,175] All these studies have in common, that they use a large current driven in the injector to heat the device. In such an experiment, however, the effects of the high current density and the temperature intermix. Additionally, due to the localized heating, the exact temperature profile over the device is unknown, making the determination of temperature induced effects difficult. In contrast, for our experiments we chose the opposite approach, globally heating the full sample, while using only a small current to probe the non-local transport response.

To study the evolution of R_{YIG} in more detail, we use an Arrhenius graph to estimate the activation energy of the electrical transport (c.f. Fig. 4.9b). By fitting the slope, we determine an activation energy $E_{\text{A}} \approx 1.9\,$eV, very close to the value $E_{\text{A}} = 2\,$eV reported for direct resistance measurements on LPE grown thin films in Ref. [174]. Interestingly, above

550 K, the slope in the Arrhenius graph changes significantly. This might be rooted in the increasing interdiffusion or some other annealing effect (c.f. Fig. 4.7a). Additionally, the finite conductivity of the YIG film will change the current distribution and thus decrease the accuracy of our simple model used to extract the resistivity.

4.2.2 Summary

We have presented measurements of the local and non-local transport response in YIG/Pt heterostructures from room temperature to beyond the Curie temperature. We found that the SMR decreases until 500 K with a functional dependence resembling the saturation magnetization $M_{\text{net}}(T)$ of YIG and then sharply drops and vanishes already 50 K below the Curie temperature T_C. We speculated that the origin of this feature is the formation of an interfacial layer with a different (lower) Curie temperature. The MMR increased from 300 K up to 450 K following a power law T^α with α changing from $\alpha = 3/2$ at room temperature to $\alpha = 1/2$ at 450 K. We attributed this change to the increasing population of thermally excited magnons and the ensuing reduction of the magnon diffusion length. Above 450 K, the MMR decreased rapidly and vanishes above 510 K, similar to the SMR. Additionally, a magnetic field orientation independent non-local offset voltage was observed above 470 K.

Finally, we studied the exact evolution of this non-local offset signal with temperature. In contrast to the approach commonly taken in literature, where the power density (i.e. the local drive current) is increased to heat the device, we heated the full YIG/Pt heterostructure in steady state. By utilizing this approach, we show that the non-local offset voltage likely only arises from a finite conductivity of the YIG films at high temperatures, giving rise to electronic leakage currents from the injector to the detector. Furthermore, we found that the sample undergoes irreversible changes when heated to above 450 K due to spurious annealing or interdiffusion effects. This puts a firm upper boundary on the operating conditions of any device using YIG/Pt heterostructures for applications. Taken together, the results presented here conclusively resolve the open discussion about the nature of the puzzling field independent non-local transport signature reported in Ref. [136].

Chapter 5

LOCAL AND NON-LOCAL SPIN SEEBECK EFFECT IN Cr_2O_3/PT HETEROSTRUCTURES

As already discussed in the previous Ch. 4, non-local transport measurements allow to experimentally access the nature of the spin angular momentum transport in magnetic insulators. Recently, non-local spin angular momentum transport was observed even in antiferromagnetic insulators, where one naively expects that it should not be possible due to the absence of low energy magnons.[76,180] However, the spin angular momentum transfer can still be mediated by (higher energy) antiferromagnetic magnons.[60,76,87,181,182] It was shown, that these antiferromagnetic magnons can only be excited for a given alignment of the spin Hall spin accumulation in the normal metal and the antiferromagnetic sublattices. In particular, the individual magnetic sublattices of the adjacent antiferromagnetic insulator need to be aligned with the spin polarization of the spin accumulation.[76]

Additionally, recent developments suggested that spin angular momentum transport should also be possible by spin superfluid transport, imposing a different requirement on the alignment of the magnetic sublattices.[60,183,184] In particular, spin angular momentum transport should be possible with the magnetization residing in a magnetic easy plane perpendicular to the spin accumulation in the normal metal. First experimental work in Ref. [60] showed that it is possible to detect the signatures of such spin superfluid transport using the second harmonic (i.e. thermally generated) non-local transport response in heterostructures of the antiferromagnetic insulator Cr_2O_3 and Pt. In this chapter, we will try to verify the signatures put forward in Ref. [60] by performing similar non-local transport measurements in Cr_2O_3/Pt heterostructures. To provide some orientation for the reader, however, first an overview over the salient features of spin superfluid transport is presented, before we critically compare our results to the findings in Ref. [60].

Spin Superfluidity

To introduced the concept of spin superfluidity in the context of non-local spin transport experiments, we consider a configuration as depicted in Fig. 5.1:[1] An easy plane antiferromagnetic insulator (AFMI) is sandwiched between two normal metal electrodes, where the **j**-**n**-plane corresponds to the easy plane of the AFMI. On the left NM/AFMI interface, a spin accumulation generated via the spin Hall effect in the NM is present. This spin accumulation **s** can then give rise to a small canting of the two magnetic sublattices $\mathbf{m}^\alpha$ and $\mathbf{m}^\beta$ towards the **t** direction (i.e. perpendicular to the paper plane). Consequently, both sublattices will start to precess around the **t** direction in the easy plane.[184] In this case, the **t** component of the two magnetizations (where the sum $m_\mathrm{t} = (\mathbf{m}^\alpha)_\mathrm{t} + (\mathbf{m}^\beta)_\mathrm{t}$ corresponds to the net magnetization) can be identified as the spin superfluid density and the angle of $\mathbf{m}^{\alpha,\beta}$ with respect to **j** as the phase φ of the wave function.[183,184] The precessing sublattice magnetization can then excite a non-equilibrium spin accumulation also in the right NM/AFMI interface, so that an electric current is generated via the inverse spin Hall effect there. Thus, in the absence of anisotropy in the **j**-**n**-plane coherent transport of the spin component perpendicular to that plane (i.e. the **t** component) is possible. In analogy to superconductivity, this superfluid spin current is not driven by a potential difference but by a phase gradient $\nabla\varphi$ of the wave function of the condensate.[138] Please note, that in contrast to the (DC) charge supercurrent in a superconductor, a superfluid spin current is not dissipiationless as long as the spin is not conserved.[183] In particular, in the case of low damping (i.e. with the dimensionless Gilbert damping constant $\alpha \ll 1$), a linear decrease of the superfluid spin current is expected for an increasing thickness of the AFMI layer (i.e. for larger separations of the two NM electrodes).[183,184] Consequently, a decay of the (non-local) current detected on the right wire as a function of the separation d_nl of the two NM electrodes $J_\mathrm{c,out} \propto 1/(l_\mathrm{m} + d_\mathrm{nl})$ is found, where $l_\mathrm{m} \propto \alpha^{-1}$ is the characteristic decay length of the superfluid spin current in the AFMI.[184]
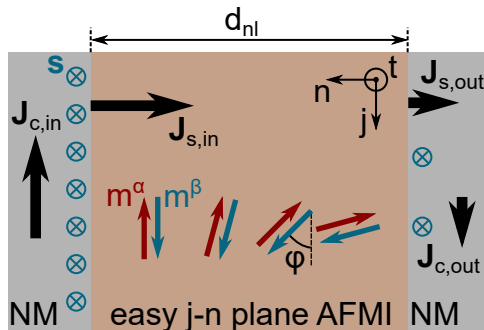

Figure 5.1: An easy **j**-**n**-plane antiferromagnetic insulator is sandwiched between two normal metal electrodes. A spin accumulation **s** along **t** (perpendicular to the easy plane) in the left NM electrode gives rise to a finite component of $\mathbf{m}^{\alpha,\beta}$ along **t**. Consequently, $\mathbf{m}^{\alpha,\beta}$ start precessing around **t** and the system can be consistently described by a phase φ and a spin superfluid density (proportional to the component of $\mathbf{m}^{\alpha,\beta}$ along **t**). The spin is thus transported from the left NM electrode to the right NM electrode and can be detected there electrically via the inverse spin Hall effect. Please note, that the (superfluid) spin current is driven by a phase gradient $\nabla\varphi$, in analogy to the electric supercurrent in a superconductor.[138] After Refs. [184] and [183].

---

[1]Please note, that a vertical stack is chosen for this discussion in contrast to the lateral stack used for the experiments, to be able to better depict the mechanism of the spin transport.

In real antiferromagnets, the anisotropy will be non-zero even within the easy plane, so that the above discussion cannot be directly applied there.[183] For finite anisotropies the spin accumulation **s** along **t** cannot generate magnons (since both magnetic sublattices are perpendicular to **s**, c.f. Sec. 1.3.2), so that no superfluid spin transport should be observed. However, if a sufficiently large spin accumulation is present, the energy barrier associated with the anisotropy within the **j-n**-plane can be overcome.[183] Thus, a critical electric current density J_{crit} (which generates the critical spin accumulation via the spin Hall effect) can be found, which is sufficient to overcome the energy barrier. Consequently, if an electric current density $J_c > J_{crit}$ is applied, superfluid spin transport can be observed even for finite anisotropies, where J_{crit} is proportional to the strength of the anisotropy.[183] An alternative way to lower the energy barrier is to apply a magnetic field, such that the Zeeman energy compensates the anisotropy energy.[183] Thus, for example if there would be an easy magnetic axis for $\mathbf{m}^{\alpha,\beta}$ along **t**, a sufficiently large magnetic field applied along the easy axis can lead to a spin flop, where $\mathbf{m}^{\alpha,\beta}$ align perpendicular to the magnetic field (i.e. reside in the **j-n**-plane).[185] In this configuration, the **j-n**-plane is then an easy plane for $\mathbf{m}^{\alpha,\beta}$, so that superfluid spin transport as discussed above (c.f. Fig. 5.1) should again be possible.

In summary, we find the following salient features for superfluid spin transport in a NM/AFMI/NM heterostructure:[183,184] First, a magnetic easy plane in the direction perpendicular to the spin accumulation is required. Second, if an additional anisotropy is present within this plane, a critical current for the onset of superfluid spin transport can be found, which is proportional to the energy barrier presented by this anisotropy. Alternatively, the anisotropy can be canceled using external magnetic fields. Third, a much slower decay of the non-local transport response is expected in the presence of a superfluid spin transport, where the non-local transport response would evolve $\propto 1/(l_m + d_{nl})$ as a function of the superfluid decay length l_m and the separation d_{nl} of the two NM electrodes.

Sample and Measurement Details

The Cr_2O_3/Pt heterostructures were prepared by Tobias Kosub (Helmholtz-Zentrum Dresden Rossendorf) by sputter deposition in an ultra high vacuum cluster on c-cut Al_2O_3 substrates, so that an out-of-plane easy axis of the Néel vector is realized.[147,148] Please note, that we should be unable to observe any features of the spin superfluid ground state in this geometry (except for large current densities), as an isotropic plane with respect to rotations of the Néel vector perpendicular the direction of the spin accumulation **t** is required (see above).[184,186] In our case, the easy axis is within the **j-n**-plane, so that this condition is not fulfilled. Nevertheless, even for this geometry, Yuan et al. argue with a spin superfluid ground state, so that the experimental results can be at least compared. For further details on the exact growth conditions please refer to Sec. 3.2 (second series **S2**). After growth, the sample was patterned by Tommy Schönherr (Helmholtz-Zentrum Dresden Rossendorf) using electron beam lithography and Ar ion milling to allow injector-detector separations down to 400 nm. The two parallel Pt wires (c.f. Fig. 4.1b)

have a length $l = 150\,\mu\text{m}$, a width $w = 500\,\text{nm}$ and a thickness of $t_{\text{Pt}} = 3\,\text{nm}$.

We measured the electric response as introduced in Sec. 2.6, using a current $I_{\text{s}} = 150\,\mu\text{A}$ if not noted otherwise. In the linear response (antisymmetric current) no non-local magnetotransport signature (c.f. Ch. 4) could be identified at any temperature or magnetic field. This is the expected behavior in the absence of spin superfluidity, as both magnetic sublattices are mostly aligned along the easy axis and thus perpendicular to the film plane. Consequently, the spin accumulation at the Pt interface is also perpendicular to the two magnetic sublattices, so that a direct generation of magnons should not be possible (c.f. Sec. 1.3.2 and Ch. 4).[76] However, as discussed above, if superfluid spin transport would be realized, such transport should still be possible. Thus, we find the absence of a non-local transport signature in the linear response to be very surprising, especially in the lights of the interpretation put forwards by Yuan et al. in Ref. [60]. The same phenomenology was also reported for the measurements in Cr_2O_3/Pt heterostructures shown in Ref. [60], where even for the Néel order aligned with the spin accumulation no contributions with linear response were observed in the non-local transport response.

Anyway, as no antisymmetric contribution is present in the voltage, only the part of the observed voltage symmetric in current

$$V^{\text{s}} = \frac{V(+I) + V(-I)}{2} \tag{5.1}$$

is discussed in this chapter (c.f. Sec. 2.6). V^{s} most importantly contains the spin Seebeck effect generated by thermal gradients in the vicinity of the local and non-local electrodes (c.f. Sec. 1.3.3).[45,72,82,187]
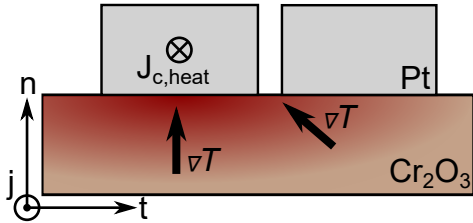

Figure 5.2: A sketch of the experimental geometry is shown here: The left Pt wire (the local wire) is heated using a large electric current. From the local wire, the heat then diffuses down- and outwards into the Cr_2O_3 layer. Consequently, $\nabla T \parallel \mathbf{n}$ below the local wire, while below the right (non-local) wire, ∇T has an additional in-plane component.

Before turning to the measurements, a brief summary of the important contributions to the local and non-local voltage is presented in the following. As introduced in Sec. 1.3.3, antiferromagnetic insulator/normal metal heterostructures are expected to show a spin Seebeck effect which is dependent on the magnetic field induced (net) magnetization $\mathbf{M} = \chi\mathbf{H}$, where $\mathbf{H}$ is the external magnetic field and χ is the magnetic susceptibility. Additionally, Pt (as most metals) is expected to exhibit an ordinary Nernst effect as introduced in Sec. 1.3.4 which has the same symmetry as the antiferromagnetic spin Seebeck effect with respect to the directions of the magnetic field and the thermal gradient. Thus the Nernst effect cannot be directly distinguished from the spin Seebeck effect.[188] We will now address the experimental geometry to establish the directions of the thermal gradients and then discuss the ensuing signatures in the transport measurements. To that end, a sketch of the heat distribution when one of the Pt wires of the non-local devices is

heated is shown in Fig. 5.2. The heat will flow from the hot Pt wire (i.e. the local wire) down- and outwards into the Cr_2O_3 layer. Consequently, while the thermal gradient below the local wire is along the surface normal ($\nabla T \parallel \mathbf{n}$), the thermal gradient below the non-local wire has an additional in-plane component along $\mathbf{t}$. With this temperature distribution in mind, we expect the local voltage V^s_{loc} to be proportional to the $\mathbf{t}$ component of the net magnetization (for the spin Seebeck effect) or the magnetic field (for the Nernst effect).[82,188]

$$V^s_{loc} \propto M_t \text{ or } H_t, \tag{5.2}$$

where M_t (H_t) is the projection of the magnetization $\mathbf{M}$ (magnetic field $\mathbf{H}$) on the $\mathbf{t}$ direction. For the non-local wire, the situation is slightly more complicated, as the thermal gradient has two components. Thus, there will be two contributions to the non-local voltage. First, similarly to the local wire the thermal gradient along the surface normal ($\nabla T \parallel \mathbf{n}$) generates[2]

$$V^s_{nl,1} \propto M_t \text{ or } H_t. \tag{5.3}$$

Additionally, the in-plane thermal gradient ($\nabla T \parallel \mathbf{t}$) will give rise to a second voltage contribution

$$V^s_{nl,2} \propto M_n \text{ or } H_n. \tag{5.4}$$

In summary, we expect the local and non-local wire to show a finite voltage due to the spin Seebeck (or Nernst) effect whenever the magnetic field is applied along the $\mathbf{t}$ direction (since $\mathbf{M} = \chi\mathbf{H}$). Additionally, the non-local wire might exhibit an additional voltage when the magnetic field is applied along the $\mathbf{n}$ direction. Finally, a strong temperature dependence of the spin Seebeck effect was reported in similar AFMI/NM heterostructures:[86,87] A strong increase of the observed spin Seebeck amplitudes towards low temperatures is found and they speculate, that the combination of a magnetic field induced splitting of the two antiferromagnetic magnon branches and a low magnon-phonon coupling strength are at the heart of this increase.[87,180,181] Furthermore, above the ordering temperature, only a very small spin Seebeck effect was reported.[86,87]

Results and Discussion

We will start by addressing the full "three dimensional" local and non-local magnetoresistive response, for a range of temperatures around $T_N \sim 310\,\text{K}$.[119] In the corresponding experiments, we rotate the magnetic field $\mu_0 H = 2\,\text{T}$ in the three mutually orthogonal rotation planes introduced in Sec. 2.1 and record the local non-local voltage response (c.f. Fig. 5.3).[3] For the local voltage V^a_{loc} only a very small modulation with the magnetic field orientation is present above the Néel temperature (red symbols) for all three rotation planes. This is the anticipated behavior for Cr_2O_3/Pt in the paramagnetic state, as the spin Seebeck effect was found to be small also in other AFMI/Pt heterostructures above the ordering temperature.[86,87,90] Additionally, the absence of a modulation of V^s_{loc} also

---

[2]Please note, that as the non-local Pt wire is cooler than the Cr_2O_3 layer, the heat flux across the interface and thus the generated voltage there will be opposite compared to the voltage observed on the local wire.

[3]The average voltage (i.e. the voltage averaged over the full rotation) has been subtracted from the data.
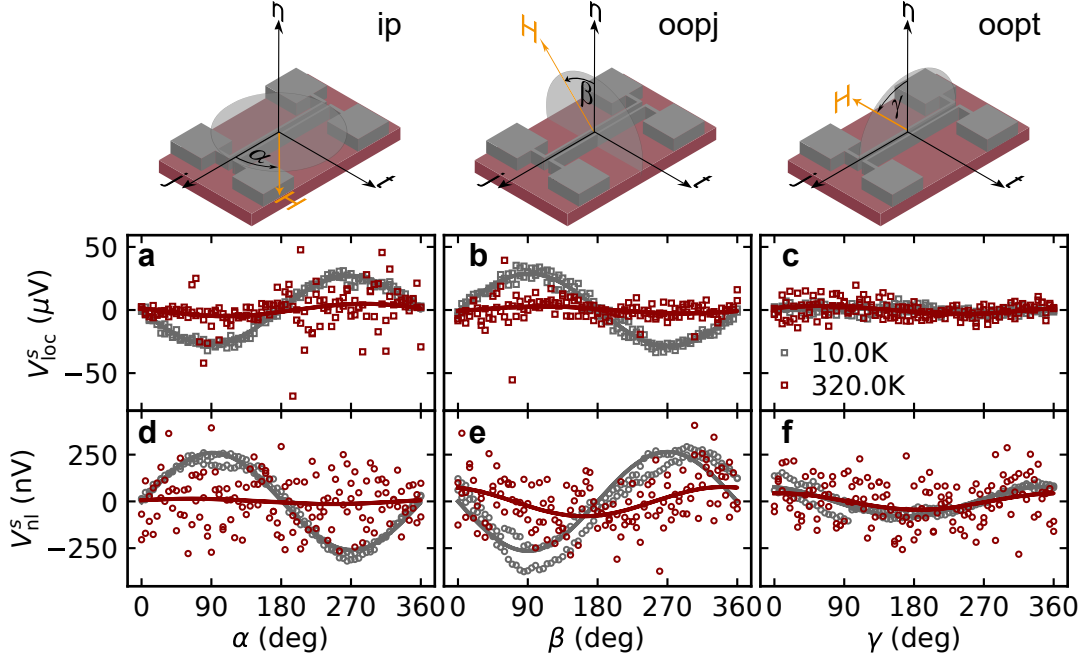
Figure 5.3: Angle resolved measurement of the voltage symmetric in current (i.e. thermal voltage) for above and below the Néel temperature of Cr_2O_3. **a-c** The local voltage only shows a clear modulation for low temperatures and ip (**a**) and oopj (**b**) rotations. The voltage is non-zero when the field induced magnetization M_t along the **t** direction is finite, i.e. has the symmetry expected for a spin Seebeck effect (c.f. Eq. (5.2)). As expected above the Néel temperature in Cr_2O_3/Pt heterostructures, no voltage modulation is observed there.[86,87] **d-f** The same fingerprint but with opposite sign is observed for the non-local signal. The shape and sign of the modulation can be understood considering the non-local thermal gradient is inverted (Pt cooler than Cr_2O_3). **f** In contrast to the local signal, the non-local voltage shows an additional contribution also for the oopt rotation. This can be motivated by considering the thermal landscape (c.f. Fig. 5.2): The heat will flow from the local electrode into any direction of the substrate, so that an additional in-plane thermal gradient is present at the non-local electrode. This in turn gives rise to an additional voltage due to the ordinary Nernst effect in the Pt layer (c.f. Eq. (5.4)). Please note, that the average voltage over the full rotation $\overline{V^s}$ has been subtracted from the data. A magnetic field of $\mu_0 H = 2\,\text{T}$ was used for the measurements.

suggests, that the Nernst effect in Pt due to the out-of-plane gradient and the magnetic field is smaller than our voltage resolution and thus can be neglected (c.f. Eq. (5.2)). If the temperature is lowered to below T_N, however, a clear $\sin(\alpha)$ and $\sin(\beta)$ modulation is visible (Fig. 5.3a and b). This again agrees with the behavior expected for the spin Seebeck effect in AFMI/NM heterostructures: The component of the induced magnetization M_t along **t** gives rise to the spin Seebeck effect in our Cr_2O_3/Pt heterostructure. Additionally, the signal is expected to increase towards lower temperatures.[86,87] This is further corroborated by the oopt measurements (Fig. 5.3c), where no modulation is observed (c.f. Eq. (5.2)). We thus conclude that the modulation of V^s_{loc} is generated by the

antiferromagnetic spin Seebeck effect and that the contribution of the Nernst effect is negligible.[76,86,87]

For the non-local voltage V_{nl}^s, a slightly different behavior is observed: While for the in-plane rotation (Fig. 5.3d) no modulation is evident above T_N, a modulation is visible for the other two rotation planes (Fig. 5.3e and f). As discussed above, this can be understood when considering the thermal landscape of the experiment (c.f. Fig. 5.2): The additional in-plane thermal gradient below the non-local Pt electrode can give rise to additional contributions to V_{nl}^s (c.f. Eq. (5.4)) due to the spin Seebeck or Nernst effect generated by the components of the magnetization or magnetic field along $\mathbf{n}$. As the non-local voltage modulation for the oopt rotation above and below T_N are similar, we conclude that additional contribution is likely caused by the ordinary Nernst effect in Pt.[4] Below T_N, V_{nl}^s exhibits a very similar behavior as V_{loc}^s, where a maximum or minimum voltage can be seen for $\mathbf{H} \parallel \mathbf{t}$. Please note, that the signs of the local and non-local voltage below T_N agrees if the spin Seebeck effect is the origin of the signals: As the thermal gradient direction on the local wire (Pt hotter than Cr$_2$O$_3$) and the non-local wire (Pt colder than Cr$_2$O$_3$) is opposite, this behavior can be expected only, if the local temperature gradients (or spin chemical potentials) contribute. In contrast, a bulk spin Seebeck effect as put forward by Shan et al. in Ref. [71] cannot explain the signal: For the bulk spin Seebeck effect, the $\nabla T \parallel \mathbf{n}$ leads to a depletion of magnons at the upper interface by a thermal drag effect, such that the spin chemical potential at the Cr$_2$O$_3$/Pt interface (and thus the spin current) inverts (i.e. a spin current flows from Pt into Cr$_2$O$_3$ and not vice-versa).[71] Since the Cr$_2$O$_3$ is thinner than the separation of the injector and detector, the absence of a bulk spin Seebeck effect in the sense of Ref. [71] is consistent with the observations in YIG/Pt heterostructures.

Consequently, we have evidence that the local and non-local voltages are dominantly generated by the antiferromagnetic spin Seebeck effect as the salient features agree with its reported behavior.[76,86–88,181] In particular, we only observe a large spin Seebeck response below T_N. Please note, that there are also recent reports of a spin Seebeck effect proportional to to the Néel vector.[92] In our measurement configuration, the Néel vector (i.e. $\mathbf{m}^\alpha - \mathbf{m}^\beta$) points along the surface normal and thus might generate additional contributions owed to the finite in-plane thermal gradients below the non-local electrode. However, as the Néel vector orientation will not change dramatically for an applied magnetic field $\mu_0 H = 2\,\text{T}$, these contribution would only give rise to a constant voltage and no modulation. Thus, such an additional constant offset voltage superposed on the non-local voltage would have been subtracted with the other offset voltages.

In the following, the evolution of the $R_{loc}^s = V_{loc}^s/I_s^2$ and $R_{nl}^s = R_{loc}^s/I_s^2$ with temperature will be illustrated and discussed.[5] To this end, angular scans of the magnetic field

---

[4] The contribution of the Nernst effect due to the in-plane thermal gradient can be significantly larger than its contribution due to the out-of-plane gradient. This can be motivated in an easy way when considering the geometry: Along the out-of-plane direction, no thermal sink on top of the Pt is available (the heat can only be lost by radiation), such that a possible temperature difference between the hot and cold side is small. In contrast, for the in-plane thermal gradient, a much larger temperature difference between the hot and cold side of the Pt electrode can be achieved as the lateral heat transport through the Cr$_2$O$_3$ is much more efficient.

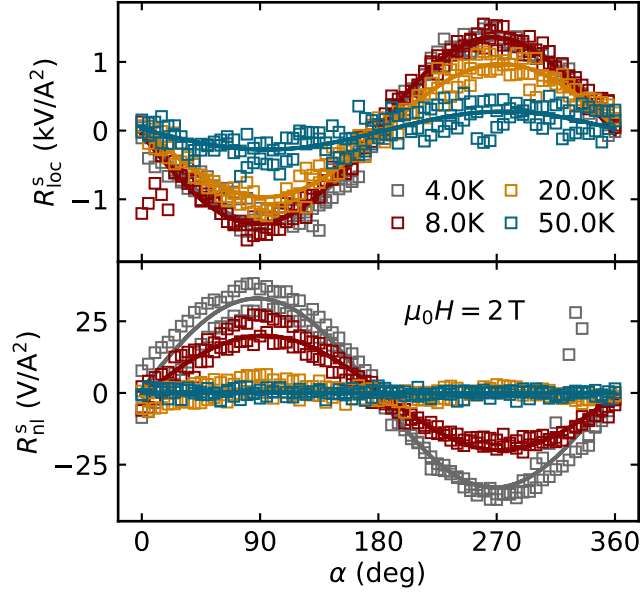[5] Please note that the voltages were normalized to allow for a better comparability with the results pre-

Figure 5.4: Angle resolved measurements of $R_{\mathrm{loc}}^{\mathrm{s}} = V_{\mathrm{loc}}^{\mathrm{s}}/I_{\mathrm{s}}^2$ and $R_{\mathrm{nl}}^{\mathrm{s}} = R_{\mathrm{loc}}^{\mathrm{s}}/I_{\mathrm{s}}^2$ are shown here for several temperatures. A clear increase of the modulation amplitude in both panels is evident towards lower temperatures. Please note, that the average over the full rotation $\overline{R^{\mathrm{s}}}$ has been subtracted.

within the sample plane were performed at several temperatures. The resulting signals are shown in Fig. 5.4 for selected temperatures. In-plane rotations were chosen, as here the additional contributions associated to the in-plane thermal gradient are not superimposed on the non-local voltage (c.f. Eq. (5.4) and Fig. 5.3). A significant change of the spin Seebeck effect as a function of temperature is evident from the data: The modulation of $R_{\mathrm{loc}}^{\mathrm{s}}$ increases when lowering the temperature from 50 K to 8 K and seems saturated for $T \lesssim 8\,\mathrm{K}$. In contrast, the angular modulation of $R_{\mathrm{nl}}^{\mathrm{s}}$, while also increasing for lower temperatures, shows no modulation at 50 K and no clear saturating behavior. To better compare the evolution of the amplitudes of the spin Seebeck effect, they were extracted using a $\sin(\alpha)$ fit (c.f. Fig. 5.5).

A very similar general dependence of the local ($\Delta R_{\mathrm{loc}}^{\mathrm{s}}$) and non-local ($\Delta R_{\mathrm{nl}}^{\mathrm{s}}$) spin Seebeck effect on temperature can be found. Namely, a saturating behavior for low temperatures and a vanishing spin Seebeck effect towards high temperatures. Interestingly, a significant difference in the temperatures where the local and non-local spin Seebeck effect saturates and where they vanish are observed: $\Delta R_{\mathrm{loc}}^{\mathrm{s}}$ saturates already below 10 K, while the non-local modulation is saturating only towards 5 K. Similarly, also the temperature where the spin Seebeck effect vanishes is shifted towards higher temperatures for the local electrode. $\Delta R_{\mathrm{loc}}^{\mathrm{s}}$ vanishes at around 100 K compared to 20 K for $\Delta R_{\mathrm{nl}}^{\mathrm{s}}$. This suggests

---

sented in Ref. [60]. To also correct for the geometry between the experiments, their data have to be multiplied with an additional factor of 1.5.

Figure 5.5: The amplitudes of the sin(α) modulation observed in $R_{\mathrm{loc}}^{\mathrm{s}}$ and $R_{\mathrm{nl}}^{\mathrm{s}}$, i.e. the spin Seebeck effect amplitudes, are summarized here. A clear increase of the spin Seebeck effect for lower temperatures can be observed. Interestingly, the local spin Seebeck effect saturates already at 10 K, while the non-local spin Seebeck effect saturates only around 5 K. The measurements were done at a magnetic field $\mu_0 H = 2$ T.
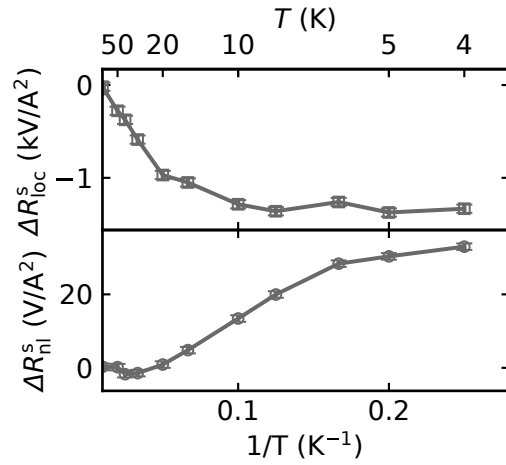
that although the general trends are consistent, the mechanism relevant for the local and non-local spin Seebeck effect might not be exactly the same (or include additional temperature dependences from heat or spin diffusion processes). So far, the exact nature of the increase of the thermal signal for low temperatures is not fully resolved: In Ref. [60] the saturation is associated with a spin-superfluid ground state in the antiferromagnet, having an onset temperature in the range of 5 K for a spontaneous breaking of the uniaxial symmetry. However, a similar behavior was already observed also in YIG/Pt, where an antiferromagnetic superfluid ground state cannot be realized due to the ferrimagnetic order and the ensuing dipolar coupling,[183] casting doubt on the explanation put forward in Ref. [60].[189] Furthermore, reports for bilayers of the antiferromagnetic insulator MnF$_2$ and Pt find a similar behavior. However, in these samples the spin Seebeck signal (corresponding to the local spin Seebeck effect discussed here) decreases again for very low temperatures ($T \lesssim 5$ K).[87] Please note, that the current driven ($P \lesssim 1$ mW) in the local electrode increases the temperature of the sample surface with respect to the base temperature of the measuring insert. Thus, we cannot exclude that the temperature of the device itself is actually higher and that the signal drops again for very low temperatures.

To further elucidate the mechanism of spin transport, we performed systematic measurements of the local and non-local spin Seebeck effect as a function of the magnetic field strength (c.f. Fig. 5.6). Similarly to the reports in Ref. [60] for Cr$_2$O$_3$/Pt with the same geometry (i.e. easy axis along the surface normal) we find an increase of $R_{\mathrm{loc}}^{\mathrm{s}}$ and $R_{\mathrm{nl}}^{\mathrm{s}}$ for increasing magnetic fields. However, a fully linear trend is reported there up to 9 T, while in our case a non-linear dependence on the magnetic field is found. This is unexpected, as the applied magnetic field is small compared to the exchange field (the leading exchange constant reported in literature is $J/k_{\mathrm{B}} \sim 87$ K corresponding to ~ 130 T).[6][190] However, if there is a small uncompensated moment in Cr$_2$O$_3$ e.g. due to dislocations,[147,156] this will give rise to an additional Zeeman energy contribution which can alter the response

---

[6]This can be roughly motivated when considering the exchange energy $g\mu_{\mathrm{B}}S\mu_0 H_{\mathrm{ex}}/k_{\mathrm{B}} \sim 440$ K with $S = 5/2$ and $g = 2$ very roughly agrees with $T_{\mathrm{N}} \sim 300$ K.[119,190] Please note, that this is only the leading exchange constant, so that further corrections have to accounted for to yield an exact value.

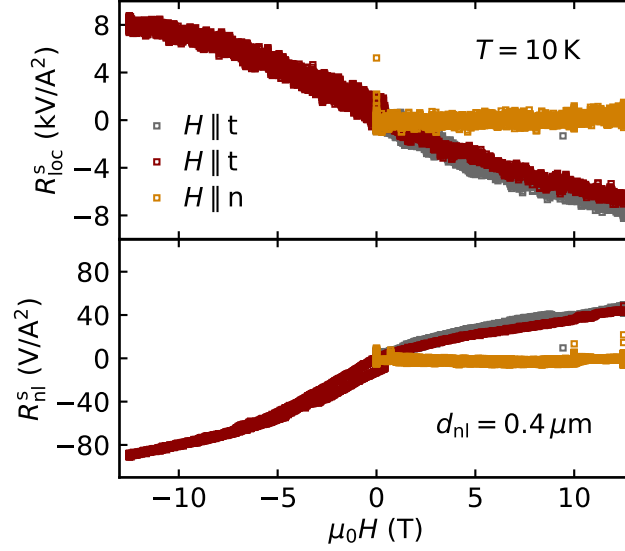Figure 5.6: R^s_{loc} and R^s_{nl} as a function of the applied magnetic field are shown here. All data were measured at 10 K. A clear increase of the local and non-local spin Seebeck effect is evident for increasing magnetic fields. Interestingly, although the local and non-local spin Seebeck effect does not increase when further lower the temperature (c.f. Fig. 5.5), increasing the magnetic field increases the spin Seebeck effect. While a strong magnetic field dependence is observed for the local and non-local spin Seebeck effect, no significant field-related change is evident when the magnetic field applied along the surface normal ($\mathbf{H} \parallel \mathbf{n}$), perpendicular to the transverse direction. Please note, that although an offset signal was subtracted (same offset for all curves in one panel), additional spurious thermoelectric voltages generated within the cryostat (which can also be field dependent), can be superimposed on the magnetic field dependence of the sample.

of the two magnetic sublattices when a magnetic field is applied (c.f. Sec. 3.2). Such an uncompensated moment is additionally supported by the fact that we do not observe any signatures of a spin flop in our Cr_2O_3 samples (c.f. Sec. 3.2). Interestingly, R^s_{loc} and R^s_{nl} increase beyond the respective saturation values observed in Fig. 5.6 ($\Delta R^s_{loc,sat} \sim 1.3\,kV/A^2$ and $\Delta R^s_{loc,sat} \sim 35\,V/A^2$), again indicating that the spin Seebeck effect is dependent on the field induced net magnetization M_t. To motive this, we consider the susceptibility of an ideal uniaxial antiferromagnet with the easy axis along the $\mathbf{n}$ direction: The susceptibility is non-zero and independent of temperature for magnetic fields applied perpendicular to the easy axis (as is the case with $\mathbf{H} \parallel \mathbf{t}$).[119] Consequently, while the induced magnetization $\mathbf{M}$ cannot be increased by lowering the temperature for fixed magnetic fields, it can be increased by applying higher magnetic fields ($\mathbf{M} = \chi\mathbf{H}$). We note, however, that in the superfluid spin current model, such an increase of the spin Seebeck effect can also be rationalized. In this scenario, the spin Seebeck effect is associated with the superfluid spin density, which is also proportional to the net magnetization perpendicular to the $\mathbf{j}$-$\mathbf{t}$

plane, i.e. M_t.[60,183,184] Consequently, it is not possible to draw final conclusions about the microscopic mechanism from the field dependence of the local and non-local spin Seebeck effect, as both, the net magnetization and the canting angle (in the superfluid scenario) are directly proportional (for small angles).
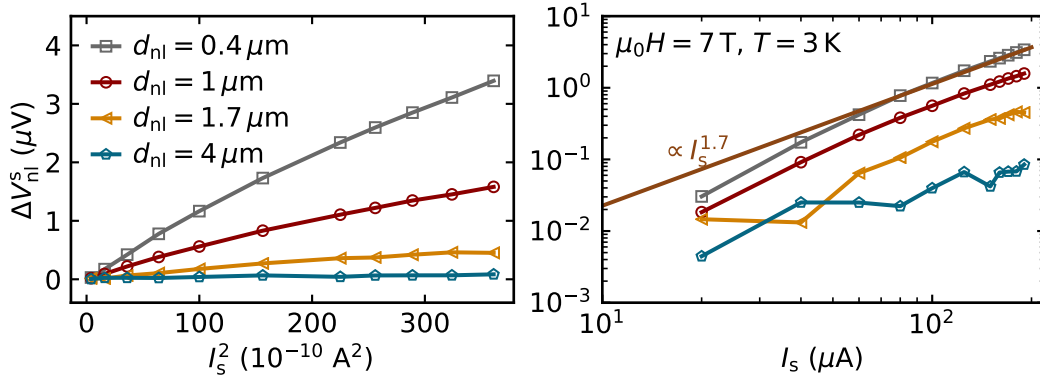

Figure 5.7:   The evolution of the non-local spin Seebeck effect as a function of the applied electric current is shown here for several different injector-detector separations d_{nl}. Although one would expect a linear increase of the voltage with the applied power (i.e. $\Delta V_{nl}^s \propto I_s^2$), we observe $\Delta V_{nl}^s \propto I_s^{1.7}$.

To address the possible existence of a condensate, we now turn to the dependence of the non-local spin Seebeck effect on the magnitude of the applied current measured at $\mu_0 H = 7\,T$ at $3\,K$. In Ref. [60], a threshold current density $j_{AC}^c \sim 1.2 \times 10^{11}\,A/m^2$ is reported for Cr_2O_3/Pt heterostructures[7] which is required to overcome the anisotropy and induce the spin-superfluid ground state. This corresponds closely to the maximum current applied here, where $I_s \sim 180\,\mu A \rightarrow j_s \sim 1.2 \times 10^{11}\,A/m^2$, so that we cannot say for certain, whether we are applying a sufficient current $I_s > I_c$ (where I_c should be similar as in Ref. [60] since the same material system is used). Anyway, no threshold current can be observed in our data, summarized in Fig. 5.8. Thus, this either suggests, that we did not apply a sufficiently large current to overcome the threshold,[8] or that no superfluid transport regime is accessible in our sample. Interestingly we find a scaling $\Delta V_{nl}^s \propto I_s^{1.7}$ for the non-local voltage amplitude (c.f. Fig. 5.7). As the non-local spin Seebeck effect is driven by Joule heating and the consequently arising temperature gradients, one would anticipate a scaling like $\Delta V_{nl} \propto \nabla T \propto I_s^2$. The deviation from the expected behavior might be rooted in the strong temperature dependence of ΔV_{nl}^s: If the current is increased, the sample is locally heated to a higher temperature than the base temperature of the measuring insert. As already a temperature increase of $2\,K$ will give rise to a significant

---

[7]Please note, that it is not stated in Ref. [60], whether I_{AC} refers to the root mean square, the peak amplitude or the peak-peak amplitude of the current, so that a comparison is challenging. However, judging from their methods section, the peak value is most likely, so that the average current is actually lower by a factor $\sqrt{2}$.

[8]We did not increase the current beyond $I_s = 180\,\mu A$ to prevent damage to the devices during this measurement run.

change of the non-local spin Seebeck effect (c.f. Fig. 5.5), the local heating might lead to an additional suppression of ΔV_{nl}^s for higher currents. In conjunction with the temperature dependence, the scaling of $\Delta V_{nl}^s \propto I_s^{1.7}$ is a good indicator that the sample surface is heated significantly with respect to the base temperature. This in turn would explain the absence of the drop of the spin Seebeck effect reported in Ref. [87] in our sample.
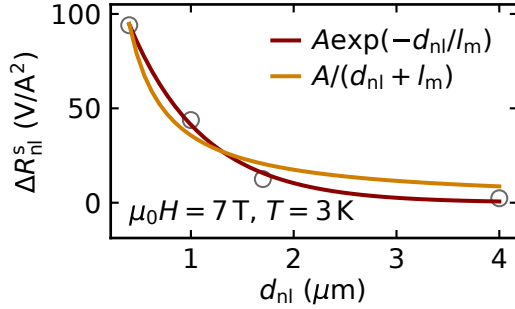

Figure 5.8: The evolution of the non-local spin Seebeck effect as a function of the injector-detector separation is shown here, measured with an applied magnetic field of $\mu_0 H = 7\,T$ at $3\,K$. Although a $(d_{nl} + l_m)^{-1}$ decay for ΔR_{nl}^s is reported in Ref. [60] (turmeric fit), our data is best described by a simple exponential decay (red line). In contrast to Yuan et al.,[60] we find a characteristic decay length of $l_m \sim 500\,nm$ and not $l_m \sim 10\,\mu m$.

Finally, we turn to the evolution of the non-local spin Seebeck effect as a function of the injector-detector separation d_{nl}: We find a simple exponential decay of the ΔR_{nl}^s (red line) fits to the observed decay best. We cannot reproduce the low temperature behavior reported by Yuan et al.,[60] where they find a $(d_{nl} + l_m)^{-1}$ decay which they describe as the smoking gun proof for the spin-superfluid ground state. Additionally, a significantly lower decay length $l_s \sim 500\,nm$ is observed here compared to $l_m \sim 10\,\mu m$ reported in Ref. [60]. However, the extraction of the magnon coherence length from the thermal signal is not trivial, since the signal depends crucially on the exact distribution of temperatures in the material. One might argue, that similar to reports in YIG/Pt there are two regimes governing the decay of the non-local spin Seebeck effect: In YIG/Pt and for small injector-detector separations, the decay is governed by drift, while for large injector-detector separations it is governed by diffusion.[45,71,72,191] However, in our case, the exponential decay with the injector-detector distance already suggests a diffusion process, which should change to the $\Delta R_{nl}^s \propto (d_{nl} + l_m)^{-1}$ decay for large separations. Since we only studied four injector-detector separations so far,[9] such a cross-over cannot be distinguished in our data. Anyway, also in other antiferromagnets, a dominantly diffusion driven non-local spin Seebeck effect was observed, consistent with being generated by the induced magnetization.[76] Another interesting finding is, that the order of magnitude of $l_m \sim 500\,nm$ roughly in agreement with the structural domain size reported for similar Cr_2O_3 samples,[156] suggesting that transport over domain boundaries is not efficient for antiferromagnets. This fact is further corroborated by measurements of the magnon-mediated magnetoresistance in γ-Fe_2O_3/Pt heterostructures, where a strong dependence of the decay length on the size of the antiferromagnetic domains is found.[192]

---

[9]Although there are more devices with different injector-detector separations available on the sample, only these four devices could be investigated so far due to limited measurement time.

Summary

In this chapter measurements of the thermally driven local and non-local spin Seebeck effect in a Cr_2O_3/Pt heterostructure were presented. We could reproduced most salient features reported in similar samples by Yuan et al. in Ref. [60]. In particular, we found a local and non-local spin Seebeck effect $\Delta R^s_{\text{loc/nl}}$ increasing drastically for $T \lesssim 50\,\text{K}$ and saturating below $T \lesssim 5\,\text{K}$ (c.f. Fig. 5.5). Furthermore, the local and non-local spin Seebeck effect increased for higher magnetic field strength (c.f. Fig. 5.6).

Yuan et al. in Ref. [60] explain all these features by claiming superfluid spin transport through Cr_2O_3, where the damping of the excitations mediating the non-local spin Seebeck effect is extremely lowered.[183,184] Assuming this model, a distinct decay of the non-local spin Seebeck effect for increasing injector-detector separation is excepted, where $\Delta R^s_{\text{nl}} \propto (d_{\text{nl}} + l_{\text{m}})^{-1}$. However, we cannot reproduce any of the smoking gun features put forward for detecting spin superfluidity in our sample: Neither is there a critical current density, below which the non-local transport is suppressed, nor do we observe the $\Delta R^s_{\text{nl}} \propto (d_{\text{nl}} + l_{\text{m}})^{-1}$ decay as put forward by Yuan et al. in Ref. [60] for the superfluid transport regime. As such, our data does not corroborate the presence of spin superfluid transport in our Cr_2O_3/Pt heterostructure: All features observed in our sample could be consistently explained, if the local and non-local spin Seebeck effect were to arise due to a magnetic field induced net magnetization.

In summary, we are unable to confirm the experimental signatures for the spin superfluid ground state put forward by Yuan et al. in Ref. [60] at least in our sample. We thus conclude that the "ordinary" non-local spin Seebeck effect, mediated by magnons and the thermal landscape in the antiferromagnetic layer is likely the origin of the observed signatures. However, there are still open questions which have to be addressed, before a final statement can be given: First, it should be clarified why there is only a signature in the spin Seebeck effect, while no such signal can be observed in the magnon-mediated magnetoresistance (i.e. in the linear response). This is a very surprising finding, as the spin species which is injected and detected is identical for the two effects when spin superfluid transport is considered. Second, experiments towards higher current densities should still be carried out to confirm the absence of a critical current even for current densities well beyond what is reported by Yuan et al. in Ref. [60].

Chapter 6

TOPOLOGICAL TRANSPORT FEATURES IN Mn$_{1.8}$PtSn THIN FILMS

Topology is currently emerging as a novel classification scheme for solid state materials.[193–195] Topological properties, for example, of the electronic band structure or the spin system can reflect in the behavior of a material. In particular, the topological properties can be connected to emergent electronic transport phenomena, such as the chiral anomaly or the quantum Hall effect.[55–57,95,193,195–197]

In the field of magnetism, Skyrmions are one example of a topologically non-trivial (chiral) spin texture and can be categorized using an (integer) winding number.[58,110,111,198] It was shown in a major effort, that also in the presence of Skyrmions, additional topological transport features are present in the electronic response:[58,105,106] If an itinerant electron travels through such a spin texture, its spin orientation adiabatically changes, such that it can acquire a Berry phase. This Berry phase in turn can become evident as an additional contribution to the Hall effect, the "topological Hall effect".[58,95,105,109] Even in the absence of Skyrmions, an additional Berry phase can also be acquired in the presence of other non-coplanar sublattice spin configurations, that have a finite scalar spin chirality $\kappa = S_i \cdot (S_j \times S_k)$, between the neighboring spins $S_{i,j,k}$ on the sites i, j, k.[95,109] As such, the microscopic spin configuration and its topology can sensitively reflect in the electronic transport properties, where the latter, in turn, can be used to determine the presence of such non-trivial spin textures.

To that end, robust techniques allowing to separate the topological and the "ordinary" contributions to the transport response are crucial. However, the exact nature and scaling of the topological contributions to the Hall effect are still not fully described in a general fashion. Thus, e.g. the topological Hall signal ρ_{xy}^{THE} is extracted heuristically from the

transverse resistivity

$$\rho_{xy} = R_0 \mu_0 H + R_S M(H) + \rho_{xy}^{\text{THE}}, \tag{6.1}$$

where R_0 is the ordinary Hall coefficient, R_S is the anomalous Hall coefficient and $M(H)$ is the magnetization.[199]

In this chapter we will discuss the Hall effect and the Nernst effect observed in thin films of $Mn_{1.8}PtSn$ as a function of temperature for varying magnetic fields along the surface normal. Additionally, due to its large topological transport response, we will use $Mn_{1.8}PtSn$ as a model system to establish a novel approach to evaluate the presence of additional topological contributions to the transport response. This approach removes the necessity for magnetization measurements, which are a key limitation for measurements on nanopatterned devices. Furthermore, artifacts introduced by the comparison of magnetization and transport measurements can be excluded using our method.

The contents of this chapter are partly reproduced from R. Schlitz et al., Nano Letters, **19**, 2366 (2019) (Ref. [3]) with permission from the American Chemical Society, that owns the copyright.

Sample and Measurement Details

The $Mn_{1.8}PtSn$ thin films with a thickness of 35 nm were grown and characterized by Peter Swekis at the Max-Planck-Institute for Chemical Physics of Solids using magnetron co–sputtering of Mn, Pt and Sn onto (001) oriented MgO substrates. The growth was performed at $T_{\text{substrate}} = 350\,°C$ in Ar atmosphere at a pressure of 3×10^{-3} mbar. The samples were post-annealed after deposition at the growth temperature for another 30 min and capped with a 3 nm thick layer of Al to protect the film from oxidizing. The crystallinity and thickness were determined using X-ray diffraction and reflectometry, respectively. Further details on the growth and crystal structure can be found in Ref. [4].

Together with Helena Reichlova (Technische Universität Dresden), magnetization loops of the as-grown samples were measured in a QuantumDesign MPMS–XL7 SQUID magnetometer for different temperatures which will be addressed during the discussion of the results (c.f. Fig. 6.5).

The samples were patterned using optical lithography and Ar ion milling. To additionally add thermometry and heating capabilities, heater and thermometer microstructures were defined in a lift-off process using 30 nm thick Pt. An optical micrograph of a finished device is shown in Fig. 6.1a. All transport measurements were performed in the vector cryostat described in Sec. 2.4 with a maximum magnetic field $|\mu_0 H_z| \leq 6\,T$ applied along the surface normal. Please note, that only data taken on one device will be discussed in this chapter. However, all findings have been reproduced in a second sample with a similar thickness of $Mn_{1.8}PtSn$ ($t_{\text{MPS}} = 35$ nm).

Our device layout allows to perform Nernst and Hall effect measurements, as depicted in Fig. 6.1b and c, respectively. On the one hand, to measure the magnetoresistive response (including the Hall effect), we drive an electrical current $I_s = 200\,\mu A$ along the Hall bar and measure the longitudinal V_{xx} and transverse V_{xy} voltages utilizing the current reversal method as described in Sec. 2.6. The magnetic field is applied along the **z**
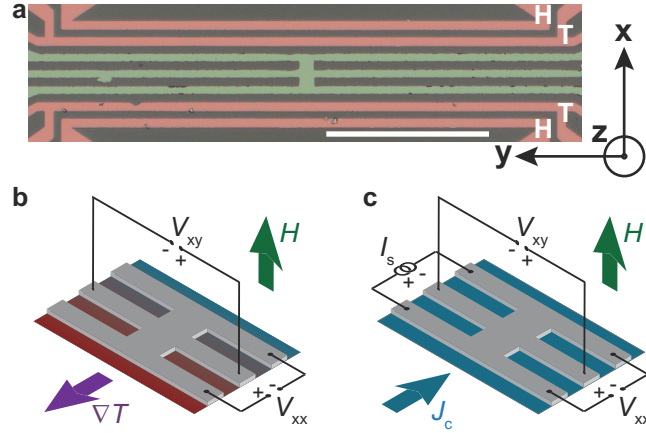
Figure 6.1: **a** A micrograph of a sample is shown. The regions shaded in red are the Pt heaters and thermometers and the highlighted green regions are the Mn$_{1.8}$PtSn Hall bar. Panel **b** and **c** depict the Nernst and Hall measurement scheme including the contact polarities, respectively. Adapted from Ref. [3]

(out-of-plane) axis, so that the Hall effect can be observed along the **y** direction. The transverse resistivity is determined from the voltage using

$$\rho_{xy} = \frac{V_{xy}}{I_s} t_{MPS}, \tag{6.2}$$

with the thickness of the Mn$_{1.8}$PtSn layer $t_{MPS} = 35\,\text{nm}$. On the other hand, the Nernst voltage can be measured by driving a thermal gradient ∇T_x along the x-direction (MgO [100] axis). This thermal gradient is generated by applying a large electric current through one of the Pt heaters above or below the Hall bar. The magnetic field is again applied along the **z** axis, such that the Nernst voltage arises along the **y**-axis and can be picked up by a Keithley 2182 nanovoltmeter (c.f. Sec. 1.3.4). A method for significantly improving the signal to noise ratio of this thermoelectric (Nernst) voltage measurement will be discussed in the next paragraphs.

Accurate measurements of the thermovoltage can be challenging in magnet cryostats due to the large temperature differences between the sample and the measurement devices. As all soldering joints can give rise to additional Seebeck voltages, this can drastically limit the stability of the observed voltages.[93] To mitigate these limitations, we use an on-chip alternating thermal gradient technique. To this end, we alternatingly drive a current $I_H = 5\,\text{mA}$ through the two heaters above ("top") and below ("bottom") the Hall bar (c.f. Fig. 6.1a). This gives rise to a heat flow from top to bottom ($\downarrow$) or from bottom to top ($\uparrow$). We simultaneously monitor the resistance $R_{T,top}$ and $R_{T,bottom}$ of the two Pt thermometers to determine the temperature difference. To obtain the temperatures T_{top} and T_{bottom} and thus the temperature difference from the respective resistances, $R_{T,top}(T)$ and $R_{T,bottom}(T)$ are measured as a function of temperature without the application of heating currents as exemplarily shown in Fig. 6.2a for one of the thermometers. This curve is then

fitted with two different polynomials in the high (red fit) and low (teal fit) temperature region. The combined fit curve is then used as calibration to determine the temperatures from the resistance of the two thermometers. The temperature gradient ∇T_x along the x-direction (MgO [100] axis) can then be inferred by

$$\nabla T_x = \frac{\Delta T(\uparrow) - \Delta T(\downarrow)}{2d_{\text{therm}}}, \tag{6.3}$$

where $d_{\text{therm}} \sim 40\,\mu\text{m}$ is the distance between the thermometers and $\Delta T(\uparrow, \downarrow) = (T_{\text{bottom}} - T_{\text{top}})(\uparrow, \downarrow)$ are the temperature differences between the two thermometers for heat flowing up and down, respectively.
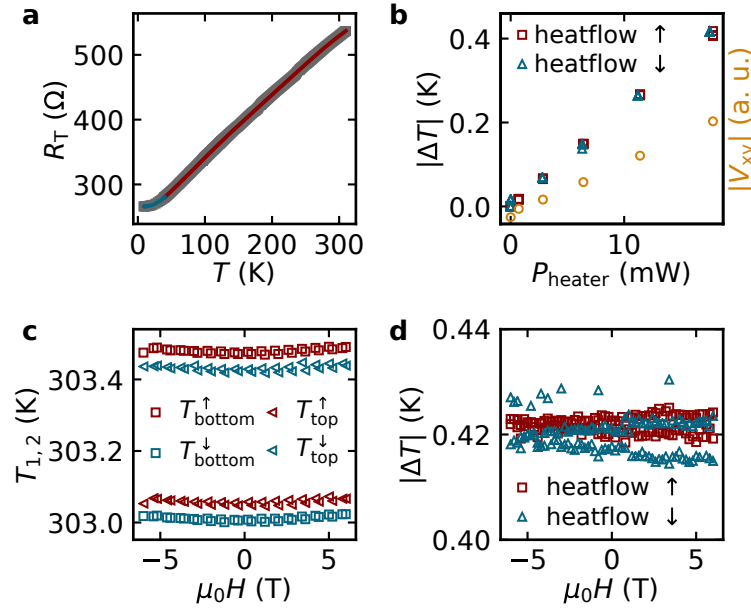
Figure 6.2: **a** The calibration curve for one of the thermometers is depicted. The red and teal fit are used to calculate the temperature for the high and low temperature region, respectively. In panel **b**, the temperature differences for both thermal gradient directions and the transverse voltage are shown. Both scale linearly with the heating power as expected, if they are generated by a thermal effect. The applied magnetic field for this measurement was $\mu_0 H_z = 2\,\text{T}$. Panel **c** summarizes the extracted temperature on the hot and cold side recorded during one magnetic field sweep for the two heat flow directions. Both temperatures (i.e. on the hot and cold side) are similar for both heat flow directions and only show a small modulation with the magnetic field. **d** Similarly, the extracted temperature difference remains mostly independent of the magnetic field, only exhibiting a small linear drift as a function of time. Adapted from Ref. [3].

The temperature difference (and thus the thermal gradient) should linearly increase with the heater power, as long as the thermal conductivity is only weakly dependent on temperature. As thermoelectric effects are $\propto \nabla T$ a linear dependence on the heating power should also be observed. This is verified by applying an increasing heater power

and observing the temperature differences and the Nernst voltage (with a fixed field of $\mu_0 H_z = 2\,\mathrm{T}$). These data are shown in Fig. 6.2b and nicely show the linear trend with the applied bower for both, the temperature difference and the Nernst voltage i.e. $\nabla T \propto P_{\mathrm{heater}}$ and thus $S_{xy} \propto \nabla T \propto P_{\mathrm{heater}}$. Additionally, we can see that the temperature differences for both heat flow directions agree nicely. Even if this fits the expectations for a perfectly symmetric device, seeing it realized in our structure verifies the quality of the lithography as well as the homogeneity of the temperature distribution. Furthermore, a perfectly symmetric thermal gradient upon reversal results in a constant temperature in the central part of the devices (i.e. where we measure the Nernst voltage), so that influences of a different local temperature can be excluded.

Finally, as magnetic field sweeps will be used to determine the Nernst signal, the thermal gradient should ideally be independent of the magnetic field. To establish and quantify a possible field dependence of the extracted temperatures, we measured the temperatures during a magnetic field sweep in the full field range at a base temperature of $300\,\mathrm{K}$. The data depicted in Fig. 6.2c show, that there is a finite dependence of the extracted temperature on the magnetic field, most likely due to the ordinary magnetoresistance of the Pt used as thermometer. However, since the same material is used for both thermometers, the temperature difference is constant to within $10\,\%$ during the field sweep. Please note, that while the magnetoresistance will increase towards lower temperatures ($\sim 10\,\mathrm{K}$), even there the temperature difference is still constant to within $10\,\%$ over the full magnetic field range (as is expected due to the same magnetoresistance in both thermometers). Furthermore, at low temperatures, the quality of the thermometry is much lower anyway, as the slope of $R_{\mathrm{T}}(T)$ is much smaller there (c.f. Fig. 6.2a). Additionally, we observe a slightly higher temperature of the thermometers, compared to the base temperature $300\,\mathrm{K}$ (i.e. the temperature of the measuring insert). This indicates that a steady state heating of the sample surface with respect to the measuring insert is present, which can be easily motivated: If there is a thermal gradient across the device that directly requires an increased temperature of parts of the device with respect to others. As the base temperature corresponds to the temperature of the heat sink (i.e. the thermometry head), the sample surface thus has to be elevated compared to that base temperature. Even the magnitude of this increase is as anticipated: the thickness of the substrate is roughly 10 times larger than the separation of the two thermometers. Thus, also the increase of the base temperature (i.e. the temperature difference from the bottom of the substrate glued to the chip carrier and the sample surface) should be roughly larger by a factor 10 compared to the temperature difference between the thermometers. Taken together, we have established that the generation of the alternating thermal gradient works as anticipated.

We will now discuss the implications of the inversion of the thermal gradient direction on the Nernst signal and the voltage extraction. As the Nernst voltage will flip its sign when ∇T inverts, the measured voltage needs to be anti-symmetrized with respect to the thermal gradient direction. This is accomplished by subtracting the voltages measured for the two thermal gradient directions $V_{xy}(\uparrow)$ and $V_{xy}(\downarrow)$ and dividing by 2. To obtain the Nernst signal $S_{xy} = E_y/\nabla T_x$, we first need to determine the electric field along the **y** direction.[138] As the Nernst effect will only generate a voltage in the region where the

thermal gradient is present (i.e. the length of the $Mn_{1.8}PtSn$ Hall bar which is heated), we use the length of the heaters to approximate the exact profile of the thermal gradient along the **y** direction, so that $E_y \approx V_{xy}/l_H$. Thus, S_{xy} is given by

$$S_{xy} = \frac{V_{xy}(\uparrow) - V_{xy}(\downarrow)}{2l_H \nabla T_x}. \tag{6.4}$$

This approach resembles the electric current reversal method introduced in Sec. 2.6 and allows to remove most of the spurious thermoelectric voltages from the measurement signal.
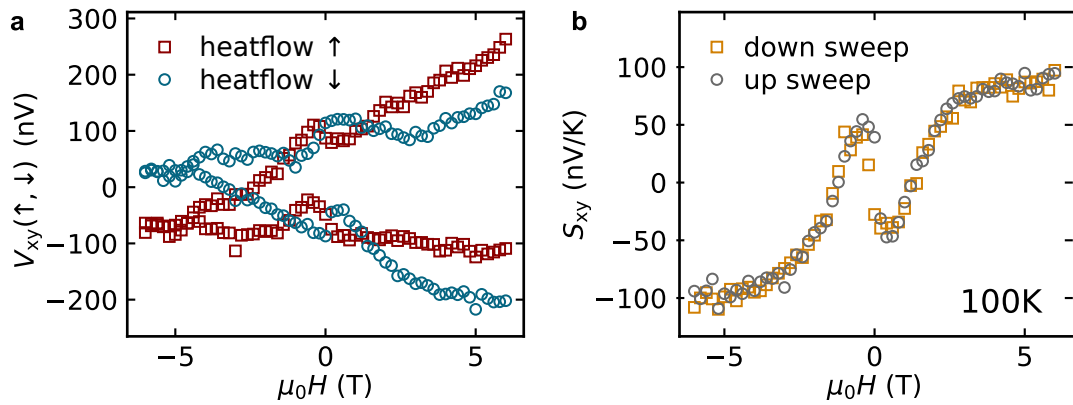
Figure 6.3: **a** The measured voltages for the two thermal gradient directions are depicted. The (anomalous) Nernst response can not be determined due to the presence of significant drifts. However, the difference between the red and teal curves $V_{xy}(\uparrow) - V_{xy}(\downarrow)$ behaves systematically: **b** The anti-symmetrized data (c.f. Eq. (6.4)) show a clear dependence of the magnetic field with the symmetry anticipated for a Nernst effect.

To verify the performance of our method, the raw data $V_{xy}(\uparrow,\downarrow)$ are shown in Fig. 6.3a for the two thermal gradient directions. There is a large, nonlinear drift in the voltage, which is mostly independent on the thermal gradient direction (similar for the teal and red curve). These are most likely caused by changes in the soldering joint temperatures on the measuring inserts inside the cryostat and are present even after long thermal stabilization. No clear magnetic field dependence of the transverse voltage can be established directly from the raw data. However, when looking at the differences between the teal and red curve, a systematic trend can be observed: The teal data is below (above) the red data for positive (negative) saturation. Thus, when calculating the Nernst signal S_{xy} as discussed above, a clear dependence on the magnetic field becomes visible. Additionally, S_{xy} measured during the up and down sweep of the magnetic field are superimposed, suggesting an excellent performance of the thermoelectric signal extraction.

Please note, that care has to be taken to ensure that all temperatures on the sample are settled. This is accomplished by delaying the measurement for a sufficient amount of time after changing the thermal landscape. For the structure used here, a waiting times

of 30 s and 5 s were chosen for the first measurement point and after the inversion of the thermal gradient direction, respectively. These times were obtained before beginning the experiments, by determining the settling time required to reach the steady state for all voltages as well as $R_{T,top/bottom}$. In summary, with the alternating thermal gradient technique, we have extended the electrical current reversal technique into the thermal domain, allowing a significant improvement of the signal to noise ratio.

Results and Discussion

We now turn to the experimental results. We start with the temperature dependent resistivity of the Mn$_{1.8}$PtSn Hall bar. As shown in Fig. 6.4, a kink around $T_{SR} \sim 185$ K is evident in the data. This is associated with a spin reorientation transition, where the magnetic system goes from a collinear (above T_{SR}) to a non-collinear state (below T_{SR}).[4,200–202] A similar behavior was observed by neutron diffraction in Mn$_2$RhSn at $T_{SR,MRS} = 80$ K.[203] Please note, that these features have been verified by Neutron scattering experiments for Mn$_{1.4}$PtSn in Refs. [200] and [204]. Additionally, magnetic susceptibility measurements in bulk material suggest that the response of the magnetic system to small excitation changes at T_{SR}.[204] However, in thin films no direct measurements confirming the non-coplanar spin structure are available to our knowledge.
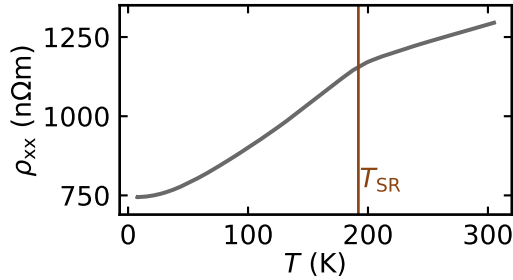
Figure 6.4: The temperature dependent resistivity of the 35 nm thick Mn$_{1.8}$PtSn thin film has a kink around the spin reorientation transition, below which the magnetic system enters a non-collinear state. Adapted from Ref. [3].

To evaluate whether the magnetization also behaves differently below and above the spin reorientation, we will discuss the magnetization loops shown in Fig. 6.5. For the extraction of the film magnetization from the raw magnetometry data (c.f. Fig. 6.5a), the diamagnetic substrate background of MgO has to be removed. This is accomplished by subtracting the linear slope observed in the saturation regime ($|\mu_0 H| > 4$ T). Please note, that the magnetometer can only determine the magnetic moment with a large uncertainty, whenever the magnetic moment is close to 0, such that we chose to mask the data around $M = 0$.[1] The film magnetization loops (c.f. Fig. 6.5b) smoothly change from 300 K to 30 K: They show an increasing saturation magnetization when the temperature is decreased. Additionally, the field required for reaching saturation is also increasing towards lower temperatures. Quantitatively, the saturation magnetization of $M \sim 350$ kA m^{-1} and $M \sim 530$ kA m^{-1} observed at 300 K and 150 K, respectively, are close to the values reported in literature.[4,200] For the magnetization loop taken at the 10 K, a large change

---

[1]The magnetometer returns a quantity determining the quality of each individual measurement (i.e. at each magnetic field). This quantity is then used to mask the data.

of both, the saturation magnetization and the shape of the loop is evident. This is associated with paramagnetic impurities in the MgO substrate giving rise to an additional, Brillouin-like,[138] substrate background. Taken together, while we also observe the kink in the resistivity of the thin film (c.f. Fig. 6.5), no anomalous behavior is observed in the magnetization loops when crossing T_{SR}. Please note, however, that also in the thin films there is a small discontinuity around T_{SR} when the magnetization is measured as a function of temperature at a fixed magnetic field.[4]
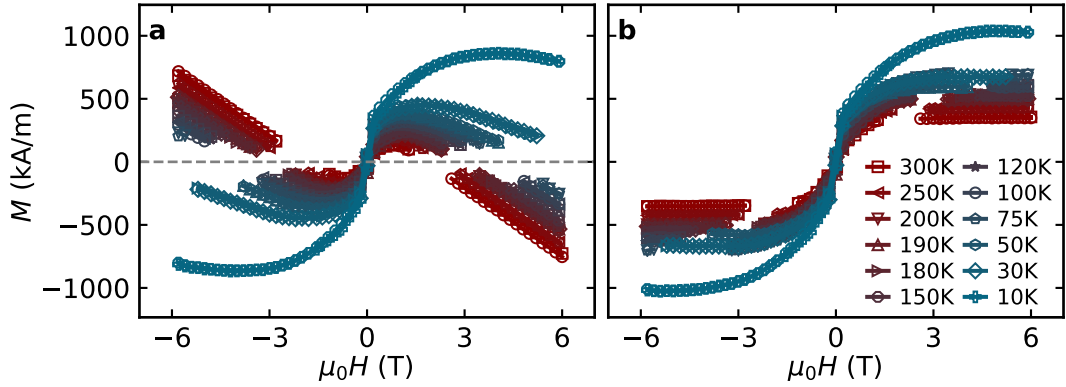
Figure 6.5: **a** The (raw) magnetometry data for a $\text{Mn}_{1.8}\text{PtSn}$ thin film with a thickness of 35 nm is shown. Where the magnetic moments of the film and the (diamagnetic) substrate are equal, the net moment of the sample vanishes, so that the extraction of the magnetic moment fails. Hence, these regions (i.e. where the magnetic moment can not be determined with certainty) were masked. **b** The magnetization of the film is extracted by subtracting the diamagnetic substrate background (i.e. the linear (negative) slope in the saturated regime) from the raw data. The significantly increased moment and altered shape at 10 K indicates that paramagnetic impurities are present in the substrates. Adapted from Ref. [3].

In the following, the different contributions to the transport signature will be discussed first for the Hall effect. Commonly, there are three contributions to the Hall signal[95]

$$\rho_{\text{xy}} = \rho_{\text{xy}}^{\text{OHE}} + \rho_{\text{xy}}^{\text{AHE}} + \rho_{\text{xy}}^{\text{THE}}. \tag{6.5}$$

First, there is the ordinary Hall effect caused by Lorentz deflection of the charge carriers

$$\rho_{\text{xy}}^{\text{OHE}} = R_0 \mu_0 H, \tag{6.6}$$

where R_0 is the ordinary Hall coefficient.[138] Second, for the anomalous Hall effect, observed in magnetic metals and scaling linearly with the (normalized) magnetization M/M_{s}

$$\rho_{\text{xy}}^{\text{AHE}} = \rho_{\text{xy}}^{\text{A}} \frac{M}{M_{\text{s}}} = (S_{\text{A}} \rho_{\text{xx}}^2 + \alpha \rho_{\text{xx}}) \frac{M}{M_{\text{s}}} \approx \lambda \rho_{\text{xx}}^n \frac{M}{M_{\text{s}}}, \tag{6.7}$$

where S_{A} determines the intrinsic and side-jump scattering contributions and α the skew

scattering contribution.[2][95,116] The alternative notation with the coefficient λ and the power n (where $n \approx 2$ would suggest a dominantly intrinsic/side-jump contribution) will be important later for the discussion of the anomalous Nernst effect (c.f. Eq. (6.12)). Third, the topological Hall effect can originate from the presence of topologically non-trivial spin textures

$$\rho_{xy}^{THE} \propto \kappa = S_i \cdot (S_j \times S_k), \tag{6.8}$$

where κ is given by the alignment of the neighboring spins $S_{i,j,k}$ on the sites i, j, k.[95,109] However, as the alignment of the individual spins crucially depends on their energetic environment, a general dependence of the topological Hall effect on the magnetic field can not be formulated. In other words, the presence of a topologically non-trivial spin texture sensitively depends on the magnetic phase diagram.[58,95]

We will now present a sketch showing the salient features of the different contributions to provide orientation for the reader. To that end, we use a Stoner-Wohlfahrt model[205] to simulate a magnetization loop along a hard magnetic axis (i.e. in a configuration similar to the thin film measurements, where the out-of-plane direction is a hard magnetic axis). The magnetization (Fig. 6.6, gray line) is then used to simulate ρ_{xy} (c.f. Eq. (6.5), red line).[3] Please note, that all coefficients and the shape of the topological contribution ρ_{xy}^{THE} are chosen to ensure the best visibility of the salient features. Additionally, the individual contribution to ρ_{xy} are shown by dashed lines. For small magnetic fields ($\mu_0 H < \mu_0 H_s$) ρ_{xy} is dominated by the evolution of the anomalous Hall effect (dashed turmeric line). If the magnetic field is increased further, ρ_{xy}^{AHE} saturates and is constant, while the topological contribution ρ_{xy}^{THE} (dashed teal line) gives rise to the hump in ρ_{xy}. Finally, for very large magnetic fields ($\mu_0 H \gtrsim 0.6\,\text{T}$), ρ_{xy} shows a linear increase with the magnetic field as expected for the ordinary Hall effect ρ_{xy}^{OHE} (dashed purple line).

Figure 6.6: The magnetization (gray line) was simulated using a Stoner-Wohlfahrt model,[205] where the magnetic field is applied along the hard axis. Furthermore, we chose the magnetic field required to saturate the magnetization as $\mu_0 H_s = 0.2\,\text{T}$. Using the magnetization, the individual contributions to the Hall resistivity ρ_{xy} (red line) according to Eq. (6.5) were calculated. Please note, that the functional of the topological contribution ρ_{xy}^{THE} was chosen in way to resemble the topological Hall effect contribution evident in our Mn$_{1.8}$PtSn films to allow for easier identification later. The code can be found in App. E.

---
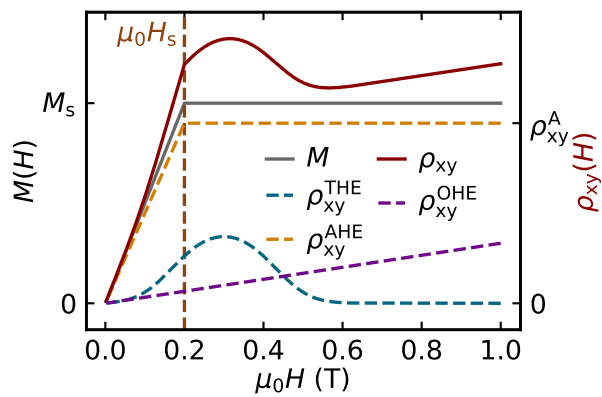
[2]Please note, that we include the saturation magnetization into the coefficients of the anomalous Hall effect for consistency with the later evaluation.

[3]For simplicity we assume ρ_{xx} is independent of the magnetic field, such that $\rho_{xy}^{AHE} \propto M$ (c.f. Eq. (6.7)).

Hence, to extract the topological Hall contribution ρ_{xy}^{THE}, we can first use the evolution of ρ_{xy} at high magnetic fields to determine the ordinary Hall effect contribution ρ_{xy}^{OHE}. The remaining (field independent) offset after removing the linear slope from the data then is the amplitude of the anomalous Hall effect ρ_{xy}^{A}. Thus, in a next step we can remove also the anomalous Hall effect ρ_{xy}^{AHE} from ρ_{xy}, if the shape of the magnetization loop (and $\rho_{xx}(H)$) is known. Consequently, only the topological contribution

$$\rho_{xy}^{THE} = \rho_{xy} - \rho_{xy}^{OHE} - \rho_{xy}^{AHE} = \rho_{xy} - R_0\mu_0 H - (S_A\rho_{xx}^2 + \alpha\rho_{xx})\frac{M}{M_s} \tag{6.9}$$

remains.

Before finally turning to the transport measurements, we will briefly touch upon the Nernst effect. A very similar discussion is also possible for the Nernst effect S_{xy}, where the ordinary Nernst effect is the term linear in the magnetic field[138]

$$S_{xy}^{OHE} = N\mu_0 H, \tag{6.10}$$

with the ordinary Nernst coefficient N. However, the resistivity and Seebeck tensors are not independent, such that the Nernst effect is sensitively linked to the resistivies (and thus also the Hall effect)[116,206]

$$S_{xy} = \rho_{xx}(\alpha_{xy} - \sigma_{xy}S_{xx}), \tag{6.11}$$

where σ_{xy} is the transverse (Hall) conductivity, S_{xx} is the Seebeck effect and α_{xy} is the transverse thermoelectric (Nernst) conductivity.[4][116] The first term in the brackets can be linked to the generation of a transverse electric current from the thermal gradient, while the latter describes the generation of a longitudinal electric current which in turn is converted to a transverse current via the Hall effect. According to Ref. [116], the anomalous Nernst effect is connected to the anomalous Hall effect like

$$S_{xy}^{ANE} = S_{xy}^{A}\frac{M}{M_S} = -\frac{\rho_{xy}^{AHE}}{\rho_{xx}}\left(T\frac{\pi^2 k_B^2}{3e}\frac{\lambda'}{\lambda} - (n-1)S_{xx}\right) \tag{6.12}$$

when assuming that the Mott relation[97,101,207,208] is fulfilled and that the anomalous Hall effect scales like $\rho_{xy}^{AHE} = \lambda\rho_{xx}^n M/M_s$ (c.f. Eq. (6.7)). k_B is the Boltzmann constant, e is the electron charge and $\lambda' = \partial\lambda/\partial E$ is the energy derivative of the anomalous Hall coefficient λ. While a more detailed discussion of the relation of the Nernst and Hall effect is beyond the scope of this thesis, some general conclusions can be drawn from Eq. (6.12): First, the anomalous Nernst effect and anomalous Hall effect will both depend on the magnetization since $S_{xy}^{ANE} \propto \rho_{xy}^{AHE} \propto M/M_s$. Additionally, the relative sign of the anomalous Nernst effect and anomalous Hall effect is not fixed, but sensitively depends on the magnitude of the Seebeck effect S_{xx}. Experiments testing the validity of the Mott relation also for the topological contribution to the Nernst effect have been reported, where first results

---

[4]Please note that the additional contribution of the thermal Hall effect has been nerglected here.[106]

suggest it is also valid in this case, so that a similar approach can be taken to connect S_{xy}^{TNE} and ρ_{xy}^{THE}.[96,106,207,209]

In summary, a very similar heuristic separation as done for the Hall effect can be made for the Nernst effect[106]

$$S_{xy} = S_{xy}^{ONE} + S_{xy}^{ANE} + S_{xy}^{TNE}, \tag{6.13}$$

where $S_{xy}^{ONE} \propto \mu_0 H$ is linear in the magnetic field, $S_{xy}^{ANE} \propto M/M_s$ scales with the magnetization and S_{xy}^{TNE} has no clear scaling with either the magnetic field or the magnetization.[106,116,138,209] As such, S_{xy}^{TNE} can be extracted in a similar fashion as discussed in the context of the Hall effect (c.f. Fig. 6.6 and Eq. (6.9)).
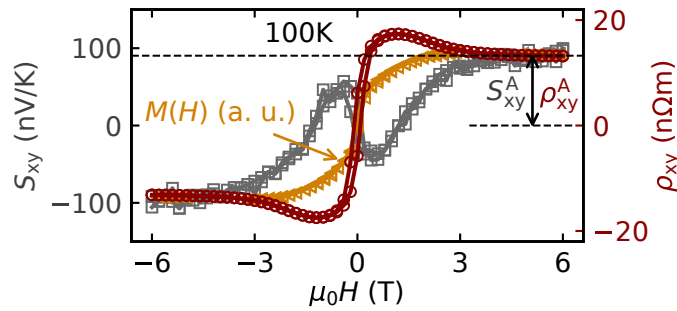
Figure 6.7: The measured transport response for the thermal (gray) and electrical (red) signal is shown. Both signals deviate significantly from the magnetization loop (turmeric) in the intermediate field range ($|\mu_0 H| < 4\,\mathrm{T}$). Adapted from Ref. [3].

Now that the salient features of the different contributions have been established, we will turn to the discussion of the magnetoelectric and magnetothermal transport response. To that end we consider an exemplary set of measurements at $T = 100\,\mathrm{K}$ (below the spin reorientation temperature) to elucidate the extraction procedure of the different Nernst or Hall contributions from the measured signals. The Nernst signal S_{xy} (determined via Eq. (6.4)) and the Hall signal ρ_{xy} (determined via Eq. (6.2)) are displayed together with the magnetization in Fig. 6.7. Both, S_{xy} and ρ_{xy} show a clear deviation from the magnetization loop contrary to the expectation for a ferromagnet: If only an ordinary and anomalous Hall effect would be present, ρ_{xy} would closely follow the magnetization loop (c.f. Eq. (6.7) and Eq. (6.12)) or have an additional contribution linear in magnetic field (c.f. Eq. (6.6) and Eq. (6.10)).[104,105,199] Thus, we can directly conclude from the shape of ρ_{xy} (and S_{xy}) that there is a finite topological Hall (and topological Nernst) effect contribution. Consequently, it appears likely that a topologically non-trivial (chiral) spin texture is present in the Mn$_{1.8}$PtSn thin film studied here.[54,58,95,106] Interestingly, the amplitudes of the anomalous Nernst effect S_{xy}^A and the anomalous Hall effect ρ_{xy}^A (c.f. Fig. 6.7) have the same sign contrary to the amplitudes of the topological signals, where the deviation from the magnetization is negative for S_{xy} and positive for ρ_{xy}. In a free electron picture, one would expect the (ordinary) Nernst effect and the (ordinary) Hall effect to have an opposite sign for our geometry (c.f. Fig. 6.1), as the electron velocity is opposite for the two measurement configurations. However, as shown in Eq. (6.12), the relative sign of

100

the anomalous Hall effect and the anomalous Nernst effect, can differ depending on the mechanism giving rise to the anomalous effects and the size of Seebeck effect S_{xx}. As we are not able to measure the Seebeck effect in our device, a definite statement as to the expected sign cannot be made.[5]

We will now turn to the (heuristic) extraction of the topological transport response. As already introduced above, this is accomplished by subtracting the ordinary Hall/Nernst effect and the anomalous Hall/Nernst effect from the measured transport signals, using the magnetization loop (c.f. Fig. 6.5 and Eq. (6.9)).[4,106,199,210,211] However, due to the exact shape of the observed transport signatures, we will first simplify Eq. (6.9) by evaluating the impact of the individual contributions. As discussed above, the ordinary Hall effect (c.f. Eq. (6.6)) can be extracted using the slope in the regime, where the magnetization is saturated. In our case, however, neither S_{xy} nor ρ_{xy} exhibit a large slope in saturation (i.e. $|\mu_0 H| > 4\,\mathrm{T}$), such that we can neglect the contributions of the ordinary Nernst and the ordinary Hall effect. Additionally, measurements of $\rho_{xx}(H)$ allow to put an upper limit to its magnetic field dependence, which we find to be smaller than $|\rho_{xx}(H)/\rho_{xx}(H=0)| \lesssim 10\,\%$. This fact, together with the dominantly intrinsic contribution to the anomalous Hall effect in $\mathrm{Mn_{1.8}PtSn}$,[4] lead to a maximum field dependence of the anomalous Hall coefficient $|\rho_{xy}^{\mathrm{A}}(H)/\rho_{xy}^{\mathrm{A}}(H=0)| \propto (\rho_{xx}(H)/\rho_{xx}(H=0))^2 \lesssim 1\,\%$ (c.f. Eq. (6.7)). Thus, assuming $\rho_{xy}^{\mathrm{A}} \approx \mathrm{const}$ seems reasonable and we get

$$\rho_{xy}(H) \approx \rho_{xy}^{\mathrm{A}} \frac{M(H)}{M_{\mathrm{s}}} + \rho_{xy}^{\mathrm{THE}}(H) \tag{6.14}$$

For the Nernst effect, this simplification is not as straightforward, as it depends linearly on the resistivity ρ_{xx} and the Seebeck effect S_{xx} (c.f. Eq. (6.12)). While we know that $|\rho_{xx}(H)/\rho_{xx}(H=0)| \lesssim 10\,\%$, the evolution (or even magnitude) of S_{xx} is unknown.[6] Therefore, we will make the same assumption (i.e. $S_{xy}^{\mathrm{A}} \approx \mathrm{const}$) as for the Hall effect, leading to a possible error of at least 10 % for the extracted topological Nernst effect

$$S_{xy}(H) \approx S_{xy}^{\mathrm{A}} \frac{M(H)}{M_{\mathrm{s}}} + S_{xy}^{\mathrm{TNE}}(H) \tag{6.15}$$

With these simplifications, we arrive at the following equations for the extraction of the

[5]The Seebeck effect cannot be quantified in our structure, since the voltage generated by the temperature gradient within the central part of the Hall bar is compensated by the voltage generated by the (inverse) temperature gradients in the leads: Both bond pads (i.e. where the wire bonds to measure V_{xx} are placed) are far away from the heated central part of the device, so that both will have an equal temperature. Consequently, $\Delta T = 0 \rightarrow V_{xx} = 0$. An improved version of the device layout with an additional set of Pt leads touching the $\mathrm{Mn_{1.8}PtSn}$ Hall bar would allow to circumvent this limitation but was not prepared during this thesis.

[6]Although the magnitude of the Seebeck effect is unknown, the presence of a finite planar Nernst effect was observed, suggesting that there certainly is a magnetic field dependent Seebeck effect.[212]

topological Hall and topological Nernst effect:

$$\rho_{xy}^{THE}(H) \approx \rho_{xy}(H) - \rho_{xy}^{A}\frac{M(H)}{M_s} \tag{6.16}$$

$$S_{xy}^{TNE}(H) \approx S_{xy}(H) - S_{xy}^{A}\frac{M(H)}{M_s} \tag{6.17}$$
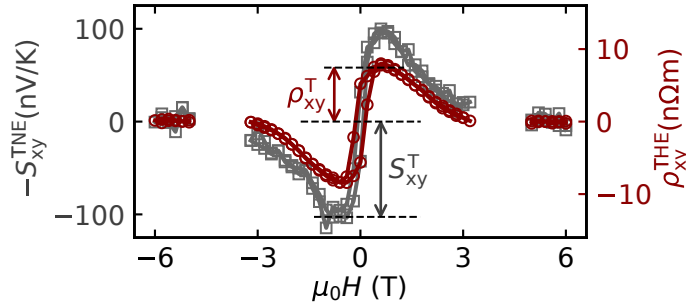

Figure 6.8: The topological transport signals extracted according to Eq. (6.17) and Eq. (6.16) are shown. Please note, that the Nernst signal has been inverted to allow an easier comparison of the signal shapes. Adapted from Ref. [3].

The thus extracted topological Nernst and Hall signals are plotted in Fig. 6.8. Please note, that for the magnetic fields where no magnetization measurements are possible (c.f. Fig. 6.5), the topological signals can also not be calculated. To allow an easier comparison of the shape of S_{xy}^{THE} and ρ_{xy}^{THE}, the topological Nernst signal is inverted in the plot. S_{xy}^{THE} and ρ_{xy}^{THE} superimpose nicely, showing that a topological response is present in the intermediate field range ($|\mu_0 H| < 4\,T$). We associate these topological signals to the presence of a non-coplanar alignment of the magnetic sublattices in the same field range, which additionally allows to motivate the magnetic field dependence: While for very small magnetic fields, the individual spins will reside within (or close to) the film plane, such that also the scalar spin chirality $\kappa = S_i \cdot (S_j \times S_k)$ (vanishing when all spins reside within one plane) will be small (c.f. Eq. (6.8)). If the magnetic field is increased, the non-coplanar alignment will be stabilized by the additional Zeeman energy, giving rise to an increasing component along the magnetic field (i.e. and thus an increasing scalar spin chirality). For even large magnetic fields, the spin configuration will finally be dominated by the Zeeman energy, such that all spins align with the magnetic field and $\kappa \to 0$. Interestingly, except for the sign, the very similar evolution of the S_{xy}^{TNE} and ρ_{xy}^{THE} might be an indicator, that the Mott relation linking the Nernst and Hall effect is also fulfilled for the topological transport effects. However, as the Seebeck effect is unknown, a test of the Mott relation is beyond the scope of this work.

We will now turn to the discussion of the temperature dependent evolution of S_{xy} and ρ_{xy} and their topological contributions S_{xy}^{TNE} and ρ_{xy}^{THE}. To this end, we repeated the measurements and the extraction of the topological response at several temperatures. The resulting data is shown in Fig. 6.9. There are two interesting evolutions visible in the
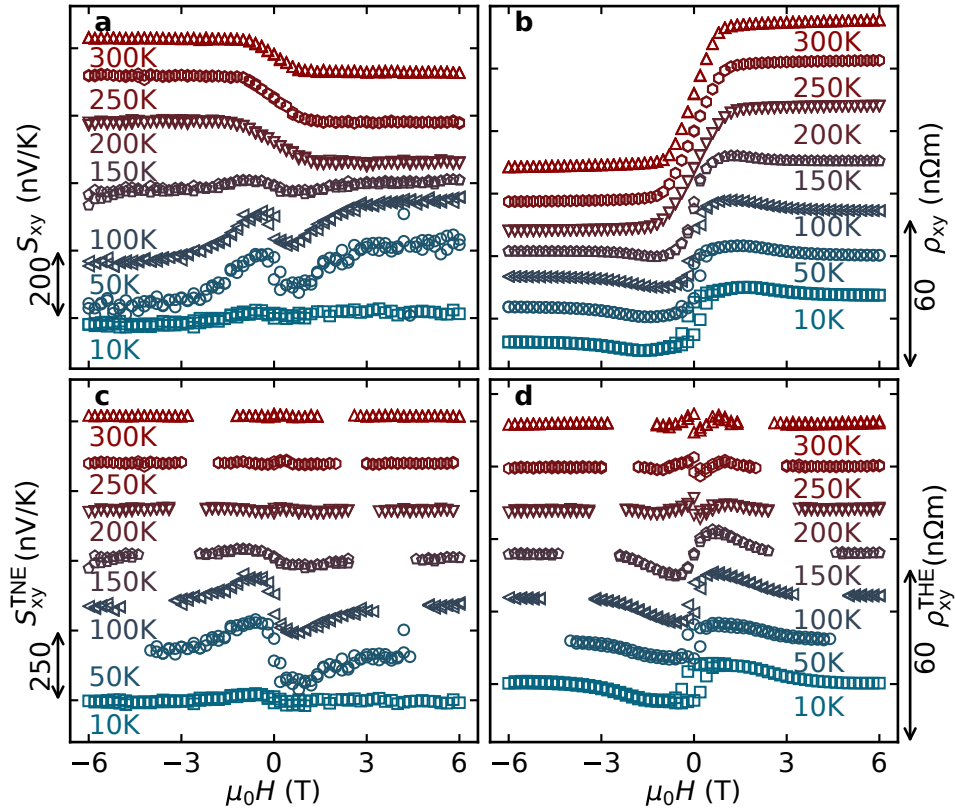
Figure 6.9: Panels **a** and **b** show temperature dependent measurements of the Nernst and Hall signals, respectively. The anomalous Nernst effect (i.e. the value in saturation) changes its sign below the spin reorientation temperature in addition to having a topological contribution. In contrast, the sign of the anomalous Hall effect does not change with temperature, while a topological contribution also appears. **c** The topological Nernst signal and **d** the topological Hall signal (extracted according to Eq. (6.16) and Eq. (6.17)) show that a topological contribution is present below T_{SR} (Nernst effect) or even in the full temperature range (Hall effect). Adapted from Ref. [3].

raw data (panels a and b). First, the anomalous Nernst effect (i.e. $S_{xy}^A = S_{xy}(H > 4\,\text{T}$, c.f. Fig. 6.7) exhibits a sign change below $T_{SR} \sim 185\,\text{K}$. While at high temperatures $T \gtrsim 170\,\text{K}$, S_{xy}^A is negative, it is positive for $T \lesssim 150\,\text{K}$ and decreases drastically for $T \lesssim 30\,\text{K}$. A very similar behavior is reported in Ref. [116] in $\text{Ga}_{1-x}\text{Mn}_x\text{As}$ with $x = 0.04 - 0.07$, where the sign change is caused by an increase of S_{xx} towards low temperatures. Thus, also the sign change observed here might be rooted in the different electronic contributions to the Nernst effect, where their relative magnitude can change as a function of temperature (c.f. Eq. (6.12)). Additionally, Eq. (6.12) together with vanishing signal for $T \lesssim 30\,\text{K}$ suggest that either S_{xx} becomes small towards low temperatures or that the dominant mechanism giving rise to the anomalous Hall effect changes, so that e.g. $n \rightarrow 1$.[213] Again, it would be interesting to perform further experiments in the future to also measure S_{xx} for $\text{Mn}_{1.8}\text{PtSn}$

thin films to be able to verify the validity of the Mott relation and to evaluate the different contributions to the Nernst effect. Finally, for completeness sake, recent reports in literature suggest, that the anomalous Nernst effect and the anomalous Hall effect can depend on different regions of the Fermi sea, such that a different evolution with temperature would be anticipated.[101,208] However, as the exact band structure and the changes it undergoes when crossing the spin reorientation are unknown, unfortunately no insight can be gained here.

The topological Nernst and Hall effect (c.f. Fig. 6.9c and d) are visible down to the lowest temperature $T = 10\,\mathrm{K}$ studied. Interestingly, the magnetic field region in which the topological Hall effect and the topological Nernst effect can be observed (and thus the non-coplanar spin structure is present) broadens towards lower temperatures. We thus speculate that the absence of thermal fluctuations results in a stabilization of the non-coplanar spin texture. Additionally, even above T_{SR} there are features visible around zero magnetic field, suggesting that even for higher temperatures, a topological spin texture is present. This would agree with reports in bulk $Mn_{1.4}Pt_{0.9}Pd_{0.1}Sn$, where the presence of antiskyrmions above T_{SR} was reported.[200] However, imperfect measurements can also give rise to such features, which we will discuss in detail after addressing the magnitudes of the different contributions to the Nernst effect and the Hall effect.
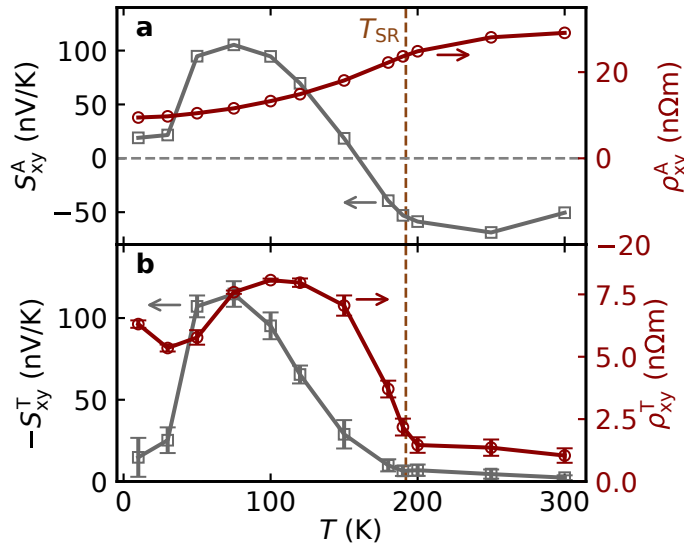
Figure 6.10: **a** The magnitudes of the anomalous Nernst and Hall effects are shown. The sign change of the anomalous Nernst effect is visible at $T = 150\,\mathrm{K}$, suggesting it might not be directly related to the spin reorientation transition. In contrast, the anomalous Hall effect only decreases monotonically towards low temperatures. In panel **b**, the magnitudes of the topological Nernst and Hall effect are summarized. Adapted from Ref. [3].

The magnitudes of the anomalous transport coefficients are summarized in Fig. 6.10a. As already discussed above, the anomalous Nernst effect changes its sign around $T = 150\,\mathrm{K}$, well below T_{SR}. The maximum magnitudes for the anomalous Nernst effect and the anomalous Hall effect (i.e. the magnitudes in saturation) are $S_{\mathrm{xy}}^{\mathrm{A}} \approx 110\,\mathrm{nV\,K^{-1}}$ and

$\rho_{xy}^{A} \approx 29 \, \text{n}\Omega\,\text{m}$, respectively. Both signal magnitudes are in agreement with the general scaling relations reported in literature for the anomalous Nernst and the anomalous Hall effect.[95,96,103,214] In particular, one of the two scaling relations states that in itinerant magnets there is a linear relation between the magnitudes of the magnetization and the anomalous Hall effect (or anomalous Nernst effect).[95,103,214] The second scaling law correlates the resistivity ρ_{xx} and the anomalous Hall effect ρ_{xy}^{A}, where depending on the transport regime and thus the dominant contributions to the anomalous Hall effect a particular relation between ρ_{xx} and ρ_{xy}^{A} can be formulated (c.f. Eq. (6.7)).[95,96] The highest amplitude of the topological Nernst and Hall effect are $S_{xy}^{T} \approx 115 \, \text{nV}\,\text{K}^{-1}$ and $\rho_{xy}^{T} \approx 8 \, \text{n}\Omega\,\text{m}$, respectively (c.f. Fig. 6.10b). The topological Nernst effect is comparable to the effect reported in bulk MnGe ($S_{xy}^{T} \sim 150 \, \text{nV}\,\text{K}^{-1}$), the only other material where the effect is reported.[106] Similarly, the amplitude of the topological Hall effect agrees well with reports on Mn_xPtSn.[4,201] Finally, both S_{xy}^{T} and ρ_{xy}^{T} decrease rapidly when approach T_{SR} but remain finite even above, where no non-coplanar spin structure (but possibly Skyrmions) should be realized.[200]
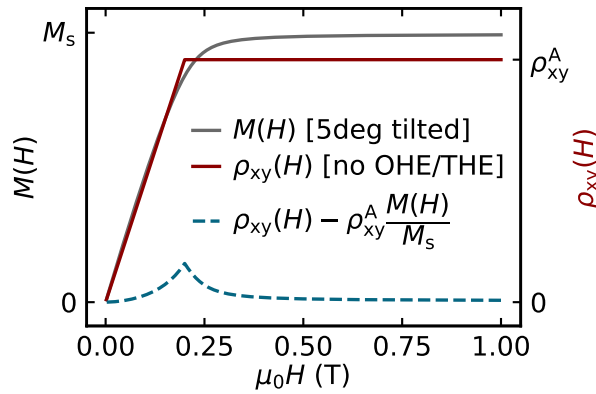
Figure 6.11: The Stoner-Wohlfahrt model introduced in Fig. 6.6 and App. E is used again to estimate the change of the magnetization loop if the magnetic field is misaligned with respect to the hard magnetic axis (gray line). We compare this magnetization "measurement" with the Hall effect ρ_{xy} (including only the anomalous Hall effect ρ_{xy}^{AHE}) obtained for perfect alignment of the magnetic hard axis and the magnetic field. If the topological Hall effect is then calculated using Eq. (6.16), a finite "topological Hall effect" (dashed teal line) is found, although $\rho_{xy}^{THE} = 0$. Thus, an imperfect conception of the experiments can give rise to artifacts, resembling a topological Hall effect.

We will now try to motivate an alternative origin for the presence of the topological transport features observed above T_{SR} shown in Fig. 6.9. In experiments, the alignment of the sample with respect to the magnetic field can be challenging, so that a finite misalignment of the magnetic field with respect to the surface normal is possible. Since we compare different measurements (i.e. transport and magnetometry measurements), done in different setups, the misalignment with respect to the magnetic field is likely different for the two measurements. Thus, we will now use the Stoner-Wohlfahrt model introduced in Fig. 6.6 and App. E to evaluate the impact of such a misalignment and the consequences

for the extraction of the topological signal using Eq. (6.8). To that end, the Hall signal ρ_{xy} shown in Fig. 6.11 was "measured" with perfect alignment of the magnetic field and the hard axis (red line, c.f. Fig. 6.6), while the magnetization "measurement" was done with a finite tilt angle of 5° with respect to the surface normal (gray line). The resultant shape of ρ_{xy} and M is clearly different, such that when we now use the imperfect magnetization measurement to remove ρ_x^{AHE} from ρ_{xy} (Eq. (6.9) and Eq. (6.8)), a finite residual is found. Thus, even in the absence of any topological contribution $\rho_x^{\text{THE}} = 0$ to the Hall effect, a residual signal (even roughly resembling the topological Hall effect observed in our device) can be found when the measurements are not carried out perfectly. Consequently, extreme care has to be taken, as to not introduce such artifacts by the comparison of the two measurements.

Motivated by the possible occurrence of artifacts, introduced by the comparison of transport and magnetization measurements, we decided to use the large topological Nernst effect and topological Hall effect observed in Mn$_{1.8}$PtSn to demonstrate an alternative method for the extraction of the topological contribution. One necessary prerequisite for this approach can be seen in Eq. (6.14) and Eq. (6.15), where the similar dependence of the ρ_{xy} and S_{xy} on the magnetization is visible. Consequently, by normalizing ρ_{xy} and S_{xy} to their respective high field saturation values ρ_{xy}^A and S_{xy}^A, one can use their difference to single out the topological contributions to the magnetoelectric and magnetothermal transport response:

$$TQ = \frac{\rho_{xy}}{\rho_{xy}^A} - \frac{S_{xy}}{S_{xy}^A} \approx \frac{\rho_{xy}^{\text{THE}}}{\rho_{xy}^A} - \frac{M}{M_s} - \left(\frac{S_{xy}^{\text{TNE}}}{S_{xy}^A} - \frac{M}{M_s} \right) = \frac{\rho_{xy}^{\text{THE}}}{\rho_{xy}^A} - \frac{S_{xy}^{\text{THE}}}{S_{xy}^A} \tag{6.18}$$

Consequently, by using this difference, the magnetization drops out completely, allowing us to remove the anomalous response without the need for magnetization data.[7] This difference is named the topological quantity TQ and can be seen in Fig. 6.12b. The Nernst signal and the Hall signal shown in panel a are normalized and subtracted, yielding TQ. Most generally speaking, the topological quantity will only be non-zero if there is an additional contribution to either the Hall effect or Nernst effect (or both) which is not connected in the exactly the same fashion as the anomalous Hall ρ_{xy}^{AHE} and the anomalous Nernst effect S_{xy}^{ANE} (including the same relative sign, c.f. Eq. (6.12)). From a physical point of view, this condition can, for example, be fulfilled by the presence of a topologically non-trivial spin structure (hence the name topological quantity). Thus we interpret a non-zero topological quantity as a measure for the presence of transport effects caused by topologically non-trivial (chiral) spin structures.[58,109,112] Interestingly, another case, where a non-zero topological quantity might be observed is when the Mott relation is violated.[116,215] Since in that case already the anomalous Hall effect and anomalous Nernst effect could exhibit a different scaling with the magnetization, an investigation

---

[7]Please note, that we here used the simplified equations Eq. (6.14) and Eq. (6.15), so that this formulation is not perfectly accurate. Generally speaking, one would first need to subtract the ordinary Hall and Nernst effect from the respective signals and then perform the subtraction while taking into account all additional scaling relations (i.e. including the dependence on ρ_{xx} and S_{xx}).

of the topological quantity for such a case might be interesting. Additionally, a theoretical investigation of what other contributions might be present in the topological quantity might allow to connect TQ to other physical phenomena but is beyond the scope of this experimental work.
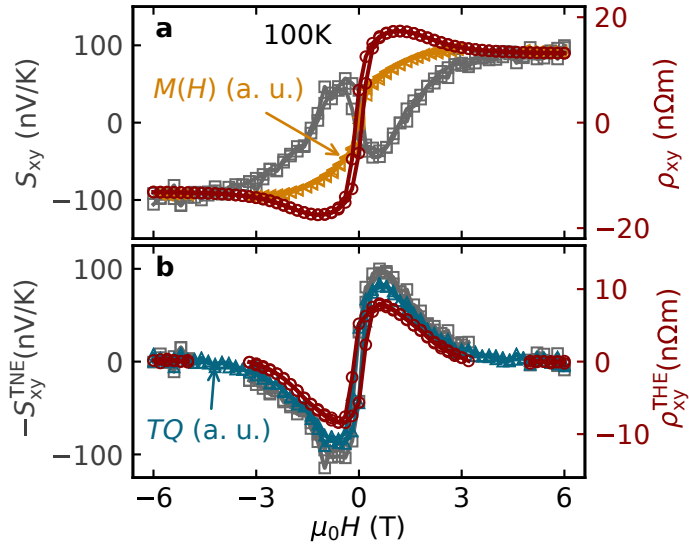

Figure 6.12: **a** The measured transport response for the thermal (gray) and electrical (red) signal is shown together with the magnetization. **b** For direct comparison, the topological transport signals extracted using the conventional approach are plotted together with the topological quantity TQ (c.f. Eq. (6.18)). Adapted from Ref. [3].

For comparison with TQ, the topological Nernst effect and the topological Hall effect extracted using the customary approach have been added in Fig. 6.12b. The field dependence of all curves agrees well and reproducibly shows the peak-dip structure for $|\mu_0 H| < 4\,\text{T}$. Consequently, our idea, that the topological features can be extracted without prior knowledge of the magnetization loops seems to be viable. Additionally, we can exclude that the observed S_{xy}^{TNE} and ρ_{xy}^{THE} are caused by artifacts introduced by the comparison of magnetometry and transport measurements (c.f. Fig. 6.11). Furthermore, the fact that TQ is non-zero only when S_{xy}^{TNE} and ρ_{xy}^{THE} are non-zero, hints at the possibility to determine the presence of topologically non-trivial spin textures also in nanopatterned materials. One of the biggest caveats of this approach is – due to the normalization prior to subtracting the curves – the missing quantitative information: Due to the possibly different contribution of the Nernst and Hall effects to the TQ, no clear assignment of the individual magnitudes can be made. This is easily seen from Eq. (6.18), where the equation system is under–defined for the determination of both, S_{xy}^{T} and ρ_{xy}^{T}. However, even though this limitation is present, a set of ranges can be stated for the two contributions, given by $S_{xy}^{\text{T}} \leq TQ \cdot S_{xy}^{\text{A}}$ and $\rho_{xy}^{\text{T}} \leq TQ \cdot \rho_{xy}^{\text{A}}$, for the topological Nernst and Hall effect, respectively. As expected, this agrees well with the topological Nernst and Hall effect observed at this temperature.
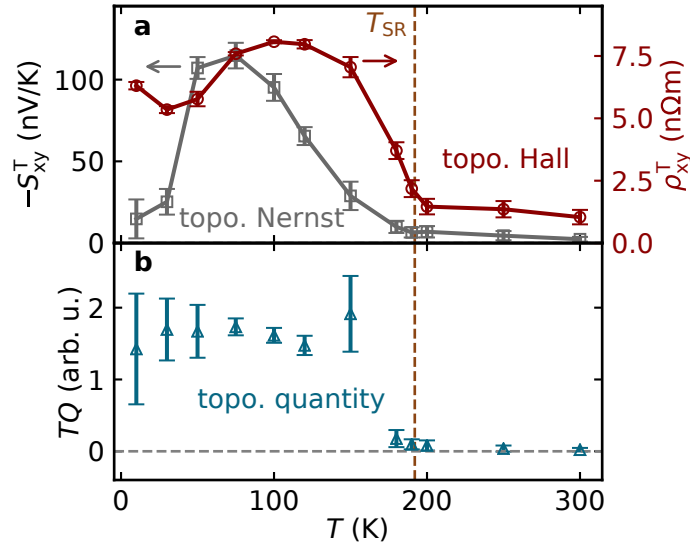
Figure 6.13: **a** The maximum amplitudes of the topological Hall effect and topological Nernst effect are summarized for comparison with **b** the maximum amplitude of the topological quantity TQ. Adapted from Ref. [3].

Finally, to determine, whether the signals we observe above T_{SR} in Fig. 6.9 might be due to such magnetization related measurement artifacts as shown in Fig. 6.11, we will now discuss the temperature dependent evolution of the topological quantity. To be able to judge the artifacts, we summarized the maximum amplitudes of S_{xy}^{TNE} and ρ_{xy}^{THE} in Fig. 6.13a and the topological quantity TQ in Fig. 6.13b. Interestingly, although the topological Nernst and Hall effect are non-zero above the spin reorientation transition, the topological quantity vanishes to within our experimental error. This observation, suggesting that Nernst and Hall effect have exactly the same shape above the spin reorientation transition, leads us to believe that the observed topological features above T_{SR} are actually caused by the comparison of transport and magnetization data. This observation in particular casts doubt on the report of a topological Hall effect up to room temperature in films of Mn$_2$PtSn presented in Ref. [211]: As discussed above (c.f. Fig. 6.11) a small misalignment of the film normal with respect to the magnetic field between different measurements can give rise to artifacts with a similar shape as the topological Nernst effect and topological Hall effect. Consequently, extreme care has to be taken in the conception and interpretation of the measurement results.

Summary

We have presented a thorough study of the Hall and Nernst effect in a Mn$_{1.8}$PtSn thin film. To this end, we have established a novel measurement scheme, the alternating thermal gradient technique, improving the extraction of thermoelectric voltages generated in the sample significantly. In addition to finding a topological Hall effect, we were thus able

to also observe a clear topological contribution to the Nernst effect when using the alternating thermal gradient technique to remove spurious thermoelectric voltages caused by the cryostat. In these first simultaneous measurements of the topological Nernst and Hall effect in a thin film, we found a quantitatively large transport response for both effects, comparable to the largest values reported in literature so far.[4,106,201,216,217]

Additionally, we used the large transport response of $Mn_{1.8}PtSn$ to show that the extraction of the topological features using only transport measurements is possible. This was accomplished by combining the Nernst and Hall signals to remove the necessity for additional magnetization measurements: As the anomalous Nernst and Hall effect depend on the magnetization in a similar fashion, they can be combined in such a way that no anomalous contribution remains in the resulting signal. This signal, which we named topological quantity TQ is only non-zero in the presence of an additional (e.g. topological) contribution to the transport response. Although the topological Hall and topological Nernst effect, extracted according to the procedure used in literature, remained finite even above the spin reorientation temperature, the topological quantity was only non-zero (within our experimental resolution) below that temperature. Hence, we concluded that no topological contribution is present above the spin reorientation temperature T_{SR}, and the topological Hall and Nernst signals observed above T_{SR} are likely artifacts introduced by the comparison of the transport and magnetization measurements. Finally, although not fully quantitative, the TQ allows to estimate a range of magnitudes of the topological Hall and Nernst effect. As such, we are confident to having added a valuable tool into the toolbox of transport measurements. In summary, we showed that an all-electrical detection of topologically non-trivial magnetization textures is possible, likely even in nanopatterned materials. We believe that this development opens up many new possibilities for studies of materials, where magnetization measurements are extremely challenging due to the small magnetic moments.

Chapter 7

SPATIALLY RESOLVED MEASUREMENTS OF THE ANOMALOUS NERNST EFFECT IN MN₃SN THIN FILMS

Antiferromagnets have recently excited a lot of research activity, as they are a potential replacement for ferromagnets in spintronic applications and could offer several advantages.[85,218] While magnetization dynamics in ferromagnetic materials occur on the GHz frequency scale, antiferromagnets have a dynamic response in the THz frequency regime.[180,218] Additionally, antiferromagnets have a high stability against external magnetic stray fields due to their vanishing magnetic moment.[146] However, for the latter reason antiferromagnets are also hard to manipulate. This limitation can be overcome in a special subset of antiferromagnets (AFM), which have a non-collinear alignment of the different magnetic sublattices.[85,218] In these non-collinear antiferromagnets, the combined symmetry of the cyrstal lattice and the spin system can lead to a time reversal and spatial inversion symmetry breaking.[95,113,219–221] These broken symmetries, in turn, allow (but do not require) a small canting of the magnetic sublattices (and thus a small net magnetization), while still maintaining an otherwise antiferromagnetic spin structure.[221–223] Thus, in these systems, the small magnetization can be used as handle to manipulate the full antiferromagnetic order parameter (i.e. the orientation of the magnetic sublattices).[107]

In addition to enabling control over the antiferromagnetic order parameter, the broken time reversal and spatial inversion symmetry breaking allows to observe a host of effects which are commonly not present in antiferromagnets.[85,218,221] In particular, effects which depend linearly on the magnetization, including the anomalous Hall effect, the anomalous Nernst effect and the magnetooptical Kerr effect have been reported in such non-collinear antiferromagnets.[103,107,112,224–229] Surprisingly these effects even showed a magnitude comparable to the respective effects in typical ferromagnets, although the net

magnetization is very small.[103,107,224] This counter-intuitive finding is motivated by the origin of the effects, which are not generated by the small magnetization but by the chirality of the spin system.[95,103,107,114,220,225] Thus, contrary to the naive expectation, large effect magnitudes can be found despite the vanishing magnetization, where the latter only acts as a handle to invert the chirality of the spin system.[107,225] Additionally, it was proposed that, similar to ferromagnets, a finite spin polarization can be present in non-collinear antiferromagnets, which might allow to perform spin transfer torque mediated magnetization switching or domain wall movement experiments.[85,221,229]

Theoretical efforts showed, that the symmetry breaking allows for the presence of the small magnetization (and thus the anomalous Hall and Nernst effect) only along a particular direction **g** for a given crystal lattice and spin structure.[35,114,221] Thus, this time-reversal odd axial vector **g** replaces the magnetization in the Hall and Nernst equations, so that e.g. the anomalous Nernst effect in non-collinear antiferromagnets can be described by[114,230]

$$V_{ANE} \propto \mathbf{E}_{ANE} \propto \nabla T \times \mathbf{g}. \tag{7.1}$$

Consequently, if an adequate thermal gradient (i.e. perpendicular to **g**) is applied to the sample, an inversion of **g** would yield an opposite V_{ANE}. This leads to the conclusion, that the anomalous Nernst voltage generated by a localized thermal gradient should allow to map the spin structure, viz. the local **g** vector orientation, of non-collinear antiferromagnets.[39,92]

Such spatially resolved anomalous Nernst effect measurements, however, require micropatterned thin layers of a non-collinear antiferromagnet to prevent short circuiting of the generated voltage through the surrounding material.[39] To that end, the measurements presented in this chapter focus on Mn_3Sn, where the growth of single crystalline thin films was demonstrated recently.[231] Mn_3Sn is one of the prime representatives of non-collinear antiferromagnets, having a triangular spin structure (c.f. Fig. 7.1a).[103,107,220,222,227,232–234] Two of the possible microscopic spin configurations which should yield an opposite V_{ANE} (i.e. have opposite **g**) are shown in Fig. 7.1b.[103,107,221,235]

The contents of this chapter have been partly reproduced from H. Reichlova et al., Nature Communications **10**, 5459 (2019) (Ref. [2]) with permission from the Nature Publishing Group. The results published in Ref. [2], were obtained in a major joint effort led by Helena Reichlova from the Technische Universität Dresden together with groups from Charles University in Prague, the Czech Academy of Sciences in Prague, the Helmholtz-Zentrum Dresden Rossendorf and the Max Planck Institute for Chemical Physics of Solids in Dresden. I was strongly involved in the experiments discussed in this publication. In particular, I participated in the low temperature experiments at the Charles University in Prague, as well as the experiments at high temperatures at the Technische Universität Dresden and contributed to the experimental conception, the discussions about the results and provided comments to improve the manuscript.
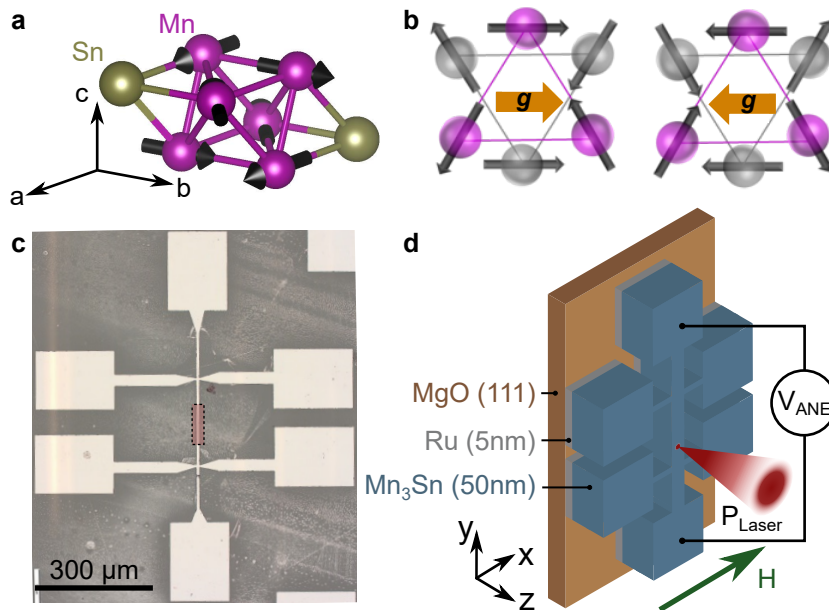
Figure 7.1: **a** Mn$_3$Sn crystallizes in a hexagonal structure (space group P6$_3$/*mmc*) as depicted here. The magnetic moments align perpendicular to the c-axis (in the a-b-plane). **b** Two exemplary microscopic spin configurations with opposite **g** vector (turmeric arrows) are sketched. **c** An optical micrograph of a Hall bar used for the experiment is shown. **d** The laser spot is scanned over the Hall bar (region highlighted red in panel **c**). A magnetic field is applied in the sample plane along the x-direction and the voltage is detected along the y-direction. Thus, with the out-of-plane laser induced gradient, the Nernst geometry is fulfilled. Adapted from Ref. [2].

Sample and Measurement Details

The first series of Mn$_3$Sn thin films was grown by confocal magnetron sputtering by Anastasios Markou and Dominik Kriegner (Max Planck Institut for Chemical Physics of Solids, MPI CPfS). The ultra high vacuum chamber was evacuated to 5×10^{-9} mbar before deposition, while the deposition was performed in an Ar atmosphere with a pressure of 3×10^{-3} mbar. MgO substrates with a (111) surface were used for the deposition. The samples consist of a 5 nm thick Ru layer deposited at 400 °C on top of which the 50 nm thick Mn$_3$Sn film was deposited at room temperature. Before capping with 3 nm Al, the films were post-annealed for 10 min at 300 °C in the deposition chamber. The samples were then patterned into a Hall bar shape by Helena Reichlova using optical lithography and wet etching (c.f. Fig. 7.1c). In this chapter we focus on one particular sample of this series.

Additionally, a second series of samples was prepared by Philipp Zilske and Jay Koo (Bielefeld University) on c-cut Al$_2$O$_3$ (0001) substrates, following a similar procedure as described above. These samples were patterned by Karsten Rott (Bielefeld University) using electron beam lithography and Ar ion milling. After patterning the Mn$_3$Sn layer,

gold contact pads for wire bonding were deposited. The particular sample from this series on which the measurements discussed later were performed has a thicknesses of $t_{Ru} = 2\,\text{nm}$ and $t_{Mn_3Sn} = 60\,\text{nm}$. The second sample series was prepared to evaluate the impact of a different substrate on the magnetic properties and the anomalous Nernst effect of Mn_3Sn.

The hexagonal crystal structure of Mn_3Sn, including the spin arrangement as determined by neutron diffraction, is shown in Fig. 7.1a.[222] However, many possible, and energetically equivalent, spin arrangements are currently discussed in literature.[223,236–238] As our films exhibit a similar Néel temperature $T_N \sim 420\,\text{K}$ as the bulk material ($T_{N,bulk} = 420\,\text{K}$),[222,223] the assumption that a similar spin configuration is realized here seems justified. For the thin film samples, the a-b-plane corresponds to the sample plane and the c-axis points along the surface normal. For further details on the growth and structure of the films please refer to Refs. [2] and [231].

For the first set of experiments discussed here, the Hall bars were mounted into an optical cryostat with magnetic field applied along the x-direction (perpendicular to the long Hall bar axis). These experiments were carried out at the Charles University in Prague together with Helena Reichlova (Technische Universität Dresden), Tomas Janda and Joao Godinho (both from Charles University in Prague) on samples from the first series. The setup features a chopped laser with $\lambda = 800\,\text{nm}$ and $P = 10\,\text{mW}$ that was scanned over the Hall bar while the voltage V_{ANE} along the y-direction was recorded with a lock-in amplifier, phase-locked to the laser chopper. Spatial contrast of V_{ANE} is obtained by scanning the laser in steps of $0.5\,\mu\text{m}$ over the sample along the x- and y-direction while recording the respective voltage.

For the second set of experiments at higher temperatures, the setup described in Sec. 2.5 is used, where a chopped laser with $\lambda = 633\,\text{nm}$ and $P = 5\,\text{mW}$ is installed.[1] Please note, that a different step size ($\Delta x = \Delta y = 1\,\mu\text{m}$) was used for these experiments. In this setup, an analogous voltage detection scheme was implemented. However, the magnetic field can now be applied in both, the x- and y-direction. The spot size (full width at half maximum) in both setups is $\approx 1.5\,\mu\text{m}$. The experimental configuration for both experiments can be seen in Fig. 7.1d.

Results and Discussion

Two scanning thermal gradient microscopy maps taken on a sample from the first series (MPI CPfS) at 400 K are shown in Fig. 7.2a and b. As mentioned above, the magnetic field is applied along the horizontal (x-)direction, while the voltage is picked up along the y-direction (c.f. Fig. 7.1d). The voltage contrast observed in the maps can be almost fully inverted with the magnetic field, going from a positive voltage (red) to a negative voltage (teal) for negative and positive magnetic fields, respectively. This agrees with the expectation for the anomalous Nernst effect in Mn_3Sn, where the observed voltage should invert its sign upon magnetization reversal.[103] Additionally, we expect V_{ANE} to depend on

---

[1]Please note, that this laser, installed at the time of the experiment, was replaced by the laser described in Sec. 2.5 after the experiments were finished.
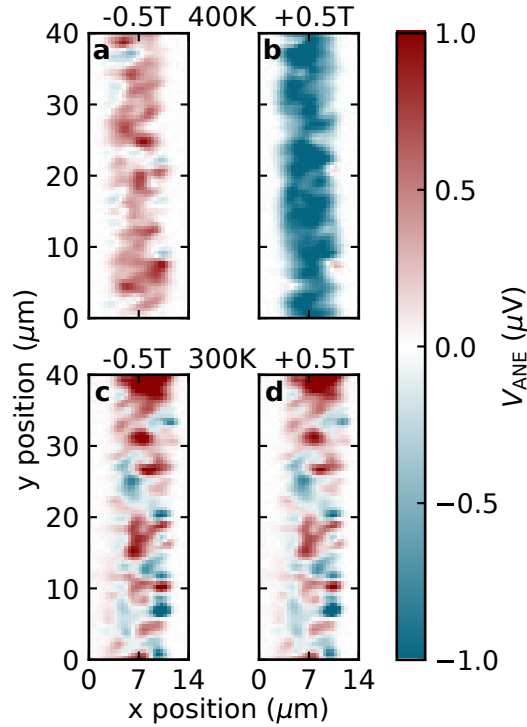
Figure 7.2: **a,b** Spatial images of V_{ANE} measured at 400 K are shown for negative and positive magnetic field ($\mu_0 H = \mp 0.5$ T), respectively. V_{ANE} changes its sign, suggesting that the voltage is of magnetic origin. **c,d** Similar measurements done at 300 K reveal a different behavior: No significant change of V_{ANE} between the map taken at a magnetic field of -0.5 T and $+0.5$ T is evident. Adapted from Ref. [2].

the orientation of the **g** vector in Mn$_3$Sn, such that we can relate the local contrast of V_{ANE} with the local orientation of **g**. One might still argue, however, that the observed contrast is due to the ordinary Nernst effect. To that end, the same measurement was carried out at 300 K. In this measurement, a completely different behavior is evident: A clear teal and red spatial contrast of V_{ANE} is also visible but seems to have a random, domain-like distribution.[2] Additionally, the spatial variation of V_{ANE}, does not seem to change for $\mu_0 H = \pm 0.5$ T. As the ordinary Nernst effect is very unlikely to exhibit such a strong spatial modulation, and should directly depend on the external magnetic field, it can be excluded as the origin of the observed signature. As 400 K is already close to $T_N = 420$ K, we thus motivate the differences in the observed behavior as follows:[103,107] At 400 K the magnetic system is sufficiently softened, by the increased thermal activation, such that the domain orientation can be controlled with the available magnetic field $|\mu_0 H| \leq 0.5$ T. In contrast, at 300 K this magnetic field is insufficient to change the domain orientation, so that a random domain state is realized here. A similar trend is also observed for bulk Mn$_3$Sn, where the coercivity decreases from $\mu_0 H_c \sim 40$ mT at 300 K to 25 mT at 400 K. As we are unable to change the V_{ANE} contrast even with 0.5 T at 300 K, a much larger coercivity than in the bulk seems to be present in our thin film.

To elucidate the exact coercivity of the sample at 400 K, we recorded maps of V_{ANE}

---

[2] Please note, that the 300 K measurement was performed before the measurement at 400 K, so that the sample was not yet polarized. However, we chose to present the measurements in the inverse order to simplify the chain of argument.

at several different magnetic fields. Since the individual maps are hard to compare on a global scale, the average signal over the region of interest (ROI, the full scanned area)

$$\overline{V_{\text{ANE}}} = \frac{\sum_{i,j} V_{\text{ANE}}^{i,j}}{N_{\text{pix}}} \tag{7.2}$$

is used as a metric, where N_{pix} is the number of pixels within the Hall bar. $N_{\text{pix}} = wh/\Delta x \Delta y$ is thus given by the width of the Hall bar $w = 7\,\mu\text{m}$, the height of the ROI $h = 40\,\mu\text{m}$ and the size of one pixel, defined by the step size of the scanning laser $\Delta x = \Delta y = 0.5\,\mu\text{m}$ between the individual voltage measurements.[3]

$\overline{V_{\text{ANE}}}$ for the abovementioned maps (taken at 400 K) is summarized in Fig. 7.3. $\overline{V_{\text{ANE}}}$ shows all salient features of a magnetic hysteresis loop, namely saturation, coercivity and remanence. The observed coercive field $\mu_0 H_c \sim 100\,\text{mT}$, is larger than what is reported in bulk Mn_3Sn (25 mT), which might be related to additional strain induced by the substrate or a slightly different stoichiometry compared to the bulk. Additionally, as expected for a Nernst type signal, the shape of the curve is antisymmetric around zero magnetic field (i.e. odd under spin reversal). The observation of a clear magnetic hysteresis loop may be surprising in the context of "ordinary" antiferromagnets. However, as discussed in the beginning of this chapter, non-collinear antiferromagnets like Mn_3Sn can show a large anomalous Hall and anomalous Nernst response resembling the response of a ferromagnet, i.e. show hysteretic behavior and large effect magnitudes.[103,107]
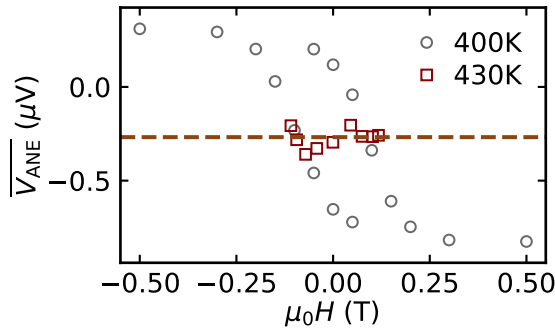
Figure 7.3: The ROI average $\overline{V_{\text{ANE}}}$ for several V_{ANE} maps taken at different magnetic fields at 400 K (gray symbols) and 430 K (red symbols) is plotted here. While a clear hysteresis loop can be seen at 400 K, no systematic evolution of the signal with the magnetic field is evident at 430 K. This suggests that the spatial and magnetic contrast is indeed caused by Mn_3Sn, having a Néel temperature of $T_N = 420\,\text{K}$. Interestingly, a finite offset voltage is always evident in the signal. Adapted from Ref. [2].

As the observed anomalous Nernst response might still be generated by a spurious ferromagnetic phase, further experiments were carried out at 430 K above T_N of Mn_3Sn. In these measurements, no clear evolution of the signal with the magnetic field can be observed at all, as one would expect above the ordering temperature of the magnetic system. Consequently, we conclude that a spurious magnetic phase can not explain the observed V_{ANE} contrast, and that the anomalous Nernst effect observed here originates from the non-collinear spin structure of Mn_3Sn as reported in literature.[103] Interestingly, both at

---

[3]Please note, that the step size of the laser is smaller than the spot size $D_L \sim 1.5\,\mu\text{m}$, so that the voltage generated in a given pixel contains a contribution from the neighboring pixels. However, the effect of this contribution is the same for all measurements, as the spot size is the same.
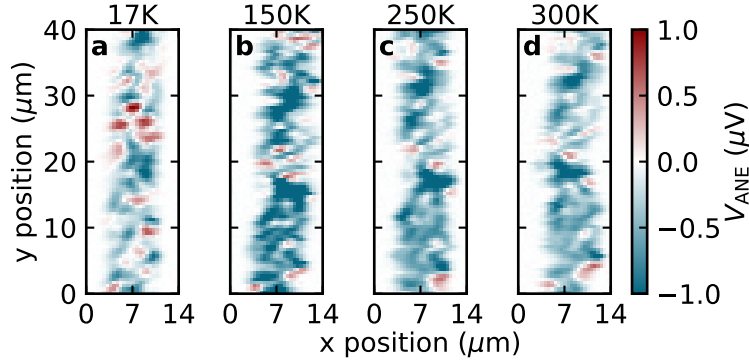
Figure 7.4: **a-d** A significant change of the spatial maps of V_{ANE} is observed when the temperature is increased from 17 K to 300 K. To perform the measurements, a magnetic field of 0.5 T was applied at 400 K. Afterwards, the field was removed and the sample cooled to 17 K. All subsequent scans were performed without applied magnetic field. Adapted from Ref. [2].

400 K and 430 K, a finite offset voltage is evident in the ROI average. Since lock-in detection was used, this signal can only be of thermal origin (or directly induced by light). We speculate that this offset is given by an inhomogeneous in-plane temperature gradient, giving rise to additional (Seebeck) signals in the sample. This will be further discussed later in this chapter (c.f. Fig. 7.7).

To further verify the origin of the observed V_{ANE} contrast to be rooted in the antiferromagnetic order of Mn₃Sn, the sample was polarized into one domain at high temperatures and subsequently cooled down to 17 K without applied magnetic field. Then, scans without any applied magnetic field were performed at increasing temperatures. Some of the resulting maps are summarized in Fig. 7.4. For the lowest temperature, the observed domain configuration differs from the one at higher temperatures, suggesting that the energy landscape of the domains changes below 50 K. This seems likely for two reasons: First, an increase of the coercivity and the exchange bias for very low temperatures was reported in similar Mn₃Sn films covered with Py.[231] Second, for bulk Mn₃Sn a spin glass phase was reported for $T \lesssim 50$ K.[107] However, the spin glass phase reported in Ref. [107] is accompanied by a large magnetization due to canting of the spins towards the c-axis (out-of-plane) direction, which we do not observe in our films. The formation of a spin glass phase in Kagome antiferromagnets is very sensitive to the strength of the anisotropies in the crystal.[239,240] Thus, as the coercivity we observe (~ 100 mT at 400 K) is significantly larger than the coercivity in bulk Mn₃Sn (~ 25 mT at 400 K), a different anisotropy in the thin film might lead to a suppression of the spin glass phase. Nevertheless, a change of the energy landscape towards low temperatures seems reasonable to assume also in the thin films. Additionally, a subtle change of the signal magnitude, which we attribute to the temperature dependence of the anomalous Nernst effect, can be observed, which will be addressed in the next paragraph.

To extract the magnitude of the anomalous Nernst effect as a function of tempera-

ture, we show the ROI average $\overline{V_{\mathrm{ANE}}}$ obtained at different temperatures in Fig. 7.5. We find a strong increase of $\overline{V_{\mathrm{ANE}}}$ from low temperatures until 150 K, where a maximum is observed. Above 150 K $\overline{V_{\mathrm{ANE}}}$ then decreases monotonously and vanishes above T_{N} as already shown above (c.f. Fig. 7.3). If the temperature evolution of $\overline{V_{\mathrm{ANE}}}$ is compared with anomalous Nernst measurements on bulk $\mathrm{Mn_3Sn}$ (red line), we find a very good agreement.[103] This fact further corroborates the absence of a spurious ferromagnetic phase.
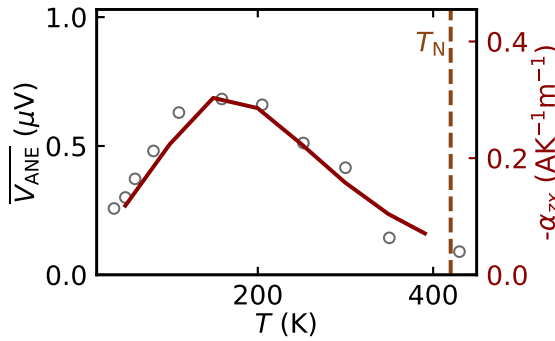
Figure 7.5: ROI average $\overline{V_{\mathrm{ANE}}}$ of the V_{ANE} maps taken at different temperatures. A good agreement of the temperature evolution of $\overline{V_{\mathrm{ANE}}}$ (gray symbols) with the Nernst coefficient reported for bulk $\mathrm{Mn_3Sn}$ (red line, Ref. [103]) can be seen. Adapted from Ref. [2].

In the following, we will demonstrate the possibility to write magnetic domains at room temperature in the $\mathrm{Mn_3Sn}$ film. To that end, we used a combination of magnetic fields and high laser power ($P = 50\,\mathrm{mW}$). The laser locally increases the temperature of the film so that the applied magnetic field is sufficient to reorient the local **g** vector in the illuminated area. As such, it is necessary, that the domain state at the operating temperature (i.e. at room temperature for typical applications) is independent of the external magnetic field to not modify the rest of the domains. This requirement is fulfilled by our material, where $\mu_0 H = 0.5\,\mathrm{T}$ is insufficient to modify the domain state at 300 K (c.f. Fig. 7.2).

A sequence of writing and erasing domains is shown in Fig. 7.6. The reading was always performed with $P = 10\,\mathrm{mW}$ and without applied magnetic field. Please note, that using a laser power of 10 mW does not affect the domain configuration at 300 K, even if the maximum magnetic field is applied (c.f. Fig. 7.2). The following procedure was used: To prepare the system into a homogeneous state (i.e. homogeneous **g**), the full device area is scanned with a high laser power ($P = 50\,\mathrm{mW}$) in $+0.5\,\mathrm{T}$ external magnetic field. The subsequently taken map ($P = 10\,\mathrm{mW}$) reveals a homogeneous V_{ANE} (c.f. Fig. 7.6a). As next step of the sequence, a negative magnetic field is applied and only the area enclosed by the dashed line in Fig. 7.6b is scanned with the high laser power. The map taken afterwards reveals an inverted contrast in the illuminated area, demonstrating the capability to prepare a domain (panel b). Please note, that the application of magnetic fields at 300 K without heating the device with the high laser power does not change the maps as already demonstrated before (c.f. Fig. 7.2c,d). In particular, scanning over the device with $P = 10\,\mathrm{mW}$ when either $\mu_0 H = \pm 0.5\,\mathrm{T}$ is applied does not change the domain configuration (i.e. the domain state is stable for $T_{\mathrm{sample}} \ll T_{\mathrm{N}}$). However, again inverting the field polarity and scanning over the original domain with the high laser power, allows to erase it again (c.f. Fig. 7.6c-e). Another important observation is that re-writing a
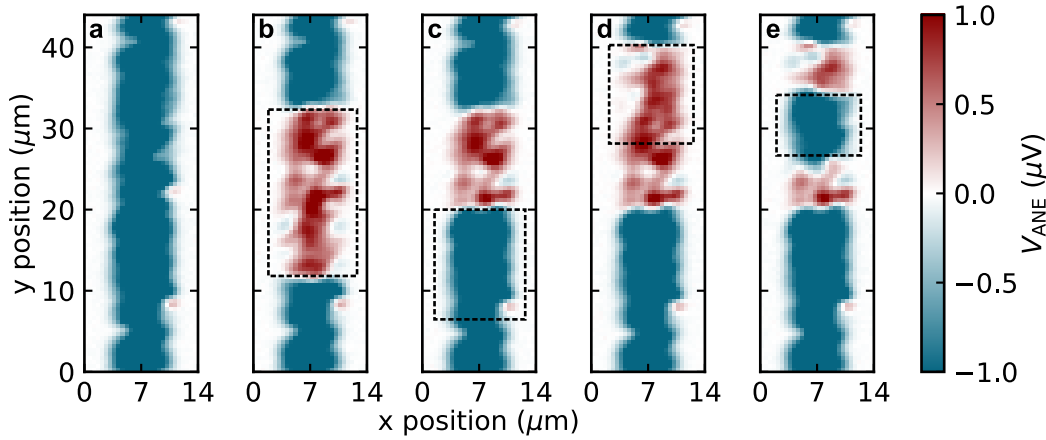
Figure 7.6: Panel **a** shows a spatial maps of V_{ANE} taken after the sample has been polarized in a single domain. Polarization is accomplished by applying a magnetic field of $\mu_0 H = 0.5\,\mathrm{T}$ and scanning the laser with $P = 50\,\mathrm{mW}$ over the full device area. In a next step, the laser ($P = 50\,\mathrm{mW}$) is scanned over the area encompassed by the dashed line while a magnetic field of $\mu_0 H = -0.5\,\mathrm{T}$ (panel **b**), $+0.5\,\mathrm{T}$ (panel **c**), $-0.5\,\mathrm{T}$ (panel **d**) and $+0.5\,\mathrm{T}$ (panel **e**) is applied. Consequently, domains can be prepared, where a positive magnetic field yields teal contrast, while negative fields yield red contrast. The sequence was performed at $300\,\mathrm{K}$ and all maps were again taken with a laser power of $10\,\mathrm{mW}$ and without applied magnetic field. Adapted from Ref. [2].

given area with the magnetic field polarity previously used does not change the contrast observed in the maps. However, writing with the opposite magnetic field polarity does reverse the sign of V_{ANE}. Consequently, deterministic control over the local domain state is possible using our heat-assisted writing approach.

We now turn to the discussion of the experiments performed on the second sample series with Al$_2$O$_3$ substrates made at Bielefeld University. To see whether (and how) the different growth conditions and the different substrate impact the anomalous Nernst effect of the Mn$_3$Sn films, a V_{ANE} map was recorded without applied magnetic field at $300\,\mathrm{K}$ (c.f. Fig. 7.7a). Very similar to the Mn$_3$Sn films of the first series, grown on MgO substrates, we find a domain-like contrast in the V_{ANE} map (c.f. Fig. 7.2c,d).[4] In addition to the domain-like contrast, an offset voltage is visible in the map, changing from negative (teal) to positive (red) as a function of the y-position. The origin of this offset will be addressed in more detail in the next paragraph. To infer the coercive field, the ROI average $\overline{V_{\mathrm{ANE}}}$ obtained from V_{ANE} maps measured at different magnetic fields is shown in Fig. 7.7b (teal symbols). A clear hysteresis loop with a coercive field of $\mu_0 H_{\mathrm{c}} \sim 20\,\mathrm{mT}$ is visible. This is comparable to the coercive field $\mu_0 H_{\mathrm{c,bulk}} \sim 40\,\mathrm{mT}$ reported for bulk

---

[4]Please note, that the magnitudes can not be directly compared between the devices, as a lower laser power ($P = 5\,\mathrm{mW}$ compared to $10\,\mathrm{mW}$ for the other measurements) and a different device geometry was used ($w = 20\,\mathrm{\mu m}$ compared to $7\,\mathrm{\mu m}$). Nevertheless, the order of magnitude of V_{ANE} agrees between the two sample series, as expected if both series consist of Mn$_3$Sn thin films.
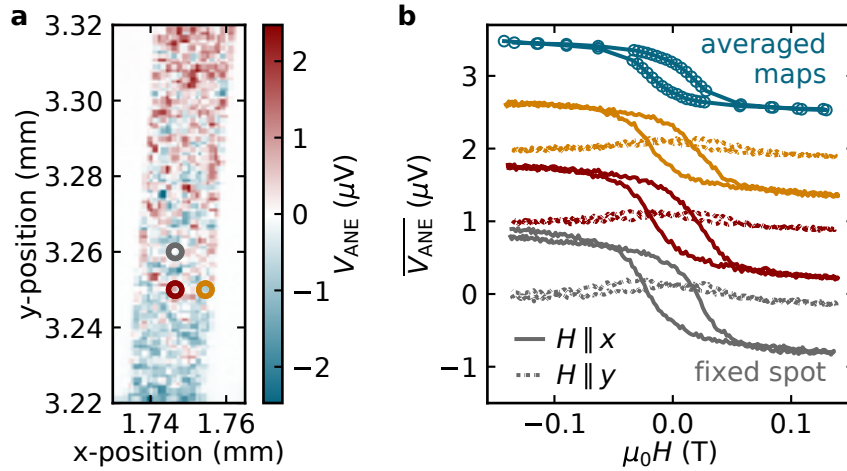
Figure 7.7: **a** Map of V_{ANE} measured at 300 K on a Ru(2 nm)/Mn$_3$Sn(60 nm) sample from the second sample series (made at Bielefeld University) without applied magnetic field. A domain-like pattern is observed, very similar to the measurements on the Mn$_3$Sn samples from the first series (c.f. Fig. 7.2c,d). Additionally, a change from positive (red) to negative (teal) V_{ANE} is evident along the vertical (y-)direction. This change is attributed to in-plane thermal gradients giving rise to a finite Seebeck voltage, which is superimposed onto the voltage generated by the anomalous Nernst effect. **b** The ROI average $\overline{V_{ANE}}$ obtained from several V_{ANE} maps taken for different magnetic fields applied along the x-direction is shown (teal symbols). Additionally, measurements of V_{ANE} as a function of the magnetic field measured with the laser spot at a fixed position are plotted. The positions of these measurements are shown by the circles in panel **a**. The hysteresis loop of the ROI average (teal symbols) shows a very similar behavior as the field dependent measurements taken with the laser at a fixed position (lines). This suggests, that the magnetic domain size is much smaller than the spot size of the laser. Only a small modulation is observed for magnetic fields applied parallel to the voltage detection direction (dashed lines, $H \parallel y$). We attribute this modulation (which is symmetric in field) to a finite magnetic field dependence of the Seebeck effect. Please note, that for the measurements in panel **b** the mean value of the V_{ANE} has been subtracted and a vertical shift of 1 μV was added for better visibility.

Mn$_3$Sn at 300 K,[103,107] while it is at least one order of magnitude smaller than the coercive field observed for the first sample series ($\mu_0 H_c > 0.5$ T at 300 K). We speculate, that this is rooted in a slightly larger net magnetization in the second sample series. This larger magnetization, due to the increased Zeeman contribution to the free energy, would allow to switch the magnetization (and thus the antiferromagnetic spin structure) already with a smaller magnetic field. However, further experiments to elucidate the impact of the growth conditions on the magnetic properties and the transport response are still ongoing, so that no final statement in this respect can be given.

Before addressing further implications of the magnetic field dependence, a possible reason for the y-position dependent offset voltage observed in the V_{ANE} map (c.f. Fig. 7.7a, second sample series) will be discussed shortly. We attribute this offset to in-plane ther-

mal gradients, giving rise to an additional Seebeck voltage on the measurement contacts: The Mn_3Sn Hall bar is terminated by a Au/Mn_3Sn junction at either side (i.e. at the top and the bottom), where the Au contact pads, used for bonding the device to the chip carrier, touch the Hall bar. Thus, a temperature difference between these Au/Mn_3Sn junctions used for measuring V_{ANE} can give rise to a non-zero Seebeck voltage.[93] If the laser is focused close to the top of the Hall bar, the upper Au/Mn_3Sn junction will have a higher temperature compared to the lower junction. Thus, a positive voltage (red) is observed. When the laser is moved towards the lower end of the Hall bar, the lower Au/Mn_3Sn junction will have a higher temperature compared to the upper junction, so that the temperature difference and thus the voltage due to the Seebeck effect will be inverted, i.e. negative (teal). Finally, with the laser spot in the center of the Hall bar, both junctions will have an equal temperature, so that the Seebeck voltage vanishes.[5] Please note, that this is likely also the origin of the offset observed in the V_{ANE} maps taken for the first sample series (c.f. Fig. 7.3). For the first sample series, however, the impact of the spot position on the Mn_3Sn Hall bar is much lower, since no gold contact pads were used (i.e. the full Hall bar including contact pads is made of Mn_3Sn). Thus, the two metal junctions which would generate the Seebeck voltage due to in-plane temperature differences in this case are the Mn_3Sn/Al junctions, where the wire bonds are bonded to the Mn_3Sn bond pads. As the bond pads are far away from the illuminated (central) part of the Hall bar (c.f. Fig. 7.1c), the exact position of the laser spot does not significantly impact the temperature difference there.

In the following, we will try to infer an upper limit for the size of the individual magnetic domains of the Mn_3Sn thin films. To this end, we performed two complementary experiments: Multiple magnetic field scans with a fixed laser spot position which yield $V_{ANE}(H)$ at a fixed position (x,y) on the sample were recorded. These are then compared to the global average $\overline{V_{ANE}}$ of the full maps taken for different, fixed magnetic fields. The results are shown in Fig. 7.7b. First, no clear difference in coercivity and saturation can be observed for the individual spots (gray, red and turmeric lines) and the global maps (teal symbols). Additionally, no Barkhausen steps can be seen for the field dependent V_{ANE} measurements with a fixed laser spot position, as one might expect if only a few domains are contributing to the signal, and the inversion of each domain is instantaneous.[241,242] In order to see Barkhausen steps, the energy landscape of the material would need to feature several separate energy minima, where the domain orientation in one domain "jumps" from one to the next minimum upon magnetization reversal (i.e. the domain orientation does not rotate coherently from one direction to the next).[242] As Mn_3Sn has three energetically equivalent domains due to its hexagonal symmetry in the a-b plane (c.f. Fig. 7.1), this assumption seems reasonable.[235] Considering our measurement resolution $\Delta V_{ANE} \sim 20\,nV$, we conclude that the maximum signal generated by an individual domain must be smaller than ΔV_{ANE} (otherwise, steps would be visible). Additionally, when the Mn_3Sn is fully polarized, all domains contribute, so that the size of $V_{ANE} \sim 0.8\,\mu m$ corresponds to the signal generated by all domains in the spot (where we

---

[5]If the laser is outside of the Hall bar, only very little of the light is absorbed (Al_2O_3 is transparent), so that no Seebeck voltage is expected in this case.

assume for simplicity, that the individual domain contributions add up). Thus, a rough estimate of the number of the magnetic domains N_{MD} in the laser spot is given by

$$N_{MD} \gtrsim V_{ANE}/\Delta V_{ANE} = 40. \tag{7.3}$$

Furthermore, the diameter of the laser spot is known (where we use the full width at half maximum $D_L \approx 1.5\,\mu m$), so that the maximum diameter of the magnetic domains can be inferred

$$D_{MD} \lesssim \sqrt{\frac{D_L^2}{N_{MD}}} \approx 240\,nm \tag{7.4}$$

Although the exact size of the crystallites is unknown in the film studied here, island growth with islands roughly 400 nm in size was observed for similar Mn$_3$Sn films.[231] This is of the same order of magnitude as the magnetic domain size estimated here.

Please note that this "domain"-model neglects all intricate details of the exact generation of the thermovoltage (scaling, intermediate magnetic states, short circuits of the anomalous Nernst voltage by the adjacent domains that are not illuminated, etc.) and is only used here to estimate the possible impact of the magnetic domain size on the observed contrast. Despite this rather simplistic approach, the comparison of global and local contrast suggests that the determination of the magnetic domain size using the scanning thermal gradient approach should be possible: If the spot size becomes comparable to the grain size (or the voltage resolution is increased), steps in the hysteresis loop should be visible. Please note, that these experiment, viz. where the magnetic field is swept while the laser spot and focus are at a constant position, require to have a completely stiff setup (i.e. a setup where the spot position is perfectly constant for any given applied magnetic field). This has to be evaluated carefully, e.g. by placing the laser close to the Hall bar edge and measuring the reflectance of the sample during a magnetic field scan. An alternative method to gain access to the microscopic domain structure would be to use a heated atomic force microscope tip as heat source to get spatial resolution on the order of a few 10 nm.[243]

Since for the samples of the second series, we have direct control of the **g** vector already with comparably small fields, we can use the vector magnetic field capabilities of the setup (c.f. Sec. 2.5) to evaluate what happens when the magnetic field is applied parallel to the voltage direction ($H \parallel y$). To this end, we take maps for a magnetic field $\mu_0 H \approx$ 130 mT applied along different directions with respect to the x-direction ($\alpha = 0$). In the ROI average of the maps summarized in Fig. 7.8a we can see the shape expected for the anomalous Nernst effect: i.e. $V_{ANE} \propto \cos(\alpha)$.[6] Consequently, we find $\overline{V_{ANE}} \approx 0$ if the magnetic field is applied parallel to the direction along which the voltage is detected ($\alpha = 90°$).

We will now turn to discuss some individual maps at specific angles (see colored circles in $\overline{V_{ANE}}$ plot in Fig. 7.8a). First of all, a fully saturated state is observed for the mag-

---

[6]The $\cos(\alpha)$ behavior stems from the fact, that the electric field generated by the Nernst effect is always perpendicular to a **H** (c.f. Eq. (7.1)), so that $V_{ANE} \propto (\mathbf{E}_{ANE})_y$ (as the voltage is measured along the y direction). Thus, we except a finite V_{ANE} only if there is a finite **g** component along the x-direction.
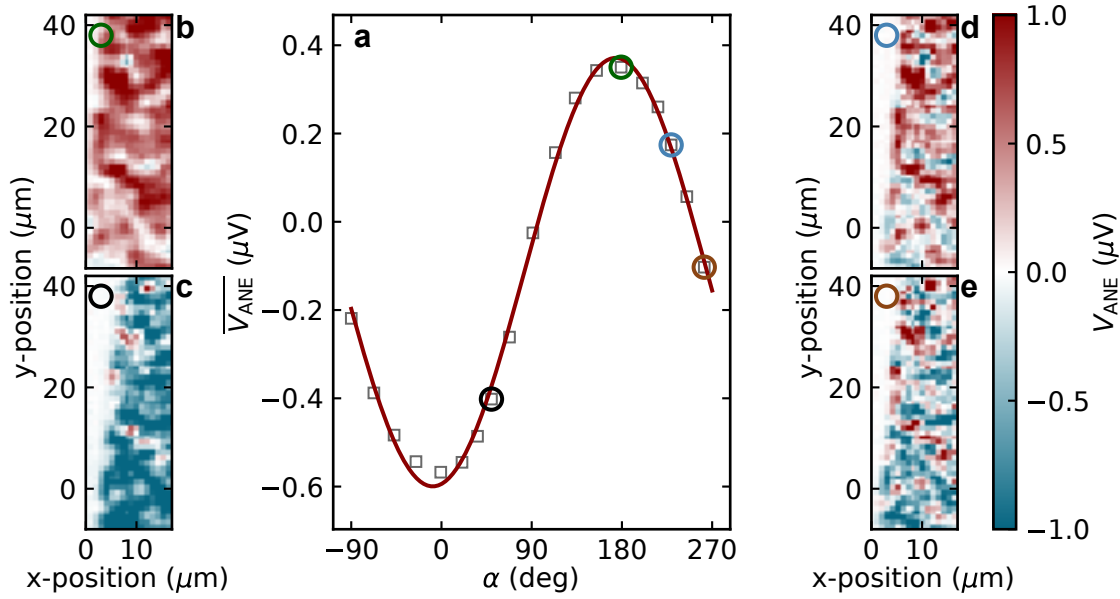
Figure 7.8: **a** The ROI average $\overline{V_{\mathrm{ANE}}}$ of V_{ANE} maps taken at different angles of the applied magnetic fields with respect to the x-direction. A $\overline{V_{\mathrm{ANE}}} \propto \cos(\alpha)$ behavior is observed as expected for the anomalous Nernst effect. **b-e** The respective V_{ANE} maps shown by the colored circles in panel a are depicted here. Surprisingly, the local anomalous Nernst effect does not change continuously and homogeneously according to the expected $V_{\mathrm{ANE}} \propto \cos(\alpha)$ behavior, but seems to break into domains. In particular, it is even non-zero if the magnetic field is aligned with the direction along which V_{ANE} is measured (i.e. $\alpha = 90°$). This suggests, that the local orientation of **g** does not rotate coherently with the magnetic field, but maintains a component along the x-direction which is non-zero even when the magnetic field is along the y-direction. Interestingly, the system populates red and teal domains equally in this case (i.e. for **H** ∥ x), so that the ROI averages. The applied magnetic field for the measurements shown here is $|\mu_0\mathbf{H}| = 130\,\mathrm{mT}$.

netic field along the x-direction (panel b). This is fully consistent with $V_{\mathrm{ANE}} \propto \cos(\alpha)$. Second, at intermediate angles (45°, 135°), still a mostly saturated behavior with a lower magnitude is observed (panels c and d). For these intermediate angles, already some domains of the respective opposite color (red and teal) are present. This is very surprising, as $V_{\mathrm{ANE}} \propto \cos(\alpha)$ should decrease homogeneously, if the **g** vector would rotate with the magnetic field. However, the observed behavior can only be consistently explained if there is a nucleation of domains which have a **g** vector which is not aligned with the magnetic field. In particular, with H parallel to the y-direction (i.e. parallel to the voltage contacts, where no anomalous Nernst effect should be observed if $V_{\mathrm{ANE}} \propto \cos(\alpha)$), still a clear V_{ANE} contrast is observed (panel e). Interestingly, a roughly equivalent population with red and teal domains is realized for $\alpha = 270°$, leading to the vanishing ROI average observed in panel a. We thus conclude, that the local orientation of **g** does not coherently rotate with the external magnetic field.

In the following a model to explain the deviation from the expected $\cos(\alpha)$ behavior
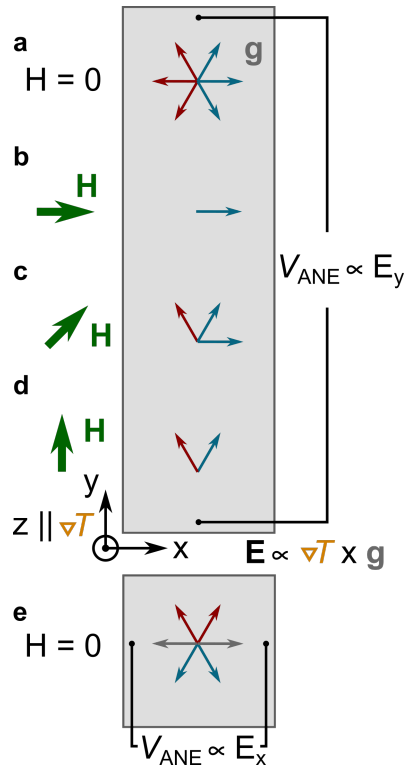
Figure 7.9: **a** After growth, the Mn_3Sn sample will have an equal distribution of all possible magnetic domains in the a-b-plane (c.f. Fig. 7.1). **b** If a magnetic field is applied along the x-direction (corresponding to a $[2\bar{1}\bar{1}0]$ crystal direction) a single domain will be preferred. Here, a homogeneous contrast will be visible in the V_{ANE} maps. **c** The possible domain configurations for a magnetic field applied at 45° from the x-direction is shown. A finite population of domains with opposite projection of **g** on the x-direction (red arrow) emerges. Thus, in this case a local contrast with of V_{ANE} might be visible, so that at least the average voltage of the map will be lowered. **d** If the magnetic field is applied parallel to the y-direction (corresponding to a $[01\bar{1}0]$ crystal direction), two domains which generate V_{ANE} signals of opposite polarity are equally populated. In this configuration, although the global average will vanish, it is still possible to observe local Nernst voltage signals. **e** The anomalous Nernst effect of the domains aligned with the x-direction generates an electric field only along the y-direction. Consequently, no voltage drop can be measured for these domains if the voltage is detected along the x-direction, so that a different behavior should be evident in this configuration.

of the local V_{ANE} contrast and a way to verify this model will be proposed. When considering the contribution of the different possible domains of Mn_3Sn, three equivalent axes rotated by 120° around the c-axis of the hexagonal crystal are present in the a-b-plane (c.f. Fig. 7.1). If we consider that our Hall bar is oriented as shown in Fig. 7.9 (i.e. with the x-direction along $[2\bar{1}\bar{1}0]$ and the y-direction along $[01\bar{1}0]$)[7] and the sample was never polarized, all six domains will be equally populated (Fig. 7.9a). Thus, the average of V_{ANE} over all domains will vanish, but a local variation should still be evident when scanning over the sample due to stochastic effects. This statement is only true as long as the magnetic domain size D_{MD} is not significantly smaller than the laser spot size D_L. The latter requirement and the impact of the ratio D_{MD}/D_L can be motivated as follows: If $D_{MD}/D_L \ll 1$ the ensuing voltage is the average over a large number $N \gg 1$ of magnetic domains, such that the stochastic variations (and thus the generated local voltage) in the laser spot are small (the variations in the laser spot will likely scale like N^{-1}). Thus, no (or a very small) local contrast of V_{ANE} will be observed, for the given domain configuration (c.f. Fig. 7.9a). If $D_{MD}/D_L \lesssim 1$, however, the number of domains $N \gtrsim 1$ will be small enough for the stochastic variations to be significant. Thus, a local voltage contrast can be observed in this case. In the limiting case, where $D_{MD}/D_L > 1$, a single magnetic domain will be illuminated, so that the local variation of V_{ANE} directly corresponds to the orientation of an individual domain. Thus, a histogram of the V_{ANE} map should reveal

---

[7]This corresponds to the alignment of the Hall bar during the measurements shown in Fig. 7.8.

four distinct voltage levels, considering the domain configuration shown in Fig. 7.9a (i.e. +1, +0.5, −0.5 and −1). If we now apply a magnetic field along one of the high symmetry directions (e.g. the x-direction), a single domain is preferentially populated (panel b), resulting in saturated, spatially homogeneous contrast (here **g** is perpendicular to the V_{ANE} measurement direction and ∇T, resulting in a maximum anomalous Nernst signal). If we now rotate the magnetic field to 45° (panel c), there are three possible domains which can be populated, where one of the domains has an opposite projection of the **g** vector on the x-direction (i.e. would generate red local contrast in a dominantly teal map). As such, although the population of the different domains will not be equal, still some (negative/teal) signal remains (corresponding to a net **g** pointing to the right). For a further rotation of the magnetic field perpendicular to x, an equal population of the two domains shown in panel d will be realized. Consequently, although the global average will cancel in this configuration, a local contrast should still be visible. If we compare this expectation with the observations shown in Fig. 7.8, we can identify all salient features described here. Please note, that the histogram does not reveal distinct voltage levels, which we attribute to the magnetic domain size being smaller than the laser spot size, allowing the realization of a multitude of voltage levels.

However, a reference experiment on a Hall bar rotated by 90° (c.f. Fig. 7.9e) is required to be certain, that the model holds. In this configuration, V_{ANE} should vanish for **H** ∥ **x**, as the electric field generated by the anomalous Nernst effect of the domains with **g** vector along the x-direction is aligned with the y-direction. Consequently, V_{ANE}, measured along the x-direction, should vanish in this case (also locally).

Summary

In this chapter, spatially resolved measurements of the anomalous Nernst effect on Mn₃Sn thin films were presented. For a first sample series, prepared on MgO substrates, an anomalous Nernst effect in agreement with reports in bulk Mn₃Sn was observed. While the magnetic coercivity of the thin films is 100 mT at 400 K (compared to ∼ 25 mT in the bulk), the magnetic coercivity at 300 K was larger than the experimentally available magnetic field ($\mu_0 H = \pm 0.5$ T). We demonstrated that this strong dependence of the coercivity on temperature can be utilized to implement a domain writing and reading sequence, allowing to prepare a defined antiferromagnetic domain state of the non-collinear antiferromagnet at 300 K. The writing is accomplished with a combination of high laser power and magnetic fields, where the prior locally reduces the coercivity by heating, leading to a reorientation of the illuminated domains by the magnetic field. In turn, we use the spatial resolution of our technique to verify the resulting antiferromagnetic domain state (i.e. the local orientation of the **g** vector of the Mn₃Sn thin films). The experimental control over the local antiferromagnetic domain structure demonstrated here is a key requirement e.g. for proposed measurements of current induced domain wall motion in non-collinear antiferromagnets.[85,218]

Additionally, a second series of Mn₃Sn thin films, grown on Al₂O₃ substrates, showed a much lower magnetic coercivity $\mu_0 H_c \sim 20$ mT at 300 K, close to the coercivity of bulk

Mn$_3$Sn. We used this low coercivity and the resulting control over the orientation of the magnetization to investigate the impact of magnetic domain formation and the domain pattern on the local and global anomalous Nernst response. From the absence of Barkhausen steps in magnetic field dependent measurements, and using a very simple estimation, we concluded that the size of the magnetic domains is smaller than $\sim 240\,\text{nm}$, which is of the same order of magnitude as the expected structural grain size. Additionally, the local anomalous Nernst contrast measured for different magnetic field orientations suggested, that magnetic domains having a **g** vector not aligned with the external magnetic field are populated. To explain this finding, a model based on the hexagonal crystal symmetry of Mn$_3$Sn being reflected in its magnetic energy landscape was proposed. Good qualitative agreement of the local anomalous Nernst response expected from this model with the experimental observations was found. If this model holds, the determination of the exact symmetry and population of the magnetic domains from spatially resolved anomalous Nernst measurements should be possible, so that future experiments might allow to clarify the exact domain structure realized within Mn$_3$Sn. However, further experiments have to be carried out to verify the validity of the model.

Chapter 8

SUMMARY AND CONCLUSIONS

In this chapter, we summarize the main experimental results presented in each individual chapter. Each of these short summaries is then combined with a short conclusion on the relevance of the work from a broader perspective.

Chapter 2 outlined the experimental setups used during this thesis work. In particular, several magnet cryostats as well as room temperature magnet setups were adapted for transport experiments. To that end, a number of measuring inserts to be used in conjunction with the different magnet setups and cryostats were designed and assembled. What these all have in common is that they accommodate a 32 contact ceramic chip carrier onto which the samples are mounted. This chip carrier system allows for a rapid sample exchange from one setup to the other. A key aspect of the design work was to engineer the chip carrier system (including all related wiring, the integration of heaters and temperature sensors, etc.) in such a way that it fits into a 24.5 mm bore and thus is compatible with all magnet transport setups used in the group. Furthermore, a program implemented in Python was developed and established for instrument control and measurement automation (c.f. App. C). Finally, a description of the measurement conventions and measuring techniques used for the electrical measurements was presented (c.f. Sec. 2.6). Taken together, the facilities required to carry out state-of-the-art electrical transport experiments up to high magnetic fields $|\mu_0 H| \leq 12.5\,\mathrm{T}$ and from $2\,\mathrm{K} \lesssim T \leq 600\,\mathrm{K}$ have been established at the institute in the course of this thesis work.

Measurements of the spin Hall magnetoresistance (SMR) in heterostructures of a disordered magnetic insulator and a spin Hall active metal were described in Ch. 3. Two systems of current scientific interest had to be discerned. The first system (c.f. Sec. 3.1) consisted of bilayers of non-crystalline (as-sputtered) $Y_3Fe_5O_{12}$ (YIG) and Pt. The non-

crystalline YIG is a paramagnetic insulator and Pt a spin Hall active metal. In these bilayers – although they did not exhibit any spontaneous (long-range) magnetic ordering – a magnetoresistance with a dependence on the orientation of the magnetic field characteristic of spin Hall magnetoresistance or Hanle magnetoresistance (HMR) was found to exist even up to 300 K. Additionally, the magnetoresistance amplitude increased towards higher temperatures, contrary to what would be expected if it depended directly on the induced magnetization: the magnetization should decrease like $1/T$ in a paramagnet. Furthermore, the evolution of the magnetoresistance with the magnetic field strength was not consistent with the naive notion of an interaction between the individual magnetic moments in the non-crystalline YIG and the interfacial spin accumulation in Pt. While the dependence of the resistivity on the magnetic field could be consistently explained, the evolution of the observed magnetoresistance with temperature was not captured by this model. Finally, we note that an alternative explanation using the Hanle magnetoresistance was discarded, due to the large magnitude of the magnetoresistance in our samples compared to the HMR reported in literature.

In a next step, measurements on bilayers of the uniaxial antiferromagnetic insulator Cr_2O_3 and Pt or Ta were addressed in Sec. 3.2. In these bilayers, the evolution of the magnetoresistance in the antiferromagnetic phase, with the magnetic field applied along different directions, was consistently explained in the SMR framework. Hereby, the presence of a small uncompensated moment was assumed to model the magnetic response of the antiferromagnet. Our results showed once again that the SMR can serve as a powerful tool to access the microscopic magnetic structure which cannot easily be determined with other experimental techniques. Furthermore, the development of the magnetoresistance across the magnetic phase transition was investigated: Very similar to the non-crystalline $Y_3Fe_5O_{12}$/Pt bilayers, a magnetoresistance with the fingerprint of the SMR or HMR was found. This effect persisted with a characteristic saturating behavior well above T_N. Interestingly, the magnetoresistance in the Cr_2O_3/Pt or Ta heterostructures exhibited a magnitude comparable to the SMR in typical heterostructures of a ferromagnetic insulator and a spin Hall active metal. Similar to the non-crystalline YIG/Pt bilayers, the magnetoresistance amplitude as a function of the magnetic field strength suggested that the induced net moment would again be relevant, while the temperature dependence contradicted this notion. This fact, and the unexpectedly large magnitude of the magnetoresistance, led us to revisit the HMR theory framework. We found a good agreement between the HMR theory and the experimental data for specific circumstances: If a significant decrease of the diffusion constant was assumed (i.e. a decrease of the time required for the electron spins to dephase), the field dependent magnetoresistance could be consistently modeled in the HMR theory framework. Measurements of the resistance of the Cr_2O_3 layer provided a clue towards a possible origin of the modified diffusion constant, where the Cr_2O_3 layers revealed a much lower thermal activation energy for the resistance compared to its band gap and thus could be assumed to have a finite conductivity at 300 K.

To understand all these experimental findings in a consistent way, we proposed an extension or modification of the present HMR and SMR theory frameworks, merging both into a joint theory. This theory included a possible exchange enhancement of the HMR,

with $H \rightarrow H + H_{\mathrm{ex}}$ as already proposed in Ref. [63] and additionally considered not only spin relaxation but also spin diffusion effects (c.f. Sec. 3.2). Several reference experiments to verify the validity of the model were proposed in this section.

Overall, we believe to have made the first step towards a generalized SMR and HMR theory framework, incorporating all possible origins of spin loss in the system. Furthermore, it should be possible to reinforce the implications of this model by comparing time dependent measurements of the magnetoresistance in bilayers of a normal metal and an insulating or conducting ferromagnet. Between the two limiting cases, a clear difference between the "original" SMR which likely happens on the timescale of magnetization dynamics ($\sim$ GHz) and the modified spin Hall "mediated" magnetoresistance (i.e. the diffusion- and exchange-enhanced HMR) which can also depend on electron dynamics ($\sim$ PHz) should be evident.

Chapter 4 focused on the non-local magnon-mediated magnetoresistance (MMR). Again two sets of experiments were presented, both carried out on the best established system for non-local detection of pure spin transport, viz. $Y_3Fe_5O_{12}$/Pt bilayers. For the first set of experiments presented in Sec. 4.1, the YIG layer in between the two Pt electrodes was removed using a focused ion beam and the ensuing changes to the local and non-local magnetoresistance were studied. Most importantly, we found that once the $Y_3Fe_5O_{12}$ channel was removed, no non-local magnetotransport signal could be observed, suggesting that the magnetic insulator is crucial for this experiment, as expected for a magnon-mediated spin transport effect. Additionally, we found that even the Ga ion irradiation used for imaging the devices is highly effective in altering the local and non-local magnetotransport properties.

Taken together, we could exclude that there are significant spurious contributions – like phonon transport through the substrate – to the non-local magnetotransport signature in $Y_3Fe_5O_{12}$/Pt heterostructures apart from the established transport of magnons.

In the second part of the chapter (c.f. Sec. 4.2), we connected to the experiments in Ch. 3 by studying the local (SMR) and non-local (MMR) magnetoresistance in $Y_3Fe_5O_{12}$/Pt heterostructures from 300 K to 600 K, well above the Curie temperature $T_C \sim 560$ K of YIG. In contrast to previous studies of the non-local MMR towards high temperature, where localized transient current heating was used, we employed steady state heating of the full device and probed the transport only with a small excitation current. This allowed to rule out higher order (magneto-thermal) contributions to the non-local magnetotransport response. Interestingly, we found a sharp drop of both, the SMR and MMR around 500 K, well below T_C of YIG. This sharp drop was associated with irreversible damage to the devices due to interdiffusion or annealing processes in the structure. Nevertheless, two subsequent measurement runs repeated on the same devices revealed the same salient features in the low temperature region ($T < 450$ K). Namely, for the SMR we found that the magnitude of the magnetoresistance is directly proportional to the net magnetization of YIG before the annealing set in. In contrast, the non-local MMR increased with a power law T^α, where the power decreased from $\alpha \sim 3/2$ at 300 K to $\alpha \sim 1/2$ at 450 K likely due to the increased population of thermal magnons, acting as scattering centers for

the non-equilibrium magnons mediating the non-local magnetotransport. Additionally, the cross conductivity through YIG between the two electrically insulated Pt wires used for the transport was extracted from the non-local offset voltage. The observed spurious transport response closely resembled the experimental signature reported as evidence for a large non-local spin transport in non-crystalline YIG films in Ref. [136]. Based on our data, we could only refute this interpretation – all salient features could be explained in terms of a purely electrical leakage current, while a magnetic origin of these signals could be excluded. Furthermore, good agreement of the thermal activation energy of the YIG resistivity with reports in literature was observed.

As a possible next step, we anticipate that by replacing Pt with Ta, the issue of inter-diffusion might be overcome, due to Ta being less prone to diffusion.[244] Additionally, it would be important to also gain access to magnetic fields larger then the 70 mT available in our home built high-temperature setup. Higher magnetic fields should allow to evaluate whether similar effects as reported in Ch. 3 are present in the paramagnetic phase of YIG, as this is the best studied material to date.

In summary, the studies discussed in Ch. 4 verify the importance of magnons and their transport properties for the discussion of the non-local magnetotransport response. Our findings thus call into question the conclusion drawn from several reports of non-local magnon-based transport in samples in which no spontaneous order, and thus no magnons should be present.

In Ch. 5, the local and non-local thermal magnetotransport (viz. the spin Seebeck effect, SSE) was investigated on Cr_2O_3/Pt bilayers. Most of the salient features found by Yuan et al. in Ref. [60] in similar samples – and put forward as evidence for superfluid spin transport – were evident also in our data. In particular, the local and non-local SSE increased towards low temperatures ($T \lesssim 10\,\mathrm{K}$) and saturated there. Interestingly, the saturation value depended on the magnetic field magnitude, as one would anticipate if the net magnetization was relevant for the observed signature. Assuming that the spin Seebeck effect is caused be the induced magnetization (i.e. by the small canting of the two magnetic sublattices in Cr_2O_3 towards the magnetic field), we could consistently explain all measured data. Most importantly, however, the dependence of the non-local SSE on the separation of the two Pt wires d_{NL} evident in our experiments was different to the distance scaling found by Yuan et al. in Ref. [60]. Namely, we observed an exponential decay of the non-local SSE ($\propto \exp(-l_m d_{NL})$), while the authors of Ref. [60] reported a dependence on the distance like $\propto (l_m + d_{NL})^{-1}$, where l_m is the decay length. As the distance dependence is the smoking gun signature of superfluid spin transport – the main claim of their paper – we could only conclude that at least in our sample, there was no evidence for spin superfluidity.

In the future, however, more experiments should be carried out, particularly for small contact separations, where a linear response (i.e. MMR) might be found in the non-local magnetotransport. To that end, a new set of samples with the easy axis in the plane have to be made to fulfill the geometrical requirements of the non-local magnon-mediated magnetoresistance (i.e. the spin accumulation and the two magnetic sublattices have to be

collinear). Such samples would allow to study both, the (antiferromagnetic) magnon driven transport as well as superfluid spin transport, if it is realized in such bilayers.

Chapter 6 was dedicated to the investigation of the topological contributions to the transverse magnetoelectric and magnetothermal transport response in thin films of $Mn_{1.8}PtSn$, i.e. the Hall effect and Nernst effect. $Mn_{1.8}PtSn$ was shown to host antiskyrmions and a large topological Hall effect,[4,200,201] making it an ideal candidate for the study of such topological contributions to electrical transport. To enable the magnetoelectric and magnetothermal characterization in one device, a novel measurement technique was established, which we named "alternating thermal gradient technique". This technique was based on the periodic inversion of the direction of heat flow using a symmetric set of heaters on both side of the $Mn_{1.8}PtSn$ Hall bar. By acknowledging that the thermoelectric response due to this gradient consequently inverted too, spurious voltage contributions due to the cryostat and measurement devices could be distinguished from the thermovoltages generated by the device. Using this approach, we could not only reproduce the large topological Hall effect, but additionally verify the presence of a similarly large topological Nernst effect in $Mn_{1.8}PtSn$. Furthermore, the possibility to combine the Hall and Nernst signal to extract what we called the "topological quantity" was demonstrated. This novel approach allowed to gauge the presence of a topological transport contribution to the Hall and Nernst signals without requiring magnetization measurements. In particular, since no measurements performed in different setups were required, possible artifacts due to the comparison of magnetotransport and magnetization measurements could be excluded.
All in all, we are confident that the "topological quantity" will proof exceedingly helpful for elucidating the topological properties of nanopatterned materials and future devices incorporating topological transport effects.

Finally, in Ch. 7 spatial images of the anomalous Nernst effect generated locally by a focused laser induced heat gradient were investigated in thin films of the non-collinear antiferromagnet Mn_3Sn. The significant anomalous Nernst effect reported in bulk Mn_3Sn[103] was also observed in the thin films investigated here. Furthermore, a similar temperature dependence as reported for bulk Mn_3Sn was found. Additional measurements above T_N revealed a vanishing signal, providing final proof of the magnetic origin of the observed signal. Interestingly, we found a strong dependence of the coercivity (i.e. switching fields) on temperature, where the switching field was reduced significantly towards high temperatures. This allowed to manipulate the antiferromagnetic domain structure at elevated temperatures with external magnetic fields. The temperature dependent anisotropy was utilized in a next step to implement an experimental scheme for preparing the system into a defined antiferromagnetic domain state: By combining a focused high power laser and magnetic fields, the magnetic state could be modified in the illuminated areas, and subsequently monitored via the magnetothermal response using a lower laser power. This experimental feat might prove particularly important to study current induced domain wall motions, where a current pulse is sent through the device

in order to move the antiferromagnetic domain walls via the spin transfer torque. To accomplish this goal, control over the domain structure and a readout scheme are required, which have been demonstrated in this work. Finally, another set of experiments was used to evaluate potential further possibilities of the method. In particular, the scanning thermal gradient microscopy technique should allow to infer the antiferromagnetic domain structure, domain distribution as well as the domain size.

In summary, we hope that the results put forward in this thesis will convince the reader of the great usefulness of (magneto-)transport measurements. Such measurements can serve as a powerful tool for the investigation of a multitude of micro- and macroscopic properties of a given material. Particularly for the understanding of thin film systems, insights gained from transport experiments can be crucial: Many properties of the electronic system like magnetism, structure and topology cannot be readily accessed in thin films by other, more direct, measurement techniques. On the downside, the assignment of a specific transport response to a particular effect can be exceedingly challenging, as different models yielding a given transport response can be found. Nevertheless, transport experiments enable straightforward access to a wide array of internal properties of the electronic system, where magnetism and topology form only a small subset of possibilities to be investigated.

LIST OF PUBLICATIONS

[1] G.-H. Park, H. Reichlova, R. Schlitz, M. Lammel, A. Markou, P. Swekis, P. Ritzinger, D. Kriegner, J. Noky, J. Gayles, Y. Sun, C. Felser, K. Nielsch, S. T. B. Goennenwein, and A. Thomas, Physical Review B **101**, 060406(R) (2020).

[2] H. Reichlova, T. Janda, J. Godinho, A. Markou, D. Kriegner, R. Schlitz, J. Zelezny, Z. Soban, M. Bejarano, H. Schultheiss, P. Nemec, T. Jungwirth, C. Felser, J. Wunderlich, and S. T. B. Goennenwein, Nature Communications **10**, 5459 (2019).

[3] R. Schlitz, P. Swekis, A. Markou, H. Reichlova, M. Lammel, J. Gayles, A. Thomas, K. Nielsch, C. Felser, and S. T. B. Goennenwein, Nano Letters **19**, 2366–2370 (2019).

[4] P. Swekis, A. Markou, D. Kriegner, J. Gayles, R. Schlitz, W. Schnelle, S. T. B. Goennenwein, and C. Felser, Physical Review Materials **3**, 013001 (2019).

[5] M. Lammel, R. Schlitz, K. Geishendorf, D. Makarov, T. Kosub, S. Fabretti, H. Reichlova, R. Huebner, K. Nielsch, A. Thomas, and S. T. B. Goennenwein, Applied Physics Letters **114**, 252402 (2019).

[6] R. Schlitz, T. Helm, M. Lammel, K. Nielsch, A. Erbe, and S. T. B. Goennenwein, Applied Physics Letters **114**, 252401 (2019).

[7] K. Geishendorf, R. Schlitz, P. Vir, C. Shekhar, C. Felser, K. Nielsch, S. T. B. Goennenwein, and A. Thomas, Applied Physics Letters **114**, 092403 (2019).

[8] H. Reichlova, R. Schlitz, S. Beckert, P. Swekis, A. Markou, Y.-C. Chen, D. Kriegner, S. Fabretti, G. H. Park, A. Niemann, S. Sudheendra, A. Thomas, K. Nielsch, C. Felser, and S. T. B. Goennenwein, Applied Physics Letters **113**, 212405 (2018).

[9] R. Schlitz, A. A. Amusan, M. Lammel, S. Schlicht, T. Tynell, J. Bachmann, G. Woltersdorf, K. Nielsch, S. T. B. Goennenwein, and A. Thomas, Applied Physics Letters **112**, 242403 (2018).

[10] R. Schlitz, T. Kosub, A. Thomas, S. Fabretti, K. Nielsch, D. Makarov, and S. T. B. Goennenwein, Applied Physics Letters **112**, 132401 (2018).

[11]J. Fischer, O. Gomonay, R. Schlitz, K. Ganzhorn, N. Vlietstra, M. Althammer, H. Huebl, M. Opel, R. Gross, S. T. B. Goennenwein, and S. Geprägs, Physical Review B **97**, 014417 (2018).

Publications prior to starting thesis work

[12]S. Pütter, S. Geprägs, R. Schlitz, M. Althammer, A. Erb, R. Gross, and S. T. B. Goennenwein, Applied Physics Letters **110**, 012403 (2017).

[13]K. Ganzhorn, T. Wimmer, J. Cramer, R. Schlitz, S. Geprägs, G. Jakob, R. Gross, H. Huebl, M. Kläui, and S. T. B. Goennenwein, AIP Advances **7**, 085102 (2017).

[14]S. Meyer, Y.-T. Chen, S. Wimmer, M. Althammer, T. Wimmer, R. Schlitz, S. Geprägs, H. Huebl, D. Ködderitzsch, H. Ebert, G. E. W. Bauer, R. Gross, and S. T. B. Goennenwein, Nature Materials **16**, 977–981 (2017).

[15]K. Ganzhorn, J. Barker, R. Schlitz, B. A. Piot, K. Ollefs, F. Guillou, F. Wilhelm, A. Rogalev, M. Opel, M. Althammer, S. Geprägs, H. Huebl, R. Gross, G. E. W. Bauer, and S. T. B. Goennenwein, Physical Review B **94**, 094401 (2016).

[16]S. T. B. Goennenwein, R. Schlitz, M. Pernpeintner, K. Ganzhorn, M. Althammer, R. Gross, and H. Huebl, Applied Physics Letters **107**, 172405 (2015).

[17]S. Meyer, R. Schlitz, S. Geprägs, M. Opel, H. Huebl, R. Gross, and S. T. B. Goennenwein, Applied Physics Letters **106**, 132402 (2015).

Bibliography

[18] W. Thomson, Proceedings of the Royal Society of London **8**, 546–550 (1856).

[19] E. H. Hall, American Journal of Mathematics **2**, 287–292 (1879).

[20] E. H. Hall, Philosophical Magazine Series 5 **12**, 157–172 (1881).

[21] *Three-axis digital compass IC HMC5883L*, opened 2020-04-08 (Honeywell, 2012).

[22] *Applications for Hall Effect IC Switches in Portable Applications*, opened 2020-04-08 (Rohm Semiconductor, 2009).

[23] B. Setiawan, R. D. Septianto, D. Suhendra, and F. Iskandar, Physics Education **52**, 065011 (2017).

[24] B. Vasic, *Coding and Signal Processing for Magnetic Recording Systems* (CRC Press, 2004).

[25] M. N. Baibich, J. M. Broto, A. Fert, F. N. V. Dau, F. Petroff, P. Etienne, G. Creuzet, A. Friederich, and J. Chazelas, Physical Review Letters **61**, 2472–2475 (1988).

[26] G. Binasch, P. Grünberg, F. Saurenbach, and W. Zinn, Physical Review B **39**, 4828–4830 (1989).

[27] M. Julliere, Physics Letters A **54**, 225–226 (1975).

[28] T. Miyazaki and N. Tezuka, Journal of Magnetism and Magnetic Materials **139**, L231–L234 (1995).

[29] J. S. Moodera, L. R. Kinder, T. M. Wong, and R. Meservey, Physical Review Letters **74**, 3273–3276 (1995).

[30] S. Mao, Y. Chen, F. Liu, X. Chen, B. Xu, P. Lu, M. Patwari, H. Xi, C. Chang, B. Miller, D. Menard, B. Pant, J. Loven, K. Duxstad, S. Li, Z. Zhang, A. Johnston, R. Lamberton, M. Gubbins, T. McLaughlin, J. Gadbois, J. Ding, B. Cross, S. Xue, and P. Ryan, IEEE Transactions on Magnetics **42**, 97–102 (2006).

[31] J. E. Hirsch, Physical Review Letters **83**, 1834–1837 (1999).

[32] S. O. Valenzuela and M. Tinkham, Nature **442**, 176–179 (2006).

[33] Y. K. Kato, R. C. Myers, A. C. Gossard, and D. D. Awschalom, Science **306**, 1910–1913 (2004).

[34] J. Wunderlich, B. Kaestner, J. Sinova, and T. Jungwirth, Physical Review Letters **94**, 047204 (2005).

[35] J. Sinova, S. O. Valenzuela, J. Wunderlich, C. Back, and T. Jungwirth, Reviews of Modern Physics **87**, 1213–1260 (2015).

[36] Y. Xu, D. D. Awschalom, and J. Nitta, eds., *Handbook of Spintronics* (Springer Netherlands, 2014).

[37] Y. Kajiwara, K. Harii, S. Takahashi, J. Ohe, K. Uchida, M. Mizuguchi, H. Umezawa, H. Kawai, K. Ando, K. Takanashi, S. Maekawa, and E. Saitoh, Nature **464**, 262–266 (2010).

[38] K. Uchida, J. Xiao, H. Adachi, J. Ohe, S. Takahashi, J. Ieda, T. Ota, Y. Kajiwara, H. Umezawa, H. Kawai, G. E. W. Bauer, S. Maekawa, and E. Saitoh, Nature Materials **9**, 894–897 (2010).

[39] M. Weiler, M. Althammer, F. D. Czeschka, H. Huebl, M. S. Wagner, M. Opel, I.-M. Imort, G. Reiss, A. Thomas, R. Gross, and S. T. B. Goennenwein, Physical Review Letters **108**, 106602 (2012).

[40] S. S.-L. Zhang and S. Zhang, Physical Review Letters **109**, 096603 (2012).

[41] S. S.-L. Zhang and S. Zhang, Physical Review B **86**, 214424 (2012).

[42] H. Nakayama, M. Althammer, Y.-T. Chen, K. Uchida, Y. Kajiwara, D. Kikuchi, T. Ohtani, S. Geprägs, M. Opel, S. Takahashi, R. Gross, G. E. W. Bauer, S. T. B. Goennenwein, and E. Saitoh, Physical Review Letters **110**, 206601 (2013).

[43] M. Althammer, S. Meyer, H. Nakayama, M. Schreier, S. Altmannshofer, M. Weiler, H. Huebl, S. Geprägs, M. Opel, R. Gross, D. Meier, C. Klewe, T. Kuschel, J.-M. Schmalhorst, G. Reiss, L. Shen, A. Gupta, Y.-T. Chen, G. E. W. Bauer, E. Saitoh, and S. T. B. Goennenwein, Physical Review B **87**, 224401 (2013).

[44] Y.-T. Chen, S. Takahashi, H. Nakayama, M. Althammer, S. T. B. Goennenwein, E. Saitoh, and G. E. W. Bauer, Physical Review B **87**, 144411 (2013).

[45] L. J. Cornelissen, J. Liu, R. A. Duine, J. B. Youssef, and B. J. van Wees, Nature Physics **11**, 1022 EP – (2015).

[46] I. M. Miron, K. Garello, G. Gaudin, P.-J. Zermatten, M. V. Costache, S. Auffret, S. Bandiera, B. Rodmacq, A. Schuhl, and P. Gambardella, Nature **476**, 189–193 (2011).

[47] C. O. Avci, K. Garello, I. M. Miron, G. Gaudin, S. Auffret, O. Boulle, and P. Gambardella, Applied Physics Letters **100**, 212404 (2012).

[48] L. Liu, C.-F. Pai, Y. Li, H. W. Tseng, D. C. Ralph, and R. A. Buhrman, Science **336**, 555–558 (2012).

[49]K. Garello, F. Yasin, S. Couet, L. Souriau, J. Swerts, S. Rao, S. V. Beek, W. Kim, E. Liu, S. Kundu, D. Tsvetanova, K. Croes, N. Jossart, E. Grimaldi, M. Baumgartner, D. Crotti, A. Fumemont, P. Gambardella, and G. Kar, in 2018 IEEE Symposium on VLSI Circuits (2018), pp. 81–82.

[50]A. Aqeel, N. Vlietstra, J. A. Heuver, G. E. W. Bauer, B. Noheda, B. J. van Wees, and T. T. M. Palstra, Physical Review B **92**, 224410 (2015).

[51]A. Aqeel, N. Vlietstra, A. Roy, M. Mostovoy, B. J. van Wees, and T. T. M. Palstra, Physical Review B **94**, 134418 (2016).

[52]K. v. Klitzing, G. Dorda, and M. Pepper, Physical Review Letters **45**, 494–497 (1980).

[53]J. Ye, Y. B. Kim, A. J. Millis, B. I. Shraiman, P. Majumdar, and Z. Tešanović, Physical Review Letters **83**, 3737–3740 (1999).

[54]P. Bruno, V. K. Dugaev, and M. Taillefumier, Physical Review Letters **93**, 096806 (2004).

[55]D. R. Yennie, Reviews of Modern Physics **59**, 781–824 (1987).

[56]C. L. Kane and E. J. Mele, Physical Review Letters **95**, 146802 (2005).

[57]M. Konig, S. Wiedmann, C. Brune, A. Roth, H. Buhmann, L. W. Molenkamp, X.-L. Qi, and S.-C. Zhang, Science **318**, 766–770 (2007).

[58]A. Neubauer, C. Pfleiderer, B. Binz, A. Rosch, R. Ritz, P. G. Niklowitz, and P. Böni, Physical Review Letters **102**, 186602 (2009).

[59]Y. Machida, S. Nakatsuji, Y. Maeno, T. Tayama, T. Sakakibara, and S. Onoda, Physical Review Letters **98**, 057203 (2007).

[60]W. Yuan, Q. Zhu, T. Su, Y. Yao, W. Xing, Y. Chen, Y. Ma, X. Lin, J. Shi, R. Shindou, X. C. Xie, and W. Han, Science Advances **4**, eaat1098 (2018).

[61]M. I. Dyakonov and V. I. Perel, Journal of Experimental and Theoretical Physics Letters **13**, 467 (1971).

[62]M. Schreier, G. E. W. Bauer, V. I. Vasyuchka, J. Flipse, K.-i. Uchida, J. Lotze, V. Lauer, A. V. Chumak, A. A. Serga, S. Daimon, T. Kikkawa, E. Saitoh, B. J. van Wees, B. Hillebrands, R. Gross, and S. T. B. Goennenwein, Journal of Physics D: Applied Physics **48**, 025001 (2014).

[63]X.-P. Zhang, F. S. Bergeret, and V. N. Golovach, Nano Letters **19**, 6330–6337 (2019).

[64]E. V. Gomonay and V. M. Loktev, Low Temperature Physics **40**, 17–35 (2014).

[65]G. R. Hoogeboom, A. Aqeel, T. Kuschel, T. T. M. Palstra, and B. J. van Wees, Applied Physics Letters **111**, 052409 (2017).

[66]L. Baldrati, A. Ross, T. Niizeki, C. Schneider, R. Ramos, J. Cramer, O. Gomonay, M. Filianina, T. Savchenko, D. Heinze, A. Kleibert, E. Saitoh, J. Sinova, and M. Kläui, Physical Review B **98**, 024422 (2018).

[67]M. I. Dyakonov, Physical Review Letters **99**, 126601 (2007).

[68]S. Vélez, V. N. Golovach, A. Bedoya-Pinto, M. Isasa, E. Sagasta, M. Abadia, C. Rogero, L. E. Hueso, F. S. Bergeret, and F. Casanova, Physical Review Letters **116**, 016603 (2016).

[69]S. Vélez, V. N. Golovach, J. M. Gomez-Perez, A. Chuvilin, C. T. Bui, F. Rivadulla, L. E. Hueso, F. S. Bergeret, and F. Casanova, Physical Review B **100**, 180401 (2019).

[70]J. Li, Y. Xu, M. Aldosary, C. Tang, Z. Lin, S. Zhang, and R. L. J. Shi, Nature Communications **7**, 10858 (2016).

[71]J. Shan, L. J. Cornelissen, N. Vlietstra, J. B. Youssef, T. Kuschel, R. A. Duine, and B. J. van Wees, Physical Review B **94**, 174437 (2016).

[72]J Shan, P. Bougiatioti, L Liang, G. Reiss, T. Kuschel, and B. van Wees, Applied Physics Letters **110**, 132406 (2017).

[73]L. J. Cornelissen, J. Shan, and B. J. van Wees, Physical Review B **94**, 180402(R) (2016).

[74]K. Ganzhorn, T. Wimmer, J. Barker, G. E. W. Bauer, Z. Qiu, E. Saitoh, N. Vlietstra, S. Geprägs, R. Gross, H. Huebl, and S. T. B. Goennenwein, arXiv 1705.02871 (2017).

[75]H. Wang, C. Du, P. C. Hammel, and F. Yang, Physical Review Letters **113**, 097202 (2014).

[76]R. Lebrun, A. Ross, S. A. Bender, A. Qaiumzadeh, L. Baldrati, J. Cramer, A. Brataas, R. A. Duine, and M. Kläui, Nature **561**, 222–225 (2018).

[77]L. J. Cornelissen, J. Liu, B. J. van Wees, and R. A. Duine, Physical Review Letters **120**, 097702 (2018).

[78]T. Wimmer, M. Althammer, L. Liensberger, N. Vlietstra, S. Geprägs, M. Weiler, R. Gross, and H. Huebl, Physical Review Letters **123**, 257201 (2019).

[79]J. Xiao, G. E. W. Bauer, K.-c. Uchida, E. Saitoh, and S. Maekawa, Physical Review B **81**, 214418 (2010).

[80]G. E. W. Bauer, E. Saitoh, and B. J. van Wees, Nature Materials **11**, 391–399 (2012).

[81]K.-i. Uchida, H. Adachi, T. Ota, H. Nakayama, S. Maekawa, and E. Saitoh, Applied Physics Letters **97**, 172505 (2010).

[82]M. Schreier, N. Roschewsky, E. Dobler, S. Meyer, H. Huebl, R. Gross, and S. T. B. Goennenwein, Applied Physics Letters **103**, 242404 (2013).

[83]S. Geprägs, A. Kehlberger, F. D. Coletta, Z. Qiu, E.-J. Guo, T. Schulz, C. Mix, S. Meyer, A. Kamra, M. Althammer, H. Huebl, G. Jakob, Y. Ohnuma, H. Adachi, J. Barker, S. Maekawa, G. E. W. Bauer, E. Saitoh, R. Gross, S. T. B. Goennenwein, and M. Kläui, Nature Communications **7**, 10452 (2016).

[84]J. Cramer, E.-J. Guo, S. Geprägs, A. Kehlberger, Y. P. Ivanov, K. Ganzhorn, F. D. Coletta, M. Althammer, H. Huebl, R. Gross, J. Kosel, M. Kläui, and S. T. B. Goennenwein, Nano Letters **17**, 3334–3340 (2017).

[85]V. Baltz, A. Manchon, M. Tsoi, T. Moriyama, T. Ono, and Y. Tserkovnyak, Reviews of Modern Physics **90**, 015005 (2018).

[86]S. Seki, T. Ideue, M. Kubota, Y. Kozuka, R. Takagi, M. Nakamura, Y. Kaneko, M. Kawasaki, and Y. Tokura, Physical Review Letters **115**, 266601 (2015).

[87]S. M. Wu, W. Zhang, A. KC, P. Borisov, J. E. Pearson, J. S. Jiang, D. Lederman, A. Hoffmann, and A. Bhattacharya, Physical Review Letters **116**, 097204 (2016).

[88] J. Holanda, D. S. Maior, O. Alves Santos, L. H. Vilela-Leão, J. B. S. Mendes, A. Azevedo, R. L. Rodríguez-Suárez, and S. M. Rezende, Applied Physics Letters **111**, 172405 (2017).

[89] J. Li, Z. Shi, V. H. Ortiz, M. Aldosary, C. Chen, V. Aji, P. Wei, and J. Shi, Physical Review Letters **122**, 217204 (2019).

[90] S. M. Wu, J. E. Pearson, and A. Bhattacharya, Physical Review Letters **114**, 186602 (2015).

[91] Y. Yamamoto, M. Ichioka, and H. Adachi, Physical Review B **100**, 064419 (2019).

[92] I. Gray, T. Moriyama, N. Sivadas, G. M. Stiehl, J. T. Heron, R. Need, B. J. Kirby, D. H. Low, K. C. Nowack, D. G. Schlom, D. C. Ralph, T. Ono, and G. D. Fuchs, Physical Review X **9**, 041016 (2019).

[93] T. J. Seebeck, in Abhandlungen der Königlichen Akademie der Wissenschaften zu Berlin (1822), pp. 265–373.

[94] A. v. Ettingshausen and W. Nernst, Annalen der Physik und Chemie **265**, 343–347 (1886).

[95] N. Nagaosa, J. Sinova, S. Onoda, A. H. MacDonald, and N. P. Ong, Reviews of Modern Physics **82**, 1539–1592 (2010).

[96] S. Onoda, N. Sugimoto, and N. Nagaosa, Physical Review B **77**, 165103 (2008).

[97] T. Miyasato, N. Abe, T. Fujii, A. Asamitsu, S. Onoda, Y. Onose, N. Nagaosa, and Y. Tokura, Physical Review Letters **99**, 086602 (2007).

[98] R. Karplus and J. M. Luttinger, Physical Review **95**, 1154–1160 (1954).

[99] J. Smit, Physica **24**, 39 –51 (1958).

[100] M. V. Berry, Proceedings of the Royal Society of London A: Mathematical, Physical and Engineering Sciences **392**, 45–57 (1984).

[101] D. Xiao, M.-C. Chang, and Q. Niu, Reviews of Modern Physics **82**, 1959–2007 (2010).

[102] E. M. Pugh and N. Rostoker, Reviews of Modern Physics **25**, 151–157 (1953).

[103] M. Ikhlas, T. Tomita, T. Koretsune, M.-T. Suzuki, D. Nishio-Hamane, R. Arita, Y. Otani, and S. Nakatsuji, Nature Physics **13**, 1085–1090 (2017).

[104] N. Kanazawa, Y. Onose, T. Arima, D. Okuyama, K. Ohoyama, S. Wakimoto, K. Kakurai, S. Ishiwata, and Y. Tokura, Physical Review Letters **106**, 156603 (2011).

[105] Y. Li, N. Kanazawa, X. Z. Yu, A. Tsukazaki, M. Kawasaki, M. Ichikawa, X. F. Jin, F. Kagawa, and Y. Tokura, Physical Review Letters **110**, 117202 (2013).

[106] Y. Shiomi, N. Kanazawa, K. Shibata, Y. Onose, and Y. Tokura, Physical Review B **88**, 064409 (2013).

[107] S. Nakatsuji, N. Kiyohara, and T. Higo, Nature **527**, 212–215 (2015).

[108] A. Sakai, Y. P. Mizuta, A. A. Nugroho, R. Sihombing, T. Koretsune, M.-T. Suzuki, N. Takemori, R. Ishii, D. Nishio-Hamane, R. Arita, P. Goswami, and S. Nakatsuji, Nature Physics **14**, 1119–1124 (2018).

[109] Y. Taguchi, Y. Oohara, H. Yoshizawa, N. Nagaosa, and Y. Tokura, Science **291**, 2573 (2001).

[110] T. H. R. Skyrme, Proceedings of the Royal Society of London A: Mathematical, Physical and Engineering Sciences **260**, 127–138 (1961).

[111] S. Mühlbauer, B. Binz, F. Jonietz, C. Pfleiderer, A. Rosch, A. Neubauer, R. Georgii, and P. Böni, Science **323**, 915 (2009).

[112] C. Sürgers, G. Fischer, P. Winkel, and H. v. Löhneysen, Nature Communications **5**, 3400 (2014).

[113] H. Chen, Q. Niu, and A. H. MacDonald, Physical Review Letters **112**, 017205 (2014).

[114] L. Šmejkal, R. González-Hernández, T. Jungwirth, and J. Sinova, arXiv 1901.00445 (2019).

[115] N. Mott and H. Jones, *The Theory of the Properties of Metals and Alloys.* (Oxford University Press-Dover Publications, New York, 1958).

[116] Y. Pu, D. Chiba, F. Matsukura, H. Ohno, and J. Shi, Physical Review Letters **101**, 117208 (2008).

[117] M. Schreier, PhD thesis (Walther Meißner Institut, Technische Universität München, 2016).

[118] K. Halbach, Nuclear Instruments and Methods **169**, 1 –10 (1980).

[119] M. Coey, *Magnetism and Magnetic Materials* (Cambridge University Press, 2010).

[120] M. Belger, Master's thesis (Technische Universität Dresden, 2018).

[121] M. Schreier, Diploma thesis (Walther Meißner Institut, Technische Universität München, 2012).

[122] Keithley Instruments, *Low Level Measurements Handbook*, 7th Edition, opened 2020-04-08 (Keithley Instruments Inc., 2014).

[123] A. Daire, W. Goeke, and M. A. Tupta, *New Instruments Can Lock Out Lock-ins*, opened 2020-04-08 (Keithley Instruments Inc., 2017).

[124] J. B. Johnson, Physical Review **32**, 97–109 (1928).

[125] H. Nyquist, Physical Review **32**, 110–113 (1928).

[126] Y.-T. Chen, S. Takahashi, H. Nakayama, M. Althammer, S. T. B. Goennenwein, E. Saitoh, and G. E. W. Bauer, Journal of Physics: Condensed Matter **28**, 103004 (2016).

[127] B.-W. Dong, J. Cramer, K. Ganzhorn, H. Y. Yuan, E.-J. Guo, S. T. B. Goennenwein, and M. Kläui, Journal of Physics: Condensed Matter **30**, 035802 (2017).

[128] D. Hou, Z. Qiu, J. Barker, K. Sato, K. Yamamoto, S. Vélez, J. M. Gomez-Perez, L. E. Hueso, F. Casanova, and E. Saitoh, Physical Review Letters **118**, 147202 (2017).

[129] Y. Ji, J. Miao, K. K. Meng, Z. Y. Ren, B. W. Dong, X. G. Xu, Y. Wu, and Y. Jiang, Applied Physics Letters **110**, 262401 (2017).

[130] E. M. Gyorgy, K. Nassau, K. Nassau, M. Eibschutz, J. V. Waszczak, C. A. Wang, and J. C. Shelton, Journal of Applied Physics **50**, 2883–2886 (1979).

[131] M. E. Lines and M. Eibschütz, Physical Review B **30**, 1416–1423 (1984).

[132] F. Yang and P. C. Hammel, Journal of Physics D: Applied Physics **51**, 253001 (2018).

[133] Y. G. Chukalkin, V. R. Shtirz, and B. N. Goshchitskii, Physica Status Solidi (a) **112**, 161–174 (1989).

[134] H. Chang, P. Li, W. Zhang, T. Liu, A. Hoffmann, L. Deng, and M. Wu, IEEE Magnetics Letters **5**, 1–4 (2014).

[135] C. Hauser, T. Richter, N. Homonnay, C. Eisenschmidt, M. Qaid, H. Deniz, D. Hesse, M. Sawicki, S. G. Ebbinghaus, and G. Schmidt, Scientific Reports **6**, 20827 (2016).

[136] D. Wesenberg, T. Liu, D. Balzar, M. Wu, and B. L. Zink, Nature Physics **13**, 987–993 (2017).

[137] J. Narayan, P. Tiwari, K. Jagannadham, and O. W. Holland, Applied Physics Letters **64**, 2093–2095 (1994).

[138] R. Gross and A. Marx, *Festkörperphysik* (Oldenbourg Wissenschaftsverlag Verlag, 2012).

[139] H. Hoffmann, F. Hofmann, and W. Schoepe, Physical Review B **25**, 5563–5565 (1982).

[140] S. Meyer, M. Althammer, S. Geprägs, M. Opel, R. Gross, and S. T. B. Goennenwein, Applied Physics Letters **104**, 242411 (2014).

[141] H. Adachi, K.-i. Uchida, E. Saitoh, J.-i. Ohe, S. Takahashi, and S. Maekawa, Applied Physics Letters **97**, 252506 (2010).

[142] N. F. Berk and J. R. Schrieffer, Physical Review Letters **17**, 433–435 (1966).

[143] S. Doniach and S. Engelsberg, Physical Review Letters **17**, 750–753 (1966).

[144] R. Doubble, S. M. Hayden, P. Dai, H. A. Mook, J. R. Thompson, and C. D. Frost, Physical Review Letters **105**, 027207 (2010).

[145] K. Oyanagi, S. Takahashi, L. J. Cornelissen, J. Shan, S. Daimon, T. Kikkawa, G. E. W. Bauer, B. J. van Wees, and E. Saitoh, Nature Communications **10**, 4740 (2019).

[146] B. Barbara, Comptes Rendus Physique **20**, 631–649 (2019).

[147] T. Kosub, M. Kopte, F. Radu, O. G. Schmidt, and D. Makarov, Physical Review Letters **115**, 097201 (2015).

[148] T. Kosub, PhD thesis (Technische Universität Chemnitz, 2016).

[149] X. He, Y. Wang, N. Wu, A. N. Caruso, E. Vescovo, K. D. Belashchenko, P. A. Dowben, and C. Binek, Nature Materials **9**, 579–585 (2010).

[150] T. Kosub, M. Kopte, R. Hühne, P. Appel, B. Shields, P. Maletinsky, R. Hübner, M. O. Liedke, J. Fassbender, O. G. Schmidt, and D. Makarov, Nature Communications **8**, 13985 (2017).

[151] W. Limmer, M. Glunk, J. Daeubler, T. Hummel, W. Schoch, R. Sauer, C. Bihler, H. Huebl, M. S. Brandt, and S. T. B. Goennenwein, Physical Review B **74**, 205205 (2006).

[152] Y. J. Kim, C.-Y. Liu, S. K. Lamoreaux, G. Visser, B. Kunkler, A. N. Matlashov, J. C. Long, and T. G. Reddy, Physical Review D **91**, 102004 (2015).

[153]S. Foner, Physical Review **130**, 183–197 (1963).

[154]K. Miura, K. Fujiwara, J. Shiogai, T. Nojima, and A. Tsukazaki, Journal of Applied Physics **127**, 103903 (2020).

[155]K. Oda, T. Moriyama, M. Kimata, S. Kasukawa, and O. N. O. Teruo, Japanese Journal of Applied Physics **59**, 010908 (2020).

[156]P. Appel, B. J. Shields, T. Kosub, N. Hedrich, R. Hübner, J. Faßbender, D. Makarov, and P. Maletinsky, Nano Letters **19**, 1682–1687 (2019).

[157]Y. Dai, S. J. Xu, S. W. Chen, X. L. Fan, D. Z. Yang, D. S. Xue, D. S. Song, J. Zhu, S. M. Zhou, and X. Qiu, Physical Review B **100**, 064404 (2019).

[158]E. Sagasta, Y. Omori, M. Isasa, M. Gradhand, L. E. Hueso, Y. Niimi, Y. Otani, and F. Casanova, Physical Review B **94**, 060412(R) (2016).

[159]E. Sagasta, Y. Omori, S. Vélez, R. Llopis, C. Tollan, A. Chuvilin, L. E. Hueso, M. Gradhand, Y. Otani, and F. Casanova, Physical Review B **98**, 060410 (2018).

[160]Y. Cheng, S. Yu, M. Zhu, J. Hwang, and F. Yang, Physical Review Letters **123**, 237206 (2019).

[161]A. Lund, S. Shimada, and M. Shiotani, *Principles and Applications of ESR Spectroscopy* (Springer Netherlands, 2011).

[162]A. R. West, *Solid State Chemistry*, Second edition (Wiley John + Sons, 2014).

[163]Y. Niimi, D. Wei, H. Idzuchi, T. Wakamura, T. Kato, and Y. Otani, Physical Review Letters **110**, 016805 (2013).

[164]J. Kim, P. Sheng, S. Takahashi, S. Mitani, and M. Hayashi, Physical Review Letters **116**, 097201 (2016).

[165]S. Streib, H. Keshtgar, and G. E. W. Bauer, Physical Review Letters **121**, 027202 (2018).

[166]K. An, A. N. Litvinenko, R. Kohno, A. A. Fuad, V. V. Naletov, L. Vila, U. Ebels, G. de Loubens, H. Hurdequint, N. Beaulieu, J. B. Youssef, N. Vukadinovic, G. E. W. Bauer, A. N. Slavin, V. S. Tiberkevich, and O. Klein, Physical Review B **101**, 060407(R) (2020).

[167]N. Thiery, A. Draveny, V. V. Naletov, L. Vila, J. P. Attané, C. Beigné, G. de Loubens, M. Viret, N. Beaulieu, J. Ben Youssef, V. E. Demidov, S. O. Demokritov, A. N. Slavin, V. S. Tiberkevich, A. Anane, P. Bortolotti, V. Cros, and O. Klein, Physical Review B **97**, 060409 (2018).

[168]S. A. Bender, R. A. Duine, A. Brataas, and Y. Tserkovnyak, Physcial Review B **90**, 094409 (2014).

[169]M. B. Jungfleisch, V. Lauer, R. Neb, A. V. Chumak, and B. Hillebrands, Applied Physics Letters **103**, 022411 (2013).

[170]S. Shukuri, Y. Wade, M. Tamura, K. Umemura, and T. Ishitani, Journal of The Electrochemical Society **134**, 1536–1540 (1987).

[171]P. J. Moll, Annual Review of Condensed Matter Physics **9**, 147–162 (2018).

[172]A. V. Chumak, A. A. Serga, and B Hillebrands, Journal of Physics D: Applied Physics **50**, 244001 (2017).

[173]W. T. Ruane, S. P. White, J. T. Brangham, K. Y. Meng, D. V. Pelekhov, F. Y. Yang, and P. C. Hammel, AIP Advances **8**, 056007 (2018).

[174]N. Thiery, V. V. Naletov, L. Vila, A. Marty, A. Brenac, J.-F. Jacquot, G. de Loubens, M. Viret, A. Anane, V. Cros, J. Ben Youssef, N. Beaulieu, V. E. Demidov, B. Divinskiy, S. O. Demokritov, and O. Klein, Physical Review B **97**, 064422 (2018).

[175]J. M. Gomez-Perez, K. Oyanagi, R. Yahiro, R. Ramos, L. E. Hueso, E. Saitoh, and F. Casanova, Applied Physics Letters **116**, 032401 (2020).

[176]O. A. Petrenko, D. M. Paul, C. Ritter, T. Zeiske, and M. Yethiraj, Physica B: Condensed Matter **266**, 41–48 (1999).

[177]E. E. Anderson, Physical Review **134**, A1581–A1585 (1964).

[178]N. Miura, I. Oguro, and S. Chikazumi, Journal of the Physical Society of Japan **45**, 1534–1541 (1978).

[179]J. F. W. Bowles, Mineralogy and Petrology **43**, 37–47 (1990).

[180]F. Keffer and C. Kittel, Physical Review **85**, 329–337 (1952).

[181]S. M. Rezende, R. L. Rodríguez-Suárez, and A. Azevedo, Physical Review B **93**, 014425 (2016).

[182]S. M. Rezende, R. L. Rodríguez-Suárez, and A. Azevedo, Physical Review B **93**, 054412 (2016).

[183]A. Qaiumzadeh, H. Skarsvåg, C. Holmqvist, and A. Brataas, Physical Review Letters **118**, 137201 (2017).

[184]S. Takei, B. I. Halperin, A. Yacoby, and Y. Tserkovnyak, Physical Review B **90**, 094408 (2014).

[185]A. N. Bogdanov, A. V. Zhuravlev, and U. K. Rößler, Physical Review B **75**, 094425 (2007).

[186]E. Sonin, Advances in Physics **59**, 181–255 (2010).

[187]C. O. Avci, E. Rosenberg, M. Huang, J. Bauer, C. A. Ross, and G. S. Beach, Physical Review Letters **124**, 027701 (2020).

[188]C. O. Avci, K. Garello, A. Ghosh, M. Gabureac, S. F. Alvarado, and P. Gambardella, Nature Physics **11**, Article, 570 EP – (2015).

[189]R. Schlitz, Master's thesis (Walther Meißner Institut, Technische Universität München, 2015).

[190]Y. Endoh, K. Kakurai, and A. K. Katori, in *Landolt-Börnstein - Group III Condensed Matter* (Springer-Verlag, 1994), pp. 176–176.

[191]J. Shan, L. J. Cornelissen, J. Liu, J. B. Youssef, L. Liang, and B. J. van Wees, Physical Review B **96**, 184427 (2017).

[192] A. Ross, R. Lebrun, O. Gomonay, D. A. Grave, A. Kay, L. Baldrati, S. Becker, A. Qaiumzadeh, C. Ulloa, G. Jakob, F. Kronast, J. Sinova, R. Duine, A. Brataas, A. Rothschild, and M. Kläui, Nano Letters 20, 306–313 (2019).

[193] N. P. Armitage, E. J. Mele, and A. Vishwanath, Reviews of Modern Physics 90, 015001 (2018).

[194] A. M. Kosevich, Low Temperature Physics 30, 97–117 (2004).

[195] Y. Tokura, K. Yasuda, and A. Tsukazaki, Nature Reviews Physics 1, 126–143 (2019).

[196] B. Yan and C. Felser, Annual Review of Condensed Matter Physics 8, 337–354 (2017).

[197] X. Huang, L. Zhao, Y. Long, P. Wang, D. Chen, Z. Yang, H. Liang, M. Xue, H. Weng, Z. Fang, X. Dai, and G. Chen, Physical Review X 5, 031023 (2015).

[198] C. Pappas, E. Lelièvre-Berna, P. Falus, P. M. Bentley, E. Moskvin, S. Grigoriev, P. Fouquet, and B. Farago, Physical Review Letters 102, 197202 (2009).

[199] N. Nagaosa and Y. Tokura, Nature Nanotechnology 8, Review Article, 899 EP – (2013).

[200] A. K. Nayak, V. Kumar, T. Ma, P. Werner, E. Pippel, R. Sahoo, F. Damay, U. K. Rößler, C. Felser, and S. S. P. Parkin, Nature 548, 561 (2017).

[201] Z. Liu, A. Burigu, Y. Zhang, H. M. Jafri, X. Ma, E. Liu, W. Wang, and G. Wu, Scripta Materialia 143, 122 –125 (2018).

[202] A. N. Bogdanov, U. K. Rößler, M. Wolf, and K.-H. Müller, Phys. Rev. B 66, 214410 (2002).

[203] O. Meshcheriakova, S. Chadov, A. K. Nayak, U. K. Rößler, J. Kübler, G. André, A. A. Tsirlin, J. Kiss, S. Hausdorf, A. Kalache, W. Schnelle, M. Nicklas, and C. Felser, Physical Review Letters 113, 087203 (2014).

[204] P. Vir, J. Gayles, A. S. Sukhanov, N. Kumar, F. Damay, Y. Sun, J. Kübler, C. Shekhar, and C. Felser, Physical Review B 99, 140406(R) (2019).

[205] S. Blundell, Magnetism in condensed matter (Oxford University Press, 2001).

[206] W.-L. Lee, S. Watauchi, V. L. Miller, R. J. Cava, and N. P. Ong, Physical Review Letters 93, 226601 (2004).

[207] D. Xiao, Y. Yao, Z. Fang, and Q. Niu, Physical Review Letters 97, 026603 (2006).

[208] J. Noky, J. Gooth, C. Felser, and Y. Sun, Physical Review B 98, 241106 (2018).

[209] N. Hanasaki, K. Sano, Y. Onose, T. Ohtsuka, S. Iguchi, I. Kézsmárki, S. Miyasaka, S. Onoda, N. Nagaosa, and Y. Tokura, Physical Review Letters 100, 106601 (2008).

[210] Z. H. Liu, Y. J. Zhang, G. D. Liu, B. Ding, E. K. Liu, H. M. Jafri, Z. P. Hou, W. H. Wang, X. Q. Ma, and G. H. Wu, Scientific Reports 7, 515 (2017).

[211] Y. Li, B. Ding, X. Wang, H. Zhang, W. Wang, and Z. Liu, Applied Physics Letters 113, 062406 (2018).

[212] V. D. Ky, Physica Status Solidi B 22, 729–736 (1967).

[213] C. Zeng, Y. Yao, Q. Niu, and H. H. Weitering, Physical Review Letters 96, 037204 (2006).

[214] N. Manyala, Y. Sidis, J. F. DiTusa, G. Aeppli, D. P. Young, and Z. Fisk, Nature Materials **3**, 255–262 (2004).

[215] K. Geishendorf, P. Vir, C. Shekhar, C. Felser, J. I. Facio, J. van den Brink, K. Nielsch, A. Thomas, and S. T. B. Goennenwein, Nano Letters **20**, 300–305 (2019).

[216] L. Vistoli, W. Wang, A. Sander, Q. Zhu, B. Casals, R. Cichelero, A. Barthélémy, S. Fusil, G. Herranz, S. Valencia, R. Abrudan, E. Weschke, K. Nakazawa, H. Kohno, J. Santamaria, W. Wu, V. Garcia, and M. Bibes, Nature Physics **15**, 67–72 (2018).

[217] T. Kurumaji, T. Nakajima, M. Hirschberger, A. Kikkawa, Y. Yamasaki, H. Sagayama, H. Nakao, Y. Taguchi, T. hisa Arima, and Y. Tokura, Science **365**, 914–918 (2019).

[218] T. Jungwirth, J. Sinova, A. Manchon, X. Marti, J. Wunderlich, and C. Felser, Nature Physics **14**, 200–203 (2018).

[219] R. Shindou and N. Nagaosa, Physical Review Letters **87**, 116801 (2001).

[220] J. Kübler and C. Felser, EPL (Europhysics Letters) **108**, 67001 (2014).

[221] L. Šmejkal, Y. Mokrousov, B. Yan, and A. H. MacDonald, Nature Physics **14**, 242–251 (2018).

[222] S. Tomiyoshi and Y. Yamaguchi, Journal of the Physical Society of Japan **51**, 2478–2486 (1982).

[223] P. J. Brown, V. Nunez, F. Tasset, J. B. Forsyth, and P. Radhakrishna, Journal of Physics: Condensed Matter **2**, 9409–9422 (1990).

[224] T. Higo, H. Man, D. B. Gopman, L. Wu, T. Koretsune, O. M. J. van 't Erve, Y. P. Kabanov, D. Rees, Y. Li, M.-T. Suzuki, S. Patankar, M. Ikhlas, C. L. Chien, R. Arita, R. D. Shull, J. Orenstein, and S. Nakatsuji, Nature Photonics **12**, 73–78 (2018).

[225] A. K. Nayak, J. E. Fischer, Y. Sun, B. Yan, J. Karel, A. C. Komarek, C. Shekhar, N. Kumar, W. Schnelle, J. Kübler, C. Felser, and S. S. P. Parkin, Science Advances **2**, e1501870 (2016).

[226] W. Zhang, M. B. Jungfleisch, W. Jiang, J. E. Pearson, A. Hoffmann, F. Freimuth, and Y. Mokrousov, Physical Review Letters **113**, 196602 (2014).

[227] K. Kuroda, T. Tomita, M.-T. Suzuki, C. Bareille, A. A. Nugroho, P. Goswami, M. Ochi, M. Ikhlas, M. Nakayama, S. Akebi, R. Noguchi, R. Ishii, N. Inami, K. Ono, H. Kumigashira, A. Varykhalov, T. Muro, T. Koretsune, R. Arita, S. Shin, T. Kondo, and S. Nakatsuji, Nature Materials **16**, 1090–1095 (2017).

[228] M. Kimata, H. Chen, K. Kondou, S. Sugimoto, P. K. Muduli, M. Ikhlas, Y. Omori, T. Tomita, A. H. MacDonald, S. Nakatsuji, and Y. Otani, Nature **565**, 627–630 (2019).

[229] J. Železný, Y. Zhang, C. Felser, and B. Yan, Physical Review Letters **119**, 187204 (2017).

[230] W. H. Kleiner, Physical Review **142**, 318–326 (1966).

[231] A. Markou, J. M. Taylor, A. Kalache, P. Werner, S. S. P. Parkin, and C. Felser, Physical Review Materials **2**, 051001(R) (2018).

[232] J. Liu and L. Balents, Physical Review Letters **119**, 087202 (2017).

[233]K. Manna, Y. Sun, L. Muechler, J. Kübler, and C. Felser, Nature Reviews Materials **3**, 244–256 (2018).

[234]H. Yang, Y. Sun, Y. Zhang, W.-J. Shi, S. S. P. Parkin, and B. Yan, New Journal of Physics **19**, 015008 (2017).

[235]T. Nagamiya, S. Tomiyoshi, and Y. Yamaguchi, Solid State Communications **42**, 385–388 (1982).

[236]J Sticht, K.-H. Höck, and J Kübler, Journal of Physics: Condensed Matter **1**, 8155–8176 (1989).

[237]N. H. Sung, F. Ronning, J. D. Thompson, and E. D. Bauer, Applied Physics Letters **112**, 132406 (2018).

[238]D. Zhang, B. Yan, S.-C. Wu, J. Kübler, G. Kreiner, S. S. P. Parkin, and C. Felser, Journal of Physics: Condensed Matter **25**, 206006 (2013).

[239]W. G. Bisson and A. S. Wills, Journal of Physics: Condensed Matter **20**, 452204 (2008).

[240]I. Ritchey, P. Chandra, and P. Coleman, Physical Review B **47**, 15342–15345 (1993).

[241]H. Barkhausen, Physikalische Zeitschrift **20**, 401–403 (1919).

[242]K. Stierstadt, in *Springer Tracts in Modern Physics* (Springer Berlin Heidelberg, 1966), pp. 2–106.

[243]E. Albisetti, D. Petti, M. Pancaldi, M. Madami, S. Tacchi, J. Curtis, W. P. King, A. Papp, G. Csaba, W. Porod, P. Vavassori, E. Riedo, and R. Bertacco, Nature Nanotechnology **11**, 545–551 (2016).

[244]K. Holloway and P. M. Fryer, Applied Physics Letters **57**, 1736–1738 (1990).

[245]J. Liu, *CYSJ166A GaAs Hall-Effekt Element*, opened 2020-04-08 (ChenYang Technologies, 2016).

[246]P. Daniil and E. Cohen, Journal of Applied Physics **53**, 8257–8259 (1982).

Appendix A

TRANSPORT SETUP DETAILS

A.1 Halbach Setup

The existing Halbach setup from the Walther Meißner Institut in Munich was equipped with Hall sensors for measuring the magnetic field in two orthogonal directions simultaneously. In this section the determination of the magnetic field angle as well as the readout electronics for the two Hall sensors will be described.

A.1.1 Determination of Magnetic Field Angle

The function to determine the angle of the magnetic field for the given rotation planes is shown below. It returns the angle of the magnetic field for the given rotation plane using the arctan2 function included in numpy and shifts the angle into the interval of $(0, 360]°$.

```python
def getAngleXYHalbach(magX, magY, plane, rot90):
    """
    Calculates the angle within the rotation plane
    specified in plane for a sample structure along
    the long edge of the CC (or rotated by 90deg ccw)
    plane can be "ip", "oopj" or "oopt"
    rot90 is a boolean
    if this is corner of CC:
                    + I/Vlong

    + Vtrans                        - Vtrans
```

145

```
                   - I/Vlong
, then rot90 is False, j is flowing downwards, if
rotated 90 deg ccw, then rot90 needs to be true.
"""
if "ip" == plane and rot90 is False:
    return 180.*np.arctan2(-magY, magX)/np.pi + 180
elif (("oopj" == plane or "oopt" == plane)
  and rot90 is False):
    return 180.*np.arctan2(magY, -magX)/np.pi + 180
elif "ip" == plane and rot90 is True:
    return 180.*np.arctan2(-magX, -magY)/np.pi + 180
elif "oopt" == plane and rot90 is True:
    return 180.*np.arctan2(magY, -magX)/np.pi + 180
elif "oopj" == plane and rot90 is True:
    return 180.*np.arctan2(-magY, -magX)/np.pi + 180
```

A.1.2   2D Hall effect measurement electronics

The measurement electronics is based on a Raspberry Pi mini computer with a so-called HAT (hardware attached on top). This high precision AD/DA board is manufactured by Waveshare and features ADS1256 analog digital converter (ADC) with eight channels and 24bit digital resolution. Additionally a 16 bit digital to analog converter (DAC) with two channels is on the board (DAC8532). The wiring scheme is displayed in Fig. A.1, where ADx refers to the ADC inputs. All three Hall voltages can be measured differentially using six of the channels. In the software, the channel with the higher number is defined as the positive input. The remaining two channels are used for measuring the supply voltage (Vcc/2) and the current flowing through the first Hall sensor.

The current reading was initially supposed to be used for the determination of the temperature. Unfortunately, no clear (stable) dependence of the resistance on temperature could be established, so that it is not feasible (the resistance is highly field dependent). However, although not implemented yet, it would be advantageous to use this value to calculate the Hall resistance of the individual sensors. Compared to the Hall voltage, the Hall resistance is much less sensitive to temperature changes according to the spec sheet of the sensors.[245]

Finally, to obtain the magnetic field from the voltage reading, a linear calibration is used, viz. $\mu_0 H = \zeta (V_H + V_0)$. Here, V_0 is an offset voltage, V_H the measured voltage and ζ is the field per voltage calibration value. ζ and V_0 are obtained by comparing the voltage readout for two magnetic field polarities to a commercial (calibrated) Lakeshore Hall probe read out by a Lakeshore 475 controller. If multiple Hall sensors are used (2D+), the Hall electronics can correct the readings for a skew of the relative orientation. More details about the exact calibration procedure in this case can be found in the comments of the code. All calibration values are stored on a file locally on the mini computer and are persistent across reboots. A default calibration curve can be selected from the available

curves, which is automatically loaded on power up.
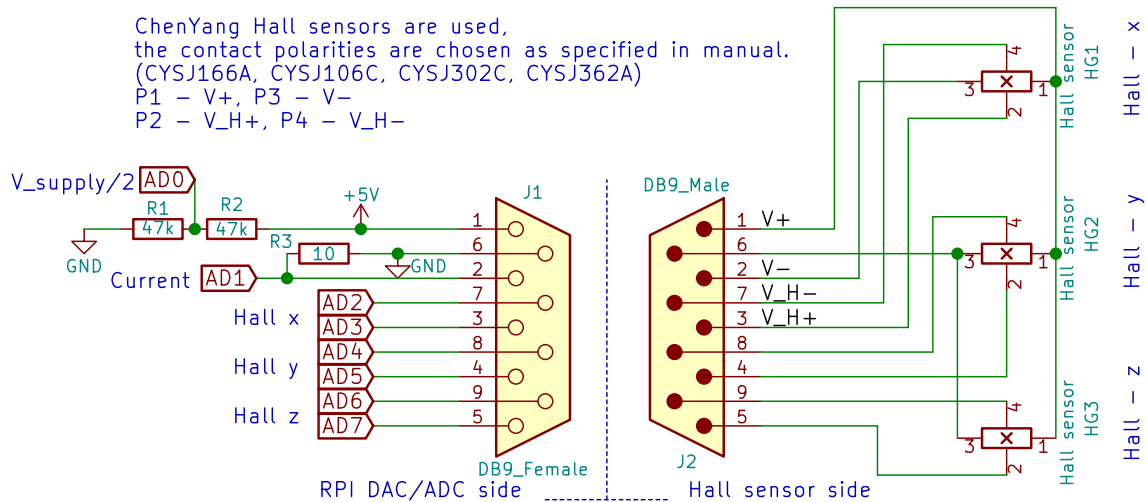
Figure A.1: Wiring of the 2D Hall probe electronics wiring. Up to three Hall sensors can be used and read out differentially. The current can be measured only for the first Hall probe.

The device communication is performed via the Ethernet interface of the Raspberry Pi mini computer supporting a subset of the standard command for programmable instruments (SCPI), most importantly the "*IDN?" command. The electronics listens to port 8888. An exemplary subset of the available commands relevant for the operation of the Halbach magnets can be found below. A full list of commands can be obtained from the device by issuing "*CMD?" to the interface of the Hall probe electronics.

```
"""
Class for interfacing the ADS1256 with the local TCP server

Usage:
Available commands:
    :(x/y/z):field:read?  - returns the lates field reading
    :(x/y/z):field:calib? - returns the current conversion
                  factor from tesla to volts
              (Tesla/Volt)
    :(x/y/z):field:calib 3 - sets the current conversion
                  factor from tesla to volts
              to 3 (Tesla/Volt)
    :(x/y/z):field:offs?  - returns the current offset of
                  the field values (Volt)
    :(x/y/z):field:offs 2  - sets the current offset of
                  the field value to 2 (Volt)
    :axisc?      - returns the current axis count
```

```
                 (1-1D, 2-2D, 3-3D)
   :axisc 3      - sets the axis count to 3, for a value of 2,
                   only the x and y axis get updated
   :curve:list?   - returns a list of all available curves
   :curve:write lala - writes the current configureation
                      to curve lala
   :curve:read lala   - reads and applies the configuration
                        from curve lala
   :curve:default?  - returns default curve
   :curve:default - sets the default curve

   :ip? - returns the current ip and gateway
   :ip 192.168.5.12,192.168.5.1 - sets the ip and gateway
                                  to the given values

   *IDN?        - returns the version of the device
   *CMD?        - returns this docstring
"""
```

Although not used for the Halbach magnets, the Hall electronics can be used as a PID controller. In this case the magnetic field is utilized for controlling the analog output of the DAC. If a bipolar control is necessary, a virtual ground has to be established at half of the supply voltage (using a operational amplifier wired as voltage follower). The control voltage output is then the differential signal between the DAC output and the virtual ground at half of the supply voltage, essentially giving a bipolar control range of $-2.5\,\mathrm{V}$ to $2.5\,\mathrm{V}$. Additionally, the analog output stage (and thus also the PID controller) can be rate limited (i.e. limiting the maximum rate of change of the control voltage) to protect two quadrant power supplies driving an inductive load from large reverse currents/voltages. Since the DAC only has two channels, the control is limited to two field directions when using the presented device.

A.2   Measuring Inserts for Cryostats

For the measuring insert used in the vector magnet cryostat following parts were used:

1. Cernox CX-1030, serial number CX-X0673

2. 10 pin Fischer Connector Buchse DBEE 1031 Z010-130

3. 40 pin Lemo Connector HGG.4B.340.CLLPV

4. 1/8" Watlow Firerod heater cartridge C1A-9606 FR 50/50

5. $\approx 4\,\mathrm{m}$ 12 twisted pair loom (24 wires)

6. Contact bridges Vogt Verbindungstechnik 1364C.68

7. Teflon tape

The second measuring insert with the puck insert has the following additional components:

1. Cernox CX-1050, serial number CX-X141220

2. Puck connector and receptacle Samtec SLH-020-1.50-G-D-A and TLH-020-0.50-G-D-A

The wiring for the puck measuring insert (which only differs by using the Samtec connectors instead of the soldering joints for the measurement contacts) can be seen in Fig. A.2. Additionally, the puck contacts and the Samtec connectors are shown in Fig. A.3
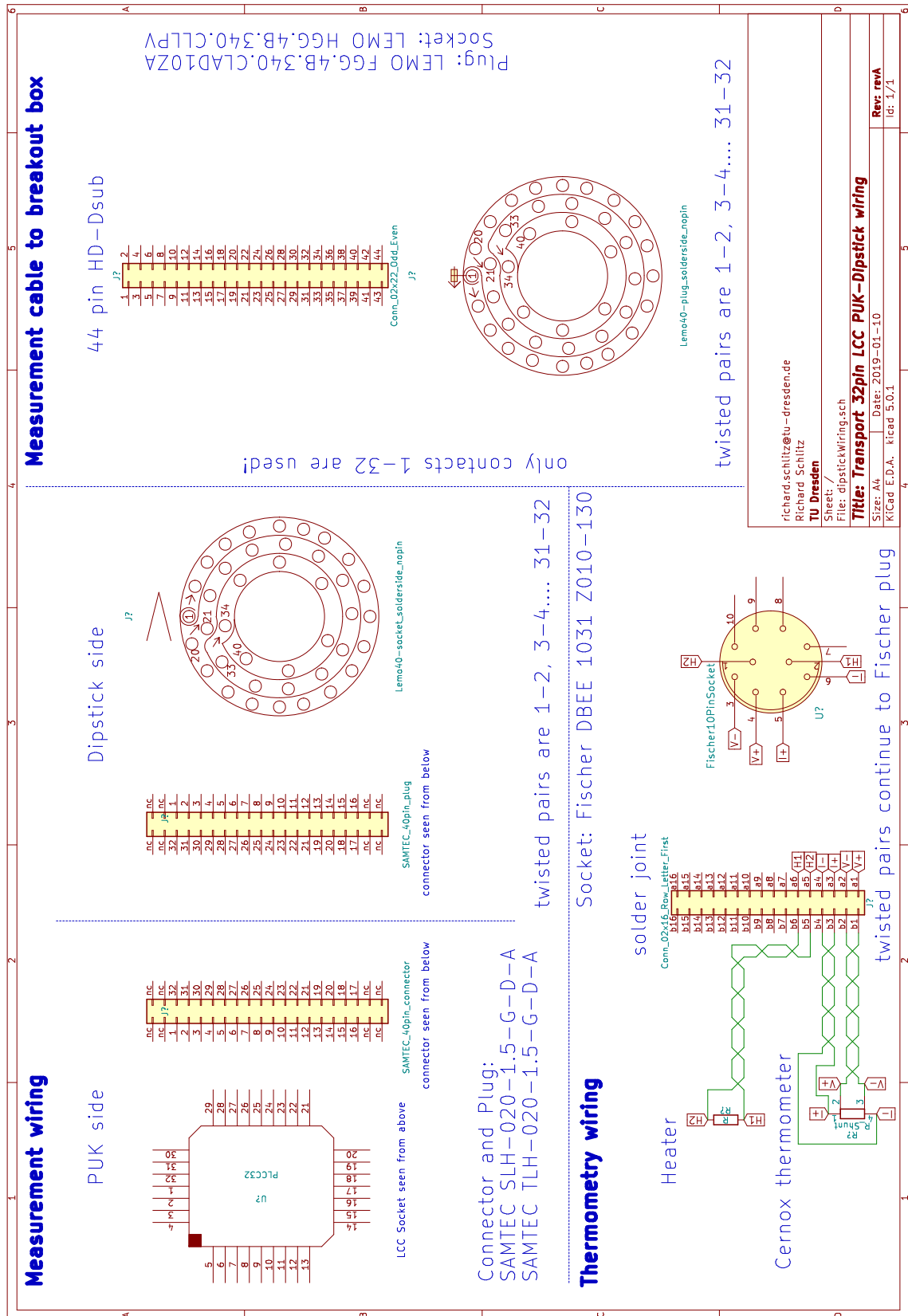
Figure A.2: Schematic of the puck measuring insert wiring. The Fischer and Lemo connectors are seen from the soldering side.
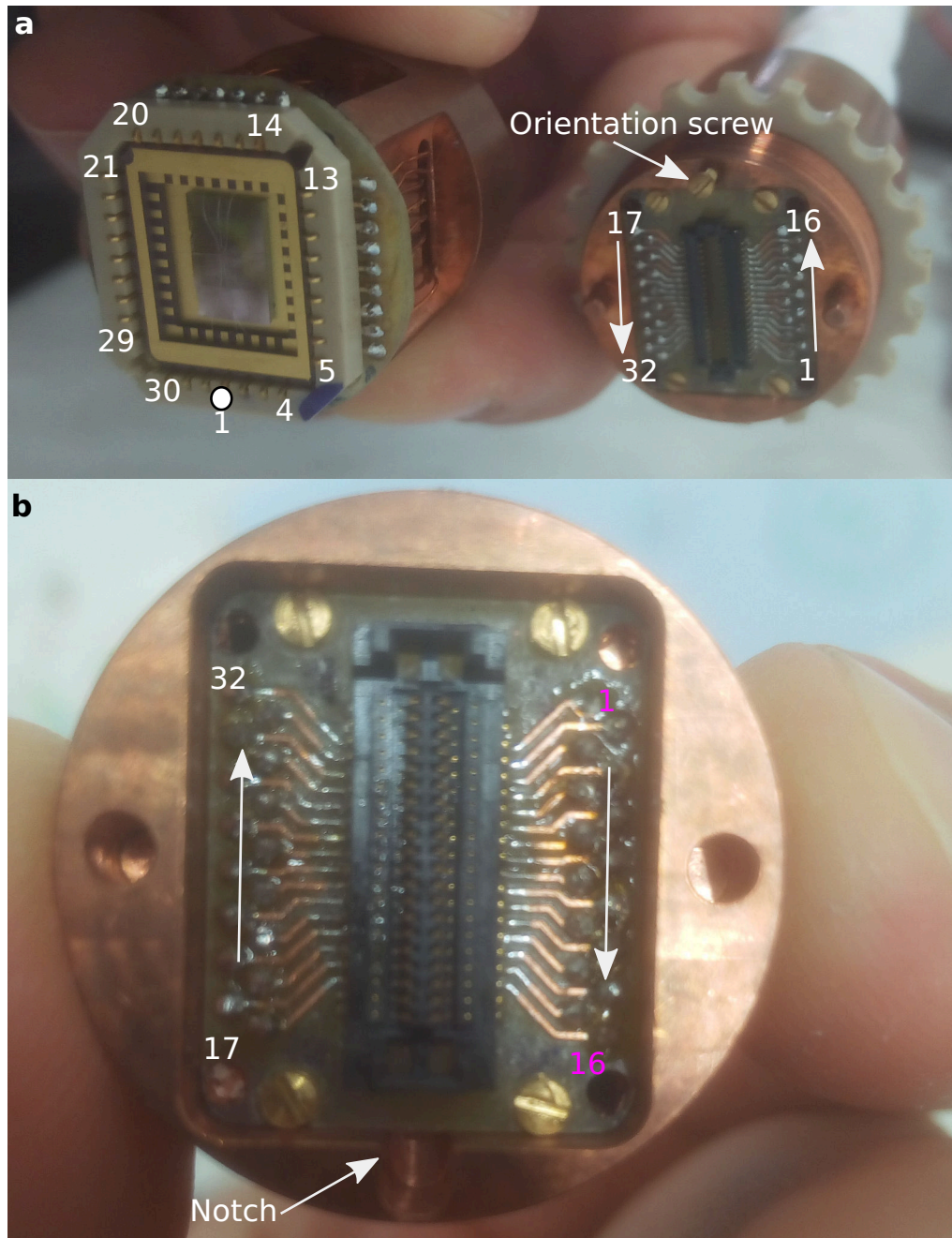
Figure A.3: Pin assignment on the Samtec connector on the puck and on the measuring insert.

A.3   Breakout Box

To fabricate one breakout box the following components are used and connected as shown in Fig. A.4.

1. 32 two row, 3 position (DPDT) switches 5A@250V RS Pro (RS 734-7050)

2. 32 straight BNC connectors $50\,\Omega$ RS Pro (RS 546-4897)

3. 44 pin HD D-Sub female connector (RS 691-9048)

4. 4 mm (banana) connector for GND
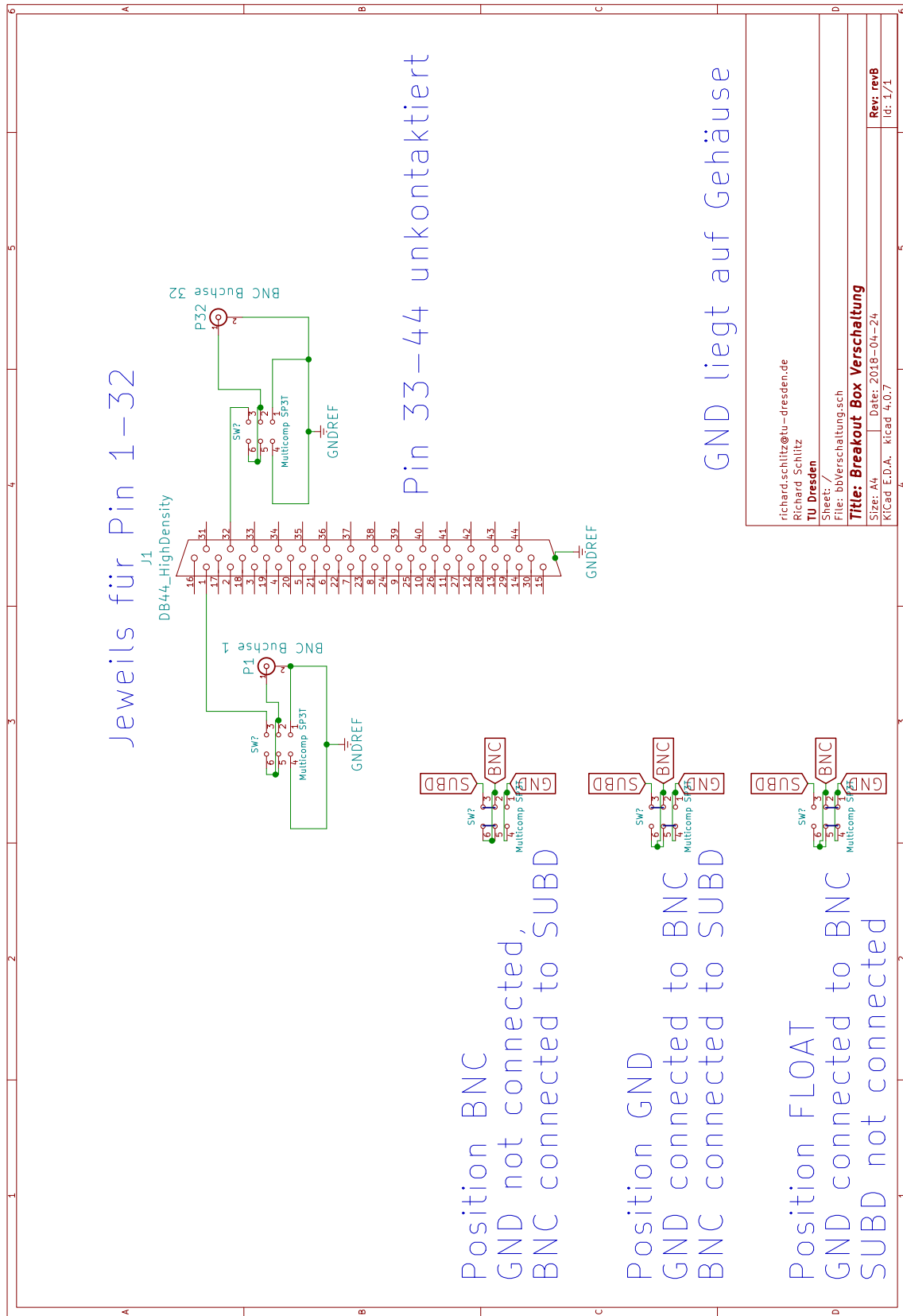
Figure A.4: Schematic of the breakout box wiring

Appendix B

SPINNING HALL MEASUREMENT APPROACH

To remove spurious voltages given by geometric misalignments of a Hall cross or bar (e.g. due to lithography) one can utilize the so-called "spinning Hall" technique for measuring the Hall voltage. This technique, being discussed in the following, develops its full potential in the temperature dependent determination of the Hall effect. Here, the offset signals can change dramatically and thus overshadow the Hall signal. To accomplish a separation of the Hall and offset voltages, one applies a current i to two of the four measurement contacts V_1 to V_4 once along the Hall bar (c.f. Fig. B.1(a)) and once perpendicular (c.f. Fig. B.1(b)).

The approach for the separation of the offset signal and the extraction of the Hall signal is originally described in Ref. [246]. The following deviation closely resembles the calculations shown in this reference.

To get an equivalent schematic for a Hall cross, one can represent this Hall device by four resistors. To that end, one considers a resistance network as shown in Fig. B.1 (a) and (b). In a perfect (homogeneous and symmetric) Hall cross, all resistors would have an equal resistance R and the voltage that is measured transverse to the current direction will be only the Hall voltage V_H. In a real system, however, there can be a slight imbalance due to inhomogeneities or fabrication errors. This is considered in the resistance network by adding and subtracting a small additional resistance r on one of the vertical branches.

We will focus on the ensuing changes first for vertically flowing current (c.f. Fig. B.1 (a). Here, the resistance imbalance between the lower part of the left and right leg will lead to a change of the voltage on the V_2 node with respect to the V_4 node. Consequently, a small offset will be present in the transverse voltage $V_t^\downarrow$ even in addition to the Hall
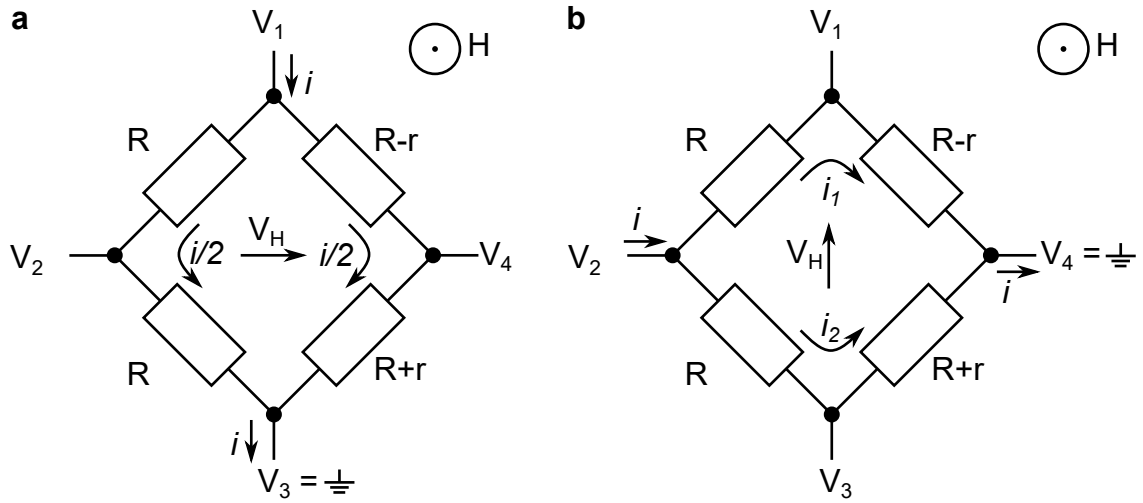
Figure B.1: The equivalent circuit for a Hall cross with vertically and horizontally flowing current is shown in panels (a) and (b), respectively. The Hall voltage is given by the cross product of the (total) current and the magnetic field directions and therefore changes its orientation when the current is rotated.

voltage when the current is flowing vertically:

$$V_t^{\downarrow} = V_2 - V_4 = \frac{(R-r)i}{2} - \frac{Ri}{2} + V_H = -\frac{ri}{2} + V_H \tag{B.1}$$

For Eq. (B.1) we assume that V_3 is GND.

When we now rotate our voltage and current contacts and consider V_4 as GND (c.f. Fig. B.1 (b)), the transverse voltage is now:

$$V_t^{\rightarrow} = V_3 - V_1 = Ri_2 - Ri_1 + V_H \tag{B.2}$$

Here, the current shares in the two branches i_1 and i_2 are not equal anymore (the resistance is not the same) Thus, we need to calculate the two currents first. This is accomplished by solving the following equation system

$$i = i_1 + i_2 \tag{B.3}$$

$$(R+r)i_1 + Ri_1 = (R-r)i_2 + Ri_2 \tag{B.4}$$

$$\implies i_1 = i\frac{2R-r}{4R}, \ i_2 = i\frac{2R+r}{4R}. \tag{B.5}$$

The result can then be put into Eq. (B.2) to obtain

$$V_t^{\rightarrow} = Ri_2 - Ri_1 + V_H = \frac{ri}{2} + V_H. \tag{B.6}$$

We can see, that the offset is now present with opposite sign, while the Hall voltage has

the same sign for both configurations. This can be motivated by considering that the Hall voltage is given by a cross product between the current direction and the magnetic field. As such, when the current is rotated (perpendicular to the magnetic field), also the resulting Hall voltage will rotate.

To finally disentangle the Hall signal and the offset, we combine the transverse voltages for both directions as follows

$$V_t^{SH} = \frac{V_t^{\downarrow} + V_t^{\rightarrow}}{2} = V_H \tag{B.7}$$

$$V_t^{offset} = \frac{V_t^{\downarrow} - V_t^{\rightarrow}}{2} = \frac{ri}{2} \tag{B.8}$$

There are still limitations to this technique which can partially be mitigated as detailed in Sec. 2.6 by additionally using a current reversal technique. However, drifts (e.g. fast changes in temperature or field) can still give rise to spurious signals since the readings for two directions are not taken instantaneously. Nevertheless this technique significantly helps to reduce the size of the offset signals. As long as a constant current is used, this technique is also applicable in Hall bar like structures, although one has to be careful not to heat the side contacts of the Hall bar (they are narrower and thus carry a higher current density).

Please note, that for applying this technique the contact polarities have to be carefully monitored. Otherwise, it is easy to get wrong results (e.g. wrong sign of the Hall voltage or offset mistaken for Hall signal). This is usually not problematic for FDMR measurements, since additional measures to verify the correctness of the signal are possible. During a temperature sweep with constant magnetic field, however, this is not straight forward.

Two exemplary angle resolved measurements on a Pt(3 nm) on CoFeB(5 nm) Hall bar on an Al_2O_3 substrate are shown in Fig. B.2. For these measurements the magnetic field of $\mu_0 H_{ext} = 1.1$ T was rotated either in plane (ip, (a)) or out of plane around the current direction (oopj, (b)). For the prior, one would not expect to observe a Hall effect at all but only the transverse magnetoresistance which is expected to show a $\cos(\alpha)\sin(\alpha)$ dependence. In the latter, however, the Hall effect should be clearly visible.

The respective upper panel in Fig. B.2 depicts the raw data for the two current directions while the spinning Hall V_t^{SH} and the offset V_t^{offset} signal are shown in the lower panels. Please note that for easier comparison the axis of $V_t^{\rightarrow}$ has been mirrored on the x-axis to superimpose the two curves. If depicted like this, one needs to "visually add" the two curves to get the difference (i.e. offset) signal and "visually subtract" the raw data to obtain the sum (i.e. spinning Hall) signal.

When looking at the raw data (c.f. Fig. B.2 upper panels) one can see a difference between the two raw measurements for both rotation planes. As detailed above, this difference can be understood as the spinning Hall signal, i.e. that there is a small Hall-like contribution also for the ip rotation. We will now focus first on the in-plane data (Fig. B.2 (a)), since here some more details and features of the spinning Hall approach become evident.
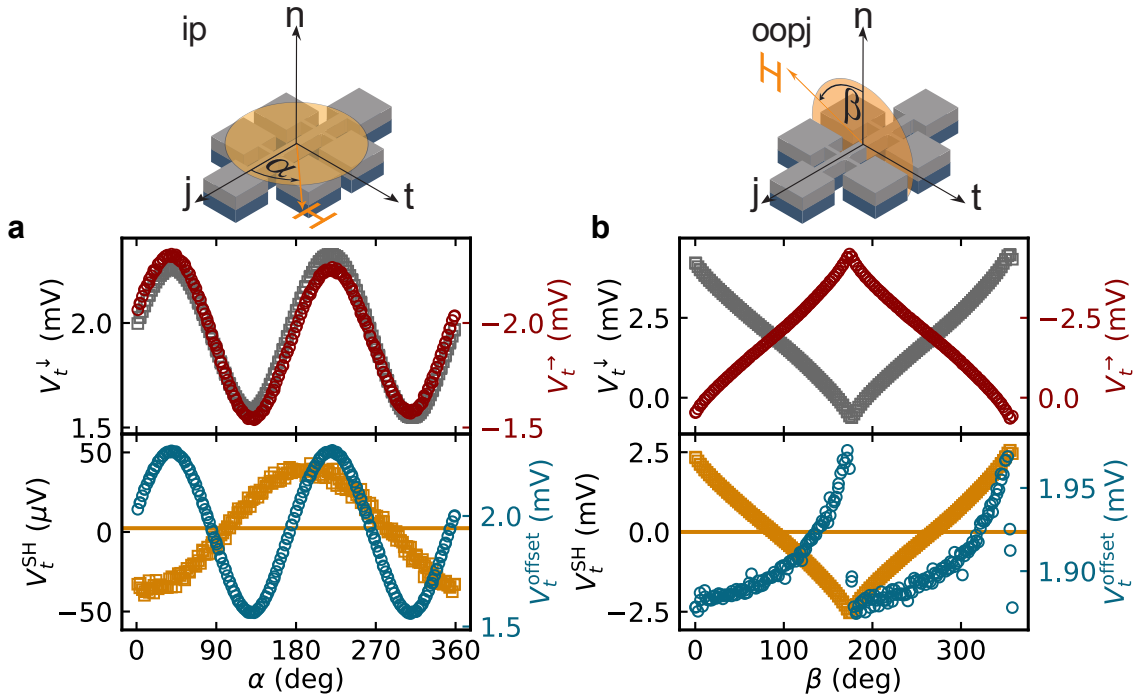
Figure B.2: Panels a) and b) show the spinning Hall method applied during an in-plane and out of plane rotation of the magnetic field. The upper panels show the raw voltages for the two current directions, while the lower panels show the spinning Hall and offset signals. The horizontal line in the lower panel is the mean value of the Hall voltage and has a value of $\overline{V_t^{\text{SH}}} = 2.4\,\mu\text{V}$ and $0.4\,\mu\text{V}$ for panel a) and b) respectively. Please note, the smaller range for V_t^{SH} as well as the mirrored scale for $V_t^{\rightarrow}$.

Firstly, the small Hall signal most likely stems from a small misalignment of the measurement insert in the Halbach magnet. Additionally, the mean signal of the spinning Hall signal $\overline{V_t^{\text{SH}}}$, graphically represented by the turmeric line in Fig. B.2 (a), is small compared to the Hall amplitude even though the Hall signal is caused only by a small misalignment.

Secondly, as detailed above, an additional transverse voltage from the transverse magnetoresistance (also named planar Hall effect) is expected for the ip rotation. One might ask at this point why this signal does not show up in the spinning Hall voltage as well but in the offset voltage. To understand this, the origin of the transverse magnetoresistance will be considered: It stems from a modulation of the resistance governed by the angle between the magnetization and the current direction (AMR) or transverse direction (SMR). As both of these directions will rotate when the current is rotated by 90° in the spinning Hall approach, also the sign of the planar Hall effect will invert (i.e. the $\cos(\alpha)\sin(\alpha)$ modulation is shifted by 90°). Thus, also the planar Hall effect is antisymmetric for the two current directions and therefore enters into the offset signal and not the spinning Hall signal.

For the oopj rotation, the separation clearly works. The spinning Hall signal essentially has no offset and a clear Hall like symmetry. Please note, that the triangular shape of the curve is caused by the shape anisotropy of the thin magnetic CoFeB film. Because of the anisotropy, the magnetization does not align with the magnetic field for all angles of the applied magnetic field. Considering the offset signal, one can also find a small modulation with the magnetic field. This most likely is the consequence of a small reorientation of the in-plane projection of the magnetic field during the rotation (i.e. misalignment of the rotation plane).

As so often in science, we usually do not start by a systematic calculation but often quickly prepare something to discuss. Since I promised to do so, the first derivation on a sheet of paper is included in this work. Obviously, it was presented and discussed during our usual after lunch coffee break.

$$U_{off} = -V_{13}\frac{r}{2R}$$

$$V_3 = ?$$

$$V_4 = \frac{V_{13}}{\ \ \ 2R}$$

$$\Rightarrow \quad \frac{i}{2}R + \frac{i}{2}R \longrightarrow$$

$$V_4 = \frac{i}{2}\cdot R$$

$$V_2 = \frac{i}{2}\cdot(R-r)$$
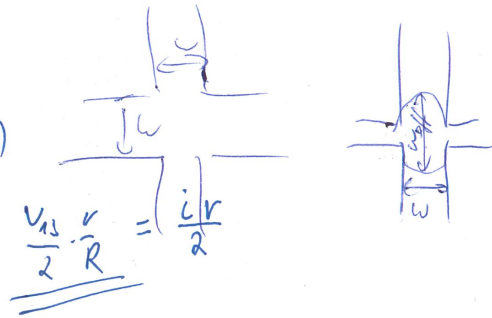
$$\Rightarrow V_4 = \frac{V_{13}}{2} - \frac{V_{13}}{2R}(R-r)$$

$$= \frac{V_{13}}{2}\cdot\left(1 - 1 + \frac{r}{R}\right) = \frac{V_{13}}{2}\cdot\frac{r}{R} = \frac{i\,r}{2}$$

$$i = V_{13}/R$$

$$V_4 = ? \qquad \rightarrow V_1 = R\cdot i^1$$
$$V_3 = R\cdot i^2$$

$$i = i^1 + i^2$$

$$i^1 = \frac{V_{24}}{2R-r} \qquad i^2 = \frac{V_{24}}{2R+r} \qquad = V_{24}\cdot\frac{2r+4R}{4R^2-r^2}$$

$$V_{13} = V_{24}\left(\frac{R}{2R-r} - \frac{R}{2R+r}\right) = V_{24}\left(\frac{R\cdot(2R+r) - R(2R-r)}{(2R-r)(2R+r)}\right) = V_{24}\left(\frac{2R^2+Rr - 2R^2+Rr}{4R^2-r^2}\right)$$

$$= V_{24}\frac{2Rr}{4R^2-r^2} = \frac{i^1}{2}r$$
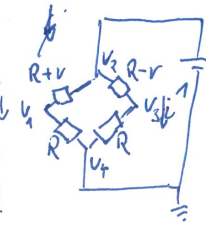
Appendix C

---

matrix Measurement Software

In the course of this thesis a measurement program was written in Python. The core of the measurement program is the *device_library*. This library contains all drivers for the measurement devices and handles the low level device communications. On top of this library, a tool chain was implemented to allow carrying out transport and other measurements. At the core of this tool chain lies the command line program "*matrix*" the first version of which was programmed by Andy Thomas (IFW Dresden)[1]. This program essentially is a "looper", which gets three filenames as input parameters. The first of those is the system file, where the devices present in the setup are defined in a transparent way (essentially wrapping the *device_library*): For the experiment it is convenient to not expose the devices directly but to access "parameters" (e.g. drive current or magnetic field). In the system file a set of parameters and their relation to the devices (i.e. a set and a read function) is defined. The second file is the input file. Here, the parameter values which are to be set (e.g. drive current magnitude) are defined line by line as can be seen in the following exemplary input file implementing a delta measurement.

```
-a 100e-6
-a -100e-6
-a 100e-6
-a -100e-6
```

Here, parameter "a" (e.g. drive current connected to the output current of a Keithley 2450 in the system file) would be set to $100\,\mu A$. Please note, that all units are supposed to be standard SI units. After the parameter values have been applied to the system, all parameters would be read from the devices (e.g. drive current read-back for parameter

---

[1] The whole software can be found in Andy Thomas' (private) Github repository. For questions regarding the distribution of the software, please contact him (a.thomas@ifw-dresden.de)

"a"). The read out values will then be written to the output file, which is the third file passed to the "*matrix*" program. After writing the output to the file, the next line will be read from the input file (i.e. in this example inverting the current polarity) until all lines have been completed. If a parameter is not present in the input file (e.g. parameter "b") but defined in the system, no commands will be issued to the corresponding device (e.g. magnetic field stays unchanged). Here, there can be the exception of a trigger function, which does not apply any value to the device but instead only triggers the device. This then is defined in the corresponding system and is done for example for the Keithley 2182 nanovoltmeter.

In addition to the command line programs, the tool chain has some graphical user interface programs to improve its usability. A flowchart displaying the typical use of the different tools is displayed in Fig. C.1.
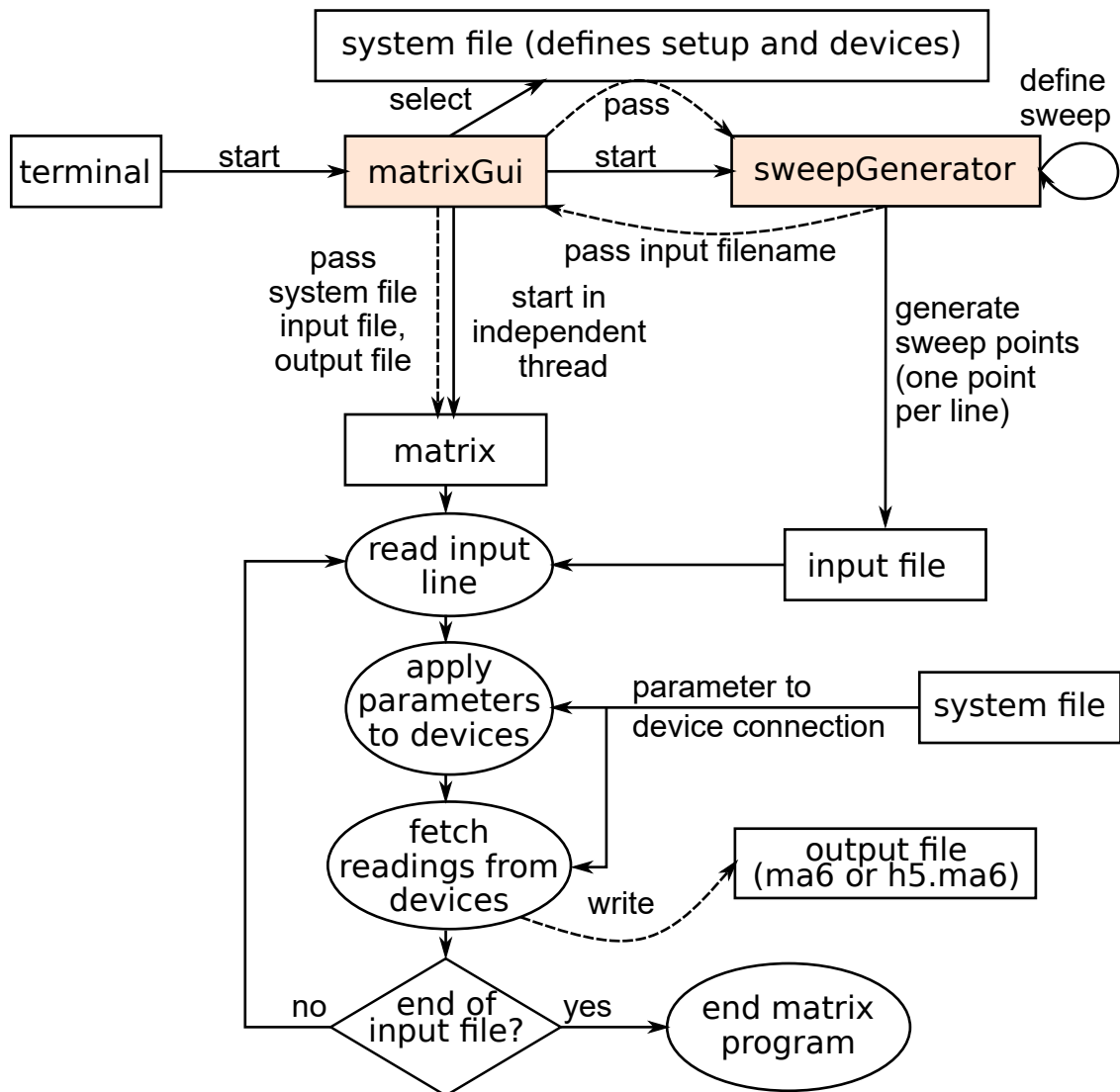
Figure C.1: Flowchart describing the program flow for a measurement. The highlighted boxes are the programs of the tool chain with a graphical user interface.

Appendix D

CALCULATION OF THE SATURATION MAGNETIZATION OF $Y_3Fe_5O_{12}$

The parameters, taken from Ref. [177], used for calculating the saturation magnetization of YIG in conjunction with the code below are summarized in Tab. D.1

	magnetization	spin S	g-factor	exchange constant
octahedral sublattice	75.8 emu/g	5/2	2	$\lambda_{11} = 47\,820$ Oe g/emu
tetrahedral sublattice	113.7 emu/g	5/2	2	$\lambda_{22} = 22\,394$ Oe g/emu
inter-sublattice				$\lambda_{12} = 71\,505$ Oe g/emu

Table D.1: Parameters used for the calculation of the saturation magnetizion of YIG as a function temperature. Taken from Ref. [177]

```python
from pylab import *
from scipy.optimize import fsolve

#functions definition
def Brillouin(S,x):
    return (((2 *S + 1 )/(2*S)) *
            1/(tanh(((2* S + 1 )* x/(2* S)))) -
            1/(2* S)* 1/(tanh(x/(2* S))));

#constants section
muBZahl = 9.27400915e-21   # erg/gauss
kBZahl = 1.3806488e-16   # erg/K
```

```python
# magnetization of the two sublattices (sorry for CGS!)
M10=75.8   # emu/g
M20=113.7   # emu/g

# Spin for two sublattices
S1=5./2.
S2=5./2.

# g-Factors for the two sublattices
g1=2.00
g2=2.00

sg1=1
sg2=1

# Exchange parameters Oe g/emu, see
# Anderson PhysRev. 143 A1581
l11wd=47820.
l22wd=22394.
l12wd=-71505.
# Please note that the - sign for l12wd is due to the exact
# definition of the equation system and numerics issues.
# It is used to establish the antiferromagnetic coupling.

# temperature range, Tlow must be >=1
Tlow=1 #in K
Thigh=650 #in K
res=0.5 #in K
length = int((Thigh-Tlow)//res + 1)

# variable initialization
M1all=zeros(length)
M2all=zeros(length)

# equations we want to solve, for furthe detail please ask :)
def equations(p,S1_,S2_,g1_,g2_,sg1_,sg2_,T_):
    M1, M2 = p
    H0 = 0
    out = [(M10*Brillouin(S1_,
                ((S1_* g1_* muBZahl)/(kBZahl* T_) *
                (l11wd * sg1_*M1 + l12wd* sg2_*M2 + H0))) -
            sign(l11wd * sg1_*M1 + l12wd* sg2_*M2 + H0)*M1)]
```

```python
    out.append((M20*Brillouin(S2_,
            ((S2_* g2_* muBZahl)/(kBZahl* T_) *
            (l12wd * sg1_*M1 + l22wd* sg2_*M2 + H0))) -
        sign((l12wd * sg1_*M1 + l22wd* sg2_*M2 + H0))*M2))
    return out

#look for solution
tcalc = linspace(Tlow, Thigh, length)
for i, t in enumerate(tcalc):
    M1all[i], M2all[i] =  fsolve(equations,[M10,M20],
                                (S1,S2,g1,g2,sg1,sg2,t))

Mnet = M2all-M1all

# plot solution, to get from emu/g to kA/m we need
# the density of YIG, which is 5.167g/cm^3
plot(tcalc,array(Mnet)*5.172,label='Mtot')
plot(tcalc,array(M1all)*5.172,c='yellow',label='MFe,a')
plot(tcalc,array(M2all)*5.172,c='black',label='MFe,d')
legend()
show()

# print the temperature und the magnetization, where the
# latter vanishes
print(tcalc[array(Mnet < 1)], Mnet[array(Mnet < 1)])

###
plt.plot(tcalc,array(Mnet)*5.172,label='Mtot')
show()
```

Appendix E

3D STONER-WOHLFAHRT MODEL TO SIMULATE THE ORIENTATION OF THE MAGNETIZATION

A 3D Stoner-Wohlfahrt simulation[205] was programmed using Python. It solves the following equation system for the direction of the normalized magnetizion $\mathbf{m}$ in spherical coordinates by minimizing the free energy F.

$$F = E_{\text{Zeeman}} + E_{\text{aniso,1}} + E_{\text{aniso,2}} \tag{E.1}$$

$$E_{\text{Zeeman}} = -\mu_0 \mathbf{H} \cdot \mathbf{m} \tag{E.2}$$

$$E_{\text{aniso,1}} = -\mu_0 (\mathbf{H}_{\text{aniso,1}} \cdot \mathbf{m})^2 \tag{E.3}$$

$$E_{\text{aniso,1}} = -\mu_0 (\mathbf{H}_{\text{aniso,2}} \cdot \mathbf{m})^2, \tag{E.4}$$

where $\mathbf{H}$ is the external magnetic field, $\mathbf{H}_{\text{aniso,i}}$ parametrizes the stength and direction of anisotropy i and m is the normalized magnetization. All energies are calculated in units of magnetic flux for the calculation. Plase note, that the dot product in spherical coordinates has be used, which is slightly more complicated (see code).

The solution is then used to model the contributions of the ordinary, anomalous and topological Hall to the complete Hall signal (c.f. Eq. (6.5) to Eq. (6.8)). Additionally, two solutions are compared, where the second one incorporates a finite misalignment of the magnetic field with respect to the uniaxial anisotropy. Thus, the impact of a misalignment of the sample normal between different measurements can be estimated. This allowed to motivate the presence of artifacts in the topological Hall/Nernst signal in Ch. 6.

```python
from pylab import *
from scipy.optimize import minimize

clr_rs = ["dimgrey", "darkred", "#D17F02", "#066682",
```

```python
            "saddlebrown", "#70068A", "darkgreen"]

# import plotting helper to have nice graph layouts
# include these three lines if ifwlib is available
#from ifwlib.evalLib import initPlottingMetric, clr_rs
#initPlottingMetric(plt, fw=80, fh=56,
#                   change_prop_cycler="rs")

mu0 = 4e-7/pi

# azimuth and polar angle of magnetic field
alpha1 = 0.0
beta1 = pi/2
# azimuth and polar angle of anisotropy one (uniaxial
# magnetocrystalline)
phi = 0
theta = 0
# azimuth and polar angle of anisotropy two
# (shape anisotropy)
phi2 = 2*pi/4
theta2 = pi/2
# strength of uniaxial anisotropy (- for hard axis)
Haniso1 = -1.2/mu0
# strength of second (shape) anisotropy (- for hard axis)
Haniso2 = 0.2/mu0

# free energy consisting of zeeman and the two anisotropy
# energies x[0] is azimuth, x[1] is polar angle of
# magnetization
def f(x, h, alpha, beta):
    zeeman = -mu0*h*(sin(beta)*sin(x[1])*cos(x[0] - alpha) +
                     cos(beta)*cos(x[1]))
    aniso = -mu0*Haniso1/2*pow((sin(theta)*sin(x[1]) *
                               cos(x[0]-phi) +
                               cos(theta)*cos(x[1])), 2)
    aniso2 = -mu0*Haniso2/2*pow((sin(theta2)*sin(x[1]) *
                                cos(x[0]-phi2) +
                                cos(theta2)*cos(x[1])), 2)
    return zeeman+aniso+aniso2

# initialize vector for solution
solution = zeros((2002, 3))
```

```python
# inital values is field orientations
x0 = [alpha1, beta1]
# define sweep parameters (+1T to -1T)
hs = linspace(1/mu0, -1/mu0, 1001)
# calculate the solution for up and down sweep
# (hs[::-1] inverts array)
for i, h in enumerate(concatenate([hs, hs[::-1]])):
    # get the solution
    res = minimize(f, x0, (h, alpha1, beta1), tol=1e-19)
    # store the solution (*res.x unpacks the values
    # the solution, i.e. x[0] and x[1])
    solution[i] = [h, *res.x]
    # generate initial value for next step and add
    # some noise (activiation energy)
    x0 = res.x+(ranf()-0.5)*20e-5

fig, ax = subplots(1,1,sharex="col", sharey="col")

# Only plot positive fields and only one sweep direction
posmask = solution[:,0]>0
posmask[1001:] = 0

# define functional for topo Hall, makes a bump with
# amplitude +-0.3 at position +- center, width of
# bump is controlled by width
def the (x, center, amp=0.33, width=30):
    return (amp*(tanh((x+center)**2*width) -
               tanh((x-center)**2*30)))

# initialize storage list for labels
lns = []
# M
lns += ax.plot(solution[posmask, 0]*mu0,
               cos(solution[posmask,1]),
               c=clr_rs[0], label="$M$")

ax2 = ax.twinx()
# THE
lns += ax2.plot(solution[posmask,0]*mu0,
               the(mu0*solution[posmask,0],0.3),
               "--", c=clr_rs[3],
               label=r"$\rho_\mathrm{xy}^\mathrm{THE}$")
# AHE
```

```python
lns += ax2.plot(solution[posmask,0]*mu0,
                0.9*cos(solution[posmask, 1]),
                "--", c=clr_rs[2],
                label=r"$\rho_\mathrm{xy}^\mathrm{AHE}$")
# rhoxy
lns += ax2.plot(solution[posmask,0]*mu0,
                0.9*cos(solution[posmask,1]) +
                the(solution[posmask, 0]*mu0, 0.3) +
                0.3*solution[posmask, 0]*mu0, c=clr_rs[1],
                label=r"$\rho_\mathrm{xy}$")
# OHE
lns += ax2.plot(solution[posmask,0]*mu0,
                0.3*solution[posmask, 0]*mu0,
                "--", c=clr_rs[5],
                label=r"$\rho_\mathrm{xy}^\mathrm{OHE}$")

# legend
labs = [l.get_label() for l in lns]
ax2.legend(lns, labs, ncol=2, loc=(0.39, 0.18))

# labels and ticks
ax.set_xlabel(r"$\mu_0 H$ (T)")
ax.set_ylabel(r"$M (H)$")
ax2.set_ylabel(r"$\rho_\mathrm{xy} (H)$", color=clr_rs[1])
ax.set_xticks(linspace(0,1,6))
ax2.set_yticks([0, 0.9])
ax.text(0.03, 1.3, r"$\mu_0 H_\mathrm{s}$", color=clr_rs[4])
ax.set_yticks([0, 1])
ax2.set_yticklabels(["0",
                     r"$\rho_\mathrm{xy}^\mathrm{A}$"])
ax.set_yticklabels(["0", r"$M_\mathrm{s}$"])
# saturation field
ax.axvline(0.2, linestyle="--", color=clr_rs[4])

#match limits
ax.set_ylim(ax2.get_ylim())

# save figure
fig.savefig("Hall_components.pdf",
            bbox_inches="tight",
            pad_inches=0.02)

# azimuth and polar angle of magnetic field
```

```python
alpha2 = 0.1
beta2 = pi/2
## initialize vector for solution2
solution2 = zeros((2002, 3))

# inital values is field orientations
x0 = [alpha2, beta2]
# define sweep parameters (+1T to -1T)
hs = linspace(1/mu0, -1/mu0, 1001)
# calculate the solution for up and down sweep
# (hs[::-1] inverts array)
for i, h in enumerate(concatenate([hs, hs[::-1]])):
    # get the solution
    res = minimize(f, x0, (h, alpha2, beta2), tol=1e-19)
    # store the solution (*res.x unpacks the values
    # the solution, i.e. x[0] and x[1])
    solution2[i] = [h, *res.x]
    # generate initial value for next step and add
    # some noise (activiation energy)
    x0 = res.x+(ranf()-0.5)*20e-5

fig, ax = subplots(1,1,sharex="col", sharey="col")

# get lines
lns = []
# M
lns += ax.plot(solution2[posmask, 0]*mu0,
               cos(solution2[posmask,1]),
               label="$M(H)$ [5deg tilted]",
               c=clr_rs[0])

ax2 = ax.twinx()
# rhoxy (only ahe)
lns += ax2.plot(solution[posmask,0]*mu0,
                0.9*cos(solution[posmask,1]),
                c=clr_rs[1],
                label=r"$\rho_\mathrm{xy}(H)$" +
                "[no OHE/THE]")
# THE extracted by subtraction
lns += ax2.plot(solution[posmask,0]*mu0,
                0.9*cos(solution[posmask,1]) -
                0.9*cos(solution2[posmask,1]),
                "--", c=clr_rs[3],
```

```python
                        label=r"$\rho_\mathrm{xy}(H) - " +
                        r"\rho_\mathrm{xy}^\mathrm{A}" +
                        r"\dfrac{M(H)}{M_\mathrm{s}}$")

# legend
labs = [l.get_label() for l in lns]
ax2.legend(lns, labs, loc=(0.22, 0.2))

# labels and ticks
ax.set_xlabel(r"$\mu_0 H$ (T)")
ax.set_ylabel(r"$M (H)$")
ax2.set_ylabel(r"$\rho_\mathrm{xy} (H)$",
              color=clr_rs[1])
ax2.set_yticks([0, 0.9])
ax.set_yticks([0, 1])
ax2.set_yticklabels(["0",
                     r"$\rho_\mathrm{xy}^\mathrm{A}$"])
ax.set_yticklabels(["0", r"$M_\mathrm{s}$"])

# match limits
ax2.set_ylim(ax.get_ylim())

# save figure
fig.savefig("Hall_misalignment.pdf",
            bbox_inches="tight",
            pad_inches=0.02)
```

ACKNOWLEDGMENTS

I am very grateful for the help I received from many many people in the course of this thesis work. Without all the staff, students and other fellow scientists keeping everything crowded and alive, doing science would not even be half the fun it is. Additionally, I am highly grateful for all the fruitful and interesting discussions I had with many scientists at conferences, seminars and other outings, allowing to exchange and test new ideas. Furthermore, I would like to thank all reviewers for their incredible job, making sure that science stays sane. Because there are more people I should thank than I can list here, I limit myself to the following people, and hope that the ones not named here find it in their heart to forgive me :). In particular, I want to thank:

- Prof. Dr. Sebastian T. B. Goennenwein for being into science as much as he is! For having an open door and thus inviting scientific, technical and other discussions. For his keen insights and annoying questions, forcing me to further improve and sharpen my arguments and manuscripts. Without his comments, his scientific integrity and honesty I would not have been able to accomplish as much as I have. Also thank you for your support and trust with regard to designing and equipping the labs and the involved spending of money for new or different lab equipment. I hope you are not disappointed with how it turned out ;). And of course for the opportunity to do my thesis work in your group.

- Prof. Dr. Felix Casanova for agreeing to review my thesis on such short notice, and for the enlightening discussions during his visit to Dresden.

- Prof. Dr. Kornelius Nielsch for hosting me at the IFW, allowing me access to the MST as well as all the other facilities available there.

- Dr. Andy Thomas for being my go to person to discuss details of plotting and the software, for providing the skeleton upon which the software is built and for being a nice sociable person to talk to. For supporting me with his insight into telling

a good story and also for allowing me to participate in many of the IMW specific activities (most notably the PhD seminar). We undertook many endeavors trying to understand puzzling pieces of network technology, often unsuccessful.

- Dr. Helena Reichlova for carrying out, pushing and organizing the experiments on Mn_3Sn and Co_2MnGa which I participated in. For sharing her keen insights into spin orbit torques in antiferromagnets and the related switching processes. For showing me that science can also be done successfully in a very relaxed and calm fashion, and for amazing me with her literature knowledge about nearly any topic we ever discussed about. Finally, for being a good moral compass, showing me the value of a good team and personal integrity above success.

- Dr. Savio Fabretti for preparing many of the sputtered samples I used during my time as PhD student, most importantly the as-sputtered YIG films. For being my go-to (half!) Italian in the group. For several evenings together building my kitchen and making home-made pizza. For funny discussions during our regular morning coffee about the optimization of pizza growth.

- Dr. Mathias Doerr for managing the Helium supply and always checking whether I forgot to communicate my requirements (which I have to confess happened rather frequently). For being incredibly knowledgeable in all matters associated with low temperatures, for sharing his history in the scientific community of the DDR and how it was "back in the old days". For his patience with the students and for his joy in teaching them physics.

- Dr. Sergey Granovsky for taking care of a lot of the infrastructure at the IFMP, for providing countless dewars of liquid nitrogen and for filling Helium in many setups. And for providing me with "this or that cable/adapter" I came asking for rather often.

- Dr. Dominik Kriegner for being the person to discuss "measurement software, crystal Hall and the OSCAR cryostat". I experienced your presence at the institute as having someone very thorough, accurate and Austrian around. It was great to see your passion about clean coding and proper conception of code structures. Thank you for all the discussions about the crystal Hall, the related science, and about how to improve the measurement programs and your help in implementing the improvements.

- Dr. Tobias Kosub for providing all the Cr_2O_3/X samples used for the measurements in this thesis as well as discussions about the origin of the anomalous Hall effect and the (spin Hall) magnetoresistance in these samples, and for several interesting discussions about measurement techniques and the current limits of electrical measurement hardware.

- Dr. Denys Makarov for enlightening discussions and his critical questioning regarding the "simple" models I often put forward in the early stages of the magnetoresistance experiments on Cr_2O_3/Pt.

- Elke Wachsmuth and Noreen Damme for keeping everything in order and forcing me to also complete the important (i.e. non-scientific) work. In particular to Elke: Thank you for ordering almost all lab equipment I bought, and for keeping a lookout for missing open orders.

- Felicitas Schlitz for proof reading the important parts of my thesis and using all her skills acquired during her studies to answer my question about English tenses.

- All other (PhD) students at the IFMP, the other parts of TUD, the IFW, the HZDR and MPI CPfS not addressed so far, for taking me in and for having many enjoyable (long) evenings, playing cards and eating good food and for providing such a nice surrounding of complaints and desperation ;).

- Last but not least, the cleaning and technical staff of the Technische Universität Dresden for keeping the university and labs an enjoyable and functional place to be in, which I think is a crucial contribution to our research work.

This is the end...

… or maybe just the beginning :)

VERSICHERUNG

Hiermit versichere ich, dass ich die vorliegende Arbeit ohne unzulässige Hilfe Dritter und ohne Benutzung anderer als der angegebenen Hilfsmittel angefertigt habe; die aus fremden Quellen direkt oder indirekt übernommenen Gedanken sind als solche kenntlich gemacht. Die Arbeit wurde bisher weder im Inland noch im Ausland in gleicher oder ähnlicher Form einer anderen Prüfungsbehörde vorgelegt.

Die Arbeit wurde an der Professur für Festkörperphysik am Insituts für Festkörper- und Materialphysik der Technischen Universität Dresden unter der wissenschaftlichen Betreuung von Prof. Dr. Sebastian T. B. Goennenwein angefertigt.

_____   _____
Ort, Datum   Unterschrift